MASARYK UNIVERSITY
Faculty of Science
Department of Condensed Matter Physics

&

IMEC Leuven, Belgium

Přemysl MARŠÍK

Advanced ellipsometric techniques and studies of low-*k* dielectric films

Doctoral thesis

Supervisor: prof. RNDr. Josef Humlíček, CSc.   Brno, 2009

Bibliografická identifikace (Bibliographical data)

Jméno a příjmení autora (First name and surname):

Přemysl Maršík

Název disertační práce (dissertation title CZ):

Pokročilé elipsometrické techniky a studie dielektrických vrstev s nízkou permitivitou

Název disertační práce anglicky (EN):

Advanced ellipsometric techniques and studies of low-*k* dielectric films

Studijní program (study program):

Fyzika (Physics)

Studijní obor (study branch):

Fyzika pevných látek (Solid state physics)

Školitelé (supervisors):

**Prof. RNDr. Josef Humlíček, CSc.
Mikhail Baklanov PhD.**

Rok obhajoby (year of defence):

2009

Klíčová slova v češtině (keywords CZ):

elipsometrie, tenké vrstvy, rotační kompenzátor, low-*k* dielektrika, porozita, elipsometrická porozimetrie, UV-kůra, zbytkový porogen, plazmové poškození

Klíčová slova v angličtině (EN):

ellipsometry, thin films, rotating compensator, low-*k* dielectrics, porosity, ellipsometric porosimetry, UV-cure, porogen residue, plasma damage

Abstrakt česky:

Disertace pokrývá dvě blízká témata: elipsometrickou metodologii a studium tenkých dielektrických vrstev. Tato práce zahrnovala i rekonstrukci elipsometru a vývoj potřebného softwaru pro zpracování a analýzu dat. V první části zopakujeme nezbytné teoretické základy a popíšeme základní elipsometrické konfigurace. Věnujeme se dvěma elipsometrickým konfiguracím: elipsometrii s rotačním analyzátorem (RAE) a s rotačním kompenzátorem (RCE). V případě RAE je vyvinuta kalibrační procedura pro neznámé nulové polohy polarizátoru a analyzátoru. V případě RCE jsou zformulovány elegantní rovnice pro redukci dat a navržen algoritmus pro kalibraci nulových poloh polarizátoru, analyzátoru a kompenzátoru. V měřených datech byly objeveny nežádoucí artefakty způsobené nedokonalostí kompenzátoru. Možný zdroj těchto artefaktů je diskutován a interpretace je podpořena simulacemi. Nakonec je zkoumán vliv artefaktů na kalibraci a zpracování dat a je navržen možný způsob ošetření výsledků.

Druhá část práce je zaměřena na elipsometrické určení optických vlastností dielektrik s nízkou permitivitou (low-k), určených pro izolaci metalizace v mikroelektronice, a jejich chování za různých podmínek typických pro tuto technologii. Studujeme porézní SiCOH materiály deponované plazmatickou technikou z chemických par (PECVD). Porosita je vytvořena ko-deponováním SiCOH matrice a dodatečné organické fáze (porogenu). Po depozici je porogen odstraněn žíháním a UV osvitem (UV-kúra) a jsou vytvořeny póry. Low-k materiály jsou také vystaveny různým plazmatům v technologii výroby mikroprocesorů. Všechny tyto kroky mají vliv na optické vlastnosti vrstev. Pozorované chování interpretujeme ve smyslu změn složení a naše závěry jsou podpořeny doplňkovými měřeními infračervené absorpce a elipsometrickou porozimetrií.

Abstract:

Thesis covers two related topics: ellipsometric methodology and studies of dielectric thin films. The work included reconstruction on an ellipsometric instrument and development of the necessary data acquisition and analysis software. In the first part, the necessary theoretical background is reviewed and the basic ellipsometric configurations are described. We focus on two ellipsometric configurations: the rotating analyzer (RAE) and the rotating compensator (RCE). In the case of RAE, a calibration process for unknown analyzer and polarizer offset is developed and implemented. In the case of RCE, we formulated elegant equations for data reduction and proposed algorithm for polarizer, analyzer and compensator offset calibration. We detected spurious artifacts in the actual data, related to a compensator imperfection. A possible source of the artifacts is discussed and the interpretation is validated by simulations. Finally, the impact of the artifacts on the calibration and data reduction procedure is examined and a possible treatment of the data is proposed.

The second part of the work is focused on the ellipsometric determination of the optical properties of low dielectric constant (low-k) films (for application as inter-metal dielectric in microelectronics) and their behavior under various conditions typical for the technology. We studied porous SiCOH materials deposited by plasma-enhanced chemical vapor deposition. The porosity is generated by co-deposition of the SiCOH matrix material with sacrificial organic phase (porogen). After the deposition, the porogen is removed by UV- assisted annealing (UV-cure), creating the pores. The low-k materials are exposed to various plasmas in the microprocessor fabrication technology. All these technological steps have effect on the optical properties of the films. We interpreted the observed behavior in terms of changes of composition and supported our conclusions by additional measurements: infrared absorption and ellipsometric porosimetry.

Contents

Introduction

In present days, ellipsometry is a widespread method for material research and technology. This work is oriented on ellipsometric techniques, both from the methodology point of view and as applied in dielectric thin film research. I devoted the first years of my PhD studies to upgrading our home-built ellipsometer for rotating compensator operation and extending its range into ultraviolet. Afterwards, I used heavily the ellipsometry in UV and VUV range and ellipsometric porosimetry for studying porous dielectric films for applications as low-k dielectric in microelectronics.

The first chapter is introducing ellipsometry, instrumentation and theoretical background. We start with description of polarized wave propagation in layered media, and develop a scheme needed for successful building of ellipsometric models and optimization. To achieve that, all the important formulas are presented including the relations for derivatives with respect to the internal parameters for implementation in gradient based optimization algorithms and for the following error propagation. Simple models of optical response of solids are briefly presented. The first chapter also includes a review of common ellipsometric configurations and describes the data acquisition, focus on signal and error processing in the case of ellipsometry with a rotating element (either analyzer or compensator).

Chapter 2 presents method for data calibration in rotating analyzer ellipsometry (RAE), with respect to analyzer and polarizer angular offsets.

Although the read-out of the angular position of the polarizers can be very accurate, the possible offsets between the actual plane of incidence, physical axes of the polarizing plates and the instrument scales must be taken into account. We adopted the idea of measurement of the ellipsometric parameters with multiple settings of the polarizer, followed by optimization of a proper model in the two dimensional parameter-space of the analyzer and polarizer offsets. Our approach is based on multiple measurements of the actual spectra of the sample, taken with various polarizer settings. Typically, two polarizer settings are chosen symmetrically ($P_1=-P_2$). Although this might be time consuming, the spectra are subsequently averaged, therefore the noise is reduced and possible systematic errors related to polarizer position symmetry might be removed. Appropriate handling of errors allows a proper weighting of the resulting spectra in the consequent analysis.

Chapter 3 is documenting my work on construction of the rotating compensator ellipsometer (RCE) and problems that emerged during the work. Operation of the RCE ellipsometer is described within the Jones vector – Mueller matrix framework. We show how the polarization state generated by the source, polarizer and the sample is analyzed by the detection branch: rotating compensator, analyzer and the detector, and how the measured signal is related to the parameters of the polarization state and therefore to the parameters of the sample. A proper parameterization of the signal leads to convenient formulas for the ellipsometric parameters. Further, we developed a method for analyzer and polarizer calibration based on the principles presented in chapter 2. The data analysis and calibration algorithm has been encoded into a computer program, briefly presented in the chapter. Based on the first actual measurements in RCE configuration, we started to study the impact of plate misalignment in multi-plate retarders. We propose a simple model for the simulation of the artifacts, and discuss their behavior in the calibration routines.

The next two chapters (4 and 5) cover my research of materials with low dielectric constant (low-*k*). We studied porous SiCOH materials deposited by plasma-enhanced chemical vapor deposition. The porosity is generated by the co-deposition of the SiCOH matrix material with sacrificial organic phase (porogen). After deposition, the porogen is removed by UV-assisted annealing (UV-cure), creating the pores. The low-*k* materials are exposed to various plasmas in the microprocessor fabrication technology.

The contemporary research on the low-*k* materials is focused on infrared and nuclear magnetic resonance spectroscopies, but almost nothing has been known about the optical properties in the visible and ultraviolet range. Chapter 4 presents ellipsometric measurements of the optical properties of low-*k* films in the range from 1.5 to 9 eV and their changes under various conditions relevant to the microelectronic technology (UV-cure, plasma exposure). By studying the constituents of the low-*k* material we are able to interpret the observed behavior in terms of the changes of composition, in particular, as the removal of the porogen. We support this interpretation with the measurement of open porosity using ellipsometric porosimetry and by infrared transmission measurements.

Chapter 5 contains experimental results aimed at optimization of the low-*k* material using two different UV-curing light sources: a monochromatic lamp with the photon energy of 7.2 eV, and a broadband lamp with lower photon energies (<6 eV). We have prepared a set of samples by varying the deposition and curing conditions, and performed an extensive analysis of the samples using spectroscopic ellipsometry, infrared transmission and ellipsometric porosimetry. We discuss the relation between the properties of the as-deposited and UV-cured samples and the amount of damage the material suffers after exposition to NH_3 cleaning plasma.

Chapter 1 : Ellipsometry on thin films

Introduction to ellipsometry and the applied techniques. Brief theoretical overview of light propagation in layered media. Notation and formalism. With help of Josef Humlíček, Eduard Schmidt, Alois Nebojsa

In this chapter we review the theoretical background for practical ellipsometry: After a brief introduction to the technique and instrumentation in section 1, we discuss in section 2 the parts of optics relevant to this work. The basics of wave optics are presented with focus on wave propagation in layered media. We develop propagation matrix formalism, using the Cartesian components of the wave-vector. For practical reasons, derivatives of the model are complete presented to be subsequently used for the error propagation, and in derivative-based optimization. Next, we shortly discuss the models of optical properties of materials needed for the spectroscopic data analysis, and review the formalism necessary to describe the polarization state of light. In the section 3 we describe the commonly used ellipsometry configurations and the data acquisition process for rotating-element ellipsometry with special attention to estimation of measurement errors. The chapter is summarized in section 4.

1.1.   What is ellipsometry?

1.1.1. Principle

Ellipsometry is an optical metrology technique based on detection of the polarization state of light interacting with planar specimen. The polarization state of the incident light is known. The change of the polarization state of the probing light is determined by the optical properties of the sample and by the thicknesses and properties of the layers present on the sample surface.

Ellipsometry is performed at a fixed nonzero angle of incidence or at multiple angles of incidence, giving additional independent data. The measurements can be performed at a single wavelength; however, spectroscopic operation usually provides significantly more information.

The technique allows a sensitive detection of structural parameters of layered samples; it is typically used for film thickness measurements in the technological applications where thin films are involved: planar technology in microelectronics, solar cells and display fabrication; or the deposition of protective coatings.

Optical properties, i.e. the dielectric response for the photon energies from the optical range; can be obtained from spectroscopic ellipsometry. They are related to the electronic and vibrational structure of measured materials.

The ellipsometric measurements are indirect and require an optimization of parameterized models to obtain the sought quantities.

1.1.2. History [1]

While the practical optics existed over centuries, the birth of its theory can be traced to 17th century when René Descartes[2] described several optical phenomena and was followed by Robert Hooke[3] and Isaac Newton[4] in explanation of the nature of light. The two great men actually disagreed over the topic. The Newtonian corpuscular theory was criticized by Hooke, whose ideas were inspiration for Christian Huygens[5] and his wave theory of light. It is relevant to mention that Newton showed the decomposition of white light to color spectrum using prisms. The refraction of light was also studied at the same time by Czech savant Jan Marcus Marci, unfortunately isolated from the scientific agitation of the western world.

Later, in the 19th century, Augustin-Jean Fresnel studied the interference and explained the behavior of light waves at the interface between two

---

[1] Inspired by lecture Brief History of Ellipsometry by Eugen A. Irene (presented in Ostuni, Italy 2008) with the help of www.wikipedia.org.
[2] Who served at Bílá hora (1620) in troops of Duke Maxmilian of Bavaria.
[3] Great experimentalist as well, "father of microscopy" and also important architect in reconstruction of London after Great Fire (1666).
[4] Let us mention without any dishonor that Newton devoted a part of his life to alchemy.
[5] Also famous watchmaker, patented pendulum clock and later pocket-watch.

Fig. 81.

Figure 1.1. Drawing from Drude's textbook.

media. Etienne-Louis Malus discovered the polarization by reflection and is known for the law describing the intensity transmitted through a couple of polarizers. The polarization properties of reflections were later explained by David Brewster, who studied also birefringence of crystals.

Treatise on Electricity and Magnetism by James Clerk Maxwell was published in 1873. This work contains the formulation of the equations for electromagnetic field and therefore creates the fundaments for the non-quantum optics.

Invention of ellipsometry is credited to Paul Drude, who described the instrument (fig. 1.1) in his "Lehrbuch der Optik", published in 1900. Drude used Nicol prisms as polarizers and Soleil-Babinet compensator.

In the 1930's, the setup was used for detection of thin surface films and the actual term "ellipsometer" appeared in the 1940's. The long tradition of ellipsometry on Masaryk University was started by Prof. Antonín Vašíček, who performed solitary research on thin film optics in Brno during World War II. In the last 50 years, ellipsometry is becoming very popular because of considerable applications of thin films in microelectronic industry, where the planar technology paradigm involves construction of complex 3D structure by stacking and patterning thin layers.

The necessity of the automation and simplicity of the instrumentation supported the evolution of rotating analyzer ellipsometers as the replacement of null-ellipsometers. In recent years, rotating compensator instruments (or phase modulation) are arriving to the commercial sphere. Most advanced designs with double rotating compensator (Mueller matrix ellipsometers) are available for research purposes.
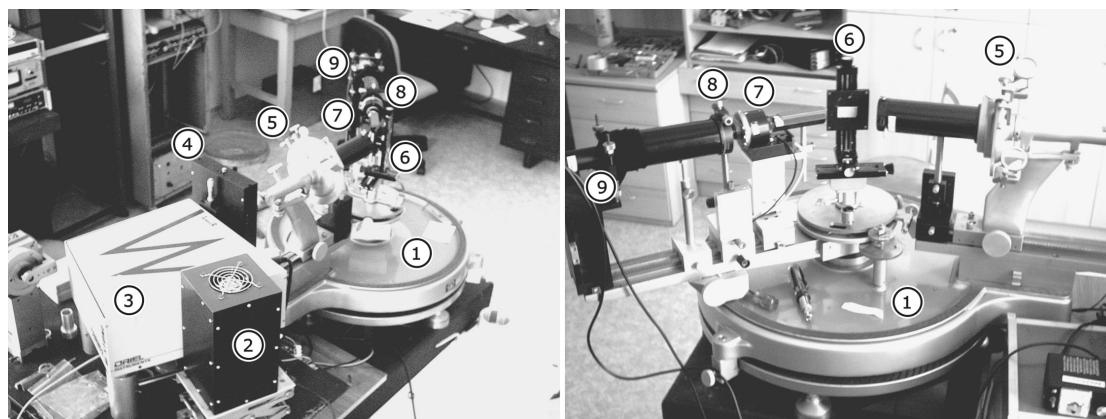
Figure 1.2. Top view (left) and side view (right) of VIS/UV rotating compensator ellipsometer: Gaertner goniometer (1), combined lamp in housing (2), monochromator (3), filter wheel (4), polarizer (5), sample holder (6), rotating compensator (7), analyzer (8) and photomultiplier (9).

David Aspnes put it: "we worked so hard that we worked ourselves off the field" in his closing lecture at International Conference on Spectroscopic ellipsometry in Stockholm, June 2007.

1.1.3. Techniques

In the present days, ellipsometry is performed in a wide range of photon energies. In the visible range (VIS) the tradition is longest and instrumentation is highly advanced. On the side of low energies, near infra-red (NIR) is typically extension of visible range, available with a proper detector (e.g. Ge photodiode). The mid infrared spectroscopic ellipsometers are commercially available, using the Fourier-transform spectroscopy. In the far infrared, several experimental setups are in operation, some taking advantage of synchrotron as a light source, reaching the wavenumber of 50 cm^{-1} (0.006 eV) or lower, for example.[6] Next, the terahertz range is about to be exploited by ellipsometry.

Most of the work was performed in the visible and UV range. The UV range is usually covered up to 6.5 eV by the VIS instruments. Above this energy, the atmospheric absorption necessitates vacuum, or more conveniently, nitrogen-purging, and UV-transparent materials to be used for the optical elements. VUV ellipsometers on the market range up to 9 eV and use MgF_2 Rochon polarizers. In the range of higher energies the technique struggles with the lack of transparent materials and polarization by reflection must be employed.[7] Synchrotron is the only possible light source for higher energies in VUV spectroscopy.

---

[6] C. Bernhard, J. Humlicek, B. Keimer, *Far-infrared ellipsometry using synchrotron light source – the dielectric response of cuprate high Tc superconductors*, Thin Solid Films **455-456,** 143-149 (2004).

[7] N. Esser, M. Rakel, C. Cobet, W. G. Schmidt, W. Braun and M. Cardona, *VUV-ellipsometry on GaN: Probing conduction band properties by core level excitations*, Phys. Stat. Sol. B **242,** 2601-2609 (2005).
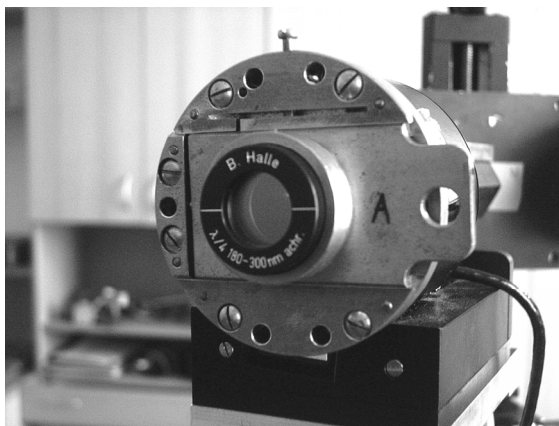
Figure 1.3. Compensator holder for interchangeable sledges with retarders.

1.1.4. Instrumentation

Gaertner

Ellipsometer used for most of the experiments is shown in fig. 1.2. It is custom build RAE/RCE instrument covering the spectral range 1.4 eV to 6.3 eV, which is based on Gaertner goniometer (variable angle of incidence). The light source is combined halogen bulb and deuterium lamp,[8] so the switching between the sources is not required. The monochromator[9] is prior to the instrument and contains three gratings covering the wavelength range from 180 nm to 5000 nm. Behind the exit slit of the monochromator, motorized filter wheel is mounted. The monochromator includes electronically operated shutter. The polarizer and analyzer are α-BBO Rochon prisms. The polarizer is located in the original Gaertner polarizer arm and operated manually. The compensator (or optionally analyzer for RAE) is kept in coaxial mounting in the shaft of piezoelectric stepping motor. Multiple broadband compensators[10] (see chapter 3 for details) have to be used to cover the measurement range. For the fast swapping of the compensators, special holder was designed[11] for the stepping motor (see fig. 1.3). The analyzer is placed in a simple holder allowing a manual setting. A photomultiplier[12] is used as the detector. The monochromator and the rotating element are controlled by a PC program through RS-232 ports. This program also collects data using a custom built amplifier[13] and a PCI measurement card.[14]

The technical enhancement of hardware and the development of software for the ellipsometer has been an important part of my PhD work at Department of Condensed Matter Physics. In fact, the first half of my thesis focuses on the theoretical background and obstacles related to the ellipsometric measurements.

---

[8] Ocean DH-2000 Deuterium Tungsten Halogen Source.
[9] Grating monochromator Oriel Cornerstone 260 ¼ M.
[10] Biplate and multi-plate achromatic retarders supplied by Bernhard Halle Nachfl. GmbH, Berlin, Germany.
[11] Inspired by the design of Gaertner compensator mounting.
[12] Hamamatsu C956-07.
[13] Built by Ing. Radoslav Švehla.
[14] PCI-1202 manufactured by ICP DAS.
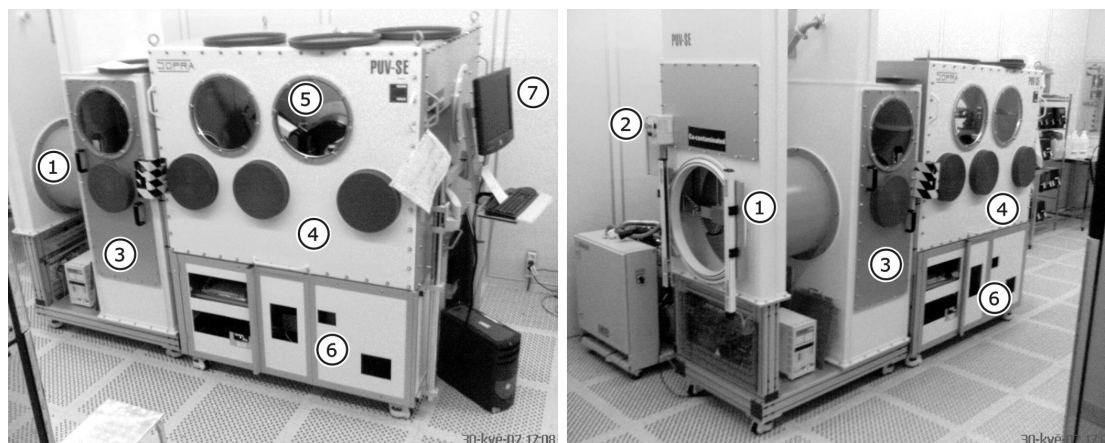
Figure 1.4. Two side views of Sopra PUV spectroscopic ellipsometer: loadlock (1), pressure/loadlock control panel (2), wafer-transfer robot section (3), glovebox (4), GES5 ellipsometer (5), control electronics (6), operator station (7).

Sopra PUV SE

Many measurements from the second half of my thesis were performed using instruments available in IMEC.[15] Spectroscopic measurements in the range from 2 to 9 eV were done on the variable angle spectroscopic ellipsometer Sopra GES 5 PUV SE.[16] This tool operates in the rotating analyzer and tracking polarizer configuration with the MgF_2 Rochon cubes used as the polarizers, a deuterium discharge light source and a photomultiplier detector. To achieve a high transmittance for ultraviolet photons, the tool is surrounded by a glove box (see fig. 1.4) purged by nitrogen, keeping the oxygen and water concentrations below 1 ppm. The ellipsometer is located in a cleanroom and is equipped with a robot and sample stage for handling 200 mm wafers.

EP-10

Porosity measurements of nano-porous thin films were performed on the IMEC prototype ellipsometric porosimeter EP10, equipped with a fixed angle of incidence (70 deg) ellipsometer Sentech 801, operating in the wavelength range between 350 and 850 nm, mounted on a high vacuum chamber with controllable pressure of solvent vapors (fig. 1.5). The ellipsometric porosimetry is based on the pressure-dependent absorption of a fluid (in our case toluene or water) into the pores. The absorbed toluene modifies the optical properties of the porous sample and the corresponding changes are measured by ellipsometry. The volume ratio of the open pores as well as the pore-size distribution[17] is then obtained by means of the effective medium theory.

---

[15] Interuniversity Microelectronics Center, Leuven, Belgium.
[16] PUV SE stands for Purged Ultra Violet Spectroscopic Ellipsometer.
[17] M. R. Baklanov, K. P. Mogilnikov, V. G. Polovinkin and F. N. Dultsev, *Determination of pore size distribution in thin films by ellipsometric porosimetry*, Vac. Sci. Technol. B **18,** 1385-1391 (2000).
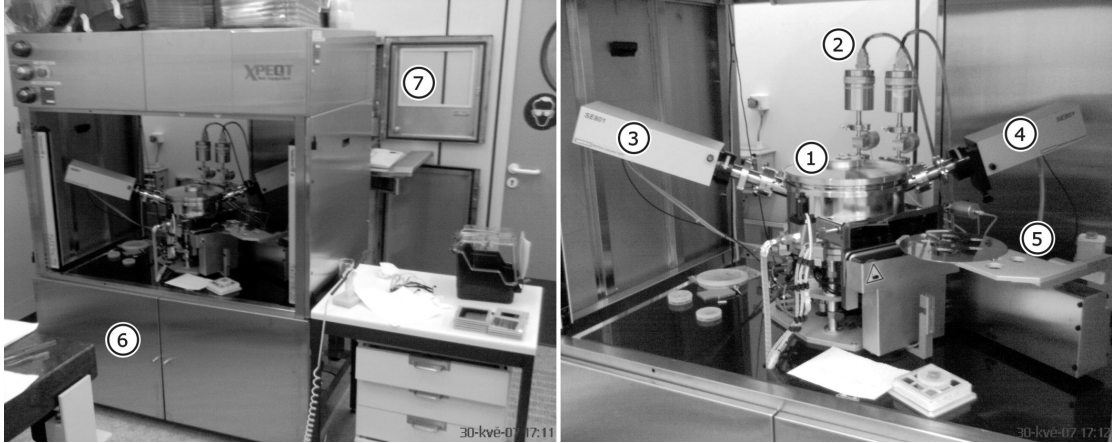
Figure 1.5. Ellipsometric porosimeter EP 10 (left) and close-up view of the chamber (right): high-vacuum chamber (1), pressure controllers (2), ellipsometer source arm (3), ellipsometer detector arm (4), loading robot (5), compartment with absorbent liquids (6), operator station (7).

1.2.   Propagation of light

In the following section we give a brief introduction to the theory of light propagation in media[18] with emphasis on situations relevant to ellipsometry.[19]

1.2.1. Plane waves

Electromagnetic field obeys *Maxwell equations*

$$\operatorname{div}\bar{D} = \rho\,, \quad \operatorname{rot}\bar{H} = \frac{\partial \bar{D}}{\partial t} + \bar{j}\,,$$

$$\operatorname{rot}\bar{E} = -\frac{\partial \bar{B}}{\partial t}\,, \quad \operatorname{div}\bar{B} = 0\,, \tag{1.1}$$

where $\bar{E}$ and $\bar{H}$ are the vectors of electric and magnetic intensities, $\bar{D}$ and $\bar{B}$ vectors of electric and magnetic inductions, $\bar{j}$ and ρ are the current and charge densities.

Stationary solution of (1.1) in nonmagnetic homogeneous and isotropic material, without free charges or currents, obeys the wave equation for the intensity E,

$$\Delta\bar{E}_\omega(\bar{k},\bar{r}) + \frac{\omega^2}{c^2}\varepsilon(\omega)\bar{E}_\omega(\bar{k},\bar{r}) = 0\,, \tag{1.2}$$

where ω is the angular frequency of light, c is its velocity in vacuum and $\varepsilon(\omega)$ is the frequency dependent dielectric function of the medium.

---

[18] M. Born, E. Wolf, *Principles of Optics (7th edition)*, Cambridge University Press (1999).

[19] J. Humlicek, in: H. Tompkins, E. Irene (Eds.), *Handbook of Ellipsometry*, William Andrew Publishing, New York (2005).
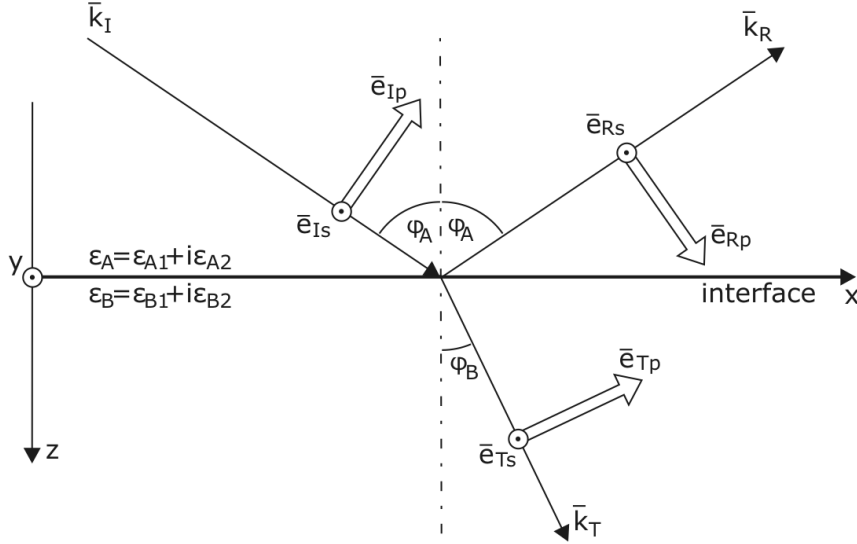
Figure 1.6. A plane wave incident on the planar interface (z=0) in the positive direction of x and z. The plane of incidence is y=0.

Let us denote the magnitude of the vacuum wave-vector as k_0, then:

$$(\Delta + k_0^2 \varepsilon)\bar{E}_\omega(\bar{k},\bar{r}) = 0, \quad k_0 \equiv \frac{\omega}{c}. \tag{1.3}$$

Equation (1.3) is solved by the plane wave

$$\bar{E}_{\bar{k},\omega}(\bar{r},t) = \bar{e}_0 E_0 \exp[i(\bar{k}\bar{r} - \omega t)], \tag{1.4}$$

where $\bar{e}_0$ is the unit polarization vector, E_0 is the (complex) amplitude of the electric field intensity. By inserting (1.4) into (1.3) we obtain the dispersion relation for the wave-vector in the media with the dielectric constant ε,

$$k_x^2 + k_y^2 + k_z^2 = k_0^2 \varepsilon(\omega). \tag{1.5}$$

1.2.2. Interface

Let us consider a planar interface between two homogeneous media A and B with the dielectric functions ε_A and ε_B (fig. 1.6). The interface is illuminated by a monochromatic plane wave with wave-vector

$$\bar{k} = (k_x, 0, k_z). \tag{1.6}$$

Equation (1.5) imposes a condition on the components of the wave-vector (1.6) in each media:

$$k_x^2 + k_z^2 = k_0^2 \varepsilon. \tag{1.7}$$

Let us express the incident wave (E_I) and reflected (E_R) and the wave (E_T), transmitted to medium B, in components related to s (from German senkrecht) and p (parallel) polarizations; for the sake of brevity we omit the time-dependent factor exp($i\omega t$).
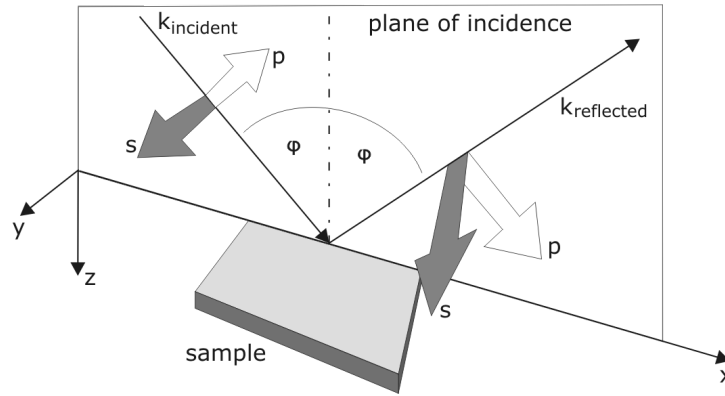
Figure 1.7. Schematic orientation of the axes.

$$\bar{E}_{Is,p}(\bar{r}) = \bar{e}_{Is,p} E_{Is,p} \exp[i(k_{xI}x + k_{zI}z)],$$

$$\bar{E}_{Rs,p}(\bar{r}) = \bar{e}_{Rs,p} E_{Rs,p} \exp[i(k_{xR}x + k_{zR}z)],$$

$$\bar{E}_{Ts,p}(\bar{r}) = \bar{e}_{Ts,p} E_{Ts,p} \exp[i(k_{xT}x + k_{zT}z)]. \qquad (1.8)$$

The boundary condition on the interface (z=0) requires the continuity of the in-plane components of the wave-vectors (*Snell's law*):

$$k_{xI} = k_{xR} = k_{xT}. \qquad (1.9)$$

Equations (1.7) and (1.9) determine the z-component of $\bar{k}_T$:

$$k_{zT}^2 = k_{zI}^2 + k_0^2 \varepsilon_B - k_0^2 \varepsilon_A. \qquad (1.10)$$

Inserting the angle of incidence φ we obtain

$$k_{zT} = k_0 \sqrt{\varepsilon_B - \varepsilon_A \sin^2 \varphi}. \qquad (1.11)$$

The intensities of electric and magnetic field are related by Maxwell's equations:

$$\bar{H} = \frac{1}{\omega \mu_0} (\bar{k} \times \bar{E}), \qquad \bar{E} = -\frac{1}{\omega \varepsilon \varepsilon_0} (\bar{k} \times \bar{H}). \qquad (1.12)$$

1.2.3. Fresnel coefficients

The continuity of the in-plane components of electric and magnetic fields on the interface determines the amplitudes of reflected and transmitted waves. We introduce the *Fresnel coefficients*[20] as the ratios of the amplitudes of the waves on the interface using the Cartesian components of the fields (see fig. 1.7) as

$$r_s \equiv \frac{E_{Rs}}{E_{Is}} = \frac{E_{Ry}}{E_{Iy}}, \qquad t_s \equiv \frac{E_{Ts}}{E_{Is}} = \frac{E_{Ty}}{E_{Iy}},$$

---

[20] See appendix 1 for a detailed derivation of the formulas in this subsection.

$$r_p \equiv \frac{E_{Rp}}{E_{Ip}} = \frac{E_{Rx}}{E_{Ix}} = -\frac{H_{Ry}}{H_{Iy}} \, , \qquad t_p \equiv \frac{E_{Tp}}{E_{Ip}} = \frac{E_{Tx}k_{zI}}{E_{Ix}k_{zT}} \sqrt{\frac{\varepsilon_B}{\varepsilon_A}} = \frac{H_{Ty}}{H_{Iy}} \sqrt{\frac{\varepsilon_A}{\varepsilon_B}} \, . \quad (1.13)$$

We define an additional coefficient for transmission of x-component of p-polarized wave:[21]

$$t_{px} \equiv \frac{E_{Tx}}{E_{Ix}} \, . \qquad\qquad (1.14)$$

By matching the tangential components of the electric field intensity E and magnetic field intensity H and using relations (1.12), we obtain the Fresnel coefficients as follows:

$$r_s = \frac{k_{z1} - k_{z2}}{k_{z1} + k_{z2}} \, , \qquad\qquad t_s = \frac{2k_{z1}}{k_{z1} + k_{z2}} \, ,$$

$$r_p = \frac{\varepsilon_A k_{z2} - \varepsilon_B k_{z1}}{\varepsilon_A k_{z2} + \varepsilon_B k_{z1}} \, , \qquad\qquad t_p = \frac{2k_{z1}\sqrt{\varepsilon_A \varepsilon_B}}{\varepsilon_A k_{z2} + \varepsilon_B k_{z1}} \, , \qquad (1.15)$$

$$t_{px} = \frac{2\varepsilon_A k_{z2}}{\varepsilon_A k_{z2} + \varepsilon_B k_{z1}} \, . \qquad\qquad (1.16)$$

This notation does not contain the angles of propagation explicitly and therefore simplifies the interpretation in the case of absorbing media, where the imaginary part of z-component of the wave-vector describes the damping of the field within the material.

The complex Fresnel coefficients describe the ratios of the absolute amplitudes of the waves as well as their relative phase. The complex ratio of the Fresnel coefficients of reflection for p and s-polarized waves is traditionally denoted as ρ and written in the form of two ellipsometric angles Ψ and Δ,

$$\rho = \frac{r_p}{r_s} = \left| \frac{r_p}{r_s} \right| e^{i(\Delta p - \Delta s)} = \tan\Psi e^{i\Delta} \, . \qquad (1.17)$$

The angles can be directly measured in the basic ellipsometric setup (see section 1.3) and can be used not only for a single interface, but for general layered structures as well.

The choice of orientation of the polarization vectors (introduced in fig. 1.6, and schematically drawn in fig 1.7) leads to the following consequences. For normal incidence, the Fresnel coefficients become identical: $r_s = r_p = r$. However, in the case of straight-through operation ($\varphi = 90°$), $r_s = 1$ and $r_p = -1$. This means, that a virtual reflection occurs, changing the orientation of the p-polarization vector.

---

[21] The advantages of the introduction of the fifth coefficient will become clear in the following calculations, see appendix 1 for details.
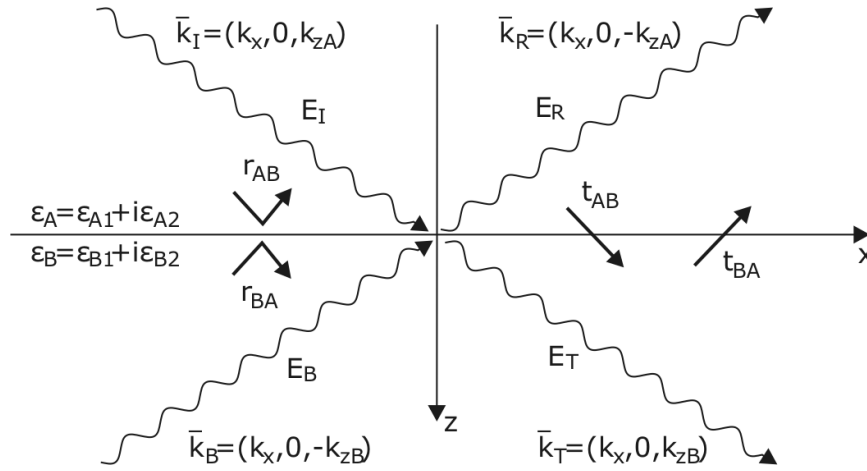
Figure 1.8. Four waves mixing on interface within the multilayer stack.

1.2.4. Layered media

The typical problem of ellipsometry is that of measurements on layered structures that are laterally homogeneous; we will restrict ourselves to that case in this work. This situation occurs when dealing with various oxide overlayers, coatings, multi-layer stacks for integrated circuit technology etc. The individual layers can be either homogeneous, with sharp interfaces, or with properties graded along the thickness. The graded layers can be approximated efficiently by a number of adequately thin homogeneous sub-layers with the properties graded discretely from one sub-layer to the next. Therefore, we need to formulate a theory for propagation of the polarized monochromatic plane-wave through any number of homogeneous layers.

Snell's law in multilayers

In the typical ellipsometric measurement, only the light from the source is incident on the sample from the ambient, and no light is assumed to come from the semi-infinite substrate or semi-infinite ambient behind the transparent specimen. Therefore, the x-components of the waves in each layer are fixed by Snell's law (1.9):

$$k_{x1} = k_{x2} = \cdots = k_{xN} = k_{xsub} , \quad \text{and} \tag{1.18}$$

$$k_{xi} = k_0 \sqrt{\varepsilon_A} \sin\varphi . \tag{1.19}$$

Subsequently, the z-component in each layer is given by

$$k_{zi} = k_0 \sqrt{\varepsilon_i - \varepsilon_A \sin^2 \varphi} , \tag{1.20}$$

where k_0 is the vacuum wave-number, ε_A, ε_i are the dielectric constants of the ambient and i[th] layer, respectively, and φ is the angle of incidence.

In the following, we will introduce the *propagation matrix* formalism for the calculation of the fields transmitted and reflected by the multi-layer structure. We will describe two processes: Four-wave matching on the interface and propagation through a single homogeneous layer.
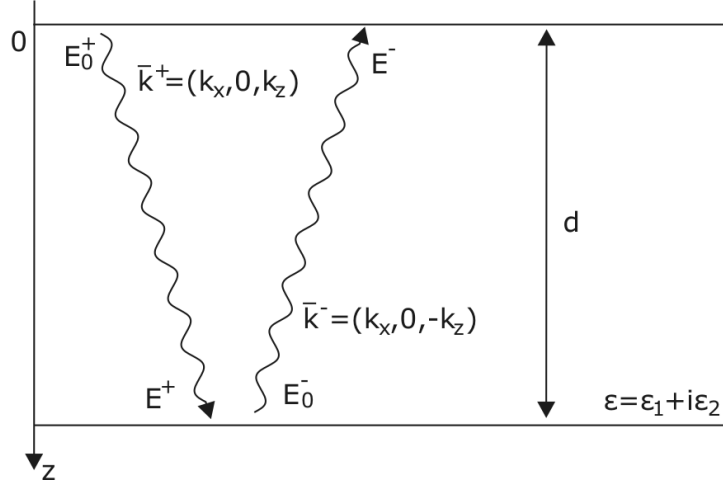
Figure 1.9. Waves propagating through a homogeneous layer with the thickness d.

Interface matrix

At any interface within the multilayer, four waves of given frequency are present (see fig. 1.8). E_I denotes the incident wave, E_R the wave partly reflected and partly transmitted from the medium B, E_T is wave transmitted from medium A and reflected from medium B and finally E_B denotes the wave coming from medium B as the result of reflections from the interfaces deeper in the stack. For s-polarization, we can write down the relations between the four waves in terms of the field amplitudes:

$$E_{Rs} = r_{ABs}E_{Is} + t_{BAs}E_{Bs}\ , \qquad E_{Ts} = r_{BAs}E_{Bs} + t_{ABs}E_{Is}\ , \qquad (1.21)$$

and for the p-polarization in terms of the in-plane components of the field amplitudes, simplifying the results. We use the definition of r_p of eq. (1.13) and t_{px} of (1.14), obtaining

$$E_{Rpx} = r_{ABpx}E_{Ipx} + t_{BApx}E_{Bpx}\ , \qquad E_{Tpx} = r_{BApx}E_{Bpx} + t_{ABpx}E_{Ipx}\ , \qquad (1.22)$$

where the subscript AB denotes the reflection (transmission) from medium A on (respective into) medium B, and vice versa. The Fresnel coefficients fulfill the following relations

$$r_{AB} = -r_{BA}\ , \qquad t_{AB}t_{BA} + r_{AB}^2 = 1\ , \qquad (1.23)$$

valid for the s-polarization, p-polarization, and the x-component of p-polarized waves. We therefore simplify the notations further by $r \equiv r_{AB}$ and $t \equiv t_{AB}$ for each polarization. Then, equations (1.21) and (1.22) can be rewritten in the following matrix form

$$\begin{bmatrix} E_I \\ E_R \end{bmatrix} = \hat{R} \cdot \begin{bmatrix} E_T \\ E_B \end{bmatrix}\ , \quad \text{where} \quad \hat{R} = \frac{1}{t}\begin{bmatrix} 1 & r \\ r & 1 \end{bmatrix}\ , \qquad (1.24)$$

valid again for the amplitudes of s-polarized waves, p-polarized waves and x-component of p-polarized waves.
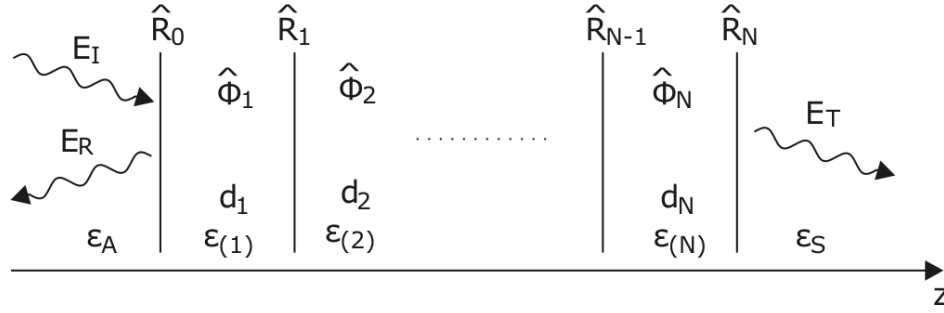
Figure 1.10. The multilayered structure. The wave propagation is described by series of matrices.

Phase matrix

The complex amplitudes of the waves propagating from one interface to another one have to be multiplied by a factor containing the change of the phase relative to the initial one accumulated during the propagation (fig. 1.9). Let us denote by E^+ the wave travelling in the positive direction of z-axis, and by E^- the wave travelling in the opposite direction:

$$E^+(x,y,z,t) = E_0^+ \exp[i(k_x x + k_z z - \omega t)],$$

$$E^-(x,y,z,t) = E_0^- \exp[i(k_x x - k_z z - \omega t)].$$ (1.25)

Consequently,

$$E_D^+ = E_U^+ \exp(ik_z d), \qquad E_D^- = E_U^- \exp(-ik_z d),$$ (1.26)

where $E_D^{+/-} = E^{+/-}(x,y,z=d,t)$ and $E_U^{+/-} = E^{+/-}(x,y,z=0,t)$. The equations (1.26) can be written in a matrix form, valid for all the relevant components (E_s, E_p, E_{px}):

$$\begin{bmatrix} E_U^+ \\ E_U^- \end{bmatrix} = \hat{\Phi} \cdot \begin{bmatrix} E_D^+ \\ E_D^- \end{bmatrix}, \quad \text{where} \quad \hat{\Phi} = \begin{bmatrix} \exp(-ik_z d) & 0 \\ 0 & \exp(ik_z d) \end{bmatrix}.$$ (1.27)

For any multi-layered structure (N being the number of layers), the field amplitudes are matched on each interface through the multiplication of the interface matrices (1.24) and the propagation matrices (1.27),

$$\begin{bmatrix} E_I \\ E_R \end{bmatrix} = \hat{M} \cdot \begin{bmatrix} E_T \\ E_B \end{bmatrix}, \quad \text{where} \quad \hat{M} = \hat{R}_0 \cdot \hat{\Phi}_1 \cdot \hat{R}_1 \cdot \hat{\Phi}_2 \cdots \hat{R}_{N-1} \cdot \hat{\Phi}_N \cdot \hat{R}_N.$$ (1.28)

In the standard situation in ellipsometry, the $(N+1)^{th}$ layer is a semi-infinite substrate or ambient medium and therefore no wave is propagating from the opposite direction to the Nth interface: $E_B=0$. Then the reflection Fresnel coefficient of the whole stack is given by

$$r_{(s,p)} = \frac{E_{R(s,p)}}{E_{I(s,p)}} = \frac{M_{21(s,p)}}{M_{11(s,p)}},$$ (1.29)

and the transmission coefficient for s and p-polarization is

$$t_{(s,p)} = \frac{E_{T(s,p)}}{E_{I(s,p)}} = \frac{1}{M_{11(s,p)}} \; . \tag{1.30}$$

The transmission coefficient for the x-component of the p-polarized wave is

$$t_{px} = \sqrt{\frac{\varepsilon_A}{\varepsilon_S}} \frac{k_{zS}}{k_{z0}} t_p \, , \tag{1.31}$$

where ε_A denotes the ambient dielectric constant and ε_S the substrate/last medium dielectric constant. The k_{z0} is the z-component of the incoming wave-vector, and k_{zS} the z-component of the outgoing wave-vector in the substrate/last medium. Typically, we measure a layered sample surrounded by ambient, having $t_p = t_{px}$.

Finally, the complex ratio ρ of eq. (1.17) and the ellipsometric angles Ψ, Δ are calculated using the r_s and r_p obtained from (1.29).

1.2.5. Calculation of derivatives

The analysis of experimental data (typically Ψ, Δ spectra) requires an inversion of the forward calculations presented in the previous subsection. With increasing number of layers, the problem becomes too complicated for a direct calculation. The sought parameters (layer thicknesses and optical constants) have to be obtained by fitting numerically the model to the data in the multi-dimensional parameter space. For a fast and reliable implementation of gradient based minimization procedures,[22] we calculate analytically the derivatives of the model functions. The derivatives are also used for parameter errors estimation.[23,24]

Here, we express the derivatives of measured quantities with respect to the dielectric function ε or thickness d of a given layer. Equivalent expressions can be found in literature.[25] The parameters ε, d of each layer can be functions of other internal parameters and the derivatives for some typical situations will be presented in the next subsection.

The derivative of ρ

The measured quantity, the ratio ρ of eq. (1.17), is differentiated as

$$\rho' = \frac{r_p' r_s - r_p r_s'}{r_s^2} \, , \tag{1.32}$$

[22] We implement the well known Marquardt-Levenberg algorithm.

[23] J. Humlicek, *Sensitivity extrema in multiple-angle ellipsometry*, J. Opt. Soc. Am. A **2,** 713-720 (1985).

[24] J. Humlicek, *Sensitivity of Optical Measurements of Planar Stratified Structures and Reduction of Experimental Data*, FOLIA Fac. Sci. Nat. Universitatis Masarykiana Brunensis, Physica **49** (1992).

[25] J. Humlicek, *Evaluation of derivatives of reflectance and transmittance by stratified structures and solution of the inverse problem of ellipsometry*, Optica Acta, **30,** 97-105 (1983).

where the derivatives of the *s* and *p* Fresnel coefficients of the layer stack are performed independently in the following way, using (1.29):

$$r_{s,p}' = \left.\frac{M_{21}'M_{11} - M_{21}M_{11}'}{M_{11}^2}\right|_{s,p}.$$

(1.33)

The derivatives of propagation matrices

The derivatives of the matrix elements can be compactly written down with the help of Einstein's notation of summations as

$$\hat{M}' = M_j^{i\,'} = \left(R_{0k}^{\,i}\Phi_{1l}^{\,k}\cdots R_{Nj}^{\,l}\right)' = R_{0k}^{\,i\,'}\Phi_{1l}^{\,k}\cdots R_{Nj}^{\,l} + R_{0k}^{\,i}\Phi_{1l}^{\,k\,'}\cdots R_{Nj}^{\,l} + \ldots + R_{0k}^{\,i}\Phi_{1l}^{\,k}\cdots R_{Nj}^{\,l\,'} \equiv$$

$$\equiv \hat{R}_0'\hat{\Phi}_1\cdots\hat{R}_N + \hat{R}_0\hat{\Phi}_1'\cdots\hat{R}_N + \ldots + \hat{R}_0\hat{\Phi}_1\cdots\hat{R}_N'.$$

(1.34)

As the derivatives are performed with respect to the thickness or optical constants of a particular layer we obtain a single non-zero term in the case of thickness, and three non-zero terms in the case of optical constants:

$$\frac{\partial\hat{M}}{\partial d_{(i)}} = \hat{R}_0\hat{\Phi}_1\cdots\frac{\partial\hat{\Phi}_{(i)}}{\partial d_{(i)}}\cdots\hat{R}_N,$$

(1.35)

$$\frac{\partial\hat{M}}{\partial\varepsilon_{(i)}} = \hat{R}_0\hat{\Phi}_1\cdots\frac{\partial\hat{R}_{(i-1)}}{\partial\varepsilon_{(i)}}\hat{\Phi}_{(i)}\hat{R}_{(i)}\cdots\hat{R}_N +$$

$$+\hat{R}_0\hat{\Phi}_1\cdots\hat{R}_{(i-1)}\frac{\partial\hat{\Phi}_{(i)}}{\partial\varepsilon_{(i)}}\hat{R}_{(i)}\cdots\hat{R}_N + \hat{R}_0\hat{\Phi}_1\cdots\hat{R}_{(i-1)}\hat{\Phi}_{(i)}\frac{\partial\hat{R}_{(i)}}{\partial\varepsilon_{(i)}}\cdots\hat{R}_N.$$

(1.36)

The partial derivatives of any Φ matrix are

$$\frac{\partial\hat{\Phi}}{\partial d} = ik_z\hat{\Phi}\begin{bmatrix} -1 & 0 \\ 0 & 1 \end{bmatrix},$$

(1.37)

$$\frac{\partial\hat{\Phi}}{\partial\varepsilon} = \frac{ik_0^2 d}{2k_z}\hat{\Phi}\begin{bmatrix} -1 & 0 \\ 0 & 1 \end{bmatrix},$$

(1.38)

for finding the derivatives of matrices *R*, we apply the chain rule again

$$\hat{R}' = \frac{1}{t^2}\begin{bmatrix} -1 & r't - rt' \\ r't - rt' & -1 \end{bmatrix}.$$

(1.39)

Let us introduce useful relations resulting directly from the matched in-plane components and the definitions of eqs. (1.13):

$$1 + r_s = t_s, \quad 1 - r_p = \sqrt{\frac{\varepsilon_B}{\varepsilon_A}}t_p, \quad 1 + r_p = t_{px}.$$

(1.40)

The derivatives of Fourier coefficients

Now, if restricting the calculations of the p-polarized part to the x-component, we can take advantage of the symmetry between the relations for the s-polarized wave, and the x-component of the p-polarized wave, obtaining

$$r' = t' \quad \text{and} \quad t - r = 1. \tag{1.41}$$

Then, the derivatives of the interface matrix R take the following simple form for both polarizations,

$$\hat{R}' = \frac{r'}{t^2} \begin{bmatrix} -1 & 1 \\ 1 & -1 \end{bmatrix}, \tag{1.42}$$

using only the derivatives of r (the reflection Fresnel coefficients):

$$\frac{\partial r_s}{\partial \varepsilon_A} = \frac{\partial t_s}{\partial \varepsilon_A} = \frac{k_{z2}}{k_{z1}} \frac{k_0^2}{\left(k_{z1} + k_{z2}\right)^2},$$

$$\frac{\partial r_s}{\partial \varepsilon_B} = \frac{\partial t_s}{\partial \varepsilon_B} = -\frac{k_{z1}}{k_{z2}} \frac{k_0^2}{\left(k_{z1} + k_{z2}\right)^2},$$

$$\frac{\partial r_p}{\partial \varepsilon_A} = \frac{\partial t_{px}}{\partial \varepsilon_A} = \varepsilon_B \frac{k_{z2}}{k_{z1}} \frac{\left(2k_{z1}^2 - \varepsilon_A k_0^2\right)}{\left(k_{z1} + k_{z2}\right)^2},$$

$$\frac{\partial r_p}{\partial \varepsilon_B} = \frac{\partial t_{px}}{\partial \varepsilon_B} = -\varepsilon_A \frac{k_{z1}}{k_{z2}} \frac{\left(2k_{z2}^2 - \varepsilon_B k_0^2\right)}{\left(k_{z1} + k_{z2}\right)^2}. \tag{1.43}$$

In these calculations we used the derivative of k_z of eq. (1.20) with respect to ε:

$$\frac{\partial k_z}{\partial \varepsilon} = \frac{k_0^2}{2k_z}. \tag{1.44}$$

At this point we have collected all parts needed for the evaluation of the derivatives. The derivatives can be calculated along with the model calculation.

We have collected suitable formulas for the derivatives

$$\frac{\partial \rho}{\partial \varepsilon_{(i)}}, \quad \frac{\partial \rho}{\partial d_{(i)}}. \tag{1.45}$$

The first of them is the derivative of the complex quantity with respect to the complex parameter. The derivatives of ρ with respect to the real and imaginary parts of ε are (we skip the layer index i):

$$\frac{\partial \rho}{\partial \varepsilon_1} = \frac{\partial \rho}{\partial \varepsilon} \frac{\partial \varepsilon}{\partial \varepsilon_1} = \frac{\partial \rho}{\partial \varepsilon}, \quad \frac{\partial \rho}{\partial \varepsilon_2} = \frac{\partial \rho}{\partial \varepsilon} \frac{\partial \varepsilon}{\partial \varepsilon_2} = i \frac{\partial \rho}{\partial \varepsilon}. \tag{1.46}$$

Consequently,

$$\frac{\partial \operatorname{Re}\rho}{\partial \varepsilon_1} = \operatorname{Re}\frac{\partial \rho}{\partial \varepsilon_1} = \operatorname{Re}\frac{\partial \rho}{\partial \varepsilon}, \qquad \frac{\partial \operatorname{Im}\rho}{\partial \varepsilon_1} = \operatorname{Im}\frac{\partial \rho}{\partial \varepsilon_1} = \operatorname{Im}\frac{\partial \rho}{\partial \varepsilon},$$

$$\frac{\partial \operatorname{Re}\rho}{\partial \varepsilon_2} = \operatorname{Re}\frac{\partial \rho}{\partial \varepsilon_2} = -\operatorname{Im}\frac{\partial \rho}{\partial \varepsilon}, \qquad \frac{\partial \operatorname{Im}\rho}{\partial \varepsilon_2} = \operatorname{Im}\frac{\partial \rho}{\partial \varepsilon_2} = \operatorname{Re}\frac{\partial \rho}{\partial \varepsilon}. \qquad (1.47)$$

The derivatives of Ψ, Δ

Now we want to obtain more convenient real measurable quantities Ψ, Δ, differentiated with respect to the real and imaginary parts of dielectric constant and thickness of any chosen layer using the definition of (1.17):

$$\tan\Psi = |\rho| = \sqrt{(\operatorname{Re}\rho)^2 + (\operatorname{Im}\rho)^2},$$

$$\frac{\partial \Psi}{\partial \varepsilon_1} = \frac{\partial \Psi}{\partial \tan\Psi}\frac{\partial \tan\Psi}{\partial \varepsilon_1} = \frac{\partial \Psi}{\partial \tan\Psi}\left(\frac{\partial \tan\Psi}{\partial \operatorname{Re}\rho}\frac{\partial \operatorname{Re}\rho}{\partial \varepsilon_1} + \frac{\partial \tan\Psi}{\partial \operatorname{Im}\rho}\frac{\partial \operatorname{Im}\rho}{\partial \varepsilon_1}\right) =$$

$$= \frac{1}{1 + \tan^2\Psi}\left(\frac{\operatorname{Re}\rho}{\tan\Psi}\frac{\partial \operatorname{Re}\rho}{\partial \varepsilon_1} + \frac{\operatorname{Im}\rho}{\tan\Psi}\frac{\partial \operatorname{Im}\rho}{\partial \varepsilon_1}\right) =$$

$$= \frac{1}{1 + \tan^2\Psi}\left(\cos\Delta\operatorname{Re}\frac{\partial \rho}{\partial \varepsilon} + \sin\Delta\operatorname{Im}\frac{\partial \rho}{\partial \varepsilon}\right), \qquad (1.48)$$

where we have applied relations (1.47). Similarly,

$$\frac{\partial \Psi}{\partial \varepsilon_2} == \frac{1}{1 + \tan^2\Psi}\left(-\cos\Delta\operatorname{Im}\frac{\partial \rho}{\partial \varepsilon} + \sin\Delta\operatorname{Re}\frac{\partial \rho}{\partial \varepsilon}\right), \qquad (1.49)$$

$$\frac{\partial \Psi}{\partial d} == \frac{1}{1 + \tan^2\Psi}\left(\cos\Delta\operatorname{Re}\frac{\partial \rho}{\partial d} + \sin\Delta\operatorname{Im}\frac{\partial \rho}{\partial d}\right). \qquad (1.50)$$

The phase angle $\Delta \in (-\pi, \pi\rangle$ is determined as $\arg(\rho)$; the derivatives are:

$$\tan\Delta = \frac{\operatorname{Im}\rho}{\operatorname{Re}\rho},$$

$$\frac{\partial \Delta}{\partial \varepsilon_1} = \frac{\partial \Delta}{\partial \tan\Delta}\frac{\partial \tan\Delta}{\partial \varepsilon_1} = \frac{\partial \Delta}{\partial \tan\Delta}\left(\frac{\partial \tan\Delta}{\partial \operatorname{Re}\rho}\frac{\partial \operatorname{Re}\rho}{\partial \varepsilon_1} + \frac{\partial \tan\Delta}{\partial \operatorname{Im}\rho}\frac{\partial \operatorname{Im}\rho}{\partial \varepsilon_1}\right) =$$

$$= \frac{1}{1 + \left(\dfrac{\operatorname{Im}\rho}{\operatorname{Re}\rho}\right)^2}\left(-\frac{\operatorname{Im}\rho}{(\operatorname{Re}\rho)^2}\frac{\partial \operatorname{Re}\rho}{\partial \varepsilon_1} + \frac{1}{\operatorname{Re}\rho}\frac{\partial \operatorname{Im}\rho}{\partial \varepsilon_1}\right) =$$

$$= \frac{1}{(\operatorname{Re}\rho)^2 + (\operatorname{Im}\rho)^2}\left(-\operatorname{Im}\rho\frac{\partial \operatorname{Re}\rho}{\partial \varepsilon_1} + \operatorname{Re}\rho\frac{\partial \operatorname{Im}\rho}{\partial \varepsilon_1}\right) =$$

$$= \frac{1}{\tan\Psi}\left(-\sin\Delta\operatorname{Re}\frac{\partial\rho}{\partial\varepsilon} + \cos\Delta\operatorname{Im}\frac{\partial\rho}{\partial\varepsilon}\right), \qquad (1.51)$$

and similarly

$$\frac{\partial\Delta}{\partial\varepsilon_2} = \frac{1}{\tan\Psi}\left(\sin\Delta\operatorname{Im}\frac{\partial\rho}{\partial\varepsilon} + \cos\Delta\operatorname{Re}\frac{\partial\rho}{\partial\varepsilon}\right), \qquad (1.52)$$

$$\frac{\partial\Delta}{\partial d} = \frac{1}{\tan\Psi}\left(-\sin\Delta\operatorname{Re}\frac{\partial\rho}{\partial d} + \cos\Delta\operatorname{Im}\frac{\partial\rho}{\partial d}\right). \qquad (1.53)$$

Note that the zero value of ρ leads to an undefined value of Δ and diverging derivatives.

Now we summarize the previous calculations. The ratio ρ of the Fresnel reflection coefficients is calculated using the propagation matrix approach. Along with the calculation, the complex derivatives of ρ with respect to any requested parameter $\varepsilon_{(i)}$ or $d_{(i)}$ are constructed using equations (1.32) to (1.44). Then the angles Ψ, Δ are evaluated according to (1.17) and the derivatives are obtained from equations (1.48) to (1.53).

1.2.6. Response functions

In previous subsections we introduced the energy dependent complex *dielectric function* ε, describing the response of the material – quantified by the polarization P – to the electric field E. The following tensor equation relates the field and polarization through the electric susceptibility χ:

$$\bar{P}_{\omega\bar{k}} = \hat{\chi}(\omega,\bar{k})\epsilon_0\bar{E}_{\omega\bar{k}} \quad \text{and} \quad \hat{\varepsilon}(\omega,\bar{k}) = 1 + \hat{\chi}(\omega,\bar{k}). \qquad (1.54)$$

In most of relevant situations the spatial dispersion is negligible and for isotropic materials the tensors ε and χ are reduced to scalars.[26]

Dielectric function of bulk sample

For a bulk sample, without any film on the surface, the dielectric function can be calculated directly from the measured ellipsometric parameters. The ratio ρ of Fresnel coefficients (1.17) is evaluated for single interface using the equations (1.15)

$$\rho = \tan\Psi e^{i\Delta} = \frac{r_p}{r_s} = \frac{\varepsilon_A k_{z2} - \varepsilon_B k_{z1}}{\varepsilon_A k_{z2} + \varepsilon_B k_{z1}} \cdot \frac{k_{z1} + k_{z2}}{k_{z1} - k_{z2}}, \qquad (1.55)$$

where ε_A, ε_B are the dielectric constants of the ambient ($\varepsilon_A \equiv 1$) and the sample material ($\varepsilon_A \equiv \varepsilon$), respectively, and k_{z1}, k_{z2} are the z-components of the wave-vectors in the ambient and in the sample material, respectively.

---

[26] The electric induction and intensity are related by $\bar{D} = \varepsilon_0\bar{E} + \bar{P}$. Similar relation is valid for magnetic induction and intensity $\bar{B} = \mu_0\bar{H} + \bar{P}_m$, where $\bar{P}_m$ is the magnetic polarization and $\bar{P}_m = \mu_0\bar{M}$.

These components can be expressed in terms of the angle of incidence φ according to eq. (1.20), resulting in

$$\rho = \frac{\sqrt{\varepsilon - \sin^2 \varphi} - \tan\varphi \cdot \sin\varphi}{\sqrt{\varepsilon - \sin^2 \varphi} + \tan\varphi \cdot \sin\varphi} . \tag{1.56}$$

This can be readily inverted, giving

$$\varepsilon = \sin^2 \varphi \left[1 + \tan^2 \varphi \frac{(1+\rho)^2}{(1-\rho)^2} \right] . \tag{1.57}$$

In the general case of a sample with overlayers, formula (1.57) can still be used, resulting in *pseudo-dielectric function* denoted as $\langle \varepsilon \rangle$.

For the practical reasons of error estimation, we will calculate the derivatives of ε with respect to the measured angles Ψ, Δ. The complex derivative is

$$\frac{\partial \varepsilon}{\partial \rho} = 4 \sin^2 \varphi \tan^2 \varphi \frac{1+\rho}{(1-\rho)^3} . \tag{1.58}$$

Then, using inverted relations (1.46) and (1.47), we obtain:

$$\frac{\partial \varepsilon_1}{\partial \Psi} = \frac{1}{\cos^2 \Psi} \left(\text{Re} \frac{\partial \varepsilon}{\partial \rho} \cos\Delta - \text{Im} \frac{\partial \varepsilon}{\partial \rho} \sin\Delta \right), \tag{1.59}$$

$$\frac{\partial \varepsilon_2}{\partial \Psi} = \frac{1}{\cos^2 \Psi} \left(\text{Im} \frac{\partial \varepsilon}{\partial \rho} \cos\Delta + \text{Re} \frac{\partial \varepsilon}{\partial \rho} \sin\Delta \right), \tag{1.60}$$

$$\frac{\partial \varepsilon_1}{\partial \Delta} = \tan\Psi \left(-\text{Re} \frac{\partial \varepsilon}{\partial \rho} \sin\Delta - \text{Im} \frac{\partial \varepsilon}{\partial \rho} \cos\Delta \right), \tag{1.61}$$

$$\frac{\partial \varepsilon_2}{\partial \Delta} = \tan\Psi \left(-\text{Im} \frac{\partial \varepsilon}{\partial \rho} \sin\Delta + \text{Re} \frac{\partial \varepsilon}{\partial \rho} \cos\Delta \right). \tag{1.62}$$

We also obtain the derivative with respect to φ:

$$\frac{\partial \varepsilon}{\partial \varphi} = \sin 2\varphi \left[1 + \left(1 + \frac{1}{\cos^2 \varphi} \right) \tan^2 \varphi \frac{(1+\rho)^2}{(1-\rho)^2} \right]. \tag{1.63}$$

Refractive index and other optical quantities

In some cases it is convenient to work with the complex *refractive index*, $N=n+ik$, where n is the refractive index and k is the extinction coefficient. This quantity is simply related to dielectric function ε:

$$N^2 = \varepsilon , \tag{1.64}$$

$$\varepsilon_1 = n^2 - k^2 , \qquad \varepsilon_2 = 2nk , \tag{1.65}$$

$$n = \sqrt{\frac{\varepsilon_1 + \sqrt{\varepsilon_1^2 + \varepsilon_2^2}}{2}}, \quad k = \sqrt{\frac{-\varepsilon_1 + \sqrt{\varepsilon_1^2 + \varepsilon_2^2}}{2}}. \qquad (1.66)$$

In the simplest intensity transmission measurement, neglecting the reflections on the interfaces, the light transmitted through absorbing medium of thickness d obeys the *Beer-Lambert law*:

$$I = I_0 e^{-ad}, \qquad (1.67)$$

where I and I_0 are the transmitted and incoming intensity of light, respectively, and a is absorption coefficient[27] related to the extinction coefficient by

$$a = \frac{4\pi}{\lambda}k, \quad k = \frac{\lambda}{4\pi}a = \frac{\lambda[nm]\cdot 10^{-7}}{4\pi}a[cm^{-1}], \qquad (1.68)$$

where λ is the vacuum wavelength of light. Figure 1.11 illustrates these relations for selected wavelengths.

The *penetration depth* d_p of light is usually defined as the depth where the field amplitude is reduced by the factor of e. For normal incidence

$$d_p = \frac{\lambda}{2\pi k}. \qquad (1.69)$$

In the case of oblique incidence at the angle φ (in the ambient with refractive index $n_a=1$) the penetration depth is

$$d_p = \frac{\lambda}{2\pi} \frac{\sqrt{2}}{\left[\sqrt{(n^2 - k^2 - \sin^2 \varphi)^2 + 4n^2 k^2} - (n^2 - k^2 - \sin^2 \varphi)\right]^{1/2}}. \qquad (1.70)$$

Transmittance T is defined as the ratio of transmitted and incident intensities,

$$T = \frac{I}{I_0}. \qquad (1.71)$$

Many results of transmission measurements in infrared range performed in this work are presented as *absorbance*

$$A = -\ln\frac{I}{I_0}. \qquad (1.72)$$

This quantity allows a simple manipulation with the results of measurement on thin films on a substrate or on multilayers. If the reflections on the surface and interfaces are neglected, the absorbance of the stack is given by the sum of the absorbances of individual layers. Further, the absorbance measured on bare substrate can be subtracted from that of a thin film-substrate sample.

---

[27] Conventionally given in cm^{-1}.
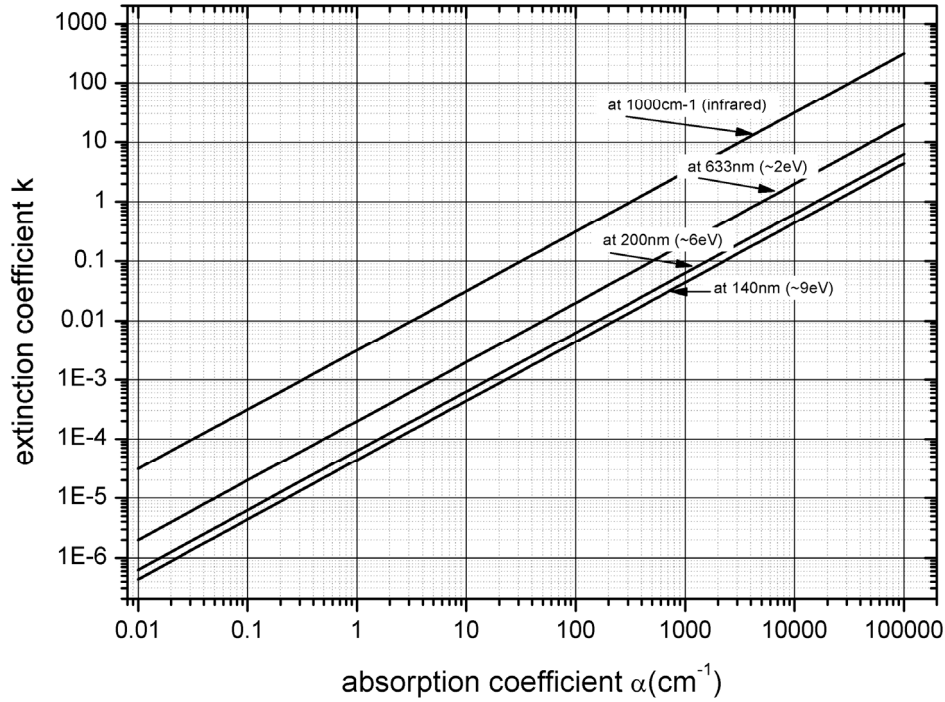
Figure 1.11. Relation between extinction and absorption coefficients for selected wavelengths.

1.2.7. Models of optical response

Harmonic oscillator model

A simple model for the optical response can be constructed assuming the presence of classical damped charged oscillators. Let us have an oscillator as pair of charges e^- and e^+ with the reduced mass μ bound by spring with spring constant $\mu\omega_0^2$. Let c be the volume density of the oscillators. For the displacement x, the following equation of motion is valid, applying a harmonic driving force:

$$\ddot{x} + G\dot{x} + \omega_0^2 x = \frac{eE}{\mu} e^{i\omega t} , \qquad (1.73)$$

where G is the damping factor, ω_0 the resonance frequency, and E the amplitude of the electric field intensity. The amplitude x_A of the displacement is

$$x_A = \frac{\dfrac{eE}{\mu}}{\omega_0^2 - \omega^2 + iG\omega} . \qquad (1.74)$$

The polarization P is the volume density of the dipole moment; according to eq. (1.54),

$$P = cex_A = \frac{\dfrac{ce^2}{\epsilon_0 \mu}}{\omega_0^2 - \omega^2 + iG\omega} \epsilon_0 E , \qquad (1.75)$$

$$\varepsilon(\omega) = 1 + \frac{\dfrac{ce^2}{\epsilon_0 \mu}}{\omega_0^2 - \omega^2 + iG\omega} \, . \tag{1.76}$$

This formula can be generalized to include multiple oscillators used to model electronic transitions and lattice vibrations of solids simultaneously. By setting one oscillator to zero resonance frequency, we obtain the response of free charge carriers, called *Drude term*, in conductors. High energy transitions (out of the range of given measurement) contribute a constant term ε_∞ of the real part. The following formula is the general *harmonic oscillator model* of the dielectric function.

$$\varepsilon(\omega) = \varepsilon_\infty + \frac{F_0}{\omega(\omega + iG_0)} + \sum_j \frac{F_j}{\omega_{0j}^2 - \omega^2 + iG_j\omega} \, , \tag{1.77}$$

where F_j, ω_{0j}, G_j ($j=0,1,2\dots$) are the oscillator strength, position, and dampening of each oscillator, respectively. The index 0 denotes the Drude term ($\omega_{00}=0$).

In previous subsections, we have presented the derivatives of the ellipsometric quantities with respect to the obtained dielectric function of given layer in the stack. If the dielectric function is parameterized according to eq. (1.77), the derivatives with respect to the individual parameters (strength, position, width) of the oscillators might be useful. Let us determine the real and imaginary part of a selected term:

$$\varepsilon_j = \frac{F}{\omega_{0j}^2 - \omega^2 + iG_j\omega} = \frac{F_j(\omega_{0j}^2 - \omega^2) + i\omega F_j G_j}{(\omega_{0j}^2 - \omega^2)^2 + (G_j\omega)^2} \, ,$$

$$\mathrm{Re}\,\varepsilon_j = \frac{F_j(\omega_{0j}^2 - \omega^2)}{A} \, , \quad \mathrm{Im}\,\varepsilon_j = \frac{\omega F_j G_j}{A} \, , \quad A \equiv (\omega_{0j}^2 - \omega^2)^2 + (G_j\omega)^2 \, . \tag{1.78}$$

The derivative of A is

$$\frac{\partial A}{\partial \omega_{0j}} = 4\omega_{0j}(\omega_{0j}^2 - \omega^2) \, , \quad \frac{\partial A}{\partial G_j} = 2G_j\omega^2 \, , \quad \frac{\partial A}{\partial F_j} = 0 \, . \tag{1.79}$$

The derivative of real part of ε is

$$\frac{\partial \mathrm{Re}\,\varepsilon}{\partial \omega_{0j}} = \frac{2F_j\omega_{0j}A - F_j(\omega_{0j}^2 - \omega^2)\dfrac{\partial A}{\partial \omega_{0j}}}{A^2} = -2F_j\omega_{0j}\frac{(\omega_{0j}^2 - \omega^2)^2 - (G_j\omega)^2}{A^2} \, , \tag{1.80}$$

$$\frac{\partial \mathrm{Re}\,\varepsilon}{\partial G_j} = \frac{-F_j(\omega_{0j}^2 - \omega^2)\dfrac{\partial A}{\partial G_j}}{A^2} = -2\omega^2 F_j G_j \frac{\omega_{0j}^2 - \omega^2}{A^2} \, , \tag{1.81}$$

$$\frac{\partial \mathrm{Re}\,\varepsilon}{\partial F_j} = \frac{\omega_{0j}^2 - \omega^2}{A} \, , \tag{1.82}$$
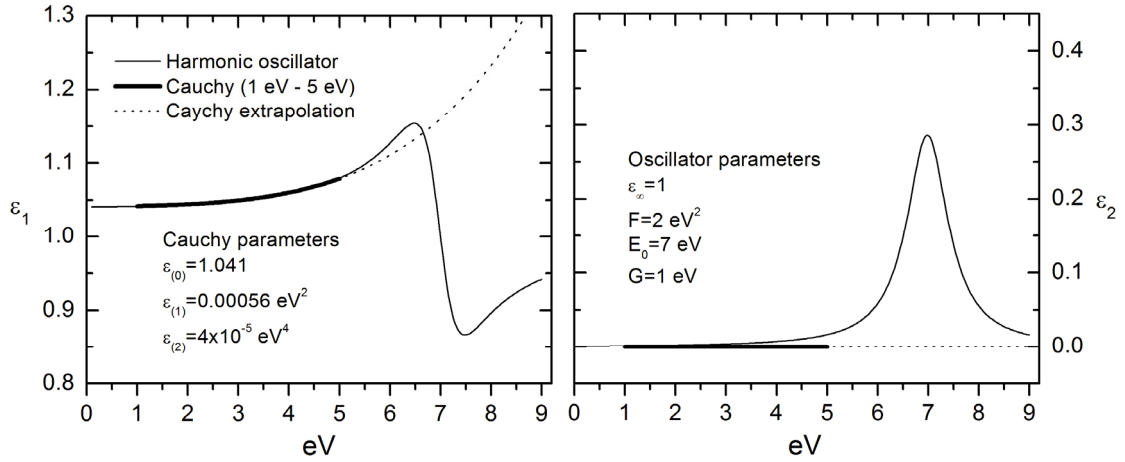
Figure 1.12. The harmonic oscillator and Cauchy models.

and that of the imaginary part of ε

$$\frac{\partial \operatorname{Im}\varepsilon}{\partial \omega_{0j}} = \frac{-\omega F_j G_j \dfrac{\partial A}{\partial \omega_{0j}}}{A^2} = -4\omega F_j G_j \omega_{0j} \frac{\omega_{0j}^2 - \omega^2}{A^2}, \qquad (1.83)$$

$$\frac{\partial \operatorname{Im}\varepsilon}{\partial G_j} = \frac{\omega F_j A - \omega F_j G_j \dfrac{\partial A}{\partial G_j}}{A^2} = \omega F_j \frac{(\omega_{0j}^2 - \omega^2)^2 - (G_j \omega)^2}{A^2}, \qquad (1.84)$$

$$\frac{\partial \operatorname{Im}\varepsilon}{\partial F_j} == \frac{\omega G_j}{A}. \qquad (1.85)$$

Cauchy model

In the case of a dielectric material, in the transparent range, the oscillator model can be approximated by a Taylor series, obtaining the popular *Cauchy model*

$$\varepsilon_1(\omega) = \varepsilon_{(0)} + \varepsilon_{(1)}\omega^2 + \varepsilon_{(2)}\omega^4, \qquad \varepsilon_2(\omega) \doteq 0, \qquad (1.86)$$

where the $\varepsilon_{(0)}$, $\varepsilon_{(1)}$, $\varepsilon_{(2)}$ are three real parameters of the model. Figure 1.12 shows the harmonic oscillator and its Cauchy approximation for the range from 1 to 5 eV. Of course, the extrapolation to higher energies shows the limitation of the Cauchy model.

Gauss-Lorentz model

A generalization of the Lorentzian harmonic oscillator results from the convolution with a Gaussian distribution, leading to the Gauss-Lorentz (G-L) profile

$$\varepsilon_{G-L}(\omega) = \frac{F}{\sqrt{2\pi}G_G} \int_{-\infty}^{\infty} \frac{\exp[-(\omega - x - \omega_0)^2/2G_G^2]}{\omega_0^2 - x^2 - ixG_L} dx, \qquad (1.87)$$

where G_L and G_G are the Lorentzian and Gaussian widths, F is the oscillator strength and ω_0 is the position. The exact shape can be approximated by rational functions using so-called *Humlicek algorithm*.[28]

Effective media approximation

In the case of two or more materials mixed on the scale smaller than the wavelength of light, but still as distinct phases, the optical properties of the resulting material are given by the optical properties of the constituents. Depending on the structure of the host/inclusion mixture various mixing models can be used.[29]

For the case of randomly mixed phases, without a dominant host, we will use the popular *Bruggeman effective media approximation*[30]

$$\sum_j v_j \frac{\varepsilon_j - \varepsilon}{\varepsilon_j - 2\varepsilon} = 0 , \tag{1.88}$$

where v_j is volume fraction of phase j, ε_j is its dielectric function, and ε is the resulting dielectric function of the mixed medium.

Let us assume two media, denoted as A and B; the two phase Bruggeman approximation reads

$$v_A \frac{\varepsilon_A - \varepsilon}{\varepsilon_A - 2\varepsilon} + v_B \frac{\varepsilon_B - \varepsilon}{\varepsilon_B - 2\varepsilon} = 0 . \tag{1.89}$$

When the optical properties of the constituents are known together with the properties of the mixture, the volume ratio of the phases can be calculated as

$$\frac{v_B}{v_A} = \frac{(\varepsilon - \varepsilon_A)(\varepsilon_B + 2\varepsilon)}{(\varepsilon_B - \varepsilon)(\varepsilon_A + 2\varepsilon)} . \tag{1.90}$$

When the composition of the mixture is known and the optical properties of the mixture and one constituent are given, the optical constants of the second constituent are

$$\varepsilon_B = \varepsilon \frac{v_B(\varepsilon_A + 2\varepsilon) - 2v_A(\varepsilon_A - \varepsilon)}{v_B(\varepsilon_A + 2\varepsilon) + v_A(\varepsilon_A - \varepsilon)} . \tag{1.91}$$

When the constituents and their volume ratio are known, the optical properties of the mixture are obtained from solution of quadratic equation

$$-2\varepsilon^2(v_A + v_B) + \varepsilon\left[v_A(2\varepsilon_A - \varepsilon_B) + v_B(2\varepsilon_B - \varepsilon_A)\right] + \varepsilon_A\varepsilon_B(v_A + v_B) = 0 . \tag{1.92}$$

[28] J. Humlicek, *Optimized computation of the voigt and complex probability functions*, J. Quant. Spectrosc. Radiat. Transfer **27,** 437-444 (1982).
[29] D. E. Aspnes, *Optical properties of thin films*, Thin Solid Films **89,** 249-262 (1982).
[30] A. V. Goncharenko, *Generalizations of the Bruggeman equation and a concept of shape-distributed particle composites*, Phys. Rev. E **68,** 041108 (2003).

For the volume fractions normalized to unity, i.e., $v_A+v_B=1$, the solution reads

$$\varepsilon = \frac{\gamma \pm \sqrt{\gamma^2 + 8\varepsilon_A\varepsilon_B}}{4}, \text{ where} \qquad (1.93)$$

$$\gamma = \varepsilon_B + (3v_A - 1)(\varepsilon_A - \varepsilon_B).$$

One of these solutions is unphysical. Here again, we express the derivatives of the Bruggeman dielectric function with respect to the volume and properties of the constituents. These expressions can be used in the calculation of the derivatives using a model containing the mixed material:

$$\frac{\partial \varepsilon}{\partial v_A} = \frac{3}{4}(\varepsilon_A - \varepsilon_B)\left(1 \pm \frac{\gamma}{\sqrt{\gamma^2 + 8\varepsilon_A\varepsilon_B}}\right), \qquad (1.94)$$

$$\frac{\partial \varepsilon}{\partial \varepsilon_A} = \frac{1}{4}\left(3v_A - 1 \pm \frac{\gamma(3v_A - 1) + 4\varepsilon_B}{\sqrt{\gamma^2 + 8\varepsilon_A\varepsilon_B}}\right), \qquad (1.95)$$

$$\frac{\partial \varepsilon}{\partial \varepsilon_B} = \frac{1}{4}\left(3v_A \pm \frac{3\gamma v_A + 4\varepsilon_A}{\sqrt{\gamma^2 + 8\varepsilon_A\varepsilon_B}}\right), \qquad (1.96)$$

where the choice of the sign is inherited from (1.93).

1.2.8. Representations of polarization

The electromagnetic wave with frequency ω travelling in the direction of z-axis can be written, in x and y components ($z=0$), as

$$E_x = X\cos(\omega t + \delta_x),$$

$$E_y = Y\cos(\omega t + \delta_y), \qquad (1.97)$$

where X and Y are the amplitudes, δ_x and δ_y are (arbitrary) phase shifts.

To describe the endpoint trajectory of the electric field vector, we need to remove the time dependence from the equations (1.97). We obtain[31]

$$Y^2E_x^2 + X^2E_y^2 - 2XYE_xE_y\cos(\delta_x - \delta_y) = X^2Y^2\sin^2(\delta_x - \delta_y). \qquad (1.98)$$

This formula describes an ellipse. It is usual to introduce the following notation:

$$X \equiv E_0\sin\Psi, \quad Y \equiv E_0\cos\Psi, \quad \delta_x - \delta_y \equiv \Delta. \qquad (1.99)$$

---

[31] This is done by application of the addition formula for the cosine function, followed by expression of $\sin\omega t$ resp. $\cos\omega t$ from each equation and substituting into the other. Finally, both equations are squared and added.
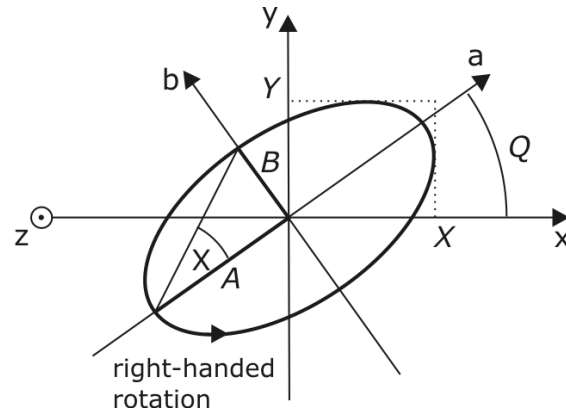
Figure 1.13. Polarization ellipse. The direction of propagation is in the positive sense of z-axis, i.e., towards the reader.

Applying the substitutions we get

$$\left(\frac{E_x}{E_0}\right)^2 + \left(\frac{E_y}{E_0}\right)^2 \tan^2\Psi - 2\frac{E_x}{E_0}\frac{E_y}{E_0}\tan\Psi\cos\Delta = \sin^2\Psi\sin^2\Delta. \quad (1.100)$$

By rotating the (x,y) coordinate system to (a,b) by a proper angle $Q \in (-90°, 90°\rangle$ we obtain the following simple equation of the polarization ellipse (see fig. 1.13)

$$B^2 E_a^2 + A^2 E_b^2 = A^2 B^2, \quad (1.101)$$

where E_a and E_b are the components of the electric field in the (a,b) system and A and B are the lengths of the semiaxes of the ellipse. The ellipticity e and the ellipticity angle[32] $X \in \langle -45°, 45°\rangle$ are given by

$$e = \tan X = \pm\frac{B}{A}, \quad (1.102)$$

where the sign denotes the sense of rotation of the electric vector.[33] In this work we use the pair Q, X for the description of the polarization state of light, and the pair ψ, Δ is reserved for the response of the sample.

For a complete description of the polarization state of the beam (including partially polarized light), we use the *Stokes vector – Mueller matrix* formalism. The Stokes vector is defined as

$$\bar{S} = \begin{bmatrix} I_0 \\ I_x - I_y \\ I_{\pi/4} - I_{-\pi/4} \\ I_R - I_L \end{bmatrix} = I_0 \begin{bmatrix} 1 \\ p\cos 2X\cos 2Q \\ p\cos 2X\sin 2Q \\ p\sin 2X \end{bmatrix}, \quad (1.103)$$

---

[32] We use the Greek capital Chi.
[33] X>0 corresponds to right-handed elliptical polarization and X<0 to left-handed polarization.
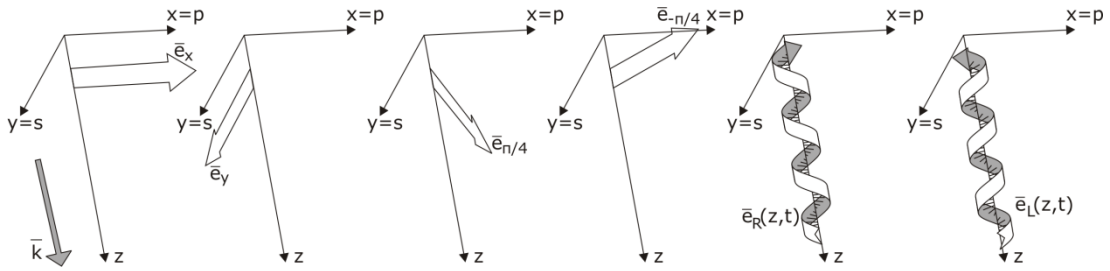
Figure 1.14. Orientation of the polarization vectors, schematic illustration.

where I_0 is the total intensity of light, I_x, I_y, $I_{\pi/4}$, $I_{-\pi/4}$ are the intensities transmitted through a linear polarizer oriented along the x-axis, y-axis, at the azimuth of $\pi/4$, at the azimuth of $-\pi/4$, respectively. The intensities I_R, I_L are transmitted by an ideal right-handed or left-handed polarizer (see fig. 1.14). We express the Stokes vector also with four real variables describing the polarization state. The Q and X are the ellipse tilt and ellipticity angles, and p is the degree of polarization ranging from 0 (completely unpolarized light) to 1 (pure polarization state). The overall intensity I_0 is usually unimportant in ellipsometry.

Changes of the Stokes vector along the optical path of the system are described by 4x4 real Mueller matrices. The Mueller matrix of the linear polarizer oriented along x-axis is

$$\hat{M}_{lin} = \frac{1}{2}\begin{bmatrix} 1 & 1 & 0 & 0 \\ 1 & 1 & 0 & 0 \\ 0 & 0 & 0 & 0 \\ 0 & 0 & 0 & 0 \end{bmatrix}. \tag{1.104}$$

For the linear retarder with the retardance δ and its fast axis oriented along the x-axis,[34] the Mueller matrix has following form

$$\hat{M}_{\delta} = \begin{bmatrix} 1 & 0 & 0 & 0 \\ 0 & 1 & 0 & 0 \\ 0 & 0 & \cos\delta & \sin\delta \\ 0 & 0 & -\sin\delta & \cos\delta \end{bmatrix}. \tag{1.105}$$

To obtain any general orientation of the polarizer or retarder, the Mueller matrices (1.104) and (1.105) can be rotated with the rotation matrix

$$\hat{R}(a) = \begin{bmatrix} 1 & 0 & 0 & 0 \\ 0 & \cos 2a & \sin 2a & 0 \\ 0 & -\sin 2a & \cos 2a & 0 \\ 0 & 0 & 0 & 1 \end{bmatrix}. \tag{1.106}$$

The matrix of the polarizer oriented at the azimuth a is given by

---

[34] The linearly polarized light along azimuth $a=45°$ ($I_{\pi/4}=1$) transmitted through quarter wave retarder ($\delta=90°$) with fast axes oriented along x-axis will get circular left-handed orientation.

$$\hat{M}_{lin}(a) = \hat{R}(-a)\hat{M}_{lin}\hat{R}(a) . \tag{1.107}$$

The matrix of a generally oriented retarder is obtained in the same manner.

The Mueller matrix of an isotropic sample is given by

$$\hat{M} = \frac{|r_s|^2 + |r_p|^2}{2} \begin{bmatrix} 1 & -\cos 2\Psi & 0 & 0 \\ -\cos 2\Psi & 1 & 0 & 0 \\ 0 & 0 & \sin 2\Psi \cos \Delta & \sin 2\Psi \sin \Delta \\ 0 & 0 & -\sin 2\Psi \sin \Delta & -\sin 2\Psi \cos \Delta \end{bmatrix} . \tag{1.108}$$

Let us now comment on the effect of chosen convention for the orientation of the axes, introduced in this chapter, particularly for the reflected beam. In the case of normal incidence on hypothetical reflector with $r_s=r_p=-1$, according to the definition (1.17), the ellipsometric angles are ψ=45° and Δ=0. Therefore, the Mueller matrix of such sample will become diagonal with the diagonal $(1,1,1,-1)$. This means that any incident polarization will be reflected back exactly; only the sense of rotation of the elliptical or circular polarization is changed as it is defined relative to the direction of propagation.

1.3.   Ellipsometric measurement

In this section we describe several common ellipsometric configurations and define the components of the ellipsometer.

We will use the complex *Jones matrices*,[35] describing the amplitude transmission in the chosen coordinate system. We write down the E_p and E_s components of the electric field. Any polarization-changing element in the optical path is described by a 2x2 matrix. For example, the transmission through the polarizer-sample-analyzer (see fig. 1.15) system will be described as

$$E_A \begin{bmatrix} 1 \\ 0 \end{bmatrix} = \begin{bmatrix} 1 & 0 \\ 0 & 0 \end{bmatrix} \begin{bmatrix} \cos A & \sin A \\ -\sin A & \cos A \end{bmatrix} \begin{bmatrix} r_p & 0 \\ 0 & r_s \end{bmatrix} \begin{bmatrix} \cos P \\ \sin P \end{bmatrix} E_P , \tag{1.109}$$

where (from right to left): the amplitude of electric field incoming from the source is written in components (p,s) according to polarizer setting *P*; the reflection on the sample of the each component is given by the complex reflectivities r_p and r_s; the following rotation matrix changes the system of coordinates to the one connected to the analyzer, and the analyzer Jones matrix selects the component parallel with the azimuth *A*.

The azimuths of the components (polarizer, analyzer, compensator) are defined as the angles between the fundamental axis of the component (transmission or fast axis) and the plane of incidence – in the sense of the

---

[35] See J. Humlicek, in: H. Tompkins, E. Irene (Eds.), *Handbook of Ellipsometry*, William Andrew Publishing, New York (2005).
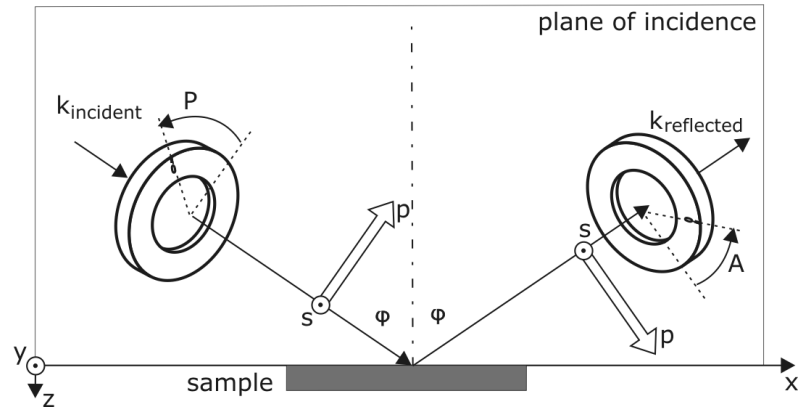
Figure 1.15. Ellipsometric configuration: The generation (left) and detection (right) branch.

rotation from the positive direction of the p-polarization vector to the positive direction of the s-polarization vector.

1.3.1. Straight-through operation

A very basic configuration used for the calibration and testing of an ellipsometer is the set up for the so-called *straight-through operation*, when the sample (sample holder or stage) is removed and the angle of incidence is set to 90 degrees.

According to the used orientation of the axes, the straight-through model must be completed by the Jones (or Mueller) matrix of virtual reflection, to compensate the change of the direction of p-polarization. The proper Jones and Mueller matrices are

$$\hat{J}_0 = \begin{bmatrix} -1 & 0 \\ 0 & 1 \end{bmatrix},$$

$$\hat{M}_0 = \begin{bmatrix} 1 & & & \\ & 1 & & \\ & & -1 & \\ & & & -1 \end{bmatrix}. \tag{1.110}$$

Here, the light propagates in the direction of x-axis and therefore the polarization vector lies in the yz-plane instead of xy-plane.

1.3.2. Rotating analyzer

As mentioned in section 1, the most popular configuration is the polarizer – sample – analyzer in reflection regime, with fixed polarizer and rotating analyzer or fixed analyzer, and rotating polarizer. Here, we derive the basic equations for the former.

According to eq. (1.109) the amplitude transmitted by the analyzer is

$$E_A = E_P \left(r_p \cos A \cos P + r_s \sin A \sin P \right). \tag{1.111}$$

This equation shows the symmetry of the rotating analyzer and rotating polarizer configurations. Applying the relation (1.17), we get

$$E_A = E_P r_s \left(\tan\Psi e^{i\Delta} \cos A \cos P + \sin A \sin P \right). \tag{1.112}$$

Then, the signal at the (polarization insensitive) detector is given by

$$I(A) = E_A \cdot E_A^* = I(P) |r_s|^2 \begin{bmatrix} \tan^2\Psi \cos^2 A \cos^2 P + \\ + \tan\Psi \cos A \cos P \sin A \sin P (e^{i\Delta} + e^{-i\Delta}) + \\ + \sin^2 A \sin^2 P \end{bmatrix}, \tag{1.113}$$

which results in the following form

$$I(A) = I_0 \left[1 + a \cos 2A + \beta \sin 2A \right], \tag{1.114}$$

where

$$I_0 = \frac{I(P) |r_s|^2 \cos^2 P}{2} (\tan^2\Psi + \tan^2 P),$$

$$a = \frac{\tan^2\Psi - \tan^2 P}{\tan^2\Psi + \tan^2 P}, \qquad \beta = \frac{2\tan\Psi \tan P \cos\Delta}{\tan^2\Psi + \tan^2 P}. \tag{1.115}$$

Then the sought ellipsometric quantities are

$$\tan\Psi = |\tan P| \sqrt{\frac{1+a}{1-a}}, \qquad \cos\Delta = \operatorname{sgn} P \frac{\beta}{\sqrt{1-a^2}}. \tag{1.116}$$

The sign of the cosΔ is given by the sign of tan$P$ or simply by the sign of P, with the polarizer setting restricted to (-90°, 90°).

The sign may also differ as a result of the opposite sense of rotation of the analyzer. In such case, the sign of β will be opposite. This results in

$$\Delta' = 180° - \Delta. \tag{1.117}$$

Thus, the observed delta can be simply corrected.

It is necessary to mention that the RAE or RPE can detect only absolute value of Δ, $\Delta \in (-180°, 180°\rangle$, because only cosine of Δ is actually measured. Determining cosΔ also results in a lower sensitivity to Δ near 180°, 0° or -180°.

1.3.3. RAEc, RCE

Improvements to the RAE scheme can be obtained with the help of a compensator (RAEc) in the polarization-state-generation branch (see fig. 1.16). By that, elliptically polarized light is shed on the sample and the above mentioned weakness of the RAE in particular Δ range is shifted, i.e., the points of lower sensitivity can be avoided. Let us consider the polarizer-compensator-sample-rotating analyzer system, described by the Jones matrices as follows
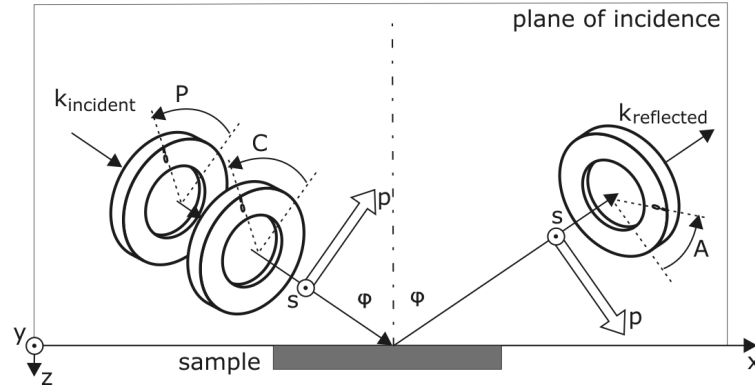
Figure 1.16. Configuration of the RAEc and null ellipsometry.

$$E_A \begin{bmatrix} 1 \\ 0 \end{bmatrix} = \begin{bmatrix} 1 & 0 \\ 0 & 0 \end{bmatrix} \begin{bmatrix} \cos A & \sin A \\ -\sin A & \cos A \end{bmatrix} \begin{bmatrix} r_p & 0 \\ 0 & r_s \end{bmatrix} \hat{C} \begin{bmatrix} \cos P \\ \sin P \end{bmatrix} E_P,$$
(1.118)

where the compensator matrix in a general position is given by

$$\hat{C} = \begin{bmatrix} \cos C & -\sin C \\ \sin C & \cos C \end{bmatrix} \begin{bmatrix} t_f & 0 \\ 0 & t_s \end{bmatrix} \begin{bmatrix} \cos C & \sin C \\ -\sin C & \cos C \end{bmatrix},$$
(1.119)

where t_f and t_s are the transmittances along the fast and slow axes of the device. The compensator matrix is multiplied from both sides by proper rotation matrices. We will limit the following calculations to the simplified situation of an ideal quarter-wave retarder: $t_f=1$, $t_s=i$, set to the azimuth $C=45°$. In this configuration, various ellipses can be generated by changing the polarizer angle. The position of the compensator fixes the ellipse tilt to 45°. The Jones matrix of the compensator to be inserted into (1.118) is

$$\hat{C} = \frac{1}{2} \begin{bmatrix} 1+i & 1-i \\ 1-i & 1+i \end{bmatrix}.$$
(1.120)

Then, after some manipulations, the signal at the detector can be again expressed in the form of eq. (1.114). The ellipsometric angles are related to the Fourier coefficients of the signal, a and β, as

$$\tan\Psi = \sqrt{\frac{1+a}{1-a}}, \qquad \sin(2P-\Delta) = \beta \frac{(\tan^2\Psi+1)}{2\tan\Psi}.$$
(1.121)

Here, the sensitivity to Δ can be tuned by setting $2P$ close to the expected value of Δ.

A significant improvement can be achieved by fixing the polarizer and analyzer, and rotating the compensator positioned either in the source or the detection branch (or in both branches). The *rotating compensator ellipsometry* (RCE) is described in detail in chapter 3.

1.3.4. Null ellipsometry

Direct measurements of the ellipsometric angles Ψ and Δ are possible in the configuration described above (fig. 1.16). The compensator (quarter wave retarder) is fixed at 45°, and the minimum (null) signal at the detector is produced by setting both polarizer and analyzer positions. The nulling condition can be written down, using eq. (1.118), as

$$\begin{bmatrix} 0 \\ 0 \end{bmatrix} = \begin{bmatrix} 1 & 0 \\ 0 & 0 \end{bmatrix} \begin{bmatrix} \cos A & \sin A \\ -\sin A & \cos A \end{bmatrix} \begin{bmatrix} \rho & 0 \\ 0 & 1 \end{bmatrix} \begin{bmatrix} 1+i & 1-i \\ 1-i & 1+i \end{bmatrix} \begin{bmatrix} \cos P \\ \sin P \end{bmatrix}. \qquad (1.122)$$

The formula leads to a linear equation for ρ

$$\rho = \frac{\sin A \left[\cos P(1+i) + \sin P(1-i) \right]}{\cos A \left[\cos P(1-i) + \sin P(1+i) \right]}. \qquad (1.123)$$

Expressing then the left- and right-hand side as

$$\tan\Psi(\cos\Delta + i\sin\Delta) = \tan A(\sin 2P + i\cos 2P), \qquad (1.124)$$

we finally obtain the ellipsometric angles in terms of the analyzer and polarizer azimuths:

$$\Psi = A, \quad \Delta = 90° - 2P. \qquad (1.125)$$

This method is also applicable to the case of slightly depolarizing sample, when partial polarization state is reflected. The minimum signal is obtained for the same values of A and P, however, the minimum signal is now nonzero.

1.3.5. Analysis of the signal with rotating elements

Let us consider a typical situation when the rotating element (analyzer, polarizer or compensator) is employed, and the signal $I(A)$ is measured as the dependence on the element azimuth A. For the sake of simplicity, we will discuss the case of rotating analyzer in this subsection.

Acquisition of data

We assume a Gaussian distribution of the signal noise, because the measurement typically involves an accumulation of detector counts over given time.[36] Moreover, in our case, the photomultiplier current is measured by a fast computer card and the measurement is repeated to obtain a statistical set (typically $N \sim 1000$) of data. The mean I, and the statistical error of mean δI are eventually extracted.

Along with the signal measurement, the background level of the intensity must be determined to exclude the possible ambient or uniform stray light from the signal as well as the detector zero offset and the dark current. Then, a constant illumination does not affect the results of the

---

[36] Strictly speaking the distribution of single measurement of intensity in counts is Poissonian (shot noise) with mean value I and error $\sqrt{I}$. Multiple measurements of the intensity further reduce the error by factor $1/\sqrt{N}$, where N is the number of measurements.

measurement. For achieving the best precision, every signal measurement (with light source on) is followed by a background measurement (light closed by a shutter). For each spectral position and each analyzer setting, we obtain:

$$I = I_{light} - I_{dark},$$

$$\delta I = \sqrt{\delta I_{light}^2 + \delta I_{dark}^2}. \qquad (1.126)$$

The measured set of data $[A_i, I_i, \delta I_i]$, $i=1..N$, must be fitted by a proper model to obtain the raw ellipsometric parameters. In the case of rotating analyzer the model is given by

$$I(A_i) = \Theta_1 + \Theta_2 \cos 2A_i + \Theta_3 \sin 2A_i = \sum_{j=1}^{3} \Theta_j \frac{\partial I(A_i)}{\partial \Theta_j}. \qquad (1.127)$$

The maximum likelihood estimation results from the minimization of the weighted sum of squares (least-squares method), leading to the set of linear ("normal") equations

$$\sum_{k=1}^{3} \Theta_k \sum_{i=1}^{N} \frac{1}{\delta I_i^2} \frac{\partial I(A_i)}{\partial \Theta_j} \frac{\partial I(A_i)}{\partial \Theta_k} = \sum_{i=1}^{N} I_i \frac{1}{\delta I_i^2} \frac{\partial I(A_i)}{\partial \Theta_j}, \text{ for j=1..3, or}$$

$$H_j^k \Theta_k = b_j, \qquad (1.128)$$

where H is the Hessian matrix, and b is the vector of right-hand side. Its solution is the estimate

$$\Theta_j = D_j^k b_k, \qquad (1.129)$$

where D is the covariance matrix, i.e., inverse Hessian.

It should be noted that the selection of analyzer settings affects the errors and correlations between the fitted parameters. Optimally we choose the analyzer positions as equidistant points. Minimum number of points is 3 per 180° of the analyzer rotation.

In the simplified case, when the errors δI_i are equal, the off-diagonal elements of the Hessian become zeros (leading to vanishing covariance between the sought parameters), and all the diagonal elements will be equal.[37]

Using the obtained parameters Θ_j we calculate the residual sum of squares

$$S_0 = \sum_{i=1}^{N} \frac{1}{\delta I_i^2} \left(I_i - I(A_i) \right)^2, \qquad (1.130)$$

and estimate the standard deviation of the measured data points per unit weight as

---

[37] For unit errors, the diagonal elements will be equally N.

$$\sigma I = \sqrt{\frac{S_0}{N-L}} , \tag{1.131}$$

where L is the number of parameters, here $L=3$. Finally, the errors of the parameters are given by

$$\delta \Theta_j = \sigma I \cdot \sqrt{D_{jj}} . \tag{1.132}$$

The presence of other possible trends in the measured signals, for example, higher harmonics is treated as the noise and included in the parameter error. For calibration purposes, the amplitudes of parasitic harmonics can be estimated together with the main parameters (see below).

Fourier coefficients

The RAE Fourier coefficients according to (1.114) are

$$a = \frac{\Theta_2}{\Theta_1} , \quad \beta = \frac{\Theta_3}{\Theta_1} , \text{ and } \quad I_0 = \Theta_1 . \tag{1.133}$$

In the case of RCE, a higher harmonic component (cos4C, sin4C) is present in the signal and carries information as well. Therefore, the dependence of the signal on the compensator azimuth is given by five numbers $\Theta_1, \dots, \Theta_5$. A detailed description is given in chapter 3.

The error of the estimated Fourier coefficient a is given by (with the error of β obtained in an analogous way)

$$\delta a = \sqrt{\left(\frac{1}{\Theta_1}\right)^2 \delta \Theta_2^2 + \left(\frac{\Theta_2}{\Theta_1^2}\right)^2 \delta \Theta_1^2} = \frac{1}{\Theta_1} \sqrt{\delta \Theta_2^2 + a^2 \delta \Theta_1^2} . \tag{1.134}$$

In the previously mentioned simplified case, where the errors of parameters $\delta \Theta_i$ being be equal, the error of δa ($\delta \beta$) is given by the relative error of the mean intensity and by the magnitude of the coefficient itself

$$\delta a \sim \frac{\delta \Theta_1}{\Theta_1} \sqrt{1 + a^2} . \tag{1.135}$$

Errors of RAE Ψ, Δ

The ellipsometric angles in the case of RAE are determined by (1.116). The estimates of errors are given by error propagation

$$\delta \Psi = \frac{|\tan P|}{1 + \tan^2 \Psi} \sqrt{\frac{1-a}{1+a}} \frac{\delta a}{(1-a)^2} , \tag{1.136}$$

$$\delta \Delta = \frac{1}{\sin \Delta} \left[\frac{a^2 \beta^2}{(1-a^2)^3} \delta a^2 + \frac{1}{1-a^2} \delta \beta^2 \right]^{\frac{1}{2}} . \tag{1.137}$$
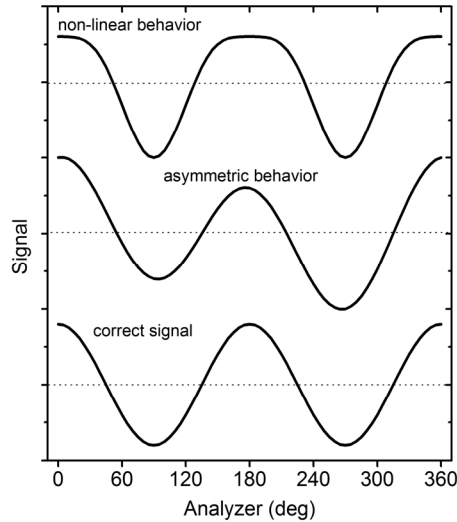
Figure 1.17. Example of signals with parasitic harmonic components.

Systematic errors

The presence of systematic errors in the measured RAE signal can be detected as non-vanishing higher and lower harmonic components, e.g.,

$$I(A) = I_0(1 + a\cos 2A + \beta\sin 2A +$$

$$+a_{asym}\cos A + \beta_{asym}\sin A + a_{nonlin}\cos 4A + \beta_{nonlin}\sin 4A)\,, \qquad (1.138)$$

where the amplitude of the lower component is related to the asymmetry of the signal, and the amplitude of the selected higher (4A) component signalizes the possible presence of detection nonlinearity.

Figure 1.17 shows calculated signals for I_0=1, a=0.8, β=0 (correct) with additional asymmetry: a_{asym}=0.2, β_{asym}=0.2 and with non-linearity: a_{nonlin}=-0.2, β_{nonlin}=0.

1.4. Summary

Section 1 contains the introduction to ellipsometry with a brief overview of its history and present applications. The instruments used in various parts of this study are listed and described.

In section 2, the basic formalism necessary for ellipsometric data analysis is developed starting with the Maxwell's equations in the plane-wave framework. We characterize the waves using components of its wave-vector, avoiding effectively the use of angle of incidence/propagation in the expressions.

We restrict ourselves to layered homogeneous and isotropic samples with a linear optical response (energy dependent dielectric function). The propagation through layered media is described with the help of propagation matrices. We express the derivatives of ellipsometric angles Ψ and Δ with respect to film thicknesses or optical constants in the model,

which is useful for the implementation of gradient-based optimization algorithms.

The link between the ellipsometrically measured quantities and the dielectric function is shown. Other optical quantities (refractive index, absorbance etc.) are introduced and related to the dielectric function.

Classical harmonic oscillator model is presented providing a useful parameterization for the dielectric function of materials. A simplification in the form of Cauchy model, and a generalization in the form of Gauss-Lorentz model, is presented as well. To treat the material mixtures, the Bruggeman effective media approximation is described.

We introduce the representation of polarization state, which is used in following chapters. Mueller matrix is defined for description of polarization properties of reflective interfaces.

Section 3 contains the descriptions of the typical ellipsometric configurations: straight-through, RAE, RAEc, RCE and null ellipsometry. Special attention is paid to signal analysis in the rotating analyzer configuration, and the measurement-error (random and systematic) estimation.

Chapter 2 : Data processing in rotating analyzer ellipsometry

This work was done during 2005 along with the reconstruction of our ellipsometer with rotating analyzer. The idea was inspired by Josef Humlíček in a discussion in Karlsruhe, February 2005.

Ellipsometry is based on precise measurements of angles and therefore sensitive to incorrectly aligned optical elements. In the first section of this chapter we will introduce the angular offsets of polarizer and analyzer in rotating analyzer ellipsometry, and discuss their impact on the measured quantities. Algorithm for data calibration is proposed and described in detail in second section of this chapter. The third section brings examples of the actual calibration.

The calibration problem of the rotating analyzer ellipsometry (RAE) data to correct the offsets of the polarizer is well known and calibration procedure AB2PD developed by J. Humlíček is available at our lab. However, we decided to improve the routine by introducing the averaging on the Fourier coefficient level, and including the possibility to treat multiple measurements taken at various polarizer settings at once. The framework of the Fourier coefficients benefits from continuity and smoothness of the transforms, as described in this chapter.

The improved algorithm has been implemented into computer program MultiAB2PD and has been regularly used for RAE measurements since then.

2.1.   Introduction of the offsets

2.1.1. Angular misalignment of the elements

In the previous chapter, I presented the way how to obtain the cosine and sine Fourier coefficients with their statistical errors (a, β, δa, $\delta\beta$) from the intensity data measured with rotating analyzer. If we exclude the possibility of the erroneous setting of the angle of incidence, spectroscopic errors, depolarization or non-linear polarization introduced by the optical elements,[38] serious flaws might still be introduced to the measurement by incorrect polarizer or analyzer settings. These errors might occur, in case of RAE, when the nominal and physical positions of the polarizer are misaligned, or when some offset or delay is present at the rotating analyzer. Let us denote by P and A the true (physical) azimuths of the elements, measured as the angle between the p-polarization vector (plane of incidence) and the transmission axis of the polarizer, into the positive direction of s-polarization vector (see fig. 2.1). Let P_r and A_r be the read-outs of the azimuths (nominal values). Then the P_0 and A_0 are the offsets.

$$P = P_r - P_0 \,, \tag{2.1}$$

$$A = A_r - A_0 \,. \tag{2.2}$$

To remove these systematic errors from the data, a calibration routine of some kind must be employed to detect the offsets. The issue of the angular misalignment is well known and several methods have been proposed.[39,40]
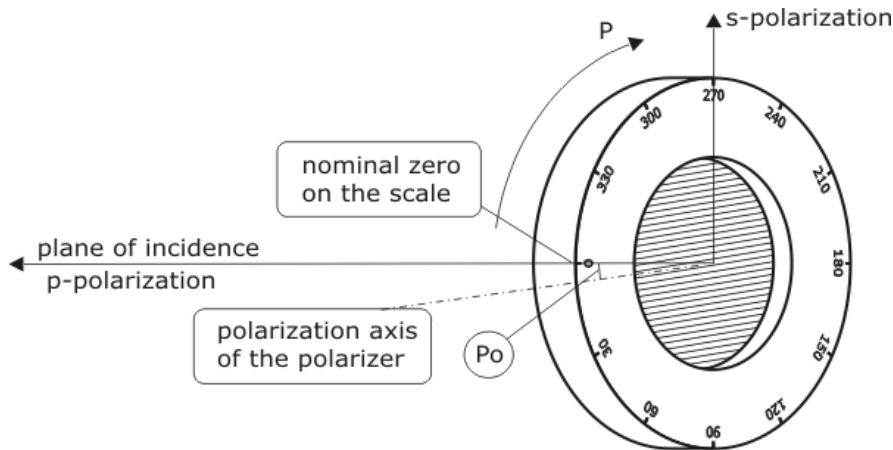
Figure 2.1. Schematic drawing of a polarizer with the offset P_0.

---

[38] The optical activity of the used quartz Rochon prisms is actually important example, but the issue is not discussed here. Basic review can be found in R. W. Collins, *Automatic rotating element ellipsometers: Calibration, operation and real-time applications*, Rev. Sci. Instrum. **61,** 2029-2062 (1990).
[39] See for example R. W. Collins, I. An, C. Chen, in: H. Tompkins, E. Irene (Eds.), *Handbook of Ellipsometry (chapter 5.6)*, William Andrew Publishing, New York (2005).
[40] Similar approach to the one presented here: B. Johs, *Regression calibration method for rotating element ellipsometers*, Thin Solid Films **234,** 395-398 (1993).
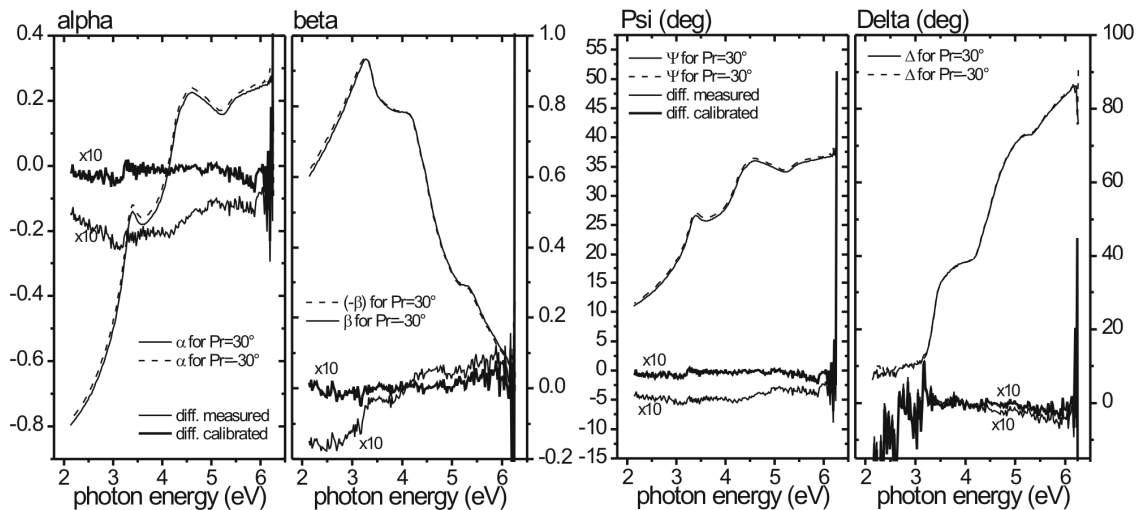
**Figure 2.2. Ellipsometric quantities measured on silicon by RAE (φ=70 deg) with two polarizer settings and their differences calculated before and after the calibration. The differences are multiplied by factor 10 for better visibility on the plots. The offsets found by the calibration procedure were P_0=-0.07 deg and A_0=-0.25 deg.**

I describe here a method based on double measurement of the actual spectra of the sample, with two different polarizer settings, typically P_{r1}=-P_{r2}, and the method is generalized for multiple polarizer settings as well. This method does not need additional calibration measurements and the measured spectra are averaged at the end of the procedure, increasing the precision of the whole experiment. The presence of the actual sample is necessary, because the exact sample position determines the incidence plane and therefore also the physical zero positions of the polarizers. A variety of different values of Ψ and Δ over the spectra typically helps avoiding weak spots of other methods, based on single wavelength pre-calibration. Also, the typical large number of the measured spectral points improves the precision of the A_0 and P_0 determination. Of course, in unfortunate cases of flat spectra, the advantages of our method are reduced.

Figure 2.2 shows an example of the measured Fourier coefficients and ellipsometric angles for reference silicon sample. Two measurements were performed, setting the polarizer at 30° and -30°. Due to the small actual misalignment of the polarizer and analyzer the Fourier coefficients differ only slightly (negative value of β for P_r=30° is plotted) as well as Ψ and Δ calculated from them. The calibration described further in this chapter was applied and the offsets were found to be P_0=-0.07° and A_0=-0.25°. The angle Ψ is more sensitive to the misalignment in this case when the analyzer shift dominates, because Ψ describes closely the position of the measured ellipse (phase shift in the harmonic $I(A)$ signal), while the angle Δ is related to the ellipticity, i.e., to the amplitude of the signal.

2.1.2. State of the art

The present work started from the baseline defined by calibration routine[41] AB2PD.exe. The program uses two .eab data files with the Fourier

---

[41] J. Humlíček, program *AB2PD.exe* (2004).

coefficients, finds the offsets, calculates calibrated Ψ and Δ, and the result is saved in .epd output file. The program needs a text input file with defined spectral range, starting values for the search and the filenames of the data and output files. The results are plotted in a graph in a full-screen DOS window with no other user interface.

The AB2PD calibration works according to following algorithm:

- The program is initialized, loads input file with the initial P_0 and A_0 estimates and two data files with the Fourier coefficients and their errors: spectra of a_{r1}, β_{r1}, δa_{r1}, $\delta\beta_{r1}$ and a_{r2}, β_{r2}, δa_{r2}, $\delta\beta_{r2}$ in identical spectral points.
- A given analyzer offset A_0 (starting estimate) is used for recalculation (rotation) of the coefficients to the corrected values a_1, β_1 and a_2, β_2, i.e. the values that would be detected using properly aligned analyzer – see equations (2.6) and (2.7).
- The polarizer offset P_0 is used for correction of the nominal polarizer settings P_{r1} and P_{r2}. Then the pairs of ellipsometric angles Ψ_1, Δ_1, $\delta\Psi_1$, $\delta\Delta_1$ and Ψ_2, Δ_2, $\delta\Psi_2$, $\delta\Delta_2$ can be calculated – see equations in previous chapter, section 1.3. Here, the errors propagate properly from the Fourier coefficients to the ellipsometric angles. If the true P_0 and A_0 are inserted, then the calculated ellipsometric angles must be mutually identical – down to the noise level.
- Resulting Ψ, Δ, δΨ, δΔ are calculated as

$$\Psi = \frac{\Psi_1 + \Psi_2}{2}, \qquad \Delta = \frac{\Delta_1 + \Delta_2}{2},$$

$$\delta\Psi = \frac{\sqrt{\delta\Psi_1^2 + \delta\Psi_2^2}}{2}, \qquad \delta\Delta = \frac{\sqrt{\delta\Delta_1^2 + \delta\Delta_2^2}}{2}. \qquad (2.3)$$

- The weighted sum of squares is calculated over the spectrum

$$S = \sum_i \left[\frac{\left(\Psi_{i1} - \Psi_{i2}\right)^2}{\delta\Psi_{i1}^2 + \delta\Psi_{i2}^2} + \frac{\left(\Delta_{i1} - \Delta_{i2}\right)^2}{\delta\Delta_{i1}^2 + \delta\Delta_{i2}^2} \right]. \qquad (2.4)$$

- The minimum of the sum is sought in the two-dimensional space A_0, P_0 employing the simplex method. The steps of this algorithm are therefore repeated from the second point until the minimum is reached.

In the following section I will introduce and describe the improved calibration method and its implementation to a computer program. During the year 2005 I was engaged with RAE ellipsometer[42] reconstruction. I wrote the software for data acquisition (Fourier coefficients) and used the presented program regularly for the calibration and data processing.

[42] See previous chapter, subsection 1.1.4. – Gaertner ellipsometer.
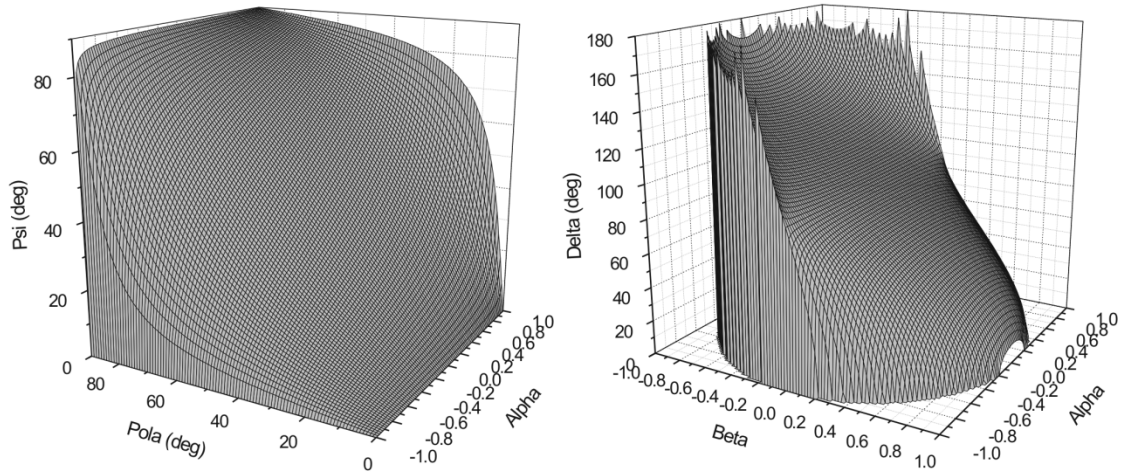
Figure 2.3. Ψ and Δ as functions of measured RAE Fourier coefficients and polarizer setting.

2.2. MultiAB2PD

2.2.1. Roadmap for MultiAB2PD

Keeping the principle of calibration as described in previous section, two main goals were set for the new version of the calibration program. The first goal was to generalize the program for handling multiple files with Fourier coefficients measured at various polarizer settings: a proper weighting in the averages and in the sum of squares together with a reasonable choice of the polarizer settings would reduce the vulnerability in situations, where the value of P_r is too close to the offset P_0.

The second goal was to perform the averaging and optimization on the level of Fourier coefficients. The transform of the coefficients to ellipsometric angles is non-linear. In some cases the symmetric distribution of the measured coefficient might result in a skewed distribution of Ψ and Δ and therefore the propagated error might be estimated incorrectly. Figure 2.3 shows the ellipsometric angles as functions of the coefficients and the polarizer setting. One can see that, particularly for the extreme values of a and β, the non-linearity might play a significant role.

The framework of the Fourier coefficients has to deal with the main problem that the coefficients measured at different polarizer setting must be different in principle. A transform of the coefficients and their errors must be developed to obtain comparable values.

Using a transform, named *flop-flip* in this chapter, the pairs of Fourier coefficients measured at a given P_r are recalculated to one arbitrarily selected polarizer position P_{FLIP}. The coefficients obtained from the flop-flip transform can be averaged, or a properly weighted sum of squares of their mutual differences can be calculated and minimized in the parameter space of the polarizer and analyzer offsets.
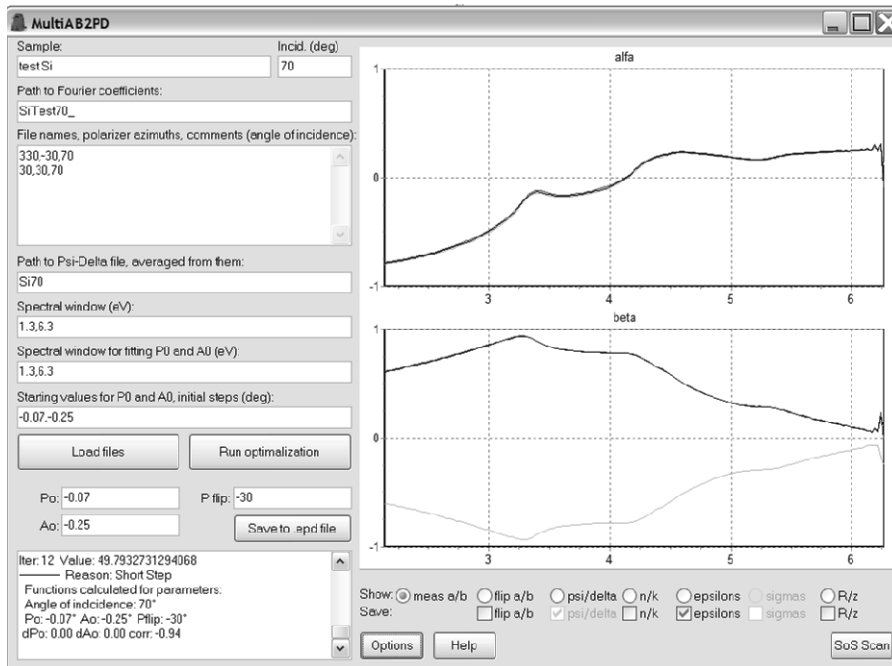
Figure 2.4. User interface of MultiAB2PD.

As a simple example we describe the favorable case when the offsets of both polarizer and analyzer are small, and the polarizer is set to two reasonable opposite azimuths, $P_{r1}=-P_{r2}$. Two sets of Fourier coefficients are measured. Let us take $P_{FLIP}=P_{r1}$. Then the flop-flip transform changes only sign of the coefficient β_2, resulting in two comparable pairs of a and β. This simple transform will work for any physical coefficient combination whatever Ψ and Δ; therefore, the averaging or optimization is not affected by the non-linearity of the functions Ψ and Δ.

The transform used for correction of the coefficients and their errors to A_0 offset is called *flop*. The recalculation of the coefficients and errors for different *P* setting is then called *flip*.

2.2.2. mAB2PD.exe

The presented method was implemented in the program MultiAB2PD (mAB2PD.exe). The structure of the input and output files is analogical with the AB2PD.exe and the program can be used in the same way by using the text input file without any operations within the user interface. However, the settings can also be modified from the window (fig. 2.4). Additional options for the output are present: pseudo-dielectric function[43] can be calculated as well as (pseudo) refractive index, penetration depth and the normal-incidence reflectivity.

To improve the performance, the Marquardt-Levenberg algorithm is employed for the sum of squares minimization. The derivatives of the flop-flip transforms are therefore necessary for the smooth operation of the method. Further in this section I describe the transforms and also pay attention to the derivatives and error propagation.

---

[43] See chapter 1 subsection 1.2.6.

2.2.3. Transforms and error propagation

Flop transform

In a measurement with the rotating analyzer, a_r, β_r are the Fourier coefficients measured with setting the P_r and using the rotating analyzer scale A_r. The signal at the detector is

$$I(A_r) = 1 + a_r \cos 2A_r + \beta_r \sin 2A_r =$$

$$= 1 + a_r \cos(2A + 2A_0) + \beta_r \sin(2A + 2A_0), \tag{2.5}$$

where we use explicitly the offsets of eq. (2.2). The constant contribution I_0 to the intensity was set to 1 without a loss of generality. Then the true coefficients a, β detected using a correct analyzer scale A are given by

$$a = a_r \cos 2A_0 + \beta_r \sin 2A_0, \tag{2.6}$$

$$\beta = -a_r \sin 2A_0 + \beta_r \cos 2A_0. \tag{2.7}$$

The transform (2.6), (2.7) is called *flop* here. The error propagated through the flop is

$$\delta a = \sqrt{\delta a_r^2 \cos^2 2A_0 + \delta \beta_r^2 \sin^2 2A_0}, \tag{2.8}$$

$$\delta \beta = \sqrt{\delta a_r^2 \sin^2 2A_0 + \delta \beta_r^2 \cos^2 2A_0}. \tag{2.9}$$

The flop is merely a rotation of the coefficients and therefore the transform is robust.

Flip transform

According to equations (1.115) in 1.3.2., the Fourier coefficients are given by the angles Ψ and Δ and the polarizer azimuth P:

$$a = \frac{\tan^2 \Psi - \tan^2(P_r - P_0)}{\tan^2 \Psi + \tan^2(P_r - P_0)}, \quad \beta = \frac{2 \tan \Psi \tan(P_r - P_0) \cos \Delta}{\tan^2 \Psi + \tan^2(P_r - P_0)}, \tag{2.10}$$

where the offset (2.1) and nominal polarizer setting P_r were introduced. Applying the previous equations, the transform *flip* couples the detected coefficients a, β to those obtained with another polarizer setting P_{FLIP} in following way:

$$a_{FLIP} = \frac{\tan^2(P_r - P_0) - \tan^2 P_{FLIP} + a\left[\tan^2(P_r - P_0) + \tan^2 P_{FLIP}\right]}{\tan^2(P_r - P_0) + \tan^2 P_{FLIP} + a\left[\tan^2(P_r - P_0) - \tan^2 P_{FLIP}\right]}, \tag{2.11}$$

$$\beta_{FLIP} = \frac{2\beta \tan(P_r - P_0) \tan P_{FLIP}}{\tan^2(P_r - P_0) + \tan^2 P_{FLIP} + a\left[\tan^2(P_r - P_0) - \tan^2 P_{FLIP}\right]}. \tag{2.12}$$
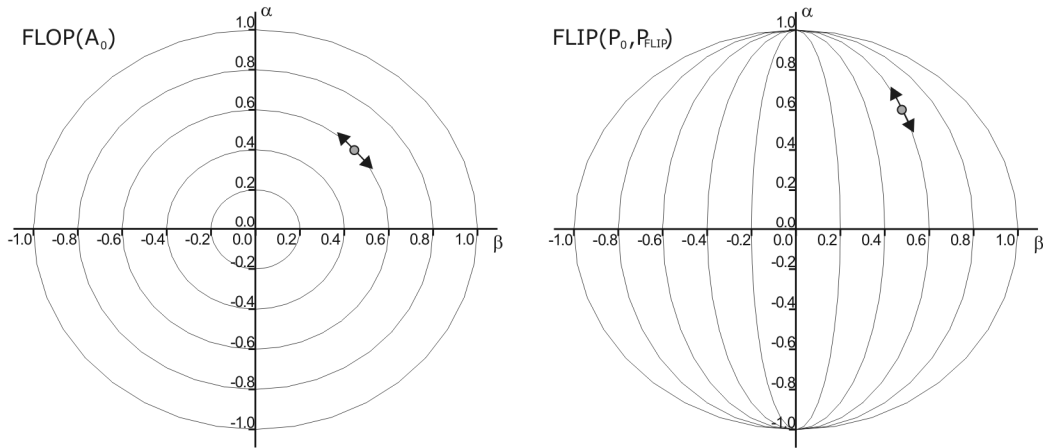
Figure 2.5. Trajectories of the Fourier coefficients in the flip-flop transform. For given input coefficients the output coefficients stay on the ellipses (circles) and the position on the ellipses is given by the input angles A_0, P_0 and P_{FLIP}.

Let us denote the denominator by D_+ for simplicity of following formulas,

$$D_+ \equiv \tan^2(P_r - P_0) + \tan^2 P_{FLIP} + a\left[\tan^2(P_r - P_0) - \tan^2 P_{FLIP}\right]. \qquad (2.13)$$

Then the errors propagated through the flip are

$$\delta a_{FLIP} = \frac{4\tan^2(P_r - P_0)\tan^2 P_{FLIP}}{D_+^2}\,\delta a, \qquad (2.14)$$

$$\delta\beta_{FLIP} = \sqrt{\left(\frac{-2\beta\tan(P_r - P_0)\tan P_{FLIP}\left[\tan^2(P_r - P_0) - \tan^2 P_{FLIP}\right]}{D_+^2}\right)^2 \delta a^2 + \left(\frac{2\tan(P_r - P_0)\tan P_{FLIP}}{D_+}\right)^2 \delta\beta^2}. \qquad (2.15)$$

Representation of the transforms

In fig. 2.5 we plotted the trajectories of the Fourier coefficients in the flop and flip transforms. The flop transform conserves $\sqrt{a^2 + \beta^2}$ and rotates the coefficients in the a, β plane along the circles plotted in the figure, uniformly with $2A_0$. The flip transform conserves $\beta/\sqrt{1-a^2}$, which defines elliptical trajectory in the plane, and is equal to $\pm\cos\Delta$. The transform can be viewed as a projected rotation of the point along a unitary circle lying in a plane tilted from the a, β plane by the angle Δ. The position on the circle (ellipse) is given by the polarizer offset P_0 and the target polarizer value P_{FLIP}, when P_r is fixed. However, the transform is not uniform; the parameterization of the rotation along the circle is given by Ψ: the coefficient a vanishes for $P=\Psi$.
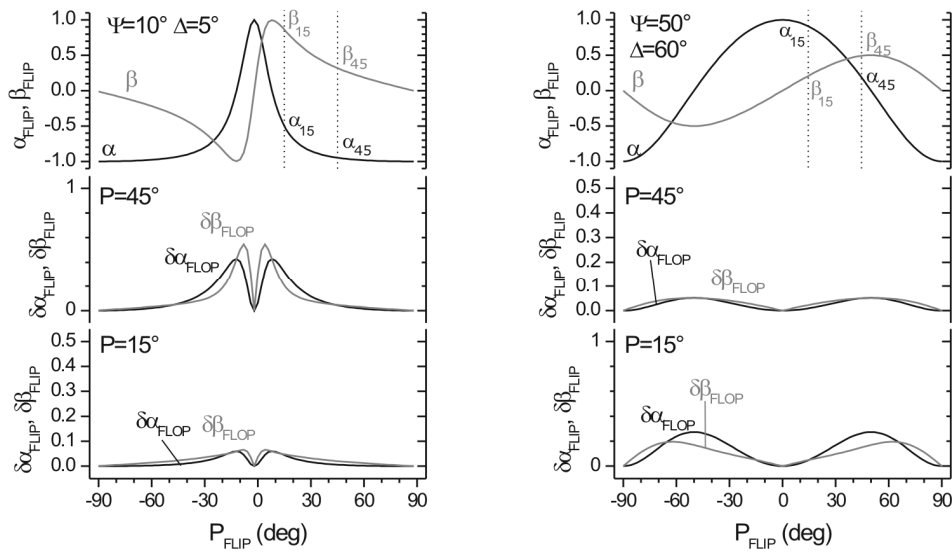
Figure 2.6. Flip-transformed Fourier coefficients and their errors for given Ψ, Δ and polarizer setting. Left graph shows the calculation for Ψ=10°, Δ=5° and P=45° resp. P=15°. Graph on the right shows the calculation for Ψ=50°, Δ=60° and P=45° resp. P=15°.

It is important to mention, that the flop-flip transform is not limited to physical Fourier coefficients, which must obey

$$\sqrt{a^2 + \beta^2} \leq 1.$$

The flop transform can, of course, rotate any two numbers and the flip transform works smoothly for any $a<1$. This has a practical advantage when $\sqrt{a^2 + \beta^2}$ is close or equal to unity – in this case the random fluctuation can result in non-physical values of the Fourier coefficients, however, they can still be transformed and used for averaging.

Another view of the flip transform is presented by the simulation shown in fig. 2.6. The Fourier coefficients were calculated for two different sets of sample properties. In the first case the ellipsometric angles were Ψ=10° and Δ=5° (left graphs) and in the second case Ψ=50° and Δ=60° (right graphs). For each situation two polarizer settings were applied, here $P_0=0$. The polarizer settings were $P=45°$ (i.e., $P\sim\Psi=50°$ for the second case) and $P=15°$ (i.e., $P\sim\Psi=10°$ for the first case). The simulated pairs of coefficients are denoted by dotted lines in the upper graphs. The only independent variable here is therefore the target polarizer setting of the flip-transform, P_{FLIP}.

The curves on the upper graphs in fig. 2.6 show dependence of the flip-transformed Fourier coefficients on the azimuth P_{FLIP}. The steepest changes in the coefficient a_{FLIP} occur at $P_{FLIP}=\Psi$. The lower graphs are showing the errors of the coefficients propagated through the transform from the input coefficients. The error on the input was set to 0.05 for both δa and $\delta\beta$. Note that the propagated error δa_{FLIP} is largest for the $P_{FLIP}=\Psi$ and therefore the overall error is much smaller if the $P=\Psi$. The vanishing

of the errors for P_{FLIP}=-90°, 0°, 90° is caused by the loss of sensitivity – any measured a, β will result in $a_{FLIP}=\pm1$ and $\beta_{FLIP}=0$ in that cases and so no error (variance) can be propagated.

The meaning of the propagated error here can be understood as the penalty for the sensitivity gained through the flip transform. The errors of measured Fourier coefficients are result of noise in the intensity measurement, and related to the magnitude of intensity (not influenced by the polarizer setting[44]). When measuring the Fourier coefficients with an inadequate polarizer setting, we cannot increase the sensitivity just by flipping the coefficient to the sensitive arrangement. The propagated error will balance out the sensitivity gain.

We have shown how the flop-flip transforms the measured Fourier coefficients if the A_0 and P_0 are given. In practical situation, we have to measure two or more spectra of the coefficients with different polarizer settings P_r. Then we choose the value of P_{FLIP} and compare the transformed coefficients. Varying the inserted values of A_0 and P_0 we obtain pairs of coefficients more or less similar to each other. This similarity is measured by the sum of squares described in the next subsection.

2.2.4. Sum of squares and its derivatives

We assume that the noise of Fourier coefficients (corrected for the misalignments) follows the normal (Gaussian) distribution. Let us denote the coefficients a_{FLIP}, β_{FLIP} as x to avoid duplicities in the next few formulas. The estimate $\tilde{x}$ minimizes the weighted sum of squares

$$S = \sum_i w_i(x_i - \tilde{x})^2, \quad \text{where} \quad w_i = \frac{1}{\delta x_i^2}. \tag{2.16}$$

The minimum of S is obtained for

$$\tilde{x} = \frac{\sum_i w_i x_i}{\sum_i w_i}. \tag{2.17}$$

The index i in the summations spans the range from 1 to 2N, where N is the number of measured pairs of Fourier coefficients. Odd indices denote a_{FLIP} and even indices denote β_{FLIP}. Equation (2.17) can be inserted into (2.16), obtaining after some manipulations[45]

$$S = \frac{1}{2\sum_j w_j} \sum_i \sum_j w_i w_j (x_i - x_j)^2. \tag{2.18}$$

The sum contains only mutual differences between the points. The minimum of the sum of squares in the A_0, P_0 space localizes the actual offsets of the polarizer and the analyzer of our instrument.

---

[44] With totally unpolarized or circularly polarizer input light.
[45] See appendix 1 for details.

We have adopted a derivative-based algorithm for the search of the minimum of S in the A_0, P_0 space. As both the coefficients and the weights are dependent on the offsets, the first and second derivatives of the sum of squares have to be calculated.

The derivative of (2.18) with respect to an offset can be written as

$$S' = \left(\frac{S_1}{\sum w}\right)' = \frac{S_1' \sum w - S_1 \sum w'}{(\sum w)^2}, \qquad S_1 = \frac{1}{2}\sum_i \sum_j w_i w_j (x_i - x_j)^2 . \tag{2.19}$$

The derivative of the sum S_1 is

$$S_1' = \sum_i \sum_j w_i w_j' (x_i - x_j)^2 + w_i w_j (x_i - x_j)(x_i' - x_j'). \tag{2.20}$$

The derivative of any weight is

$$w_i' = \left(\frac{1}{\delta x_i^2}\right)' = -2\frac{\delta x_i'}{\delta x_i^3}. \tag{2.21}$$

In the following we will write down the necessary derivatives,

$$\frac{\partial a_{FLIP}}{\partial A_0}, \frac{\partial \beta_{FLIP}}{\partial A_0}, \frac{\partial \delta a_{FLIP}}{\partial A_0}, \frac{\partial \delta \beta_{FLIP}}{\partial A_0}, \tag{2.22}$$

$$\frac{\partial a_{FLIP}}{\partial P_0}, \frac{\partial \beta_{FLIP}}{\partial P_0}, \frac{\partial \delta a_{FLIP}}{\partial P_0}, \frac{\partial \delta \beta_{FLIP}}{\partial P_0}. \tag{2.23}$$

Derivatives with respect to A_0

The derivatives with respect to A_0 are

$$\frac{\partial a_{FLIP}}{\partial A_0} = \frac{\partial a_{FLIP}}{\partial a}\frac{\partial a}{\partial A_0}, \qquad \frac{\partial \beta_{FLIP}}{\partial A_0} = \frac{\partial \beta_{FLIP}}{\partial a}\frac{\partial a}{\partial A_0} + \frac{\partial \beta_{FLIP}}{\partial \beta}\frac{\partial \beta}{\partial A_0}. \tag{2.24}$$

The derivatives of a_{FLIP}, β_{FLIP} with respect to a, β we already used in (2.14) and (2.15) are:

$$\frac{\partial a_{FLIP}}{\partial a} = \frac{4\tan^2(P_r - P_0)\tan^2 P_{FLIP}}{D_+^2}, \tag{2.25}$$

$$\frac{\partial a_{FLIP}}{\partial \beta} = 0, \tag{2.26}$$

$$\frac{\partial \beta_{FLIP}}{\partial a} = \frac{-2\beta \tan(P_r - P_0)\tan P_{FLIP}\left[\tan^2(P_r - P_0) - \tan^2 P_{FLIP}\right]}{D_+^2}, \tag{2.27}$$

$$\frac{\partial \beta_{FLIP}}{\partial \beta} = \frac{2\tan(P_r - P_0)\tan P_{FLIP}}{D_+^2}. \tag{2.28}$$

We have again used the substitution (2.13). The derivatives of (flop-transformed) a, β with respect to A_0 are

$$\frac{\partial a}{\partial A_0} = -2a_r \sin 2A_0 + 2\beta_r \cos 2A_0 , \tag{2.29}$$

$$\frac{\partial \beta}{\partial A_0} = -2a_r \cos 2A_0 - 2\beta_r \sin 2A_0 . \tag{2.30}$$

The derivatives of the errors δa_{FLIP}, $\delta \beta_{FLIP}$ are slightly complicated

$$\frac{\partial \delta a_{FLIP}}{\partial A_0} = \frac{\partial \delta a_{FLIP}}{\partial a} \frac{\partial a}{\partial A_0} + \frac{\partial \delta a_{FLIP}}{\partial \beta} \frac{\partial \beta}{\partial A_0} + \frac{\partial \delta a_{FLIP}}{\partial \delta a} \frac{\partial \delta a}{\partial A_0} + \frac{\partial \delta a_{FLIP}}{\partial \delta \beta} \frac{\partial \delta \beta}{\partial A_0} , \tag{2.31}$$

$$\frac{\partial \delta \beta_{FLIP}}{\partial A_0} = \frac{\partial \delta \beta_{FLIP}}{\partial a} \frac{\partial a}{\partial A_0} + \frac{\partial \delta \beta_{FLIP}}{\partial \beta} \frac{\partial \beta}{\partial A_0} + \frac{\partial \delta \beta_{FLIP}}{\partial \delta a} \frac{\partial \delta a}{\partial A_0} + \frac{\partial \delta \beta_{FLIP}}{\partial \delta \beta} \frac{\partial \delta \beta}{\partial A_0} . \tag{2.32}$$

The derivatives of the errors propagated through the flip transform are:

$$\frac{\partial \delta a_{FLIP}}{\partial a} = \frac{\partial^2 a_{FLIP}}{\partial a^2} \delta a , \tag{2.33}$$

$$\frac{\partial \delta a_{FLIP}}{\partial \beta} = 0 , \tag{2.34}$$

$$\frac{\partial \delta \beta_{FLIP}}{\partial a} = \frac{1}{\delta \beta_{FLIP}} \left(\frac{\partial \beta_{FLIP}}{\partial a} \frac{\partial^2 \beta_{FLIP}}{\partial a^2} \delta a^2 + \frac{\partial \beta_{FLIP}}{\partial \beta} \frac{\partial^2 \beta_{FLIP}}{\partial \beta \partial a} \delta \beta^2 \right) , \tag{2.35}$$

$$\frac{\partial \delta \beta_{FLIP}}{\partial \beta} = \frac{1}{\delta \beta_{FLIP}} \left(\frac{\partial \beta_{FLIP}}{\partial a} \frac{\partial^2 \beta_{FLIP}}{\partial a \partial \beta} \delta a^2 + \frac{\partial \beta_{FLIP}}{\partial \beta} \frac{\partial^2 \beta_{FLIP}}{\partial \beta^2} \delta \beta^2 \right) , \tag{2.36}$$

$$\frac{\partial \delta a_{FLIP}}{\partial \delta a} = \frac{\partial a_{FLIP}}{\partial a} , \tag{2.37}$$

$$\frac{\partial \delta a_{FLIP}}{\partial \delta \beta} = 0 , \tag{2.38}$$

$$\frac{\partial \delta \beta_{FLIP}}{\partial \delta a} == \frac{1}{\delta \beta_{FLIP}} \left(\frac{\partial \beta_{FLIP}}{\partial a} \right)^2 \delta a , \tag{2.39}$$

$$\frac{\partial \delta \beta_{FLIP}}{\partial \delta \beta} = \frac{1}{\delta \beta_{FLIP}} \left(\frac{\partial \beta_{FLIP}}{\partial \beta} \right)^2 \delta \beta . \tag{2.40}$$

We need, in addition, the second derivatives to them insert into (2.33), (2.35) and (2.36):

$$\frac{\partial^2 a_{FLIP}}{\partial a^2} = \frac{-8 \tan^2 (P_r - P_0) \tan^2 P_{FLIP} \left[\tan^2 (P_r - P_0) - \tan^2 P_{FLIP} \right]}{D_+^3} , \tag{2.41}$$

$$\frac{\partial^2 \beta_{FLIP}}{\partial a^2} = \frac{4\beta \tan(P_r - P_0)\tan P_{FLIP}\left[\tan^2(P_r - P_0) - \tan^2 P_{FLIP}\right]^2}{D_+^3}, \quad (2.42)$$

$$\frac{\partial^2 \beta_{FLIP}}{\partial a \partial \beta} = \frac{-2\tan(P_r - P_0)\tan P_{FLIP}\left[\tan^2(P_r - P_0) - \tan^2 P_{FLIP}\right]}{D_+^2}, \quad (2.43)$$

$$\frac{\partial^2 \beta_{FLIP}}{\partial \beta^2} = 0. \quad (2.44)$$

Finally the derivatives of the error δa, $\delta \beta$ propagated through the flop transform with respect to A_0 are

$$\frac{\partial \delta a}{\partial A_0} = \frac{\sin 4A_0}{\delta a}(-\delta a_r^2 + \delta \beta_r^2), \quad (2.45)$$

$$\frac{\partial \delta \beta}{\partial A_0} = \frac{\sin 4A_0}{\delta \beta}(\delta a_r^2 - \delta \beta_r^2). \quad (2.46)$$

The function flop, implemented in the program MultiAB2PD, transforms the Fourier coefficients, propagates the errors, and calculates the derivatives of eqs. (2.29), (2.30), (2.45) and (2.46).

Derivatives with respect to P_0

At this point, all derivatives (2.22) with respect to A_0 have been calculated. Now, we move towards the derivatives (2.23) of the flip with respect to P_0. We introduce the value of D_-:

$$D_- \equiv \tan^2(P_r - P_0) - \tan^2 P_{FLIP} + a\left[\tan^2(P_r - P_0) + \tan^2 P_{FLIP}\right]. \quad (2.47)$$

Then,

$$\frac{\partial a_{FLIP}}{\partial P_0} = \frac{4(a^2 - 1)\tan(P_r - P_0)\tan^2 P_{FLIP}}{\cos^2(P_r - P_0)D_+^2}, \quad (2.48)$$

$$\frac{\partial \beta_{FLIP}}{\partial P_0} = \frac{2\beta \tan P_{FLIP} D_-}{\cos^2(P_r - P_0)D_+^2}, \quad (2.49)$$

$$\frac{\partial \delta a_{FLIP}}{\partial P_0} = \frac{\partial^2 a_{FLIP}}{\partial a \partial P_0}\delta a, \quad (2.50)$$

$$\frac{\partial \delta \beta_{FLIP}}{\partial P_0} = \frac{1}{\delta \beta_{FLIP}}\left(\frac{\partial \beta_{FLIP}}{\partial a}\frac{\partial^2 \beta_{FLIP}}{\partial a \partial P_0}\delta a^2 + \frac{\partial \beta_{FLIP}}{\partial \beta}\frac{\partial^2 \beta_{FLIP}}{\partial \beta \partial P_0}\delta \beta^2\right). \quad (2.51)$$

Now, the second mixed derivatives have to be expressed:

$$\frac{\partial^2 a_{FLIP}}{\partial a \partial P_0} = \frac{8\tan(P_r - P_0)\tan^2 P_{FLIP} D_-}{\cos^2(P_r - P_0)D_+^3}, \quad (2.52)$$

$$\frac{\partial^2 \beta_{FLIP}}{\partial a \partial P_0} = \frac{2\beta \tan P_{FLIP} \left\{ \begin{array}{l} 8\tan^2(P_r - P_0)\tan^2 P_{FLIP} - \\ -D_+\left[\tan^2(P_r - P_0) + \tan^2 P_{FLIP}\right] \end{array} \right\}}{\cos^2(P_r - P_0)D_+^3}, \qquad (2.53)$$

$$\frac{\partial^2 \beta_{FLIP}}{\partial \beta \partial P_0} = \frac{-2\tan P_{FLIP}D_-}{\cos^2(P_r - P_0)D_+^2}. \qquad (2.54)$$

Putting all the elements together we obtain the desired derivatives of the flip-transformed Fourier coefficients and their errors.

In the program implementation, the flip function transforms the Fourier coefficients, propagates the errors, and calculates the derivatives with respect to P_0, a, β, δa and $\delta\beta$. Together with the results and derivatives of the flop function, the sum of squares and its derivatives with respect to A_0 and P_0 can be expressed according to (2.19), (2.20) and (2.21).

Second derivatives

The needed second derivatives are calculated numerically, using two point central differences with a reasonably chosen step h:

$$\frac{\partial^2 S(A_0, P_0)}{\partial A_0^2} \doteq \frac{1}{2h}\left[\left.\frac{\partial S(A_0, P_0)}{\partial A_0}\right|_{Ao+h} - \left.\frac{\partial S(A_0, P_0)}{\partial A_0}\right|_{Ao-h} \right], \qquad (2.55)$$

$$\frac{\partial^2 S(A_0, P_0)}{\partial A_0 \partial P_0} = \frac{\partial^2 S(A_0, P_0)}{\partial P_0 \partial A_0} \doteq$$

$$\doteq \frac{1}{4h}\left[\left.\frac{\partial S(A_0, P_0)}{\partial A_0}\right|_{Po+h} - \left.\frac{\partial S(A_0, P_0)}{\partial A_0}\right|_{Po-h} + \left.\frac{\partial S(A_0, P_0)}{\partial P_0}\right|_{Ao+h} - \left.\frac{\partial S(A_0, P_0)}{\partial P_0}\right|_{Ao-h} \right], \qquad (2.56)$$

$$\frac{\partial^2 S(A_0, P_0)}{\partial P_0^2} \doteq \frac{1}{2h}\left[\left.\frac{\partial S(A_0, P_0)}{\partial P_0}\right|_{Po+h} - \left.\frac{\partial S(A_0, P_0)}{\partial P_0}\right|_{Po-h} \right], \qquad (2.57)$$

Using the derivatives, the gradient of the sum and its Hessian matrix[46] can be constructed and employed in the Marquardt-Levenberg minimization algorithm. This method localizes the minimum and the resulting Hessian matrix can be inverted obtaining the covariance matrix[47]

$$\hat{D} = \hat{H}^{-1} = \begin{pmatrix} D_{Ao} & C_{AoPo} \\ C_{AoPo} & D_{Po} \end{pmatrix} = \begin{pmatrix} \delta A_0 & 0 \\ 0 & \delta P_0 \end{pmatrix}\begin{pmatrix} 1 & \rho \\ \rho & 1 \end{pmatrix}\begin{pmatrix} \delta A_0 & 0 \\ 0 & \delta P_0 \end{pmatrix}. \qquad (2.58)$$

---

[46] The Hessian is the matrix of mixed second derivatives of the sum divided by factor 2.

[47] More details of error analysis of ellipsometric measurements can be found in J. Humlicek, *Sensitivity of Optical Measurements on Planar Stratified Structures and Reduction on Experimental Data*, FOLIA Fac. Sci. Nat. Uni. Brunensis Masarykianae, Physica **49** (1992).

Although the errors δA_0, δP_0 and the correlation coefficient ρ of the estimated offsets A_0 and P_0 are not particularly interesting, they can still serve for reliability check: high values of the errors and correlation detect a problematic configuration of the experiment.

Nevertheless, even the MultiAB2PD program is not propagating the errors of the offsets to the resulting Ψ and Δ. Once the offsets are obtained by the optimization, they are taken as known, and used for the correction of the measured data – the flop-flip transform is performed again for the measured Fourier coefficients for chosen P_{FLIP}. The weighted average of the Fourier coefficients (now fairly close to each other) is calculated, and the statistical error of the mean is expressed properly at each spectral point

$$\tilde{a}_{FLIP} = \frac{\sum_{i=1}^{N} \frac{a_{FLIPi}}{\delta a_{FLIPi}^2}}{\sum_{i=1}^{N} \frac{1}{\delta a_{FLIPi}^2}}, \quad \tilde{\beta}_{FLIP} = \frac{\sum_{i=1}^{N} \frac{\beta_{FLIPi}}{\delta \beta_{FLIPi}^2}}{\sum_{i=1}^{N} \frac{1}{\delta \beta_{FLIPi}^2}}, \tag{2.59}$$

$$\delta\tilde{a}_{FLIP} = \sqrt{\frac{\sum_{i=1}^{N}\left(\frac{a_{FLIPi} - \tilde{a}_{FLIP}}{\delta a_{FLIPi}}\right)^2}{(N-1)\cdot\sum_{i=1}^{N}\frac{1}{\delta a_{FLIPi}^2}}}k_{N-1}, \quad \delta\tilde{\beta}_{FLIP} = \sqrt{\frac{\sum_{i=1}^{N}\left(\frac{\beta_{FLIPi} - \tilde{\beta}_{FLIP}}{\delta \beta_{FLIPi}}\right)^2}{(N-1)\cdot\sum_{i=1}^{N}\frac{1}{\delta \beta_{FLIPi}^2}}}k_{N-1}, \tag{2.60}$$

where N is the number of the measurements with different polarizer settings $P_{1..N}$ and k_{N-1} is the Student coefficient.

Finally, the ellipsometric angles Ψ, Δ with proper errors $\delta\Psi$, $\delta\Delta$ can be calculated using equations (1.116) in 1.3.2. and (1.136) and (1.137) in 1.3.5. with the value of P_{FLIP} as the polarizer setting.

2.2.5. Geometrical interpretation and the false optima

The proposed method is not completely resistant to failure. Several critical situations can be traced down looking at the geometry of the flop-flip transform and the optimization process.

Let us consider the situation when two polarizer settings $P_{r1}=-P_{r2}$ were chosen and two pairs of Fourier coefficients a_{r1}, β_{r1}, a_{r2}, β_{r2} were measured. The coefficients can be plotted as points in the β, a plane. Then, for the successful search of the P_0 using flip transform, the points must lie on the same ellipse centered at the origin. To achieve this, the flop transform can rotate the points. In fig. 2.7a) we illustrated the situation using two general values of the coefficients. Rotating the points in the plane around the origin leads to two possible solutions for A_0 that can locate the two points on the same ellipse. One of the solutions is correct and the other would typically lead to meaningless result on a known sample. For an unknown sample, one has to treat the calibration carefully.
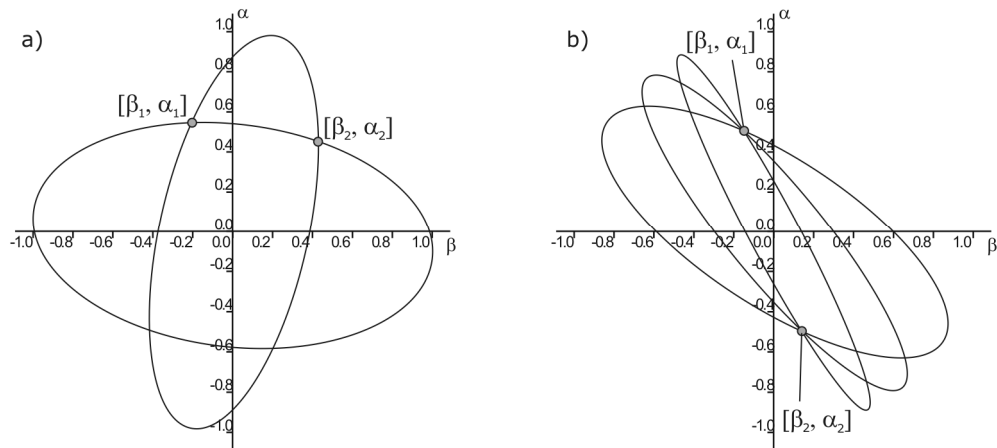
Figure 2.7. Possible situations in the calibration from two measurements. a) general situation have two possible solutions. b) symmetrical situation complicates the search.

In fig. 2.7b) another interesting situation is illustrated. When the $P_1 \doteq -P_2 \doteq \Psi$, the coefficients will form a pair of points placed symmetrically with respect to the origin. Now not only two ellipses can be drawn through the points, but infinite number of them satisfies the condition. The optimum still exists;[48] i.e., only one ellipse will be suitable for the extraction of P_0, but the sum of squares will have shape of narrow valley in the vicinity of the minimum. There will be a strong correlation between A_0 and P_0 and weaker minimization algorithm would fail in the search. The mentioned problem typically disappears with spectroscopic measurement, since the varieties of Ψ values suppress this problem.

2.3.   Testing

The performance of the finalized calibration routine mAB2PD.exe was tested and compared with the AB2PD.exe. Two tests are described in this section.

2.3.1. Simulated measurement on bulk silicon

The first test shows the operation of the calibration routines on a simulated measurement of bulk silicon, therefore in a situation close to reality. I took reference Si dielectric function data in the range from 1.3 to 6.3 eV, defined the angle of incidence ($\varphi=70°$) and chose the polarizer settings $P_{r1}=-P_{r2}=30°$.

The angular offsets A_0 and P_0 were introduced and the spectra of the Fourier coefficients a_{r1}, β_{r1}, a_{r2}, β_{r2} were simulated, adding Gaussian noise with the standard deviations $\delta a_r=\delta\beta_r=0.002$ to the resulting values.[49]

---

[48] The worst case occurs for $\Psi=45°$.

[49] This magnitude of the noise is comparable to the typical noise observed in the measurements on our ellipsometer.

Table 2.1. Input settings of the polarizer and the misalignments and the resulting values of the misalignments obtained from the two compared routines.

	input		AB2PD		mAB2PD	
$|P_r|$ (°)	P_0 (°)	A_0 (°)	P_0 (°)	A_0 (°)	P_0 (°)	A_0 (°)
30	1	-2	1.00	-2.00	1.00	-1.99
30	10	-20	10.01	-19.98	9.99	-19.99
30	20	-20	19.99	-20.01	19.99	-19.99
30	22.5	-20	22.49	-20.00	22.49	-20.00
30	25	-20	24.98	-20.01	24.98	-20.01
30	27.5	-20	27.40	-20.05	27.45	-20.06

The pairs of spectra were calibrated by both the AB2PD and the new MultiAB2PD. The starting point for the A_0, P_0 search was chosen close to the values used in the simulation, because the convergence properties of the algorithms were not in question in the test.[50] The whole range of energies (1.3 eV to 6.3 eV) was used for the calibration. The chosen parameters of the simulation and the resulting offsets are listed in Table 2.1. Both routines reached very similar and accurate estimates of the offsets. Using the calculated ellipsometric angles Ψ and Δ corrected to the offsets, the dielectric functions were calculated. Figure 2.8 shows the qualitative comparison of the resulting dielectric functions in the case, when P_0=25° and A_0=20°, i.e., for unrealistically large offsets. The curves of ε_1 and ε_2 were shifted by 10 in the case of the AB2PD for better visibility. The differences are caused by the difference of the algorithms themselves. In this situation, the noise generated by the AB2PD is
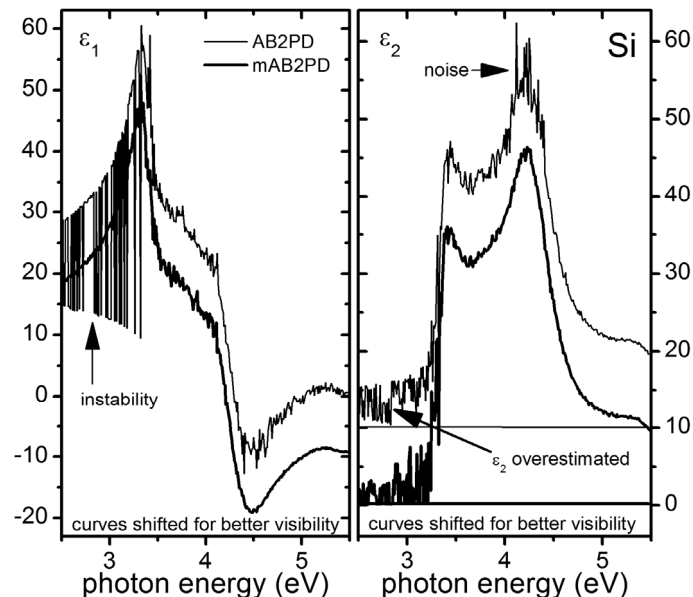

Figure 2.8. Comparison of the calibration routines on simulated measurements of bulk silicon in the resulting dielectric function.

---

[50] Of course, the derivative-based Marquardt-Levenberg method converges much faster than the simplex method.
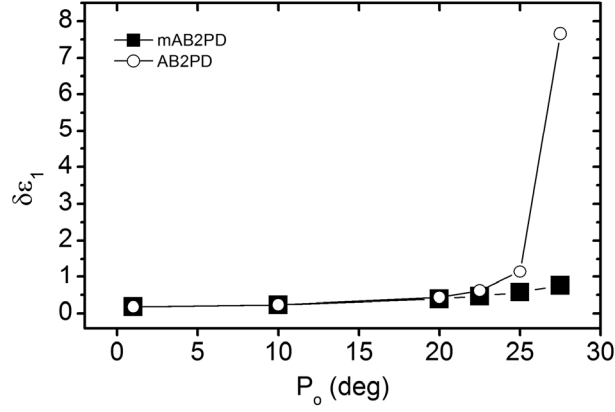
Figure 2.9. Comparison of the deviation of the resulting dielectric function from the reference values for the two calibration routines as a dependence on the polarizer offset.

significantly higher than the noise from mAB2PD. More flaws of the AB2PD can be observed in the region of the low absorption, where the averaging of Δ around 0° or 180° may lead to discontinuities, as seen in the real part of dielectric function and to some shift of the values of the imaginary part from zero.

To compare the noise of the resulting measurements we have restricted the range to 3.5 - 6.3 eV, where the major discrepancies are not present. For the quantitative comparison of the calibration programs, we calculated the mean square deviation between the reference and calculated dielectric functions

$$\delta\varepsilon_1 = \sqrt{\frac{\sum_{i=1}^{N}\left(\varepsilon_{1ref.i} - \varepsilon_{1calc.i}\right)^2}{N}} \ , \quad \delta\varepsilon_2 = \sqrt{\frac{\sum_{i=1}^{N}\left(\varepsilon_{2ref.i} - \varepsilon_{2calc.i}\right)^2}{N}} \ , \quad (2.61)$$

where N is the number of points in the spectral range, $N=300$ in our case. The resulting deviations for ε_1 and ε_2 are comparable ($\delta\varepsilon_1 \sim 1.2\delta\varepsilon_2$) for each of the programs and the dependence of the error $\delta\varepsilon_1$ on the polarizer offset is presented in fig. 2.9 for the same configurations as described in Table 2.1. For small polarizer offsets the two routines are resulting on the same values, but for large offsets, the MultiAB2PD proves a better stability and lower noise. Both methods are almost identical in the treatment of the analyzer offset; and consequently we do not pay any particular attention to the performance comparison in case of variable A_0.

2.3.2. Maps of Ψ and Δ

The second test of the routines was performed on non-realistic (pseudo) spectra with constant values of Ψ and Δ. For any given ellipsometric angles the (pseudo) spectra of 1000 pairs of Fourier coefficients a_{r1}, β_{r1}, a_{r2}, β_{r2} have been simulated with the addition of noise $\delta a_r = \delta\beta_r = 0.01$, the input analyzer and polarizer offsets $A_0 = -5°$ reps. $P_0 = 3°$, and the nominal polarizer setting $P_{r1} = -P_{r2} = 30°$. The two (pseudo)spectra have been used for the calibration to obtain the estimated offsets and the resulting averaged Ψ and Δ have been compared with the input ones.
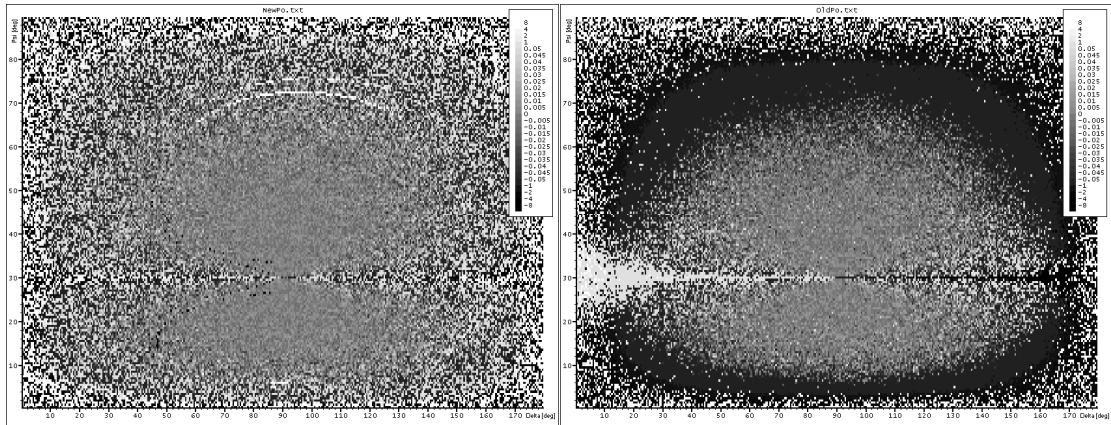
Figure 2.10. Comparison of resulting and input P$_0$ of the calibration MultiAB2PD (left) and the original AB2PD (right).
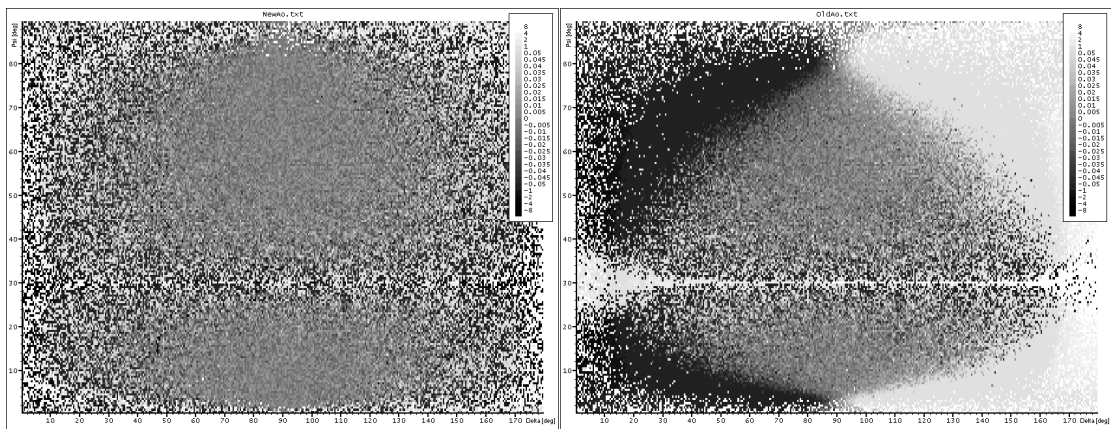

Figure 2.11. Comparison of resulting and input A$_0$ of the calibration MultiAB2PD (left) and the original AB2PD (right).

The simulation and calibration was repeated for Ψ=0.5° to 89.5° with the step 0.5°, and Δ=0.5° to 179.5° with the step of 0.5°. The AB2PD and MultiAB2PD programs were compared again.

Figures 2.10 and 2.11 show the difference of the estimated and the input P_0, and estimated and input A_0 for both routines. The routines are comparable in the central area of the maps except for the horizontal stripe where Ψ=P_r. As discussed in the previous section, the condition $P_1 \doteq -P_2 \doteq \Psi$ leads to high a correlation between the estimated offsets. Here, as P_0 is relatively small, the horizontal stripe contains values close to the condition. When leaving the central area of the maps, the noise in the estimated offsets is growing for the MultiAB2PD, while large systematic shifts are observed for the AB2PD. The borders and corners of the maps are containing values of failure for both programs.

Further, fig. 2.12 and fig. 2.13 show the difference between the resulting averaged and the input Ψ, and the resulting and the input Δ. In the maps for Ψ wide central area of correct results is observed for both routines, and especially for MultiAB2PD. The Δ maps show relatively limited area of correct results surrounded with ear-shaped areas of a high
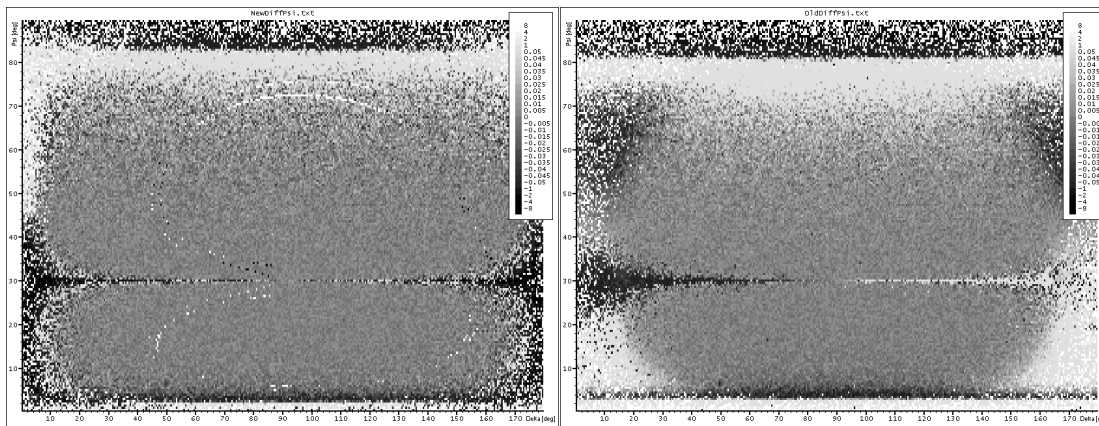
Figure 2.12. Comparison of resulting and input Ψ of the calibration MultiAB2PD (left) and the original AB2PD (right).
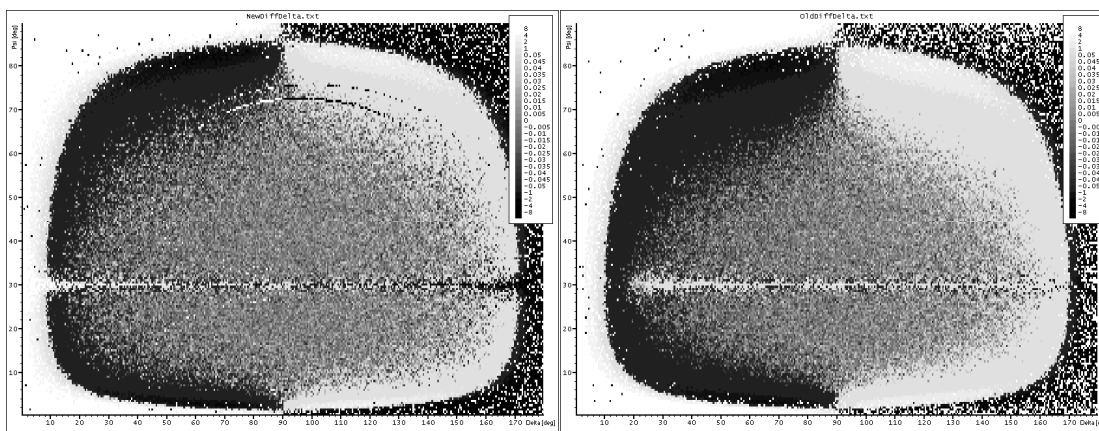

Figure 2.13. Comparison of resulting and input Δ of the calibration MultiAB2PD (left) and the original AB2PD (right).

systematic shift in resulting Δ. In the border areas, the results are completely wrong. We can assume that the error of the Δ estimation have a negative influence on the other estimated parameters in the AB2PD due to the minimization of the squared difference of the ellipsometric angles. The MultiAB2PD avoids this by performing the optimization on the level of Fourier coefficients.

Note that the color scale is not linear. The mid-gray hues cover the range from -0.05 to 0.05, while above and below the step between the two neighboring colors is one, up to 8 and down to -8.

2.4.   Conclusions

2.4.1. Discussion

I have presented a method of calibration of the RAE data for the analyzer and polarizer offsets by matching the Fourier coefficients measured with different polarizer settings. A proper treatment of the error propagation is taken into account. The method has been implemented in the computer program MultiAB2PD, and regularly used for experimental data processing. The program is controlled from a window-based user interface

and contains additional features as pseudo-dielectric function and normal incidence reflectivity calculations.

The program has been compared with the calibration program AB2PD, based on the similar method, but using slightly different algorithm, as described in the text. All tests were performed for calibration of a pair of spectra; however, the new program MultiAB2PD allows multiple files on input, which can improve the accuracy and stability in difficult situations.

The results showed that there is a performance gain for the presented algorithm, however, in the more likely, favorable situations, both routines give identical results. In the situations far from the optimum, the results of the routines are still comparable, but the MultiAB2PD produces in slightly less noise in the output data. Greater benefit is achieved in more extreme situations; however, it is always better to arrange the measurements to avoid them.

2.4.2. Outlook

The possibility of an analytical solution of the calibration problem in the case of two measurements should be explored.

As suggested in the text, independent estimations of the A_0 and P_0 offsets might be possible for multiple measurements with different polarizer settings.

The findings should help in a simplification (linearization) of the multiple-measurement problem.

Chapter 3 : Rotating compensator ellipsometry

The construction of an automatic rotating compensator ellipsometer and associated problems – 2006. With: Alois Nebojsa, Radoslav Švehla, Eduard Schmidt and Josef Humlíček.

The traditional, rotating analyzer ellipsometry is currently being replaced by more advanced configurations with rotating compensator (dual rotating compensators, phase-modulators) both in the scientific and commercial environment.

The ellipsometry with rotating compensator (RCE) have several advantages over the rotating analyzer (RAE):

- Keeping the polarizer (at the beginning of the optical path) and the analyzer (at its end) fixed, the polarization selectivity of the source or detector is avoided.
- In majority of cases, the rotating compensator is self-calibrated. It is not necessary to know its absolute azimuth.
- The ellipsometric angle Δ is measured with a constant sensitivity in the range from -180° to 180°.
- The degree of polarization is detected. This allows us to trace sample or instrument imperfections.

The primary goal of the presented work has been the enhancement of our rotating analyzer ellipsometer (the spectral range from 1.4 to 6.2 eV) to the rotating compensator configuration. This chapter describes the theoretical background needed for the data acquisition and processing.

The first section of this chapter deals with the signal analysis and determination of the ellipsometric parameters. The formulas are simplified by introducing a modified parameterization of the detected signal.

The second section proposes a method of the polarizer and analyzer offset calibration. The method has been implemented into a computer program and the results obtained from the real data are discussed. Spurious features are observed in the measurement, and identified as the compensator misalignment artifacts. The achromatic compensator design is explained in section three together with the method of determination of the polarization properties (retardance, offset, degree of polarization). Section four introduces the multi-plate misalignment as a possible source of the observed artifacts. The impact on the data processing and calibration is also discussed. A possible technique of the artifact elimination through a generalized compensator model is proposed and tested.[51]

3.1.   The RCE measurement

3.1.1. Description of the system

In this section, I will describe the RCE system and its operation. The description is matched to the construction of the tool actually used for the study, but the conclusions are valid for any similar system.

The basics of ellipsometric configurations, the definitions of the azimuths and other parameters and the formalism for handling of the polarized light are given in paragraph 1.2.8.

The ellipsometer consists of two principal parts. The first part – *polarization state generator* – includes the light source with a monochromator, focusing optics, the polarizer and the sample (see fig. 3.1). The linearly polarized light with a chosen orientation, generated by the source and the polarizer, is shed on the sample. The structure and the optical properties of the material determine the polarization state, which is described by two parameters: X – ellipticity and *Q* – ellipse tilt. Additionally, the depolarization on the sample may lead to a mixed outgoing polarization state, described by the degree of polarization *p*. The reflection can also be described by two ellipsometric parameters Ψ and Δ. The two pairs of the quantities are closely related.

---

[51] P. Marsik and J. Humlicek: *Multi-plate misalignment artifacts in rotating-compensator ellipsometry: Analysis and data treatment*, Physica Status Solidi (c) **5** 1064 (2008).
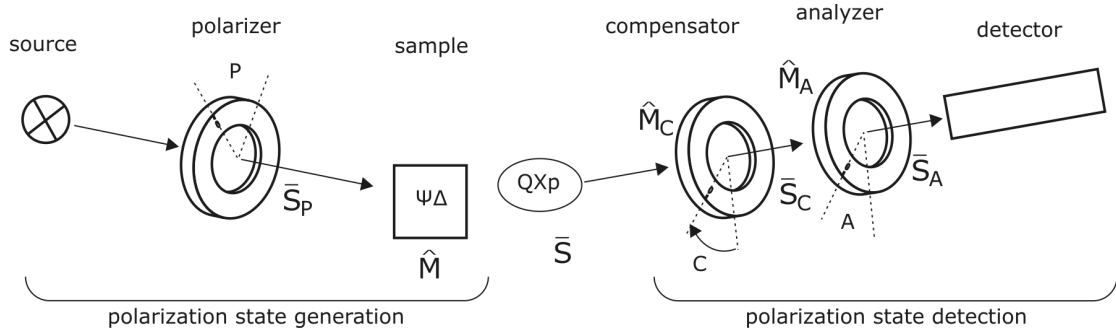
Figure 3.1. Schematic diagram of the RCE measurement system.

The second part is the *polarization state detector*, consisting of the compensator, analyzer and the detector.[52] The three parameters of the polarized light – Q, X, *p* – have to be determined. In contrary to the rotating analyzer configuration, the rotating compensator allows the acquisition of all three parameters with a high accuracy in the whole range of possible values.

3.1.2. Polarization state generation

The polarization state is generated by the polarizer and by the reflection from the sample. We assume that a pure polarization state is generated by the polarizer. A possible depolarization might be included as the presence of the orthogonal polarization in the mixed state outgoing from the sample. We do not address the mechanisms of depolarization on the sample in this work.

The Stokes vector of the beam transmitted through the polarizer is

$$\bar{S}_P = \frac{1}{2}\begin{bmatrix} 1 \\ \cos 2P \\ \sin 2P \\ 0 \end{bmatrix},$$

(3.1)

where *P* is the polarizer azimuth; it assumes the unit intensity generated by the light source. The Mueller matrix of the isotropic sample is given by

$$\hat{M} = R\begin{bmatrix} 1 & -\cos 2\Psi & 0 & 0 \\ -\cos 2\Psi & 1 & 0 & 0 \\ 0 & 0 & \sin 2\Psi \cos \Delta & \sin 2\Psi \sin \Delta \\ 0 & 0 & -\sin 2\Psi \sin \Delta & -\sin 2\Psi \cos \Delta \end{bmatrix},$$

(3.2)

where Ψ, Δ are the ellipsometric angles (depending on the sample properties and the angle of incidence). The power reflectivity *R* is

$$R = \frac{|r_s|^2 + |r_p|^2}{2}.$$

(3.3)

---

[52] Generalizations to the scheme can be done, for example, by configuring the elements to transmission measurement or by adding a second compensator behind the polarizer.

The Stokes vector of light reflected from the sample is given by the appropriate multiplication, resulting in

$$\bar{S} = \hat{M}\bar{S}_P = \frac{R}{2}\begin{bmatrix} 1 - \cos 2\Psi \cos 2P \\ \cos 2P - \cos 2\Psi \\ \sin 2P \sin 2\Psi \cos \Delta \\ -\sin 2P \sin 2\Psi \sin \Delta \end{bmatrix}. \tag{3.4}$$

Now we are going to relate the expression of the Stokes vector (3.4) to the description using the angles Q (ellipse tilt) and X (ellipticity) as defined in 1.2.8.

$$\bar{S}_{QX} = \begin{bmatrix} 1 \\ \cos 2X \cos 2Q \\ \cos 2X \sin 2Q \\ \sin 2X \end{bmatrix}. \tag{3.5}$$

The polarizer azimuth P is a parameter of the transforms

$$\frac{\cos 2P - \cos 2\Psi}{1 - \cos 2\Psi \cos 2P} = \cos 2X \cos 2Q, \tag{3.6}$$

$$\frac{\sin 2P \sin 2\Psi \cos \Delta}{1 - \cos 2\Psi \cos 2P} = \cos 2X \sin 2Q, \tag{3.7}$$

$$\frac{-\sin 2P \sin 2\Psi \sin \Delta}{1 - \cos 2\Psi \cos 2P} = \sin 2X. \tag{3.8}$$

For the inverse expressions, we first extract cos2Ψ from the first equation

$$\cos 2\Psi = \frac{\cos 2X \cos 2Q - \cos 2P}{\cos 2X \cos 2Q \cos 2P - 1}; \tag{3.9}$$

then,

$$\cos \Delta = \frac{\cos 2X \sin 2Q(1 - \cos 2P \cos 2\Psi)}{\sin 2P \sin 2\Psi}, \tag{3.10}$$

$$\sin \Delta = \frac{\sin 2X(\cos 2P \cos 2\Psi - 1)}{\sin 2P \sin 2\Psi}. \tag{3.11}$$

We have obtained relations between the state of the polarized light itself and the polarization properties of the sample. In the general case of an anisotropic sample, the reflection is determined by several independent quantities in the Mueller matrix (3.2). In the present configuration, the last column of the Mueller matrix is not available, because the light incoming on the sample is linearly polarized. A supplementary compensator must be used in the state generation branch to allow detection of the full Mueller matrix.

3.1.3. Detection of the polarization state

Stokes vector at the detector

Let us express the signal at the detector as a function of the compensator position *C* for any polarization state generated by the source, the polarizer and the sample. The subsequent analysis of the intensity signal is directed towards obtaining the parameters of the polarization: the ellipticity X, the ellipse tilt *Q* and the degree of polarization *p*. The Stokes vector of the generally polarized light with unit intensity is

$$
\bar{S} = \begin{bmatrix} 1 \\ p\cos 2X \cos 2Q \\ p\cos 2X \sin 2Q \\ p\sin 2X \end{bmatrix} \equiv \begin{bmatrix} 1 \\ pC_X C_Q \\ pC_X S_Q \\ pS_X \end{bmatrix},
\tag{3.12}
$$

introducing a simplified notation for the values of goniometric functions

$$
\cos 2X \equiv C_X, \ \sin 2X \equiv S_X, \ \cos 2Q \equiv C_Q, \ \sin 2Q \equiv S_Q.
\tag{3.13}
$$

The Stokes vector of the light transmitted through the compensator and the analyzer has following form

$$
\bar{S}_A = \hat{M}_A \bar{S}_C = \hat{M}_A \hat{M}_C \bar{S}.
\tag{3.14}
$$

The Mueller matrix of the analyzer consists of harmonic functions of the azimuth *A* of the transmission axis of the analyzer

$$
\hat{M}_A = \frac{1}{2} \begin{bmatrix} 1 & \cos 2A & \sin 2A & 0 \\ \cos 2A & \cos^2 2A & \cos 2A \sin 2A & 0 \\ \sin 2A & \cos 2A \sin 2A & \sin^2 2A & 0 \\ 0 & 0 & 0 & 0 \end{bmatrix} \equiv
$$

$$
\equiv \frac{1}{2} \begin{bmatrix} 1 & C_A & S_A & 0 \\ C_A & C_A^2 & C_A S_A & 0 \\ S_A & C_A S_A & S_A^2 & 0 \\ 0 & 0 & 0 & 0 \end{bmatrix},
\tag{3.15}
$$

where

$$
\cos 2A \equiv C_A, \ \sin 2A \equiv S_A.
\tag{3.16}
$$

The compensator is a device creating a phase-shift (retardation) between the light polarized in the direction of its fast and slow axes. The phase shift (retardance angle) is denoted as *δ*, the azimuth of the fast axis as *C*. The Mueller matrix of the compensator is

$$\hat{M}_C = \begin{bmatrix} 1 & 0 & 0 & 0 \\ 0 & \cos^2 2C + \cos\delta\sin^2 2C & -\sin 2C\cos 2C(\cos\delta-1) & -\sin\delta\sin 2C \\ 0 & -\sin 2C\cos 2C(\cos\delta-1) & \sin^2 2C + \cos\delta\cos^2 2C & \sin\delta\cos 2C \\ 0 & \sin\delta\sin 2C & -\sin\delta\cos 2C & \cos\delta \end{bmatrix} \equiv$$

$$\equiv \begin{bmatrix} 1 & 0 & 0 & 0 \\ 0 & C_C^2 + C_D S_C^2 & -S_C C_C(C_D-1) & -S_D S_C \\ 0 & -S_C C_C(C_D-1) & S_C^2 + C_D C_C^2 & S_D C_C \\ 0 & S_D S_C & -S_D C_C & C_D \end{bmatrix}, \tag{3.17}$$

where

$$\cos 2C \equiv C_C, \quad \sin 2C \equiv S_C, \quad \cos\delta \equiv C_D, \quad \sin\delta \equiv S_D. \tag{3.18}$$

The appropriate multiplication leads to

$$\bar{S}_C = \hat{M}_C \bar{S} = \begin{bmatrix} 1 \\ pC_X C_Q(C_C^2 + C_D S_C^2) + pC_X S_Q(-S_C C_C(C_D-1)) + pS_X(-S_D S_C) \\ pC_X C_Q(-S_C C_C(C_D-1)) + pC_X S_Q(S_C^2 + C_D C_C^2) + pS_X(S_D C_C) \\ pC_X C_Q(S_D S_C) + pC_X S_Q(-S_D C_C) + pS_X C_D \end{bmatrix}. \tag{3.19}$$

Signal at the detector

The detector behind the analyzer measures the light intensity. Consequently, we need to express the uppermost element of the Stokes vector, multiplying the first row of the Mueller matrix of the analyzer by the column vector of eq. (3.19):

$$I = S_{A1} = \bar{M}_{A1}\hat{M}_C\bar{S} = \bar{M}_{A1}\bar{S}_C =$$

$$= \frac{1}{2}\Big\{1 + C_A\Big[pC_X C_Q(C_C^2 + C_D S_C^2) + pC_X S_Q(-S_C C_C(C_D-1)) + pS_X(-S_D S_C)\Big] +$$

$$+ S_A\Big[pC_X C_Q(-S_C C_C(C_D-1)) + pC_X S_Q(S_C^2 + C_D C_C^2) + pS_X(S_D C_C)\Big]\Big\}. \tag{3.20}$$

We proceed by introducing the following identities

$$S_C^2 = \frac{1-C_{2C}}{2}, \quad C_C^2 = \frac{1+C_{2C}}{2}, \quad 2S_C C_C = S_{2C}, \tag{3.21}$$

$$\text{where } C_{2C} = \cos 4C, \quad S_{2C} = \sin 4C. \tag{3.22}$$

Inserting them into eq. (3.20) we obtain

$$2I = 1 + C_A\Big[\frac{p}{2}C_X C_Q(1 + C_D + C_{2C}(1-C_D)) + \frac{p}{2}C_X S_Q S_{2C}(1-C_D) + pS_X(-S_D S_C)\Big] +$$

$$+ S_A\Big[\frac{p}{2}C_X C_Q S_{2C}(1-C_D) + \frac{p}{2}C_X S_Q(1 + C_D - C_{2C}(1-C_D)) + pS_X(S_D C_C)\Big]. \tag{3.23}$$

The next step will express the intensity in terms of harmonics of the azimuth C:

$$2I = 1 + pC_X \frac{1+C_D}{2}(C_A C_Q + S_A S_Q) + C_C pS_X S_D S_A + S_C(-pS_X S_D C_A) +$$

$$+C_{2C} pC_X \frac{1-C_D}{2}(C_A C_Q - S_Q S_A) + S_{2C} pC_X \frac{1-C_D}{2}(C_A S_Q + C_Q S_A). \quad (3.24)$$

Finally, we have the intensity in following form

$$I(C) = I_0 + a_2 I_0 \cos 2C + \beta_2 I_0 \sin 2C + a_4 I_0 \cos 4C + \beta_4 I_0 \sin 4C, \quad (3.25)$$

where the coefficients are

$$I_0 = \tfrac{1}{2}\left[1 + p\cos 2X \cos^2 \tfrac{\delta}{2} \cos 2(A-Q)\right], \quad (3.26)$$

$$a_2 I_0 = \tfrac{1}{2} p\sin 2X \sin\delta \sin 2A, \quad (3.27)$$

$$\beta_2 I_0 = -\tfrac{1}{2} p\sin 2X \sin\delta \cos 2A, \quad (3.28)$$

$$a_4 I_0 = \tfrac{1}{2} p\cos 2X \sin^2 \tfrac{\delta}{2} \cos 2(A+Q), \quad (3.29)$$

$$\beta_4 I_0 = \tfrac{1}{2} p\cos 2X \sin^2 \tfrac{\delta}{2} \sin 2(A+Q). \quad (3.30)$$

The signals in the RCE measurement consist of two harmonic components, one with the argument $2C$ and the second with the argument $4C$ (see fig. 3.2). The dependence on the compensator azimuth C can be described by four Fourier coefficients. Their magnitudes are given by the polarization state (Q-tilt, X-ellipticity, p-degree of polarization), by the position of the analyzer (azimuth A), and by the retardance of the compensator δ. In particular, the $2C$ component vanishes for the linearly polarized light and the $4C$ component vanishes for circularly polarized light. Both components are diminishing with decreasing degree of polarization, and disappear for the completely unpolarized light.
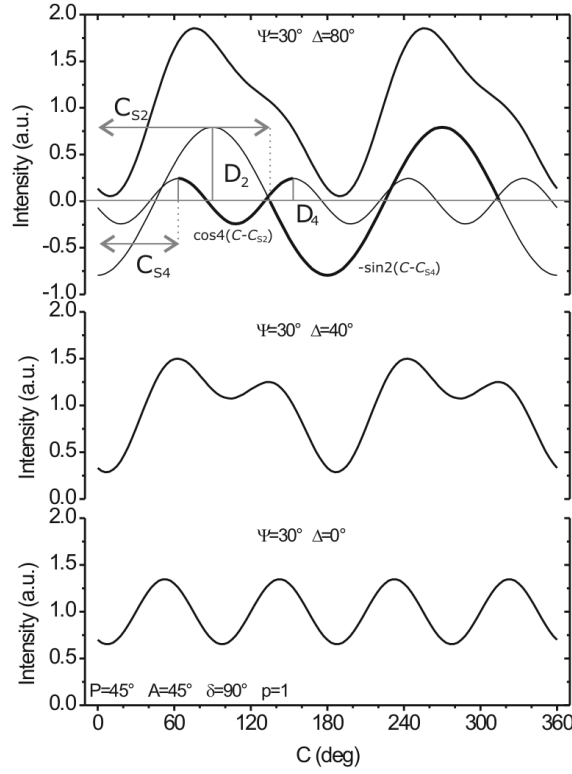
Figure 3.2. Simulated signal in the RCE measurement for 3 different sample parameters. The polarizer and the analyzer settings are both 45° and the retardance of the compensator is 90°. The degree of polarization is 1. The upper plot shows the harmonic components of the signal and indicates the meaning of the parameters.

Analysis of the signal

In order to relate the signal parameters to those of the polarization state in a straightforward and convenient way, we introduce here a parameterization of the signal by means of the amplitudes and phase-shifts of the components as follows[53]

$$I(C) = I_0\left[1 - D_2 \sin 2(C - C_{S2}) + D_4 \cos 4(C - C_{S4})\right], \qquad (3.31)$$

where

$$D_2 = \sqrt{a_2^2 + \beta_2^2}\ , \quad \frac{a_2}{D_2} = \sin 2C_{S2}\ , \quad \frac{\beta_2}{D_2} = -\cos 2C_{S2}\ , \qquad (3.32)$$

$$D_4 = \sqrt{a_4^2 + \beta_4^2}\ , \quad \frac{a_4}{D_4} = \cos 4C_{S4}\ , \quad \frac{\beta_4}{D_4} = \sin 4C_{S4}\ . \qquad (3.33)$$

We define the phase difference of the $2C$ and $4C$ components as T [54]

$$T = C_{S4} - C_{S2}\ . \qquad (3.34)$$

---

[53] The form (-sin2C) and (cos4C) is chosen intentionally to simplify the following expressions.
[54] T here is capital Tau.

For specifying the angles C_{S2}, C_{S4}, and T uniquely, we adopt the following convention

$$C_{S2} \in \langle 0, \pi \rangle, \quad C_{S4} \in \langle 0, \tfrac{\pi}{2} \rangle, \quad T \in \langle 0, \tfrac{\pi}{2} \rangle. \tag{3.35}$$

The relations presented here are analogical to ones published in the literature,[55] but the choice of the parameterization leads to simplified and more intuitive formulas.

General polarization state

Now we will express the desired relations between the signal and the polarization state parameters for the case of **general elliptical polarization** of the light incoming to the detection branch. The special cases of linear or circular polarization will be treated afterwards. Combining (3.27), (3.28) and (3.32) we obtain

$$\sin 2C_{S2} = \mathrm{sgn}(\sin 2X)\sin 2A, \quad \cos 2C_{S2} = \mathrm{sgn}(\sin 2X)\cos 2A. \tag{3.36}$$

Then

$$C_{S2} = A \quad \text{for} \quad X > 0, \tag{3.37}$$

$$C_{S2} = A + \frac{\pi}{2} \quad \text{for} \quad X < 0, \tag{3.38}$$

applying the restriction $X \in \langle -45°, 45° \rangle$. Both formulas are valid if $k\pi$ ($k \in Z$) is added to any side of the equation, but the addition is not necessary due to the convention (3.35). The two possible solutions are arising from the behavior of the 2C component: it vanishes for X=0 and changes sign when X is crossing zero; therefore, the starting (zero) point of the $(-\sin 2C)$ function is shifted by π/2.

If we assume the analyzer position *A* known and the compensator correctly aligned, at least approximately, the above expressions lead to the determination of the sign of ellipticity X. If the position of analyzer or compensator offset is completely unknown, then the sign of X cannot be specified.

The above formulas do not contain any other information about the polarization state, but can be used for the calibration of the compensator offset C_0, when the analyzer offset A_0 is known[56] and the detected starting point is C_{rS2}:

$$C_0 = C_{rS2} - A. \tag{3.39}$$

---

[55] I. An, J. A. Zapien, C. Chen, A. S. Ferlauto, A. S. Lawrence, R. W. Collins, *Calibration and data reduction for a UV-extended rotating-compensator multichannel ellipsometer*, Thin Solid Films **455-456,** 132-137 (2004).
[56] The issue will be discussed in details further. Offset C_0 is defined according to previous chapter as C_r-C_0=C.

Here, the knowledge about the sign of the ellipticity X, i.e., the sense of rotation of the electric vector, is needed to distinguish the fast and slow axis of the compensator.

Next, combining equations (3.29), (3.30) and (3.33) we get the expression for the tilt Q

$$\cos 4C_{S4} = \cos 2(A + Q), \quad \sin 4C_{S4} = \sin 2(A + Q). \tag{3.40}$$

Therefore

$$4C_{S4} = 2(A + Q) + 2k\pi. \tag{3.41}$$

Now we express C_{S4} using (3.34) and (3.37) or (3.38)

$$4C_{S4} = 4(C_{S2} + T) = 4(A + (+\tfrac{\pi}{2}) + T) = 4A + 4T + (+2\pi). \tag{3.42}$$

Then

$$Q = A + 2T. \tag{3.43}$$

Here we have used only the difference of the phase shifts of the harmonic components. Then ellipticity X is related to the ratio of the amplitudes of the components as

$$\tan 2X = \text{sgn}(X)\frac{1}{2}\frac{D_2}{D_4}\tan\frac{\delta}{2}, \tag{3.44}$$

$$X = \text{sgn}(X)\frac{1}{2}\arctan\left(\frac{1}{2}\frac{D_2}{D_4}\tan\frac{\delta}{2}\right), \tag{3.45}$$

where the correct sign has to be used according to eqs. (3.37) and (3.38). For the extraction of the degree of polarization p, we have to use the mean intensity value I_0 (3.26) obtaining

$$p = \frac{D_4}{\cos 2X\left[\sin^2\frac{\delta}{2} - D_4\cos^2\frac{\delta}{2}\cos 4T\right]} \tag{3.46}$$

or

$$p = \frac{D_2}{\left|\sin 2X\right|\sin\delta - D_2\cos 2X\cos^2\frac{\delta}{2}\cos 4T}. \tag{3.47}$$

Both expressions apply; however, their sensitivity of each will be dependent on the ellipticity X. For nearly linear polarizations, $D_4 > D_2$ and equation (3.46) leads to a better precision; for nearly circular polarizations, $D_2 > D_4$ and (3.47) gives a more precise result.

When the analyzer azimuth is set to zero (which can be assumed without loss of generality) and the compensator retardance δ is 90°, then the above equations gain the following simple form

$$Q = 2T, \tag{3.48}$$

$$X = \text{sgn}(X)\frac{1}{2}\arctan\left(\frac{1}{2}\frac{D_2}{D_4}\right), \tag{3.49}$$

$$p = \frac{2D_4}{\cos 2X\left[1 - D_4\cos 4T\right]} \quad \text{or} \quad p = \frac{2D_2}{2\sin 2X - D_2\cos 2X\cos 4T}. \tag{3.50}$$

In this case, the absolute value of the compensator azimuth (or the offset C_0) does not need to be known, as only relative phase and amplitudes of the two harmonic components are used in the expressions, except for the sign of the ellipticity.[57]

Linear and circular polarizations

As mentioned above, we will complete the relations with special cases of the polarization state. For **linear polarization** (X=0), the 2*C* component vanishes and the exact compensator azimuth has to be known for the extraction of the tilt *Q*. Using equation (3.41) we get

$$Q = 2C_{S4} - A. \tag{3.51}$$

For the degree of polarization *p*, only one relation is available, namely

$$p = \frac{D_4}{\sin^2\frac{\delta}{2} - D_4\cos^2\frac{\delta}{2}\cos 4C_{S4}}. \tag{3.52}$$

For the **circular polarization**, the 4*C* component vanishes. The ellipticity X is equal to $\pm 45°$ and the sign is given by C_{S2} in (3.37) and (3.38). The tilt *Q* is not defined, and the degree of polarization is

$$p = \frac{D_2}{\sin\delta}. \tag{3.53}$$

Until now, I described the polarization state generation and detection by the rotating compensator. I assumed perfectly aligned and flawless optical elements. The possible compensator offset C_0 does not influence the results in the case of a generally polarized beam; moreover, it can be extracted from the measured parameters. In the typical situation of spectroscopic measurement, the information about the compensator offset is obtained in selected parts of the spectra, where the light is elliptically polarized, and used for the evaluation in other parts, where the ellipticity is close to 0. This approach is useful only in the case when the position of fast axis does not depend on the photon energy. This is true in the case of retarders constructed from birefringent crystals, where the orientation of the axis is defined by the crystalline structure.

---

[57] The sign of the ellipticity X can be usually determined ex post from the physical sense of the results.

3.2.   Polarizer and analyzer calibration

In chapter 2, I explained the impact of polarizer and analyzer offsets[58] on the data processing in RAE and described a method of calibration based on dual measurement of the sample spectra with two different polarizer settings. The measurements with rotating compensator are vulnerable to possible incorrect polarizer and analyzer settings as well and the method of calibration presented in this chapter will be based on the same principle as in the case of rotating analyzer. This is an alternative to the procedure of An et al. found in the literature.[55]

Let us consider two measurements of the sample parameters with two polarizer settings P_{r1} and P_{r2}. The results are acquired according to the previous subsection in the form of spectra of Q_{r1}, X_{r1} and Q_{r2}, X_{r2}. We will assume that the depolarization is negligible.[59] The calibration is limited to isotropic samples.

3.2.1. Analyzer offset calibration

Dividing equations (3.11) and (3.10) we obtain the following relation binding the ellipticity X and tilt Q with given sample parameter Δ,

$$\tan\Delta = -\frac{\tan 2X}{\sin 2Q}.\tag{3.54}$$

Consequently

$$\frac{\tan 2X_1}{\sin 2Q_1} = \frac{\tan 2X_2}{\sin 2Q_2}.\tag{3.55}$$

This equation is valid for the true parameters of the polarization ellipses. The detection of the ellipticity X is not dependent on the analyzer position (except for the sign) and therefore we will use the simplified notation $X_1 \equiv X_{r1}$ and $X_2 \equiv X_{r2}$. For non-zero analyzer offset, the values of Q are shifted by A_0 due to (3.43),

$$Q = Q_r - A_0.\tag{3.56}$$

Then, by inserting (3.56) into (3.55), we obtain

$$\tan 2A_0 = \frac{\tan 2X_1 \sin 2Q_{r2} - \tan 2X_2 \sin 2Q_{r1}}{\tan 2X_1 \cos 2Q_{r2} - \tan 2X_2 \cos 2Q_{r1}}.\tag{3.57}$$

Here we have obtained the analyzer offset A_0 analytically, and independently[60] of the polarizer offset P_0, but the value is restricted to the range $\pm 45°$. The corrected pairs of parameters Q_1, X_1 and Q_2, X_2 are used further for the P_0 calibration.

---

[58] The offsets are defined by $A_0=A_r-A$, $P_0=P_r-P$.
[59] The origin and the impact of the depolarization on the measured quantities is not studied in the present work.
[60] Compare with the previous chapter.

3.2.2. Polarizer offset calibration

Equation (3.9) for cos2Ψ allows equating the two pairs of measured ellipse parameters as

$$\frac{\cos 2X_1 \cos 2Q_1 - \cos 2(P_{r1} - P_0)}{\cos 2X_1 \cos 2Q_1 \cos 2(P_{r1} - P_0) - 1} = \frac{\cos 2X_2 \cos 2Q_2 - \cos 2(P_{r2} - P_0)}{\cos 2X_2 \cos 2Q_2 \cos 2(P_{r2} - P_0) - 1}. \tag{3.58}$$

Its solution can be found, after lengthy manipulations, in the following form

$$\sin 2\left(P_0 - \frac{P_{r1} + P_{r2}}{2}\right) = \gamma \cdot \sin(P_{r2} - P_{r1}), \quad \text{where} \tag{3.59}$$

$$\gamma = \frac{-\kappa_1 \kappa_2 + 1 - \sqrt{(\kappa_1 \kappa_2 - 1)^2 - (\kappa_2 - \kappa_1)^2}}{\kappa_2 - \kappa_1} \quad \text{and} \tag{3.60}$$

$$\kappa_i = \cos 2X_i \cos 2Q_i. \tag{3.61}$$

Using $P_{r1} = -P_{r2} \equiv -P_r$ we arrive at

$$\sin 2P_0 = \gamma \cdot \sin 2P_r. \tag{3.62}$$

Again, the polarizer offset P_0 is obtained analytically.

3.2.3. CalibRCE

The relations of the previous and present sections were used in the following algorithm for data reduction and calibration.

- Two measurements of the spectra of the four Fourier coefficients (a_{2r1}, β_{2r1}, a_{4r1}, β_{4r1}, a_{2r2}, β_{2r2}, a_{4r2}, β_{4r2}) are performed with two different polarizer settings P_{r1} and P_{r2}. The measurement errors are acquired together with the data.
- The spectral dependence of retardance of the compensator δ is assumed to be known (typically it is measured independently).
- Both spectra are analyzed according to the above expressed relations obtaining two raw spectra of Q_{r1}, X_{r1}, p_{r1}, C_{0r1}, Q_{r2}, X_{r2}, p_{r2}, C_{0r2}, together with the propagated errors.
- For the analyzer offset calibration, the ellipticity X must be non-zero, being not influenced by the compensator offset. Practically, we select the spectral points, where the estimated X (in absolute value) is reasonably greater than the error δX – in each of the two spectra.
- The selected pairs of points are used for the A_0 calibration obtaining set of results and errors. The final A_0 is found as the weighted average of the set.
- Now the actual analyzer position is known and both spectra can be corrected. Particularly the true value of C_0 is extracted from the points where X>>δX and the rest of the spectra is processed using this value.
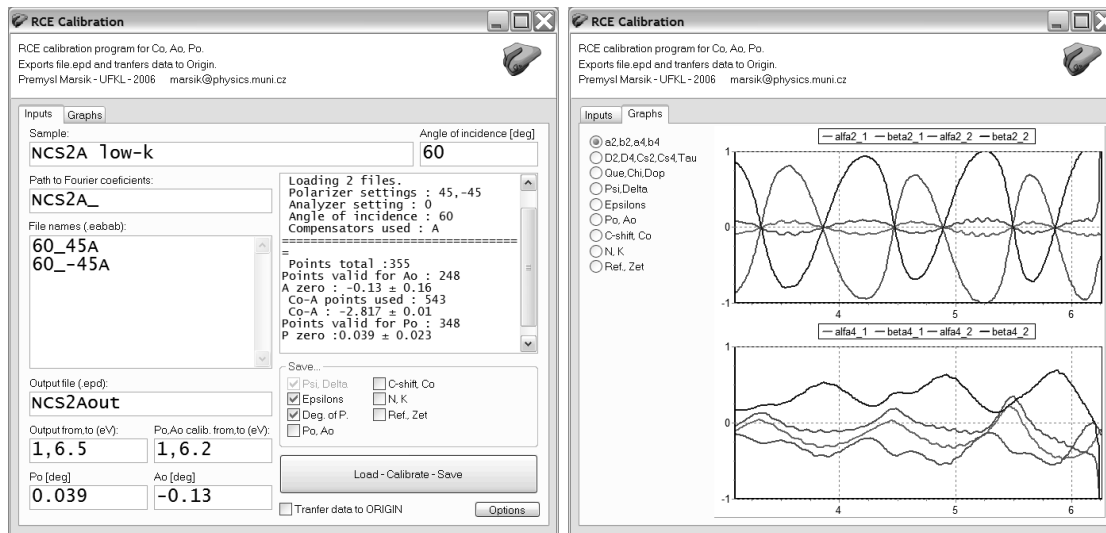
Figure 3.3. The screenshots of the program CalibRCE. The left picture shows the main control tab. Right picture shows the tab with graphs.

- Having obtained the parameters of the ellipses (Q_1, X_1, p_1, C_{01}, Q_2, X_2, p_2, C_{02}), we proceed to the polarizer offset calibration. The procedure can be performed at each point, resulting in the spectrum of the estimates of P_0 and their errors. The final P_0 is determined as the weighted average over the spectrum.

- The sample parameters Ψ_1, Δ_1, Ψ_2, Δ_2 with errors are calculated. The final results are obtained by averaging the pairs.

The disadvantage of this procedure is the necessity to measure two spectra. However, the averaging of the two spectra reduces noise, but it is also likely to remove artifacts related to the polarizer sign symmetry, as discussed below.

The algorithm has been implemented in the computer program CalibRCE (see fig. 3.3). The program works with input files containing the Fourier coefficients (.eabab) and is able to combine data measured with several compensators, since the measurable range is separated to sub-ranges covered by different retarders.

The program performs the calibrations, and the spectra of all relevant quantities are calculated and viewed in the window. The desired results are saved in the .epd file and can be also exported directly to Origin® using Dynamic Data Exchange (DDE) technology.
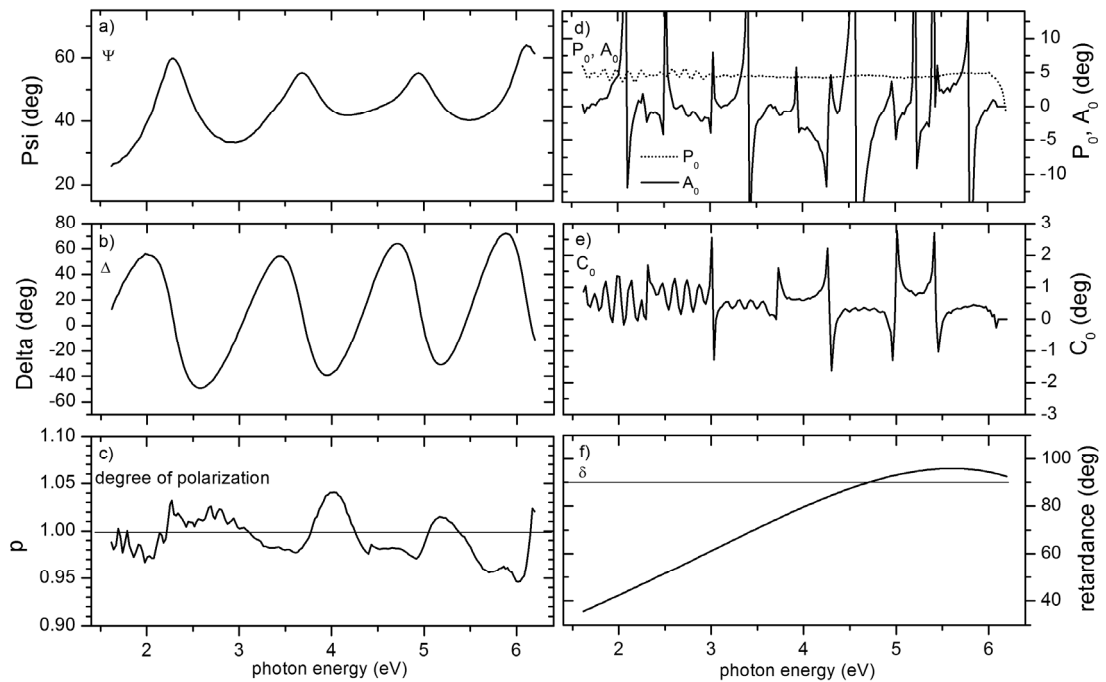
Figure 3.4. Results from a measurement on thin film of low-*k* material NCS processed by CalibRCE program. The angle of incidence was 60°. The left column of graphs shows the resulting ellipsometric angles a) Ψ b) Δ and c) the degree of polarization. The graphs in the right column shows the results of d) P_0, A_0 and e) C_0 calibration. Graph f) shows the retardance used for the analysis.

Example of calibration

As an example of the operation of CalibRCE, I have chosen one of my first measurements of the low-*k* dielectric film NCS with the thickness of approximately 400 nm on silicon substrate, under angle of incidence 60°. A single broadband compensator was used for the whole spectrum. Figure 3.4 shows the resulting spectra calculated by CalibRCE. The dependencies of Ψ and Δ are smooth, with Δ crossing 0 (the range of Δ is -180° to +180°).

The degree of polarization is found to be close to 1, however it seems to be distorted and coupled to the ellipsometric parameters.

The spectrum of the offset A_0 shows localized deviations in the spectral positions, where Δ and therefore X are equal to zero. Several unexpected sharp structures are observed. Nevertheless, the averaged value (A_0=-0.6°) was used in the compensator offset correction.

The spectrum of C_0, averaged from the two measured spectra, shows the expected deviations for the linearly polarized light, but also distinct oscillations are observed. Furthermore, the values between each two peaks are not comparable; obviously, the ellipticity (sense of rotation of the electric field vector) has some influence on the detected C_0. Again, the average C_0 is used for the analysis with nearly-linear polarization.

Finally, the spectrum of polarizer offsets P_0 is reasonably flat. The last graph of fig. 3.4 shows the retardance of the compensator, measured independently.
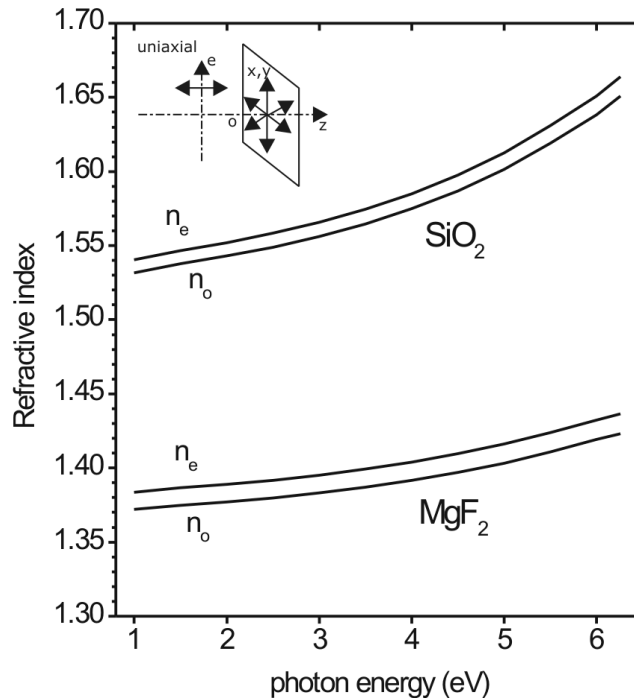
Figure 3.5. Uniaxial birefringence of quartz and magnesium fluoride.

Several of the mentioned features are artifacts resulting from small misalignments between the plates of the multi-plate compensator. In the next section, the construction of the retarders and the origin and treatment of the artifacts will be discussed.

3.3.   Compensator construction and properties

3.3.1. Construction of the multi-plate compensator

Various designs of the compensators are possible and available, but here we will restrict ourselves to the simple single-plate design and the combination of the plates to a multi-plate compensator.

To create a retarder, one can polish a plate of birefringent material with the optical axis in the plane of the surfaces, which is perpendicular to the rotational axis of the device. Figure 3.5 shows refractive indices of the two candidate materials: quartz[61] and magnesium fluoride.[62] Both materials exhibit higher refractive index for the extraordinary ray, therefore the optical axis of the materials coincides with the slow axis of the retarder. For the use as a rotating compensator, the retardance close to 90° (quarter-wave) between the fast and slow axis is desired. The phase difference between the components polarized orthogonally in the directions of the fast and slow axes is given by

---

[61] G. Ghoaadwd G. Ghosh, *Dispersion-equation coefficients for the refractive index and birefringence of calcite and quartz crystals*, Opt. Commun. **163,** 95-102 (1999).
[62] M. J. Dodge, *Refractive properties of magnesium fluoride*, Appl. Opt. **23,** 1980-1985 (1984).

$$\delta + 2\pi k = \frac{2\pi}{\lambda} d(n_e - n_o),$$ (3.63)

where k is the order of retardation, d the thickness of the plate and λ the wavelength. For the zero-order retardation at 2 eV, a quartz plate (with n_e-n_o=0.0091) is only 17 μm thick. Since it is not technologically possible to manufacture such a thin plate, the biplate design is adopted. Two plates are polished to an almost same thicknesses of ~1 mm, with a difference equal to the thickness necessary for the zero-order (here 17 μm). The plates are mounted together with the optical axes crossed. The high order of retardation generated in the first plate is compensated in the second plate. Resulting retardation is of the required zero-order. Still, the retardation is increasing with photon energy and a narrow range is covered by the wanted λ/4 retardation.

The retarder used in most of examples in this chapter (denoted as compensator A) is constructed as a four-plate combination. It principally consists of two biplate retarders, one made of quartz and the second made of MgF$_2$, mounted together with their fast axes crossed. The retardation generated by the first biplate is then compensated by the second one, and the dispersions of the two materials ensure a very flat energy dependence of retardance as seen in fig. 3.4 or fig. 3.6. Of course, this complicated design is sensitive to precise alignment of the individual plates. As shown in the next subsections, the misalignment of the elements is responsible for the observed artifacts shown in fig. 3.4.

3.3.2. Measurement of compensator properties

We have assumed the retardance of the compensator to be known. The actual, spectrally dependent, retardance has to be determined by proper measurements.

In this subsection, we describe a method for the measurement of retardance δ, together with the offset C_0 and the degree of polarization p, based on a dual straight-through measurement directly with the RCE setup. This method combines the conventional measurement with equal analyzer and polarizer setting ($A=P$) with the second possible principal setting with the polarizer and analyzer axes crossed ($A=P+90°$). Only the difference of the analyzer and the polarizer azimuths has to be known.

For the straight-through RCE measurement with the polarizer setting P and analyzer setting A, the signal at the detector is

$$I(C_r) = I_0(1 + a_{r4} \cos 4C_r + \beta_{r4} \sin 4C_r),$$ (3.64)

where the 2C component vanishes. Combining the results of section 1 of this chapter, the Fourier coefficients are

$$a_{r4} = D_4 \cos(2A + 2P + 4C_0),$$ (3.65)

$$\beta_{r4} = D_4 \sin(2A + 2P + 4C_0),$$ (3.66)

where

$$D_4 = \frac{p(1 - \cos\delta)}{2 + p(1 + \cos\delta)\cos(2A - 2P)} \, . \tag{3.67}$$

As mentioned above, the two principal settings of the analyzer and the polarizer are available. The first measurement is performed for $A=P$. Without loss of generality, the azimuths can be chosen as $A=P=0$. Then

$$a_{r4} = D_4^+ \cos 4C_0, \qquad \beta_{r4} = D_4^+ \sin 4C_0 \quad \text{and} \tag{3.68}$$

$$D_4^+ \equiv \frac{p(1 - \cos\delta)}{2 + p(1 + \cos\delta)} \, . \tag{3.69}$$

If no depolarization is present, this measurement is sufficient for the retardance evaluation, since, for $p=1$,

$$D_4^+ = \frac{1 - \cos\delta}{3 + \cos\delta} \, . \tag{3.70}$$

Otherwise, the second measurement is performed for the settings of $P=0$, $A=90°$, leading to

$$a_{r4} = -D_4^- \cos 4C_0, \qquad \beta_{r4} = -D_4^- \sin 4C_0 \quad \text{and} \tag{3.71}$$

$$D_4^- \equiv \frac{p(1 - \cos\delta)}{2 - p(1 + \cos\delta)} \, . \tag{3.72}$$

Here, for the degree of polarization equal to unity, only a trivial result is obtained ($D_4^-=1$). Combining the two measurements, the resulting δ, p and C_0 are evaluated as

$$\cos\delta = \frac{D_4^- - D_4^+ - 2D_4^+ D_4^-}{D_4^- + D_4^+ + 2D_4^+ D_4^-} \, , \tag{3.73}$$

$$p = \frac{4D_4^+ D_4^-}{(D_4^- + D_4^+)(1 - \cos\delta)} \, , \tag{3.74}$$

$$\tan 4C_0 = \frac{\beta_{r4}}{a_{r4}} \, . \tag{3.75}$$

In the last equation, the pair of Fourier coefficients might be used from each of the measurements.
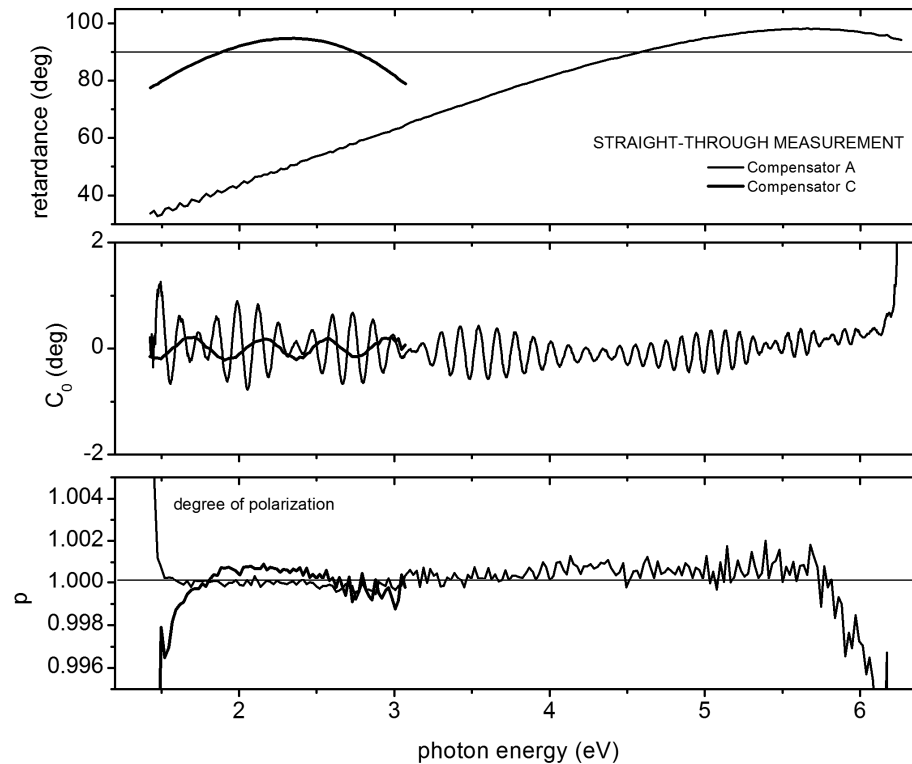
Figure 3.6. Properties of two achromatic retarders, measured in straight-through RCE operation.

Real-world example

We have applied the above described method to two broadband compensators available at our laboratory.[63] The compensator denoted by A is a four-plate achromatic device, nominally designed for the range from 180 to 300 nm (4.1 to 6.9 eV). The compensator denoted as C is a biplate, designed for the range from 480 to 680 nm (1.8 to 2.6 eV).

Figure 3.6 shows the retardance angles, position of the fast axes and the degree of polarization for the compensators A and C. The construction of A allows its usage in the whole available range of the ellipsometer, i.e., from 1.4 to 6.2 eV. The measured retardances meet the specifications of the manufacturer, and the degree of polarization of both retarders lies close to unity. A small ripple is observed in the low energy region for retardance of A, but far below the range of operation. However, the measurements of the offsets C_0 revealed spurious oscillations for both of the devices as presented in fig. 3.6. This behavior is highly undesirable, as it produces artifacts in measured spectra, as shown previously in fig. 3.4.

An analysis of the origin of these artifacts, and a possible treatment of the data, will be discussed in the next section.

---

[63] The retarders were supplied by Bernhard Halle Nachfl. GmbH, Berlin, Germany. The devices are mounted in cylindrical holders with the diameter of 25 mm; the aperture diameter is 9.5 mm.
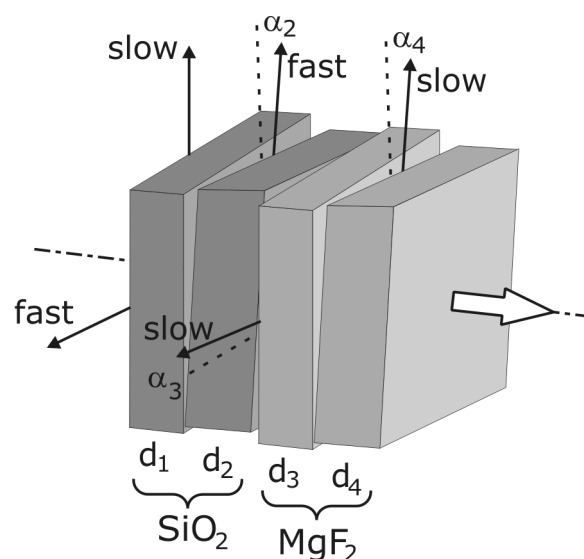
Figure 3.7. Schematic picture of four-plate misaligned retarder.

3.4.   Compensator artifacts

Achromatic or super-achromatic retarders can be constructed by combining several biplate retarders into one device. However, the usage of the retarders with such complex construction can be limited due to the occurrence of undesired artifacts in the RCE spectra. Two possible sources of artifacts have been pointed out:[64]

- Multiple reflections on the internal interfaces and on the thin air gaps between the individual plates, resulting in the degraded polarization and forming a ripple in the measured degree of polarization.[65,66]
- Angular misalignment of the plates with respect to the rotational axis of the compensator, resulting in the non-linear polarization eigenstates of the compensator.[67] This effect is energy dependent and can be observed as pronounced oscillations in the evaluated quantities in RCE.[68]

---

[64] Another source of discrepancies can be related to optical activity of quartz, but this issue is not discussed here.

[65] K. Ebert, D. E. Aspnes, *Biplate artifacts in rotating-compensator ellipsometers* Thin Solid Films **455,** 779-783 (2004).

[66] D. K. Aitken, J. H. Hough, *Spectral Modulation, or Ripple, in Retardation Plates for Linear and Circular Polarization*, Publ. Astron. Soc. Pac. **113,** 1300-1305 (2001).

[67] B. Boulbry, B. Bousquet, B. Le Jeune, Y. Guern, J. Lotrian, *Polarization errors associated with zero-order achromatic quarter-wave plates in the whole visible spectral range*, Optics Express **9,** 225-235 (2001).

[68] J. Lee, P. I. Rovira, I. An, R. W. Collins, *Alignment and calibration of the MgF2 biplate compensator for application in rotating compensator multichannel ellipsometry*, J. Opt. Soc. Am. **18,** 1980-1985 (2001).
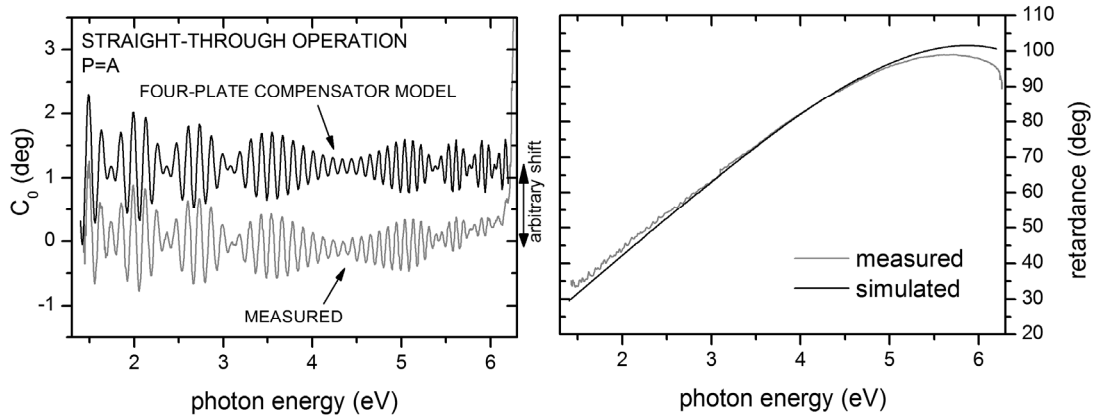
Figure 3.8. The measured and simulated artificial oscillations in the angular offset C_0 (left), the measured and simulated retardance δ (right).

Although the artifacts can be suppressed by a proper construction and improved adjustment of the parts of the compensator, the understanding of the origin and a possible treatment of the data should be elaborated for high precision ellipsometric measurements. In this section, we focus on the latter effect and its influence in the straight-through and sample measurements.

3.4.1. Multi-plate misalignment

To simulate the artifacts observed in the case of compensator A (fig. 3.6), we have constructed a model based on the following assumptions: The compensator is composed of four ideal retarding plates, two made of quartz and two of MgF$_2$. Each plate is described by its fixed physical azimuth of the fast axis a_i, and the energy-dependent retardance δ_i, according to the dispersion of the refractive index for the given material. The transmission of light through the plates is lossless, without depolarization and without reflections on the surfaces. The spurious effects are therefore originating from small deviations from the perfect angular alignment of the plates. The compensator is described by the multiplied Mueller matrices[69] of a series of single-plate retarders

$$\hat{C}_{4-plate} = \hat{C}_4(a_4,\delta_4) \cdot \hat{C}_3(a_3,\delta_3) \cdot \hat{C}_2(a_2,\delta_2) \cdot \hat{C}_1(a_1,\delta_1), \qquad (3.76)$$

where the retardance is given by (3.63). For a good match of the modeled and measured retardances, the correct difference between the thicknesses of the individual plates must be provided (for SiO$_2$ d_2-d_1=11.4 µm and for MgF$_2$ d_4-d_3=14.9 µm), whereas the absolute values of thicknesses influence merely the shape of the artifacts (each thickness is around 800 µm).[70]

Figure 3.7 shows the scheme of the discussed device: two quartz plates are followed by the MgF$_2$ plates. The azimuths of the fast axes of the individual plates were chosen as: a_1=0°, a_2=89.7°, a_3=90°, a_4=-0.3°.

---

[69] Obviously, the Jones matrix formalism is sufficient here.
[70] The construction details were provided by Dr. Götz Zinner (B. Halle Nachfl. GmbH), who is gratefully acknowledged.
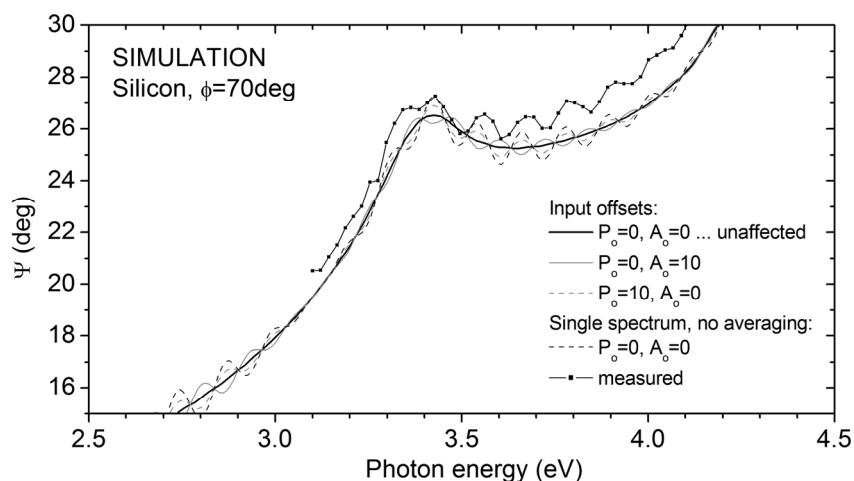
Figure 3.9. The simulated ellipsometric angle Ψ obtained by the averaging of two spectra obtained with the opposite polarizer settings for the polarizer and the analyzer offset calibration. For zero offsets, the artifacts are completely removed by the averaging (black solid), although the single spectrum is affected by the artifacts (black dashed line). With non-zero analyzer and polarizer offsets, the oscillations appear even after averaging (gray solid and dashed lines). The single measured spectrum (offsets close to zero) is showing a similar behavior (black line with symbols).

Using the model, I have simulated the straight-through measurement as described in the previous section (fig. 3.8). The precise shape of the spurious oscillations is strongly influenced by the values of refractive indices and their dispersions, the thicknesses of the plates and by the angular misalignments. A fair agreement with the experimental data was obtained by a trial-error scheme without any optimization.

The misalignment demonstrates itself as the oscillations of the angular offset, but the overall behavior is more complex. For a sample measurement, the artifacts cannot be compensated by the assumption of variable C_0. There are no longer axes transmitting unchanged linear polarizations and the definition of fast and slow axes loses sense.

Although the detected retardance and the artificial oscillations of C_0 remain equal for the reverse beam propagation through the compensator, the resulting effect on the sample spectra is different - therefore the correct order of the plates must be preserved to simulate these phenomena.

The impact of the compensator misalignment on measured quantities will be discussed in the following subsection.

3.4.2. Effect on the calibration

For practical purposes, the impact of the artificial offset of the compensator azimuth on the calibration procedure and the evaluated ellipsometric quantities is of primary importance. I performed a series of simulated measurements with various analyzer and polarizer offsets to understand the impact of the misalignment on the calibration procedure. The bare silicon substrate, with the well known optical properties was chosen for the simulation.
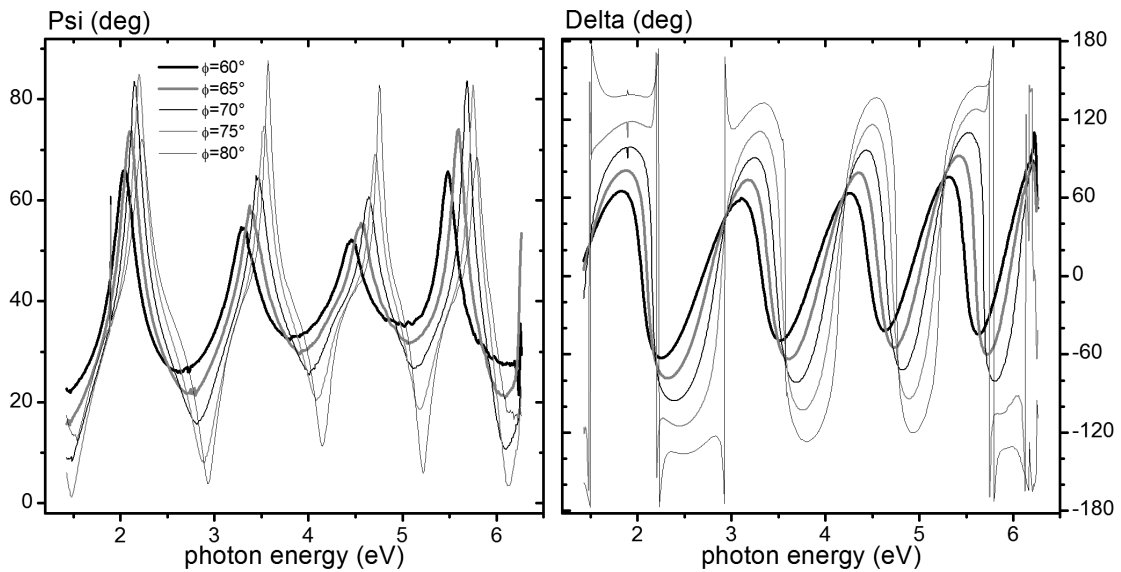
Figure 3.10. Measured spectra of NCS thin film.

Figure 3.9 shows a part of Ψ spectrum simulated with various assumptions. The single spectrum simulated with zero analyzer and polarizer offset contains the undesired oscillations and the same is true for actually measured spectrum (since the actual offsets A_0 and P_0 are small).

If two spectra are simulated as acquired with polarizer settings ±30° with an analyzer and polarizer offsets, the calibration procedure, described in section 3.2, can be used. Within the procedure, A_0 and P_0 contain artificial oscillations, but the averaging leads to a good agreement with the input values (the maximum difference being ~0.01 deg), as the oscillations occur almost symmetrically around the constant true values.

In fig 3.9 the results are plotted for selected input A_0 and P_0 settings. It was found that in the presence of a angular offset of the polarizer or analyzer, the Ψ spectrum (and Δ as well, not shown), averaged from the two measured (simulated here) is affected by the oscillations. In the favorable case of zero offsets, however, the artifacts vanish.

Thin film example

As an example of the reduction of the artifacts I have selected a series of measurements on thin film (thickness 400 nm) of low-*k* dielectric NCS on Si substrate. Figure 3.10 shows the Ψ and Δ spectra for multiple angles of incidence. All the spectra were measured at two polarizer settings, ±45°, and calibrated with the CalibRCE program. Two compensators were used for the measurement. The compensator A covered the range from 3.1 to 6.3 eV, and the compensator C (biplate) covered the rest, i.e., from 1.4 to 3.1 eV. The calibration of the polarizer and analyzer offsets produced reasonable results: for the five measured pairs of spectra all the obtained polarizer offsets fell between -0.058° and 0.012° and the analyzer offsets between 0.18° and 0.29°.
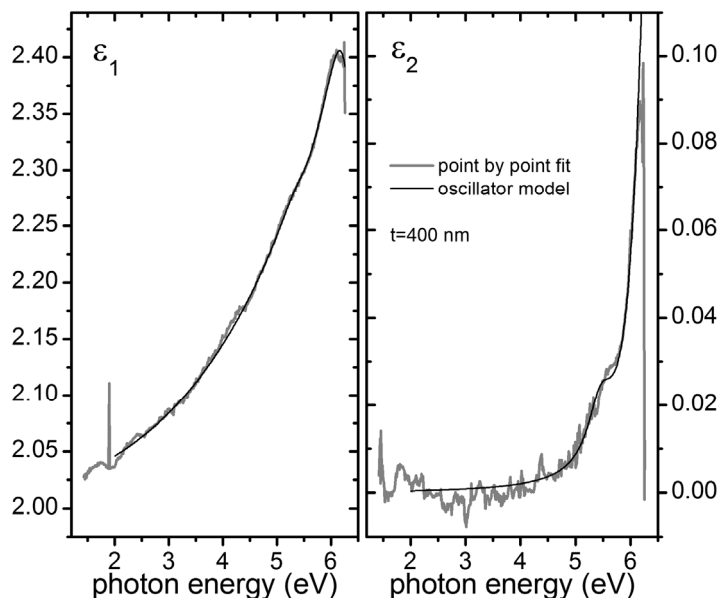
Figure 3.11. Fitting of the measured data of NCS film by the dielectric function using point-by-point or parameterized model. Thickness of the film was in both cases fixed to 400 nm.

The spectra of Ψ and Δ are smooth, with visible discrepancies in Ψ in the regions where the Δ crosses 0, i.e. in the points where the knowledge of the compensator offset is needed. The measured points are supplemented with proper errors and a subsequent analysis of the data is possible without risking a misinterpretation.

Figure 3.11 shows models of the dielectric function of the film fitted to the data set discussed above. Two approaches were chosen for comparison. First, the simple Cauchy dispersion with two harmonic oscillators (located at 5.5 eV and 6.3 eV) was fitted to the data. The thickness was estimated to be 400 nm. Then the point-by-point search for the two parts of the dielectric function was performed with the thickness fixed at 400 nm. The two approaches agree very well and no noticeable oscillations are present in the point-by-point analysis.

3.4.3. Generalized RCE

In the previous subsection, I have shown the impact of the usage of the misaligned compensator in the conventional way of signal analysis, i.e. assuming a perfect device defined by its retardance and azimuth. However, the knowledge of the origin of the artifacts can be used to analyze the signal in a more complex way. The elements of the Mueller matrix of the compensator can be used for a generalization of the set of formulas presented in section 3.1. Then, even an imperfect compensator could be used for fairly precise measurements.

According to the restrictions of the four-plate model presented above, only 6 non-zero elements of the Mueller matrix of the complete compensator (3.76) play role in the analysis. We introduce angles Y and Z by

$$\cos Y \equiv \frac{m_{22} - m_{33}}{\sqrt{(m_{23} + m_{32})^2 + (m_{22} - m_{33})^2}} , \tag{3.77}$$

$$\sin Y \equiv \frac{m_{23} + m_{32}}{\sqrt{(m_{23} + m_{32})^2 + (m_{22} - m_{33})^2}} , \tag{3.78}$$

$$\cos Z \equiv \frac{m_{24}}{\sqrt{m_{24}^2 + m_{34}^2}} , \tag{3.79}$$

$$\sin Z \equiv \frac{m_{34}}{\sqrt{m_{24}^2 + m_{34}^2}} , \tag{3.80}$$

where the elements of the Mueller matrix are denoted by m_{ij}. Using such a device in the RCE configuration leads to the signal at the detector consisting again of the two harmonic components, which can be analyzed according to eqs. (3.31) to (3.35). The generalized equations read as follows:

$$2Q = Y - 2Z + 2A - 4T , \tag{3.81}$$

$$\tan 2X = \text{sgn}(X) \cdot \frac{1}{2} \frac{D_2}{D_4} \sqrt{\frac{(m_{23} + m_{32})^2 + (m_{22} - m_{33})^2}{m_{24}^2 + m_{34}^2}} , \tag{3.82}$$

$$p = \frac{2D_4}{\cos 2X \left\{ \sqrt{(m_{23} + m_{32})^2 + (m_{22} - m_{33})^2} - D_4 \begin{bmatrix} (m_{22} + m_{33})\cos 2(Q - A) + \\ +(m_{23} - m_{32})\sin 2(Q - A) \end{bmatrix} \right\}} , \tag{3.83}$$

$$2C_0 = 2C_{S2} - Z + 2A , \tag{3.84}$$

where C_0 is the position of the fast axis of the first plate.

In order to test the generalized equations on actually measured spectra, we have performed the RCE measurements on a polished steel. Steel is well suited for this task, since it provides flat, monotonic spectra. A single spectrum[71] in the range from 1.4 to 6.2 eV was measured using the compensator A, angle of incidence was 80°, polarizer azimuth 30°, and analyzer azimuth 0°. Using the conventional way of the data analysis, assuming the compensator with retardance δ and azimuth offset C_0, pronounced oscillations were detected in the ellipsometric angles, see fig. 3.12. The generalized equations (3.81) to (3.84) were used on the same data, with the Mueller matrix elements taken from the model (3.76) presented in fig. 3.8. As previously mentioned, the model was in a qualitative agreement with the straight-through data, but neither fitting nor further improvement of the model took place. Figure 3.12 shows that even using only the approximate model, the oscillations in Ψ, Δ and C_0

---

[71] Therefore, no P_0 and A_0 calibration and no averaging is performed.
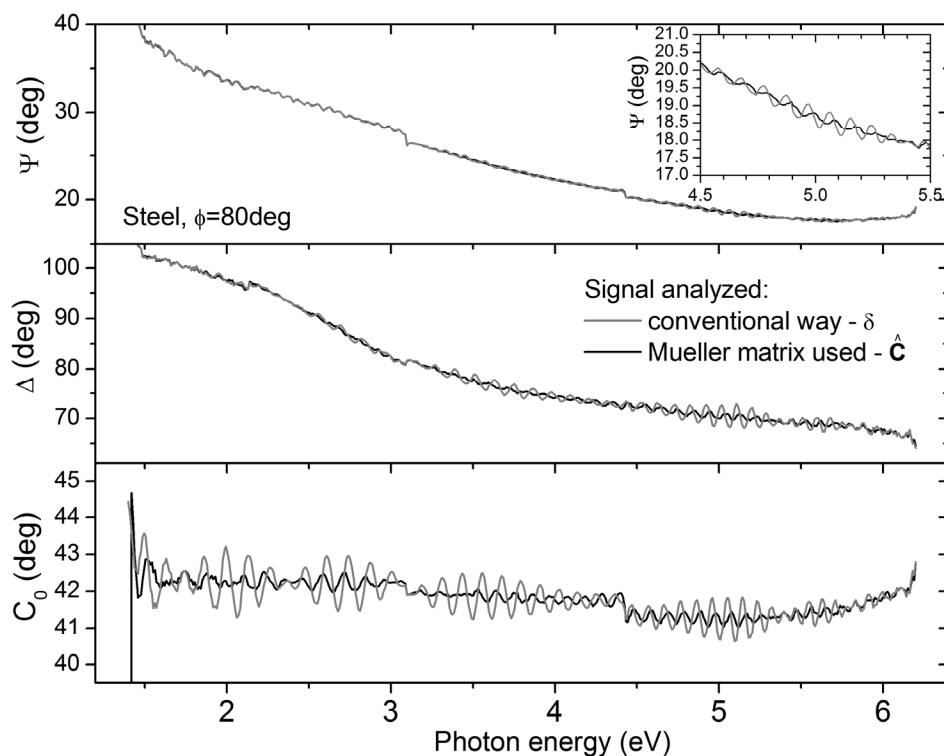
Figure 3.12. Measured data of a polished steel sample. The data has been processed by the conventional way using the energy dependent retardance (gray lines) and the Mueller matrix of the misaligned compensator (black lines). Although we have used only an approximate model, the oscillations in Ψ, Δ and C_0 have been substantially reduced.

have been substantially reduced. A careful optimization of the parameters would be needed to achieve perfect results with the misaligned compensator.

3.5.   Conclusions

The rotating compensator ellipsometer operating in the range from 1.4 to 6.2 eV was constructed.[72] The necessary data acquisition and processing routines were developed, coded and tested in real operations.

First, the data acquisition and ellipsometer controlling program[73] was implemented generating raw data in the form of Fourier coefficients.

Second, the data processing and calibration program CalibRCE was developed using the theoretical fundaments presented in this chapter.

---

[72] With great help from Eduard Schmidt and Radoslav Švehla.
[73] SamuraiRCE.exe (2006), based on RAE data acquisition and control program Samurai.exe (2005). This program evolved from previous version Ninja.exe (2004), after replacement of the rotating motor by stepping motor. The mentioned programs were developed by the author. The original controlling software which laid basis for the future progress was programmed by Alois Nebojsa.

All routines process measured data together with their errors, allowing a reasonable weighting in subsequent model optimizations.

The initial measurements proved a fair performance of the implemented software, however, undesired artefacts were observed in the measured spectra. In the following, I have studied the artifacts originating from the angular misalignment of the individual plates of the four-plate compensator, and have described their impact on the rotating compensator measurement and calibration. I have adopted a simple model based on the Mueller matrix framework to simulate the artifacts. Finally, I have proposed an appropriate treatment of the affected data by using the Mueller matrix of the misaligned compensator instead of a single value of retardance.

3.5.1. Outlook

The possible influence of the optical activity of quartz (present both in the polarizers and compensator) on the measurements should be evaluated.

If the model of the misaligned compensator can be improved to match the experimental data, the procedure of data analysis using the generalized device should be implemented in practical usage.

To avoid the multi-plate artifacts, single plate retarders might be used, either Berek or monoplate designs.[74,75]

The operation of the rotating compensator ellipsometer excludes the detection of the whole Mueller matrix of the sample. This feature can be added by the dual rotating compensator configuration, Mueller matrix ellipsometry.[76]

---

[74] M. Asar, D. E. Aspnes, *Optical anisotropy relevant to rotating-compensator polarimeters: application of the monoplate retarder*, Thin Solid Films **455-456,** 50-53 (2004).

[75] M. Asar, D. E. Aspnes, *The nearly aligned rotating-monoplate compensator*, Phys. Stat. Sol. A **205,** 739-742 (2008).

[76] C. Chen, I. An, G. M. Ferreira, N. J. Podraza, J. A. Zapien, and R. W. Collins, *Multichannel Mueller matrix ellipsometer based on the dual rotating compensator principle,* Thin Solid Films **455-456,** 14-23 (2004).

Chapter 4 : Optical properties of low-*k* dielectrics

Study of optical properties of low-k dielectrics and their changes during UV-cure and plasma treatments. This work was done at IMEC during 2007 with help and inspiration from Salvador Eslava, Adam Urbanowicz, Mariana Pantouvaki, Tomin Liu, German Aksenov, Patrick Verdonck, David De Roest, Denis Shamiryan and Mikhail Baklanov.

In the present generation of silicon-based microelectronic, the traditional dielectric - silicon dioxide with the dielectric constant (*k*-value) of 4.2 - is being replaced by materials optimized for the *k*-value demanded by the technology. For the interconnect application (fig. 4.1), the dielectric constant should be as low as possible to reduce the capacitance between the wires and therefore the signal delay of interconnects.[77,78] On the contrary, the transistor gate application requires high capacitance with decreasing form factor (below 1 nm of thickness) and therefore high dielectric constant (high-*k*) materials have to be used.

---

[77] K. Maex, M.R. Baklanov, D. Shamiryan, F. Iacopi, S.H. Brongersma, Z.S. Yanovitskaya, *Low dielectric constant materials for microelectronics*, J. Appl. Phys. **93,** 8793-8841 (2003).
[78] M. Baklanov, K. Maex, M. Green (Eds.), *Dielectric Films for Advanced Microelectronics*, Wiley (2008).
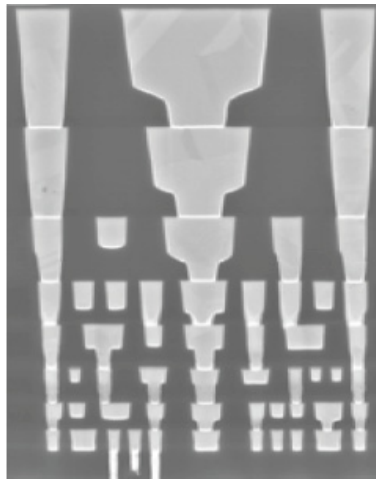
Figure 4.1. TEM view of multiple layers of Cu interconnects separated by low-*k* dielectric.

Most of the presently popular low-*k* dielectrics are multi-constituent amorphous materials and need several technological steps to prepare. Moreover, the properties of the final, on chip implemented, low-*k* dielectric are also influenced by the processing steps (patterning, polishing, cleaning). Therefore, the employment of multiple analysis techniques is necessary for an appropriate description of the material's behavior.

The present chapter focuses on the optical properties of the low-*k* films in visible and ultraviolet, up to 9 eV. The chemical composition of these films is analyzed using FTIR spectroscopy. In the section 1, the structure of SiCOH low-*k* dielectrics and their preparation is described. Section 2 lists the relevant properties of low-*k* materials and introduces the methods employed in our research. Although there are more viable approaches in low-*k* interconnects technology (spin-on deposition, polymers, air-gaps), we limit the discussion only to the materials and processes actually used in our experiments.

We have performed the study on dielectrics developed and manufactured by two industrial suppliers. Both these films are porous and have chemical structure similar to SiO_2, with part of Si-O bonds replaced by $Si-CH_3$. However, not all technical details were accessible, the exact chemical composition of the precursors is not disclosed and the deposition hardware and also processing methods differ. Although, according to FTIR spectra, they have quite similar chemical composition. The low-*k* films subjected to our experiments are development samples and the observed properties do not necessarily reflect the final properties of the commercial products. Section 3 contains results obtained on the material codenamed **Alpha** in this work and contains data published in,[79,80] related to the

---

[79] P. Marsik, P. Verdonck, D. Schneider, D. De Roest, S. Kaneko and M. R. Baklanov, *Spectroscopic ellipsometry and ellipsometric porosimetry studies of CVD low-k dielectric films*, Phys. Status Solidi C **5,** 1253-1256, (2008).

[80] P. Marsik, P. Verdonck, D. De Roest and M. R. Baklanov, *Porogen residues detection in optical properties of low-k dielectrics cured by ultraviolet radiation*, Thin Solid Films, doi:10.1016/j.tsf.2009.12.110 (2010).

changes of the optical properties during the UV cure and detection of the porogen residues in the optical spectra. Section 4 deals with the changes related to plasma modification of the samples.[81] Section 5 contains results collected from additional experiments on material codenamed **Beta**. The presented work includes data published in.[81,82]

4.1. Structure and preparation of low-*k* dielectrics

4.1.1. SiCOH materials

For the lowering of the dielectric constant (i.e. polarizability) of SiO_2, the Si-O bonds have to be replaced with less polarizible ones[83,84,85] or their density have to be reduced by lowering the overall density of the material.[86,87] The actual porous SiCOH low-*k* dielectrics combine both approaches. The Si-O bonds are partly replaced by $Si-CH_3$ ending groups, which are also important for reduction of the hydrophilicity of the SiO_2.

Figure 4.2 shows the porosity dependencies of the dielectric constants and refractive index of silicon dioxide and SiCOH dielectrics with increasing concentration of CH_3 groups according to literature.[85] The effective medium mixed from the dielectric and air was calculated using Bruggeman approximation.

The presence of pores in the SiCOH material is most commonly achieved using a two step process (see fig. 4.3). In the first step, a film is deposited through plasma enhanced chemical vapor deposition (PECVD) of SiCOH matrix material (containing Si-O and $Si-CH_3$ bonds) together with a sacrificial C_xH_y precursor (porogen). Alternatively, a solution of the nano-clustered SiCOH material can be deposited by the spin-on technique. The porogen (solvent) is subsequently removed by thermal annealing or irradiation by UV light or by electron beam, obtaining the porous low-*k*

---

[81] P. Marsik, A. M. Urbanowicz, K. Vinokur, Y. Cohen and M. R. Baklanov, *Changes of UV Optical Properties of Plasma Damaged Low-k Dielectrics for Sidewall Damage Scatterometry*, Material Research Society Symposium Proceedings **1079,** 1079-N07-04 (2008).

[82] S. Eslava, G. Eymery, P. Marsik, F. Iacopi, C. E. A. Kirschhock, K. Maex, J. A. Martens, and M. R. Baklanov, *Optical property changes in low-k films upon ultraviolet-assisted curing*, J. Electrochem. Soc. **155,** G115-G120 (2008).

[83] J.Y. Kim, M.S. Hwang, Y.H. Kim, H.J. Kim, Y. Lee, *Origin of low dielectric constant of carbon-incorporated silicon oxide film deposited by plasma enhanced chemical vapor deposition*, J. Appl. Phys. **90,** 2469 (2001).

[84] A. Grill and V. Patel, *Low dielectric constant films prepared by plasma-enhanced chemical vapor deposition from tetramethylsilane*, J. Appl. Phys. **85,** 3314-3318 (1999).

[85] S. Jain, V. Zubkov, T. Nowak, A. Demos, and J. C. Rocha, *Porous low-k dielectrics using ultraviolet curing*, Solid State Technology **48,** 43 (2005).

[86] A. Grill and V. Patel, *Ultralow-k dielectrics prepared by plasma-enhanced chemical vapor deposition*, Appl. Phys. Lett. **79,** 803-805 (2001).

[87] A. Grill, V. Patel, K.P. Rodbell, E. Huang, M.R. Baklanov, K.P. Mogilnikov, M. Toney, H.C. Kim, *Porosity in plasma enhanced chemical vapor deposited SiCOH dielectrics: A comparative study*, J. Appl. Phys. **94,** 3427 (2003).
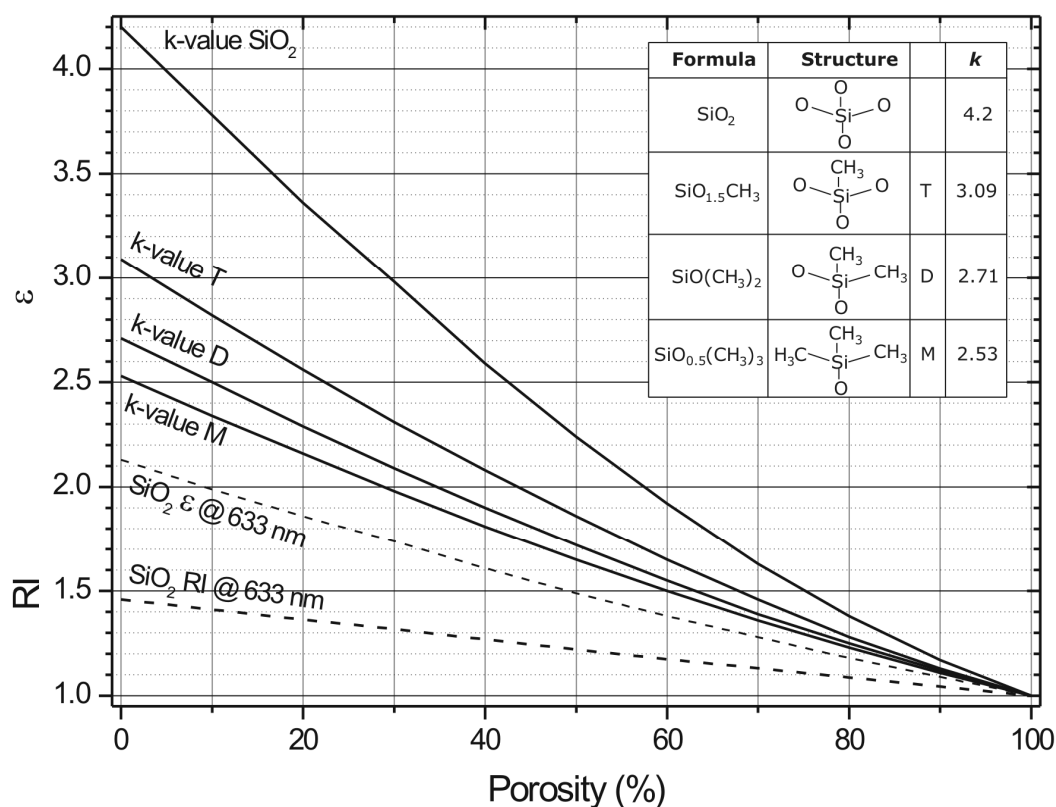
Figure 4.2. Calculated dielectric constants of SiCOH and refractive index of SiO$_2$ as the function of porosity. The inset shows the structure of single units of SiCOH and the associated k-values, adopted from Jain et al., Solid State Technol. 48 (2005).

film.[88] Our research is focused on UV-cured PECVD dielectrics with the k-values around 2.3 and 2.5.

4.1.2. Ultraviolet curing

In recent years, significant efforts have been invested in studies of UV assisted thermal curing, in terms of curing light wavelength and the resulting changes of the SiCOH material deposited by either PECVD[89] or spin-on,[90,91] and their

---

[88] S. I. Nakao, J. Ushio, T. Ohno, T. Hamada, Y. Kamigaki, M. Kato, K. Yoneda, S. Kondo and N. Kobayashi, *UV/EB cure mechanism for porous PECVD/SOD low-k SiCOH materials*, Proceedings of the Interconnect Technology Conference (IEEE, New York), 66-68 (2006).

[89] F. Iacopi, Y. Travaly, B. Eyckens, C. Waldfried, T. Abell, E. P. Guyer, D. M. Gage, R. H. Dauskardt, T. Sajavaara, K. Houthoofd, P. Grobet, P. Jacobs, and K. Maex, *Short-ranged structural rearrangement and enhancement of mechanical properties of organosilicate glasses induced by ultraviolet radiation*, J. Appl. Phys. **99,** 053511 (2006).

[90] A. M. Urbanowicz, B. Meshman, D. Schneider, M.R. Baklanov, *Stiffening and hydrophilisation of SOG low-k material studied by ellipsometric porosimetry, UV ellipsometry and laser-induced surface acoustic waves*, Phys. Status Solidi A **205,** 829 (2008).
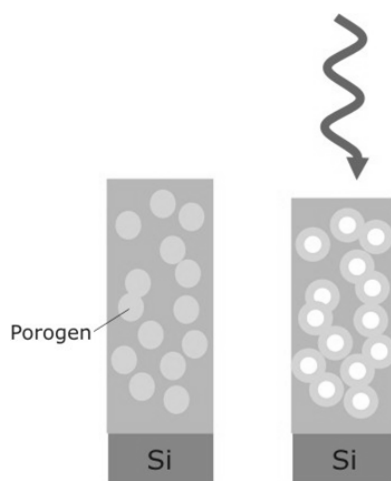
Figure 4.3. The co-deposited SiCOH matrix and porogen. After deposition, the porogen is decomposed and removed by UV-cure.

effect on the porogen based PECVD[92] or spin-on[93] low-*k*. The most important effects of these cures, apart from the porogen or solvent residues removal (when applicable), are the photochemical changes of the matrix material followed by densification and shrinkage. The UV light promotes cross-linking of the matrix and reorganizes the Si-O-Si skeleton towards a more stable network structure.[94,95] During the UV irradiation, an important part of the material, the -CH$_3$ groups, responsible for hydrophobic properties and low dielectric constant can be partially removed and replaced by Si-H bonds.[88,96] This replacement process is much stronger for high-energetic photons with energies above 6.5 eV (wavelengths below 190 nm) because of the threshold energy that is necessary to break the Si-CH$_3$ bond.[97] The carbon depletion and increase

[91] S. Eslava, F. Iacopi, A. M. Urbanowicz, C. E. A. Kirschhock, K. Maex, J. A. Martens, and M. R. Baklanov, *Ultraviolet-assisted curing of organosilicate glass low-k dielectric by excimer lamps*, J. Electrochem. Soc. **155,** G231-G236 (2008).

[92] C. H. Huang, H. L. Huang, C. I. Hung, N. F. Wang, Y. H. Wang, and M. P. Houng, *Bond structure in porous SiOCH low-k film fabricated by ultraviolet irradiation*, Jpn. J. Appl. Phys. **47,** 1532-1535 (2008).

[93] A. Zenasni, B. Remiat, C. Waldfried, Ch. Le Cornec, V. Jousseaume, G. Passemard, *Thermal furnace cure and Ultraviolet assisted curing impact on SiCOH spin-on low dielectric constant material*, Thin Solid Films,**516,** 1097-1103 (2008).

[94] A. Grill and D.A. Neumayer, *Structure of low dielectric constant to extreme low dielectric constant SiCOH films: Fourier transform infrared spectroscopy characterization*, J. Appl. Phys. **94,** 6697 (2003).

[95] A. Zenasni, V. Jousseaume, P. Holliger, L. Favennec, O. Gourhant, P. Maury, and G. Gerbaud, *The role of ultraviolet radiation during ultralow k films curing: Strengthening mechanisms and sacrificial porogen removal*, J. Appl. Phys. **102** (2007).

[96] J. Ushio, T. Ohno, T. Hamada, S. I. Nakao, K. Yoneda, M. Kato, and N. Kobayashi, *Ultraviolet-curing mechanism of porous-SiOC*, Jpn. J. Appl. Phys. Part 2-Letters & Express Letters **46,** L405-L407 (2007).

[97] L. Prager, P. Marsik, J. W. Gerlach, M. R. Baklanov, S. Naumov, L. Pistol, D. Schneider, L. Wennrich, P. Verdonck, M. R. Buchmeiser, *Effect of pressure on efficiency of UV curing of CVD-derived low-k material at different wavelengths*, Microelectron. Eng. **85,** 2094-2097 (2008).
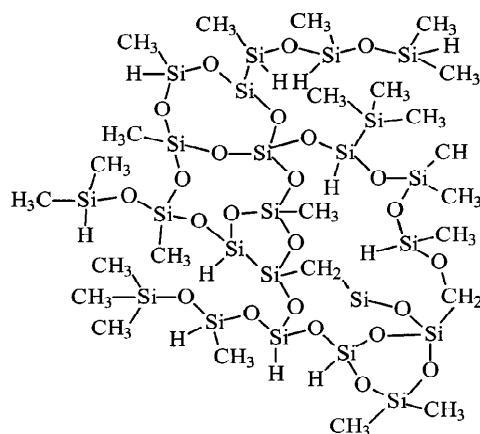
Figure 4.4. Structure of SiCOH material. Various types of bonds are present Si-O, Si-CH$_3$, Si-H and -CH$_2$- bridges.

of the Si-H bond concentration is also responsible for reduced chemical and plasma damage resistance, important for successful integration in the industrial process conditions.

The removal of porogen can be analyzed by Fourier transform infrared spectroscopy[98,99,100] (FTIR) as a gradual decrease of CH$_x$ vibrations around 2900 cm^{-1}. We assume that after breaking of the C-H bonds, some of the carbon containing porogen residues might remain in the interior of the pores. In recent works of Favennec[99] and Zenasni[95] the possible existence of residues of incomplete porogen removal (C=C signature in FTIR and nuclear magnetic resonance (NMR)) has been reported for UV and thermal cures. Gates[101] reported formation of C=C sp^2 structures in thermally cured, porogen based low-*k* dielectric.

4.1.3. Recent challenges

The infrared absorption of low-*k* dielectrics has been widely discussed and understood, but only limited attention is paid to the optical properties of the low-*k* dielectrics at higher photon energies;[102] it is mostly reduced to the evaluation of refractive index (RI) in the visible range, and the changes are interpreted as a result of porogen removal and densification. Nevertheless, the exact knowledge of the properties is important for reliable optical metrology in the industrial scale process conditions. For

---

[98] N. Kemeling, K. Matsushita, N. Tsuji, K. Kagami, M. Kato, S. Kaneko, H. Sprey, D. de Roest, and N. Kobayashi, *A robust k similar to 2.3 SiCOH low-k film formed by porogen removal with UV-cure*, Microelectron. Eng. **84,** 2575-2581 (2007).
[99] L. Favennec, V. Jousseaume, G. Gerbaud, A. Zenasni, and G. Passemard, *Ultralow k using a plasma enhanced chemical vapor deposition porogen approach: Matrix structure and porogen loading influences*, J. Appl. Phys. **102** (2007).
[100] P. Verdonck, D. De Roest, S. Kaneko, R. Caluwaerts, N. Tsuji, K. Matsushita, N. Kemeling, Y. Travaly, H. Sprey, M. Schaekers, and G. Beyer, *Characterization and optimization of porogen-based PECVD deposited extreme low-k materials as a function of UV-cure time*, Surf. Coat. Technol. **201,** 9264-9268 (2007).
[101] S. M. Gates, D. A. Neumayer, M. H. Sherwood, A. Grill, X. Wang, and M. Sankarapandian, *Preparation and structure of porous dielectrics by plasma enhanced chemical vapor deposition*, J. Appl. Phys. **101** (2007).
[102] K. Postava, T. Yamaguchi, *Optical functions of low-k materials for interlayer dielectrics*, J. Appl. Phys. **89,** 2189 (2001).

example, the validity of the widely used Cauchy model for the refractive index is limited due to the non-zero absorption in near ultraviolet and the use of the Cauchy model may lead to systematic errors of thickness measurements. Recently Eslava[82] presented a study of the UV optical response of selected PECVD porogen based low-*k* dielectrics, which opened questions about some of the observed features. UV absorption can also be correlated with the electrical properties of low-k materials such as leakage current and breakdown voltage.

Low-*k* dielectrics are exposed to various etching, stripping and cleaning plasmas in the Cu/low-*k* integration scheme. The chemical and mechanical stability is therefore a key merit of the material optimization. It was shown that oxidizing and reducing plasma chemistries for the photoresist mask removal affect the porous dielectric,[103,104] causing $-CH_3$ depletion in the surface layer, leading to hydrophilic SiO_2 like material.[105] The presence of water deteriorates the dielectric properties and is highly undesired. Plasma induced damage is the crucial issue in the low-*k* integration.

In the present chapter, we focus on the changes of optical properties of low-*k* dielectrics during the UV-cure and plasma exposure, interpret the changes in terms of mixtures of the matrix and porogen materials, and study the impact of residues of the incomplete porogen removal on the optical spectra.

4.2. Properties of low-*k* dielectric and used methods

4.2.1. Dielectric properties

From the technological standpoint, the most important quality of the low-*k* dielectric is the static dielectric constant – the **k-value**. This is measured by *mercury probe* using a doped (conductive) silicon substrate. The mercury droplet forms a planar contact on the film with a well-defined area. The capacitance of the layer is determined using low frequency (1 MHz) alternate-current measurements. The thickness has to be known to obtain the film's permittivity.

For implementation in microelectronics, also other dielectric properties are important (leakage current, dielectric breakdown), but these characteristics are beyond the scope of this work.

---

[103] N. Posseme, T. Chevolleau, T. David, M. Darnon, O. Louveau, and O. Joubert, *Mechanisms of porous dielectric film modification induced by reducing and oxidizing ash plasmas*, J. Vac. Sci. Technol.B **25,** 1928-1940 (2007).

[104] X. F. Hua, M. S. Kuo, G. S. Oehrlein, P. Lazzeri, E. Iacob, M. Anderle, C. K. Inoki, T. S. Kuan, P. Jiang, and W. L. Wu, *Damage of ultralow k materials during photoresist mask stripping process*, J. Vac. Sci. Technol. B **24,** 1238-1247 (2006).

[105] D. Shamiryan, M. R. Baklanov, S. Vanhaelemeersch, and K. Maex, *Comparative study of SiOCH low-k films with varied porosity interacting with etching and cleaning plasma*, J. Vac. Sci. Technol. B **20,** 1923-1928 (2002).

4.2.2. Mechanical properties

Good mechanical stability of the film is necessary for successful implementation of the material in the dual-damascene integration scheme. Particularly the patterned layer has to sustain the chemical-mechanical planarization (CMP). The **mechanical properties** (Young's elastic modulus and hardness) are measured by *nanoindentation* or *LSAW*. In the nanoindentation measurement, a defined tip is pressed to the unknown material with controlled force load while the displacement of the tip is measured. The elastic modulus is then determined from the load-displacement curve.

The laser-induced surface acoustic wave spectroscopy (LSAW) is based on the measurement of the dependency of the phase velocity on the frequency of the mechanic oscillations travelling along the surface of the material. Fitting the theoretical model to experimental results gives the mass density and the elastic modulus of the material.[106,107]

4.2.3. Porosity

The above mentioned macroscopic quantities of the porous dielectric are caused by its microstructure, primarily by its **porosity**. Several techniques are used to measure the porosity: positron annihilation lifetime spectroscopy, small angle x-ray scattering[87] and techniques based on pressure dependent adsorption.[108] The low temperature measurements of liquid nitrogen adsorption are popular outside the semiconductor industry, but for planar nano-porous thin films the fast and nondestructive *ellipsometric porosimetry* (EP) is the best option.[109]

All porosimetry data in this work were obtained using the EP-10 tool described in chapter 1 subsection 1.1.4. The method is based on the pressure dependence of capillary condensation. In a vacuum chamber, the film optical properties and thickness are continually measured in-situ by ellipsometry. The pressure of selected solvent vapors (typically toluene) is slowly raised up to an equilibrium pressure (P_0) for the free surface condensation at room temperature. For $P<P_0$, the toluene condenses inside the convex curvatures of the pores. Thus, the optical properties of the film are changed according to the effective media approximation and the absorbed volume fraction is detected by the ellipsometric

---

[106] D. Paehler, D. Schneider, M. Herben, *Nondestructive characterization of sub-surface damage in rotational ground silicon wafers by laser acoustics,* Microelectron. Eng **84,** 340-354 (2007).

[107] D. Schneider, S. Fruhauf, S. E. Schulz, T. Gessner, *The current limits of the laser-acoustic test method to characterize low-k films*, Microelectron. Eng **82,** 393-398 (2005).

[108] P. I. Ravikovitch and A. V. Neimark, *Density functional theory of adsorption in spherical cavities and pore size characterization of templated nanoporous silicas with cubic and three-dimensional hexagonal structures*, Langmuir **18,** 1550-1560 (2002).

[109] M. R. Baklanov and K. P. Mogilnikov, *Non-destructive characterisation of porous low-k dielectric films*, Microelectron. Eng **64,** 335-349 (2005).

measurement. For $P=P_0$ all open pores are filled and total open porosity can be obtained.[110,111]

The absorption pressure is related to the meniscus curvature, i.e., to the pore size (cylindrical shape is assumed) through the Kelvin equation

$$\frac{2}{r_k} = -\frac{RT}{\gamma V_L} \ln\left(\frac{P}{P_0}\right), \tag{4.1}$$

where r_k is Kelvin radius, γ and V_L are the surface tension and the molar volume of the absorptive and P_0 is the equilibrium pressure of a flat liquid surface, respectively. The dependencies of the absorbed volume on the toluene pressure (adsorption and desorption isotherms) are used to calculate the pore-size distribution (PSD). The Kelvin equation is no longer valid for very small pores with a diameter less than 2 nm. The more detailed Dubinin and Radushkevich theory[112] is used for calculations of the low pore-size distribution. The analysis software (porell.exe) for the in-situ ellipsometric data produced by the ellipsometric porosimeter was developed in Novosibirsk.[113] The imperfect match of the used theories typically result in an artificial ridge in the PSD around 1 nm of radius.

4.2.4. Hydrophobic properties

The k-value of water reaches 80 and therefore its presence in the porous material deteriorates the desired dielectric properties. The films must keep **hydrophobicity** after the UV-cure and also after the technological steps. Plasma induced hydrophilicity is referred to as plasma damage. The hydrophobicity can be measured as the water contact angle on the surface of the film, but important information about the volume hydrophilicity can be detected by EP using water as the absorptive, called *water based ellipsometric porosimetry* (WEP).

4.2.5. Optical properties

Optical properties of our films in the visible and UV range (up to 9 eV) have been determined using *spectroscopic ellipsometry*, employing the tools described in chapter 1 subsection 1.1.4.

4.2.6. Chemical composition

The presence of water – among other species – in the volume can be also detected by *Fourier-transform infrared spectroscopy* (FTIR) as signature

---

[110] M. R. Baklanov, K. P. Mogilnikov, V. G. Polovinkin and F. N. Dultsev, *Determination of pore size distribution in thin films by ellipsometric porosimetry*, Vac. Sci. Technol. B **18,** 1385-1391 (2000).

[111] K. P. Mogilnikov and M. R. Baklanov, *Determination of Young's Modulus of Porous Low-k Films by Ellipsometric Porosimetry,* Electrochem. Solid-State Lett. **5,** F29-F31 (2002).

[112] C. Nguyen, D. D. Do, *The Dubinin-Radushkevich equation and the underlying microscopic adsorption description*, Carbon **39,** 1327-1336 (2001).

[113] K. P. Mogilnikov, V. G. Polovinkin, F. N. Dultsev and M. R. Baklanov, *Calculation of pore size distribution in the ellipsometric porosimetry*, Material Research Society Symposium Proceedings **565,** 81-86 (2000).

of −OH vibrations. Mid-infrared FTIR is the most popular technique of low-*k* characterization, giving insight into the **chemical composition**. The infrared absorption of the in the range 400 – 4000 cm^{-1} was measured by a FTIR spectrophotometer Biorad QS2200 ME with 4 cm^{-1} spectral resolution. We present the measured data in the form of absorbance of the film, after subtraction of the absorbance of the substrate silicon.

To assess the changes of **composition** across the thickness of a low-*k* film (for example after plasma exposure), some samples were studied using *TOF SIMS* (time-of-flight secondary ion mass spectroscopy). This method uses accelerated ions for sputtering the surface of the material. The secondary ions are analyzed using mass spectroscopy. During long sputtering times deeper layers are uncovered and therefore a depth profile of the concentration can be revealed. The profile of density can also be detected using X-ray reflectivity (*XRR*).

4.3.   Properties of Alpha material

Most of the research presented in chapter 4 and chapter 5 was performed on materials Alpha. The materials are denoted as Alpha1 (higher porosity and *k*-value around 2.3) and Alpha2 (high modulus, lower porosity, and *k*~2.5).

In this section we focus on the optical properties of Alpha1 material, while some results on Alpha2 are presented for comparison.

The studied samples were prepared by PECVD mixing of the SiCOH matrix precursor (containing Si-O and Si-CH$_3$ bonds) and the sacrificial C$_x$H$_y$ precursor (porogen). The substrate was heated to 300 °C, the radio frequency power of the plasma source was 2050 W and the pressure in the chamber was 853 Pa. The flow rate of the matrix precursor to porogen precursor was set to 1:5 to obtain samples with a final target porosity of 33% and *k*-value of 2.3 (the ratio 2.6:1 for Alpha2 with the porosity around 25% and *k*=2.5). The typical as-deposited thickness of the samples was 220 nm. Along with hybrid low-*k* films, we prepared reference samples depositing either the porogen material itself or the SiCOH matrix without additional porogen. All samples were deposited and UV-cured on 300 mm low-doped Si substrates in an ASM Eagle 12® system.

The deposited low-*k* films were heated up to 430°C in nitrogen atmosphere (pressure 6000 Pa) and exposed to nearly monochromatic UV light with the wavelength of 172 nm from Xe excimer lamps. Under these conditions, the porogen decomposes with formation of volatile compounds and the pores are created. This process will be referred to as the UV-cure. The time of cure was varied from 10 seconds (to observe the early stages of the curing process) up to 1800 seconds (over-curing the material). Samples of uncured material were kept as a reference. An additional sample was exposed to a broadband (λ>200 nm) light source for a moderate curing time to assess the possible effect of the UV light source.

Table 4.1. Alpha low-*k* materials. The *k* and Young's modulus values are provided by manufacturer (measured at IMEC).

material	porosity	RI	k	E_{NI}(GPa)
Alpha2	26	1.36	2.5-2.55	~ 9
Alpha1	31	1.37	2.25-2.3	~ 4

In the curing chamber, several bulbs are located near the sample surface, resulting in a wide range of incident angles of curing light. This arrangement reduces the formation of interference fringes over the thickness of the material that would be expected for the case of strictly normal incidence. Good homogeneity through the thickness was validated with TOF-SIMS profiling of atomic composition.

4.3.1. Changes of optical properties during the UV-cure

The optical properties of low-*k* films have been determined by the variable angle spectroscopic ellipsometry in the range from 2 to 9 eV to characterize the process of porogen decomposition and removal during the UV-cure on a series of samples, UV-cured for various times. Additional samples have been prepared by the deposition and curing of the porogen film, without SiCOH matrix, and the matrix material itself, without porogen. The analysis of the optical response of the porous dielectric as a mixture of matrix material, porogen and voids, together with Fourier transform infrared analysis, allows sensitive detection of the volume of the porogen and indicates the existence of decomposed porogen residues inside the pores, even for a long curing time.

Table 4.2 summarizes properties of the discussed sample series. The dielectric constant *k* was measured using the mercury probe on identical samples deposited on doped wafers.

Table 4.2. Properties of UV-cured Alpha1 low-k samples.

Cure time (s)	k-value	Shrinkage (%)	E (GPa)	ρ(gcm^{-1})	Porosity (%)	RI @633nm
0	2.8	0	6.78	1.3	15	1.49
10	2.42	3.5				1.39
50	2.34	5.9	1.76	1.1	33	1.38
150	2.29	10.1				1.37
300	2.29	13.6	1.78	1.06	31	1.37
600	2.34	17.1				1.39
1800	2.49	23.2	4.2	1.15	26	1.42

The shrinkages were calculated from the ellipsometrically determined thicknesses before and after UV-cure for each sample. The initial thickness of the film was approximately 220 nm. The Young's modulus and density was measured by LSAWS. Open porosity was measured by the ellipsometric porosimetry as well as RI at 633 nm.[114]

FTIR

Basic information about the low-*k* composition is deduced from the FTIR by most of the researchers in the field. The mid-infrared absorbance spectra of UV-cured Alpha1 films were measured[100] on freshly deposited and cured samples. The ageing of the films will be discussed further in this section. The absorbance spectra (fig. 4.5) were treated by the baseline subtraction and simple renormalization; maximum absorbance is set to 1. The peak identification is based on publications of Grill[94] and Gates.[101]

The spectra of as deposited and cured films are dominated by the Si-O-Si network band around 1050 cm^{-1} with a pronounced shoulder related to the cage-like structure at 1140 cm^{-1}. The transition from the cage to network structure with increasing UV-curing time has been reported. The presence of Si-bonded methyl groups is observed as a sharp peak at 1275 cm^{-1}. Two highly correlated effects of the applied UV-cure can be observed in FTIR spectra of low-*k* samples: the reduction of Si-CH$_3$ peak, and the growth of Si-H vibrations at 890 and 2240 cm^{-1}. This mechanism is attributed to the Si-CH$_3$ scission by 7.2 eV photons and to the replacement by Si-H groups. The removal of hydrocarbon groups (CH$_x$) from the porogen can be observed as a reduction of the band around 2900 cm^{-1}. A small structure at 1600 cm^{-1} related to the C=C bond can be detected for uncured and cured samples, but the amplitude is very low and has been overlooked by most authors.

Figure 4.6 shows a detail of FTIR spectra pointing to the decrease of Si-CH$_3$ bonds at 1274 cm^{-1} (bending vibrations of MeSiO$_3$). A small shoulder is expected[99] at 1260 cm^{-1}, caused by presence of silicon atoms double-occupied by methyl groups (bending vibrations of Me$_2$SiO$_2$). Bending vibrations of the methyls bonded to silicon is observed at 1412 cm^{-1} (SiMe$_x$). The peak at 1457 cm^{-1} is attributed to the bending modes of CH$_2$ isolated from silicon (i.e., of the porogen). The structures around 800 cm^{-1} are related to Si-C bonds as well, but are excluded from further analysis because of the overlap of the peaks. The presence of Si-H groups manifests itself as sharp peak at 890 cm^{-1} (bending vibrations of H-Si-O), and as the flat double-peak structure around 2232 cm^{-1} (stretching vibrations of H-SiO$_3$).

A detailed view of the porogen peaks around 2900 cm^{-1} is presented in fig. 4.7. We identified three peaks and one broad background band, but a more precise fitting suggests the presence of several overlapped vibrations caused by the stretching of C-H$_2$ and C-H$_3$ bonds. The highest peak at 2968 cm^{-1} is attributed to CH$_3$ and shows also response of the Si-bonded methyls. For that reason, this peak remains present for long

---

[114] The PUV SE measurements are less sensitive at 2 eV; the 633 nm (1.96 eV) is actually outside the measurement range of PUV SE.
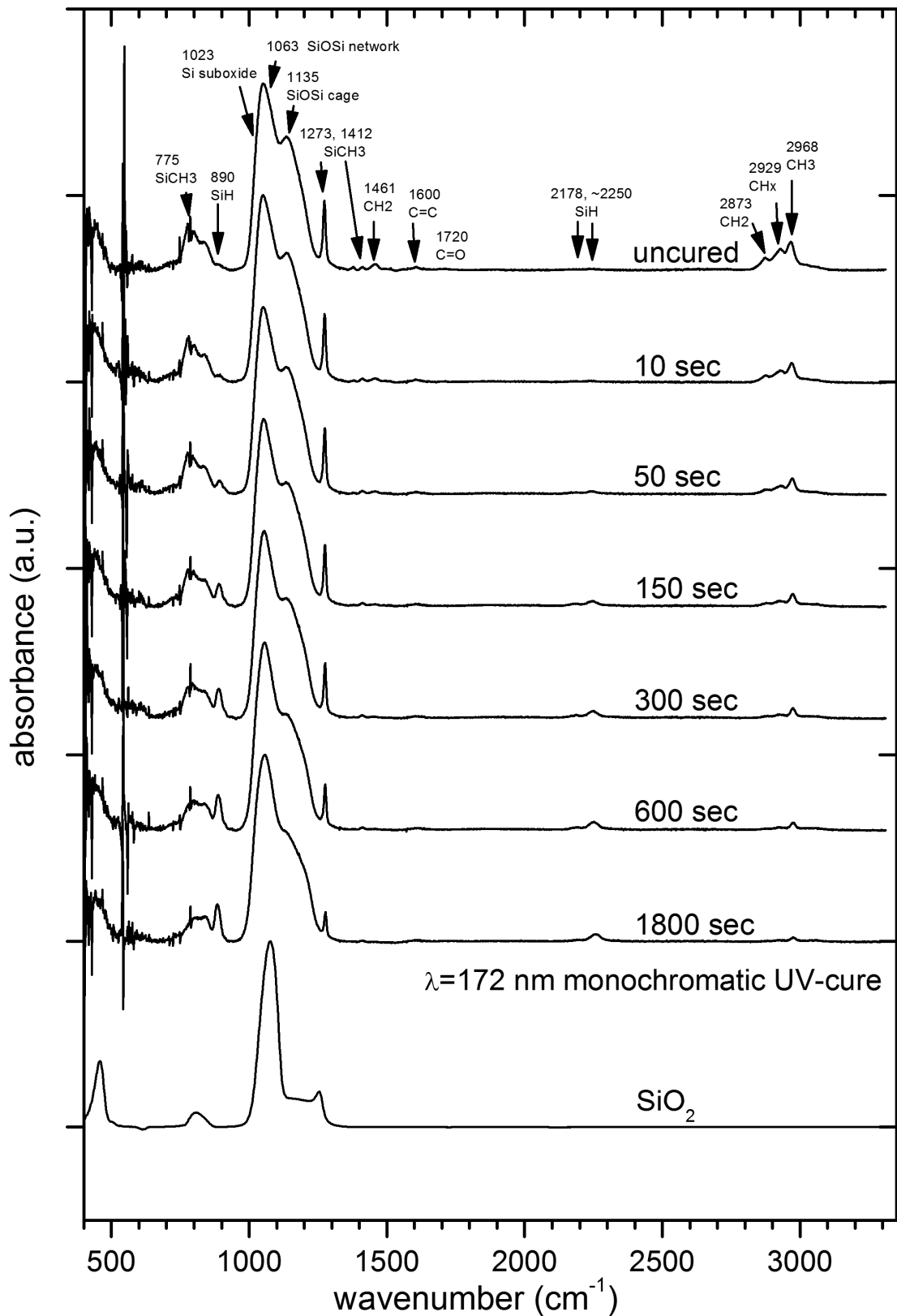
**Figure 4.5. FTIR spectra of Alpha1 cured by monochromatic (λ=172 nm) UV lamp. Reference thermal oxide on silicon is added for comparison.**
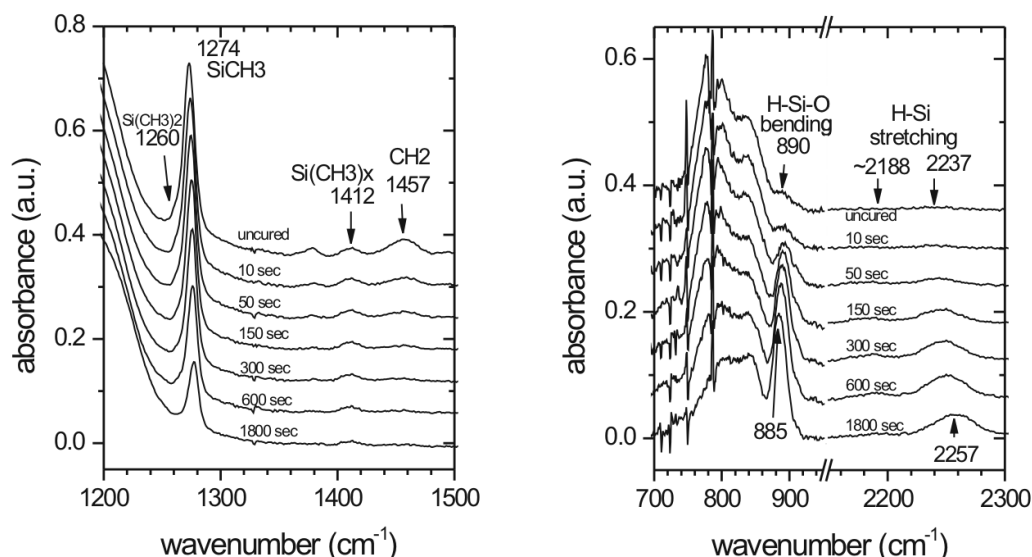
Figure 4.6. Detailed view of Si-CH₃ (left) and Si-H (right) vibrations of UV-cured low-*k* films.
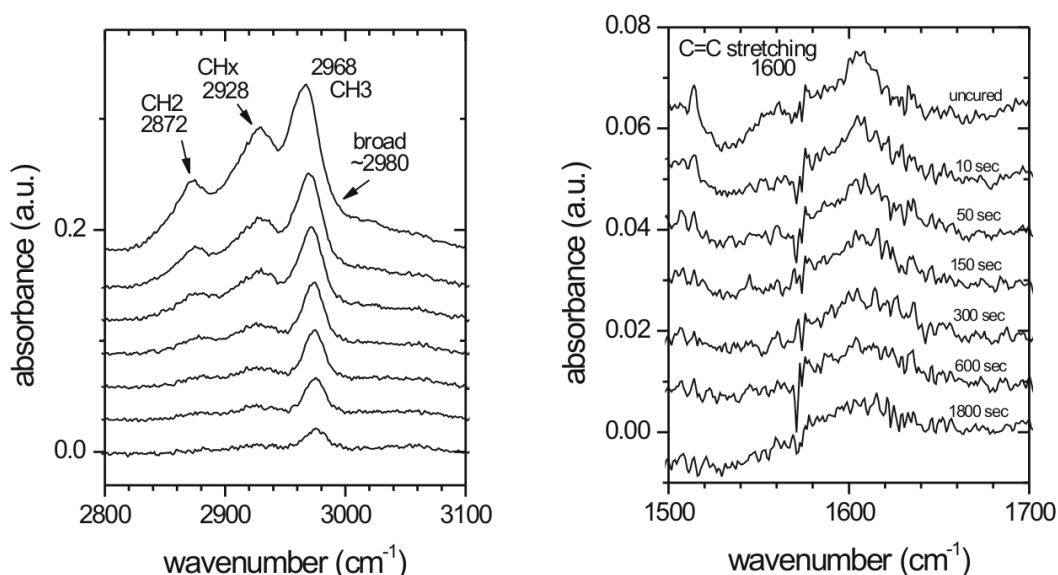

Figure 4.7. Detailed view of porogen CHₓ removal during UV-cure of low-*k* films. The C=C band at 1600 cm⁻¹ remains unchanged during the cure.

curing times and the removal follows a different trend compared to the rest of the peaks in the porogen band (see fig. 4.8). Traces of stretching vibrations of C=C at 1600 cm^{-1} are present in all samples. This fact is generally overlooked due to small amplitude of the peak (~1% of the Si-O-Si peak).

Figure 4.8 reviews the porogen band fitted by 4 Gaussian peaks and shows the evolution of the peak area during the UV-cure. About a half of the band area is assigned to the broad background band, but this assignment is only phenomenological. The different behavior of the "peak 1" (at 2968 cm^{-1}) is caused by the fact that it is related to the response of Si-bonded methyls as well as methyls present in the porogen.
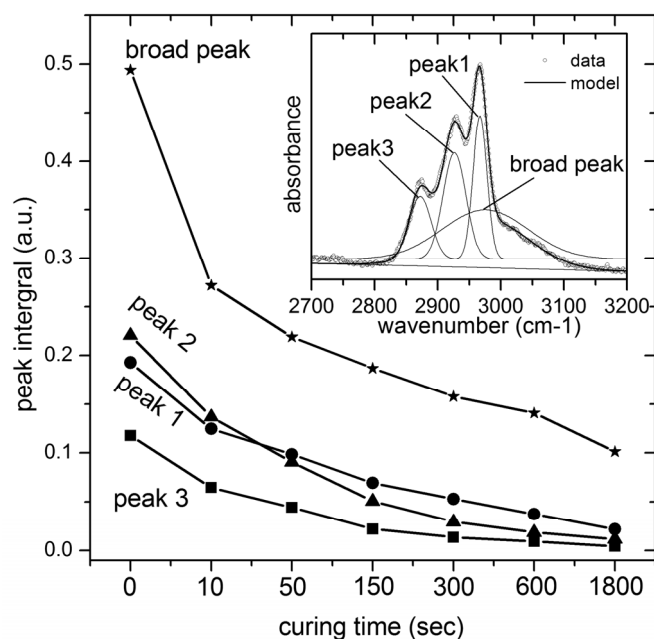
Figure 4.8. Results of peak fitting of the porogen CH$_x$ band of low-*k* films.

Ellipsometric porosimetry

EP measurements on four selected samples from the studied series were performed to explore the pore structure and porosity. During the absorption and desorption cycle, the RI and thickness is continuously measured by ellipsometry. Figure 4.9 shows the evolution of the thicknesses. The initial contraction of the samples (except for the uncured one) is caused by the effect of the attractive forces of the toluene molecules in the micropores.[111,115] The secondary increase of the thickness takes place when (almost) all the pores are filled and the film swells. The hysteresis visible in the behavior of uncured sample can be explained by the presence of cavities and bottleneck structure of the pores.

Figure 4.10 shows the evolution of refractive index at 633 nm of the films. The initial value is measured in vacuum and the increase is related to pore-filling by absorbed liquid toluene. As described in previous section, the RI increase can be recalculated to the actual volume ratio of the filled open pores. The resulting RI at the equilibrium pressure provides the open porosity percentage as presented in Table 4.2.

The pore size distributions (PSDs) of the samples are presented in fig. 4.11. The ridge around 1 nm of radius is artificial and is caused by an imperfect match of the theories used for micropores (under 1 nm) and meso/macro pores (above 1 nm). The pronounced mismatch between the absorption and desorption PSD in the case of uncured sample is the result of the hysteresis of the absorption and desorption isotherms as discussed above.

---

[115] P. I. Ravikovitch and A. V. Neimark, *Density Functional Theory Model of Adsorption Deformation,* Langmuir, **22,** 10864-10868 (2006).
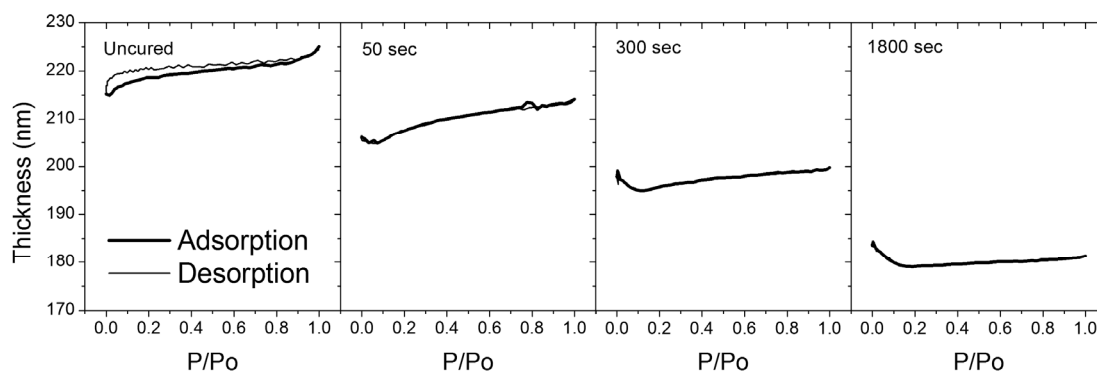
Figure 4.9. Thickness evolution of the low-*k* films during the absorption and desorption of the toluene.
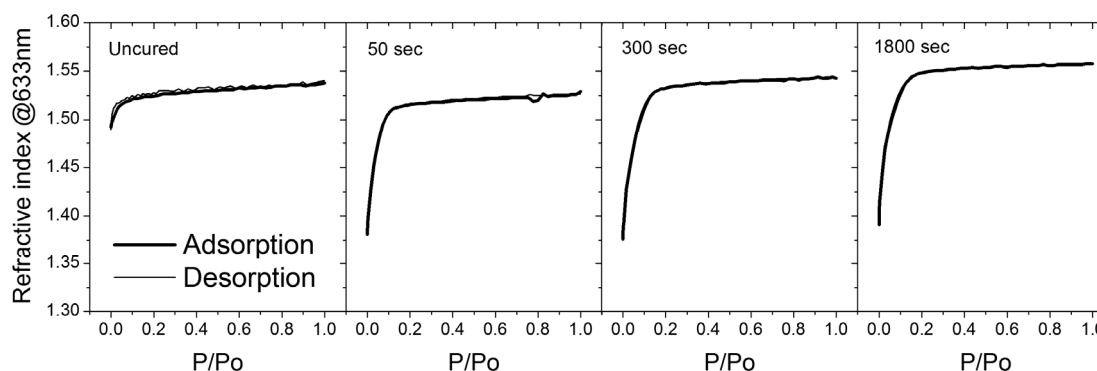

Figure 4.10. RI evolution of the low-*k* films during the absorption and desorption of the toluene.
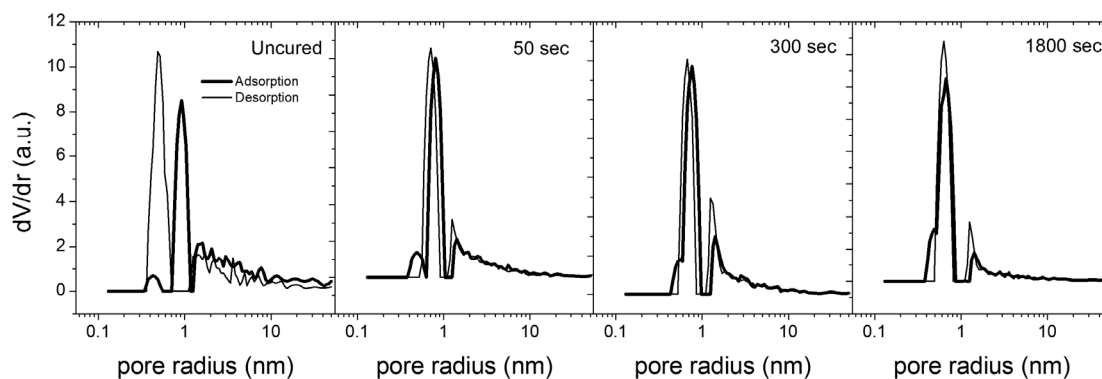

Figure 4.11. Pore size distributions of the low-*k* films.

Spectroscopic ellipsometry

The optical properties of the UV-cured samples were measured using Sopra PUVSE. For all of the samples, we have measured at three angles of incidence: 60, 70 and 80 degrees. The measured spectra of the ellipsometric angles Ψ and Δ were fitted by a single layer optical model (substrate – layer – ambient) using the Marquardt-Levenberg algorithm. The dielectric function ε of the low-*k* film was modeled by generalized
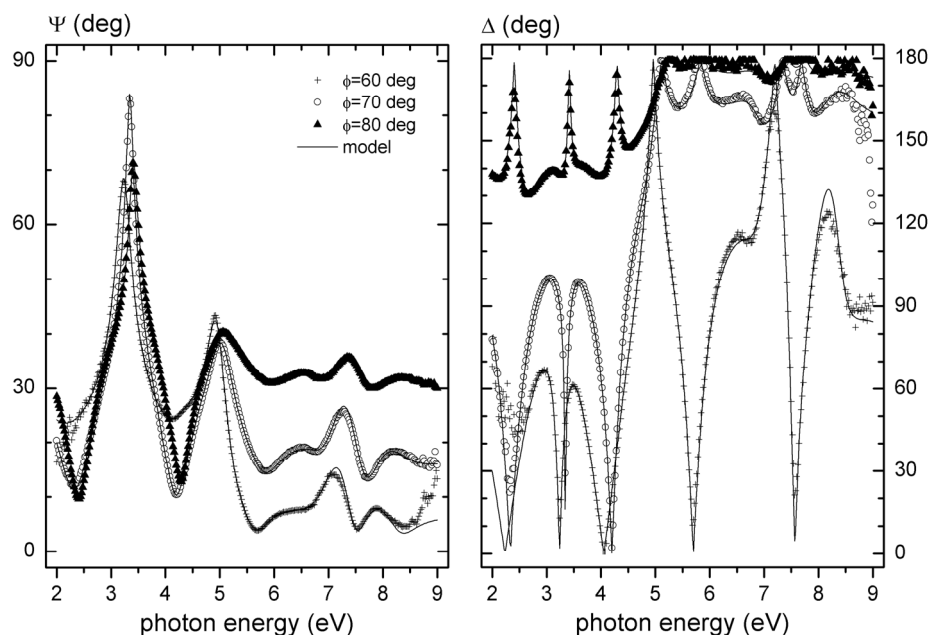
Figure 4.12. Spectro-ellipsometric data of a 227 nm thick uncured low-*k* dielectric film. The symbols represent the measured angles Ψ, Δ for three angles of incidence (crosses – 60 deg, circles – 70 deg, triangles – 80 deg). The solid line represents the fitted model.

Gauss-Lorentz (G-L) peaks, calculated using rational approximations.[116] We have observed that the fitted G-L profiles tended either to Gaussian or Lorentzian shapes and therefore we simplified the model by fixing some of the peaks as Gaussians and the remaining as Lorentzians (thus limiting the number of parameters), while keeping a very good quality of the fit.

Figure 4.12 shows the measured spectra at three angles of incidence for the uncured low-*k* sample with the thickness of 227 nm. The pronounced interference structure due to multiple reflections on the interfaces proves the film's transparency in the whole measured range. The amplitude of the interference oscillations is damped in the region of higher absorption of the film around 6.5 eV and above 8 eV. The information in the data above 8.5 eV is limited due to the low intensity of detected light.

The measured spectra are modeled using the propagation matrices approach (see chapter 1 section 1.2) in the substrate-film-ambient system. Although some inhomogeneity might be expected in the film thickness due to the depth-dependent effect of the UV-cure caused by the absorption and interference, the data are fitted well with the single layer model, only a small increase of the fitting error is observed for longer curing times.

We have modeled the ellipsometric spectra for all low-*k* samples using seven peaks: a Gaussian band at 4.1 eV, three Lorentzians at 4.7 eV, 5.5 eV, 6.4 eV creating the pronounced peaks, Gaussian bands at 8.1 eV and 9.9 eV to model the absorption edge with a shoulder and one δ-shaped peak at 11 eV that represents the contribution of absorption bands above

[116] J. Humlicek, *Optimized computation of the Voigt and complex probability functions*, J. Quant. Spectrosc. Radiat. Transfer **27,** 437-444 (1982).
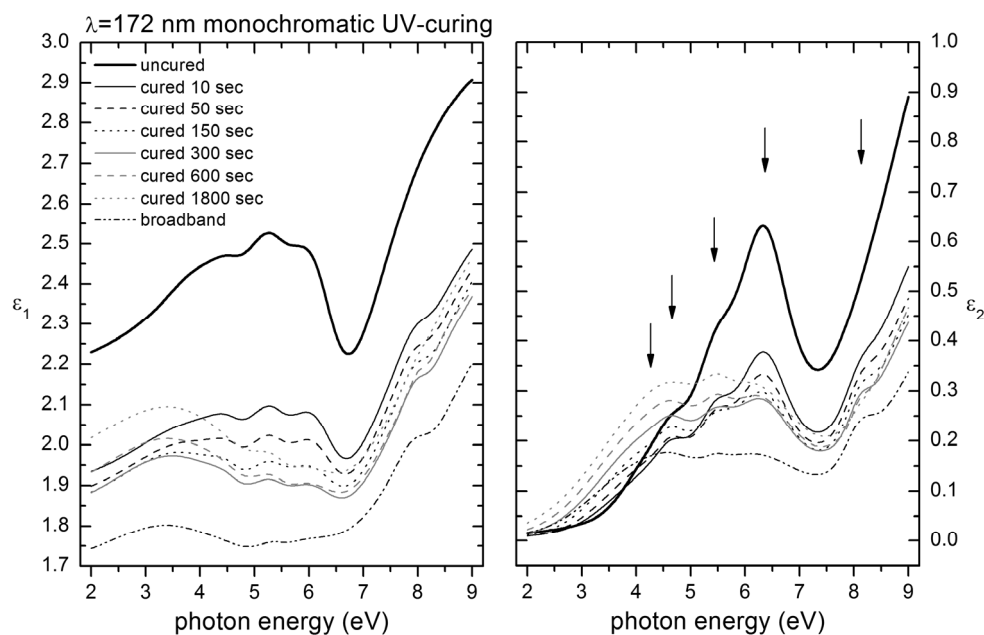
Figure 4.13. Dielectric functions of uncured (solid thick black line) and UV-cured low-k dielectric films. The optical function of the sample cured by a broadband lamp is plotted for comparison (dash dot dot line). The arrows show the positions of the G-L peaks.

the measured range to the dispersion of the real part of the dielectric function. The dielectric functions are plotted in fig. 4.13 and the positions of the model peaks are marked by arrows in the graph.

The dominant absorption band observed between 3 eV and 7 eV must be attributed to the organic content of the low-*k* material, as the silicon dioxide itself is transparent in that range and possible defects and impurities of the silica reported in the literature[117] should provide a very low extinction, and can be detected only in transmission measurements on thick samples.

The absorption in the ultraviolet range is responsible for the behavior of the refractive index in the visible range. In fig. 4.14, we plot the evolution of the refractive index at the wavelength of 633 nm (RI), and the shrinkage of the samples during the UV-cure.

The time evolution of the spectra, and particularly of the RI at 633 nm, can be separated into two phases with a different characteristic behavior. In the first phase (between 0 and 150 seconds), the rapid removal of a significant volume of the porogen occurs, observed as the significant decrease of extinction at 6.4 eV and above. The 6.4 eV band was previously attributed to the porogen, because of the correlation with the removal of CH_x groups observed around 2900 cm^{-1} in the FTIR spectra. The overall decrease of refractive index is produced by the changes in the absorption above the measured energy range, which is related to the porogen removal and porosity generation. In the second phase, the residual porogen is transformed from the hydrocarbon structure to

---

[117] G. Pacchioni, L. Skuja, and D. L. Griscom (Eds.), *Defects in SiO2 and related dielectrics: Science and Technology*, Kluwer, Dordrecht (2000).
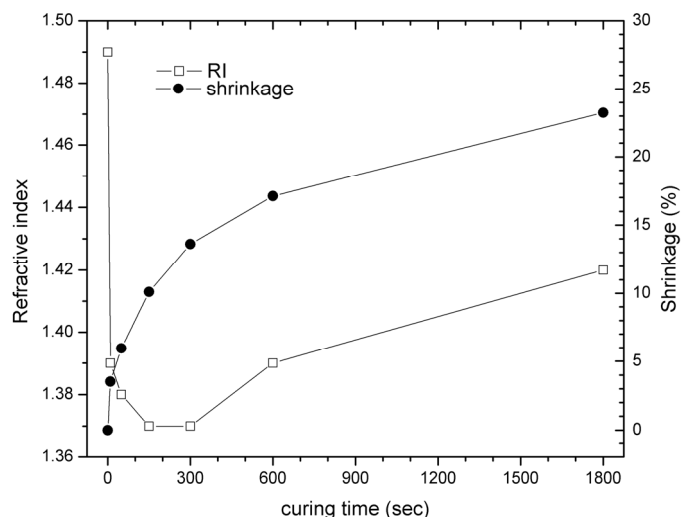
Figure 4.14. The thickness changes (solid circles) and refractive index at 633 nm (open squares) evolution of UV-cured low-k samples.

a structure similar to amorphous carbon, producing a characteristic band around 4 eV originating from the π-π* transitions of sp^2 bonded carbons.[118,119] The RI at 633 nm increases as a result of two influences: 1) the shrinkage densifies the material and 2) the growing absorption band of the residues increases the refractive index due to the well-known Kramers-Kronig relations. The FTIR and NMR porogen residue (C=C) absorption has been reported previously,[95,99,101] without any link to the optical properties.

In fig. 4.13, we plot also the spectra of an additional sample, cured by a broadband light source with λ>200 nm for a moderate time. The absorption of the porogen residue is much lower, showing the possibility to reduce the porogen residues by using a different curing technique. This result is also consistent with published work,[95] where a broadband curing light source had been used and the plotted refractive index evolution suggests that porogen is removed efficiently without creation of the residues. Our further investigations of different UV curing sources are presented in the next chapter.

To check the validity of the applied G-L model, we have performed point-by-point calculation of the dielectric function using the thickness of the film obtained from the G-L model. The comparison is plotted in fig. 4.15 for the case of uncured and 1800 sec cured samples.

The main features of the spectra are present in the parameterized model, but a few small structures can be observed in the point by point calculation.

---

[118] M. Gioti, S. Logothetidis, *Dielectric function, electronic properties and optical constants of amorphous carbon and carbon nitride films*, Diamond Relat. Mater. **12,** 957-962 (2003).

[119] S. Kassavetis, P. Patsalas, S. Logothetidis, J. Robertson, S. Kennou, *Dispersion relations and optical properties of amorphous carbons,* Diamond Relat. Mater. **16,** 1813-1822 (2007).
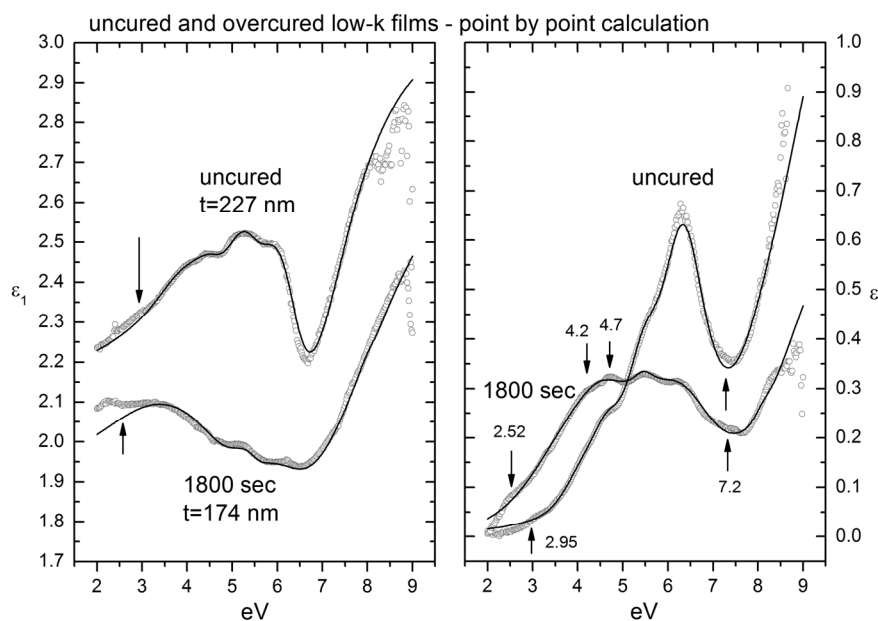
Figure 4.15. Point-by-point extraction of dielectric functions of uncured and overcured low-*k* films. The arrows point to additional features not contained in the G-L model.

A shoulder at 7.2 eV is observed for both uncured and cured samples. For the uncured sample, a small peak at 2.95 eV is present and a similar structure is visible at 2.52 eV on the cured sample. The distinction between the broad peak at 4.2 eV and the sharp tip at 4.7 eV for the cured sample is clearer in the point-by-point data.

4.3.2. Additional series

To complement the knowledge of the optical properties of the low-*k* dielectrics and their evolution during the UV-cure, we present here also results from supporting experiments.

Alpha2 curing

In fig. 4.16 we plot the dielectric functions of UV-cured low-*k* material Alpha2, similar to Alpha1, deposited with a lower porogen precursor ratio.

Table 4.3. Overview of Alpha2 samples cured by monochromatic lamp (λ=172 nm).

| Cure time (s)	thickness (nm)
0	218
13	217
40	208
80	202
160	197
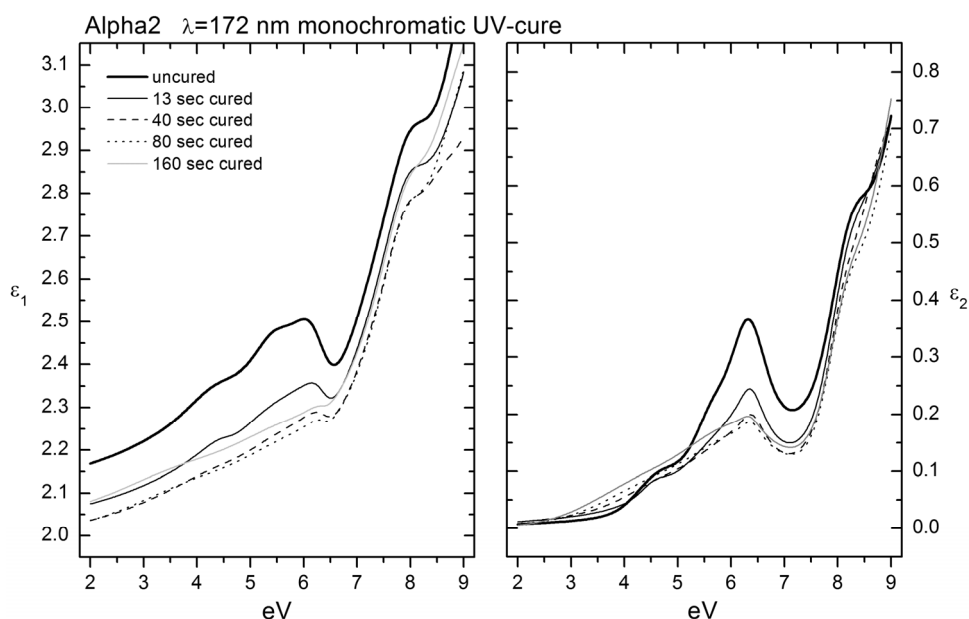
Figure 4.16. Dielectric functions of uncured (solid thick black line) and UV-cured low-*k* dielectric films.

The series was cured by monochromatic lamp (λ=172 nm) up to 160 sec. The lower porogen content leads to a lower absorption peak at 6.4 eV, compared with Alpha1 discussed above. The material has a lower porosity and therefore better mechanical properties. No porosity or FTIR measurements were performed on the series. Due to deposition recipe evolution, these samples are somewhat different from the ones presented in the next chapter.[120]

Alpha1 broadband curing

We have prepared a series of Alpha1 samples cured by the broadband lamp providing softer UV light with photon energies below 6 eV.

Table 4.4. Overview of Alpha1 samples cured by the broadband lamp (λ>200 nm).

cure time (T)	thickness (nm)
0	206
0.2	194
0.5	185
1	190
2	183
5	172

---

[120] The present series of samples was collected at the beginning of 2007, next chapter describes samples prepared in September 2007.
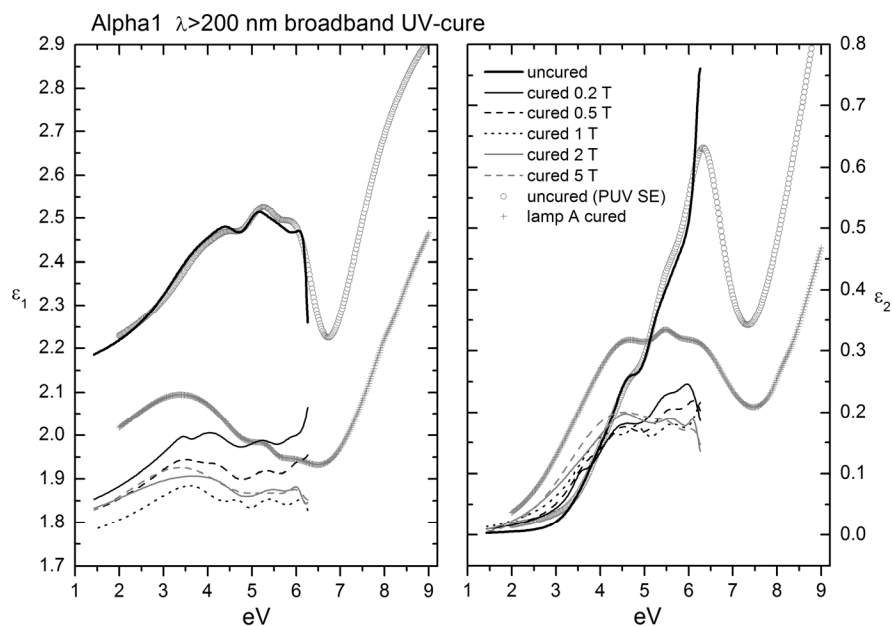
**Figure 4.17. Dielectric functions of uncured film (solid thick black line) and films UV-cured with broadband (λ>200 nm) lamps. The symbols represent the reference measurements on the uncured sample (circles) and the monochromatic lamp UV-cured (1800 sec) sample (crosses).**

The curing times were distributed close to the optimum (the lowest RI and k-value) curing time denoted as T. These samples were measured by spectroscopic ellipsometry in the range from 1.4 to 6.2 eV on the Gaertner ellipsometer (see paragraph 1.1.4). Figure 4.17 shows the G-L model fitted to the measured data. We have also plotted previous measurements (Sopra PUV SE) performed on the series cured by monochromatic lamp. The measurements on uncured samples match well (the accuracy of the Gaertner measurements above 6 eV is decreasing). In comparison with the sample overcured by the monochromatic lamp, the new samples exhibit a much lower absorption in the UV range related to the porogen and residues. The broadband UV lamp probably performs better in terms of the porogen removal efficiency.

Figure 4.18 shows FTIR measurements on the series of broadband cured samples. The porogen removal is related to the reduction of CH_x band around 2900 cm^{-1}. A decrease of the C=C band 1600 cm^{-1} is present (though not visible on the graphs). Only a small reduction of $Si-CH_3$ bond (1275 cm^{-1}) and the generation of Si-H (890 cm^{-1} and 2200 cm^{-1}) is observed. The photon energies of the broadband lamp are evidently not sufficient to break the $Si-CH_3$ bond. Also, no significant transition between the cage (1135 cm^{-1}) and network (1063 cm^{-1}) structure of the Si-O-Si is present.

We have studied comprehensively the impact of the UV-curing lamp on the low-k material properties. The results of this study are presented in the next chapter.
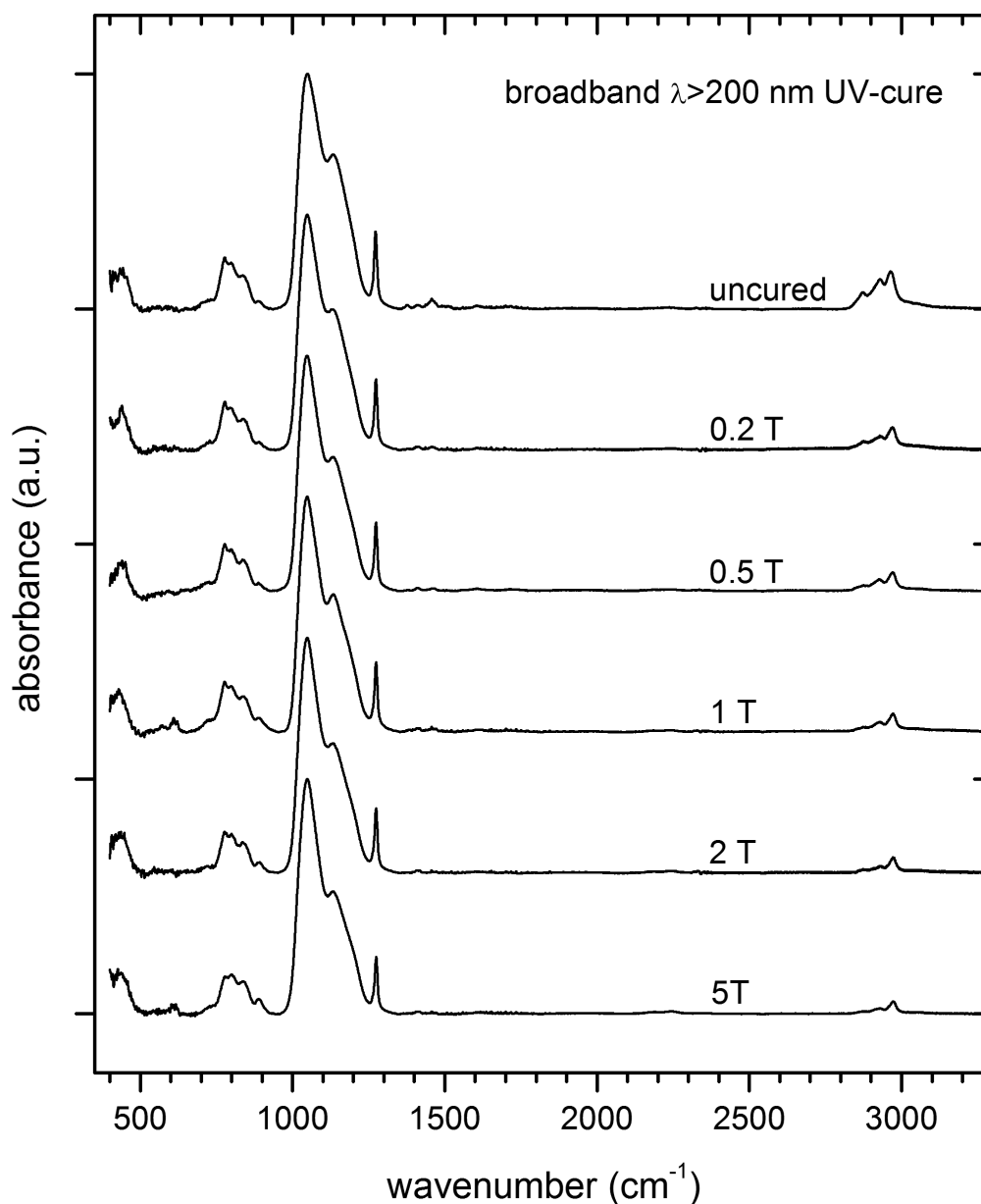
Figure 4.18. FTIR spectra of Alpha1 cured by the broadband (λ>200 nm) UV lamp.

4.3.3. Porogen and matrix properties

In order to complement the knowledge of the evolution of optical properties of the hybrid low-*k* film, we have prepared samples of the constituents: the porogen film and the film of SiCOH matrix without pores. The samples were studied in the same manner as the low-*k* films.

Porogen

The porogen was deposited as a dense (non-porous) layer with the thickness of about 140 nm. The layer is very soft, has a low adhesion to the surface and can be easily removed mechanically. We have applied the UV-cure with the variable time on the porogen samples, and observed a rapid decrease of the thickness, but no complete removal of the material
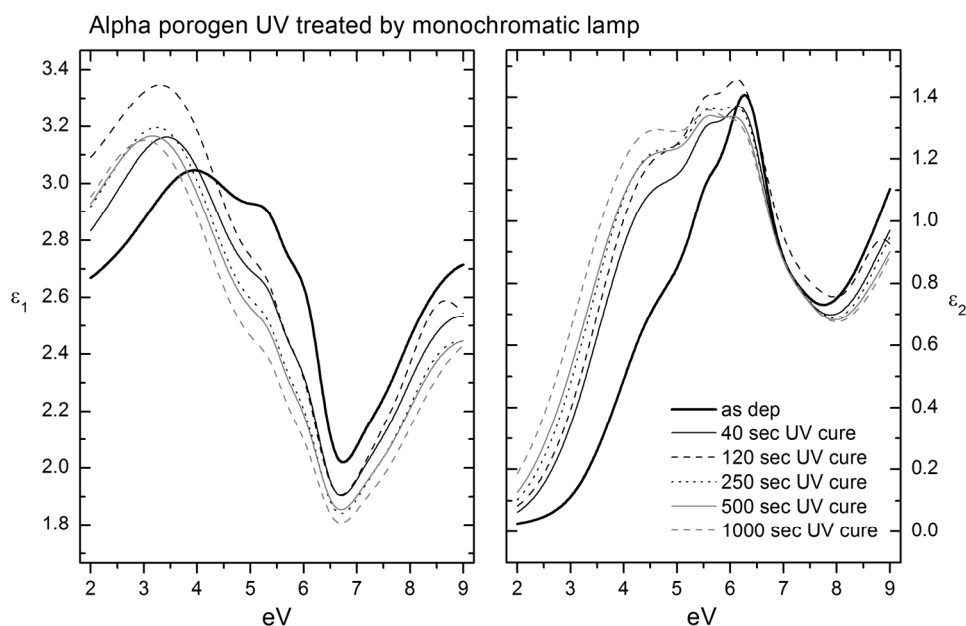
Figure 4.19. Dielectric functions of uncured (solid thick black line) and UV treated porogen of material Alpha.

up to the longest curing times. One sample was left uncured, as a reference.

Table 4.5 lists the studied porogen-only samples. The series of samples was not prepared at once, but in three separate runs. This may explain the differences in the initial thickness and also in the evolution of the optical properties. The initial thicknesses were measured after the deposition using the process-line ellipsometer KLA Tencor F5. The thicknesses after the cure were obtained from the fitting of the data measured with Sopra PUV SE. The first set contained the uncured and 40 sec cured samples. The second set contained the 120, 250 and 500 sec cured samples. Finally the 1000 sec cured sample was prepared.

Table 4.5. Overview of porogen-only samples.

| Cure time (s)	init. thickness (nm)	cured thickness (nm)	relative thickness
0	119.6	119.6	1.00
40	119.6	47.8	0.40
120	153.9	53.3	0.35
250	153.9	48.2	0.31
500	152.5	44.3	0.29
1000	166.7	40.2	0.24
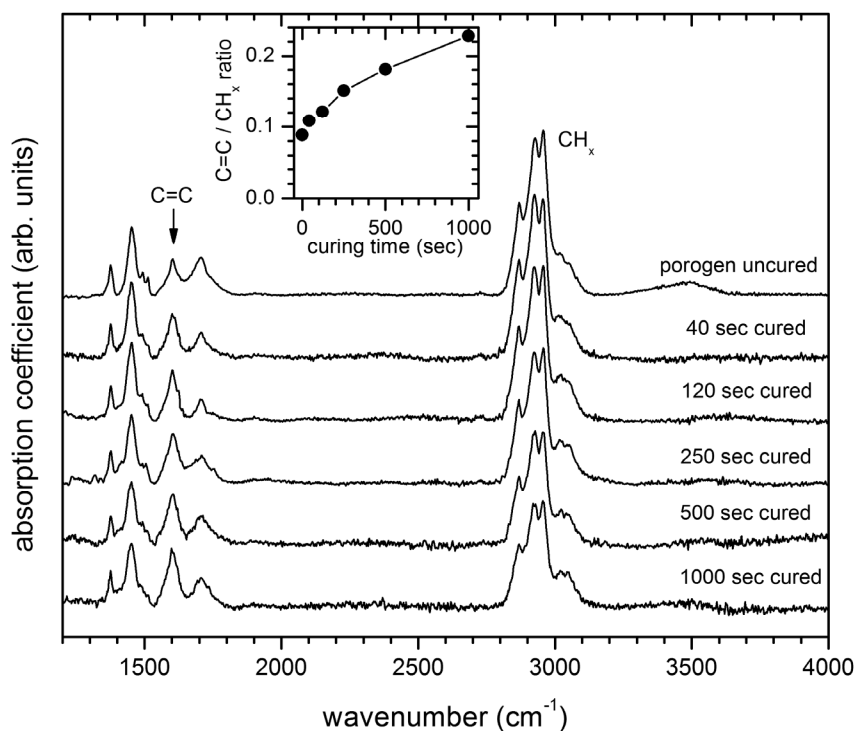
Figure 4.20. FTIR spectra of the porogen films treated by monochromatic UV lamps. The absorbances were normalized to a common thickness.

Figure 4.19 shows the optical functions of the porogen films. The porogen material manifests similar features as observed in the hybrid low-*k* film. During the UV-cure of porogen layers, most of the volume was removed in the early stages (60 % in 40 sec) and optical properties changed: we have observed a growth of the absorption band at 4.5 eV and related changes of the real part of dielectric function. We did not reach a complete removal of the layer: after 1000 sec of UV-cure, we still detect ~25% of the initial thickness.

The ellipsometric porosimetry with toluene exhibited a rather unusual behavior: the samples were swelling, while the refractive index stayed constant or decreased during the toluene adsorption. We attribute this behavior to the toluene (RI=1.49) intrusion into the initially dense packed porogen mass (RI=1.63), enabled by the extremely poor mechanical stability of the film.

Figure 4.20 shows the spectra of the infrared absorption coefficient of the porogen layers at various curing times. The spectra have been normalized to a common thickness to enable a better visibility of the compositional changes. The relative weight of the C=C absorption at 1600 cm^{-1} increases during the UV-cure (see the inset). Although the exact mechanism of the porogen decomposition is not described here, we assume that the UV radiation is breaking the C-H or C-C bonds, causing a partial removal of the carbon-containing groups, but some of the radicals are rearranged, creating carbon double bonds, and forming an amorphous carbon residue.
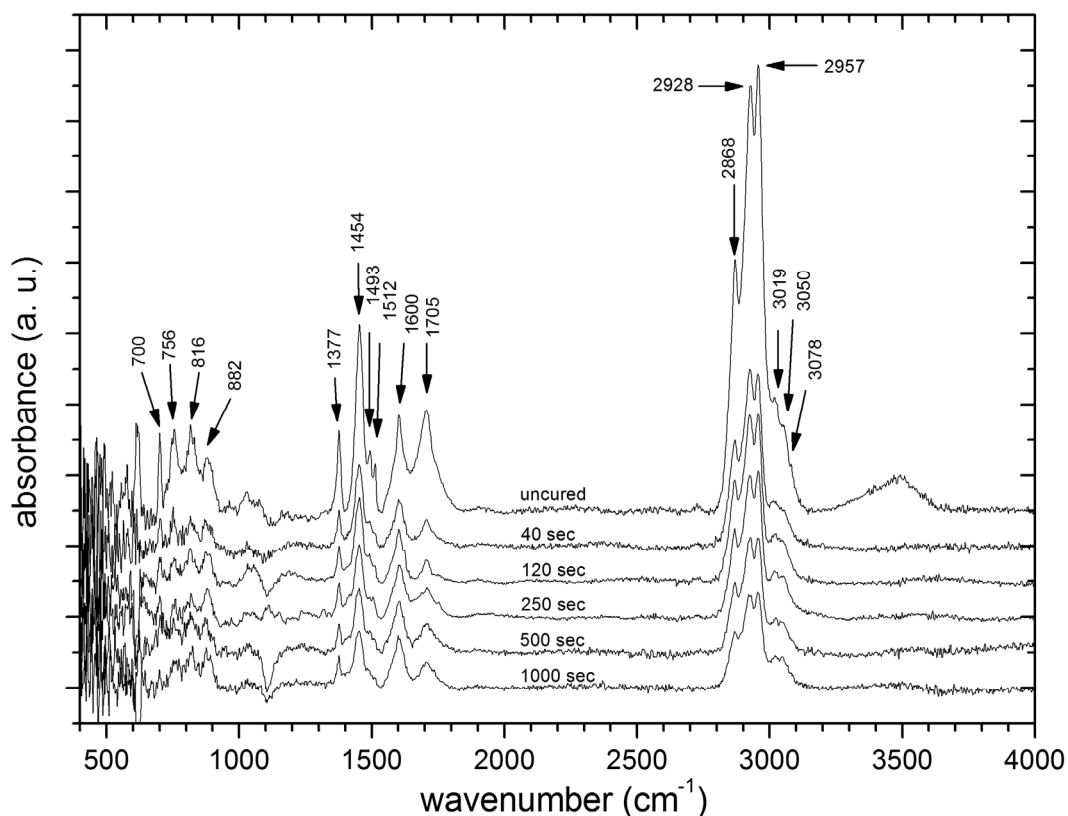
Figure 4.21. FTIR absorbances of the porogen films treated by monochromatic UV lamps.

The measured absorbances of the porogen films are plotted again in fig. 4.21 without the normalization. We observe that most of the material is removed in early stages of the UV exposure – the amplitude of the CH_x band around 2900 cm^{-1} and of the C=C peak at 1600 cm^{-1} is reduced significantly during the first 40 seconds. While the CH_x continues to decrease during the next stages of the UV exposure, the C=C peaks remain more or less constant. However, it is necessary to mention that the initial thicknesses were different (see Table 4.5) and therefore the direct comparison is hindered.

Table 4.6. Overview of the SiCOH matrix samples.

| Cure time (s)	thickness (nm)
0	74.8
120	58.3
250	68.7
500	56.3
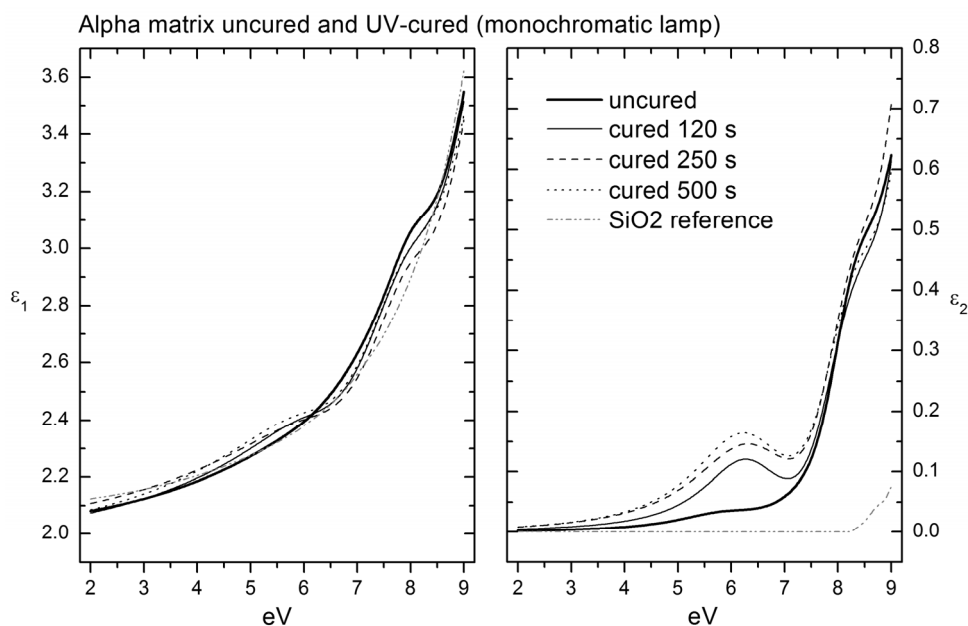
Figure 4.22. Dielectric functions of uncured (solid thick black line) and UV treated matrix of Alpha. Thermal oxide is drawn for comparison.

Matrix

The matrix SiCOH material was deposited as approximately 75 nm thick layers with no porosity. Table 4.6 shows the samples, prepared in two runs: the uncured and 250 sec cured samples first, and then the 250 sec and 500 sec cured samples. The initial thickness was not measured on the second set and was probably lower than 75 nm.

The matrix material shows the dispersion (see fig. 4.22) similar to silicon dioxide with slightly lower values of the refractive index (RI=1.45 compared to 1.46 of SiO_2). The material is highly transparent in the visible and ultraviolet range with a low and broad absorption band around 5.5 eV and a shoulder at 8.5 eV at the absorption edge. We also applied UV-cures to the matrix material and observed some shrinkage (10% after 250 sec of UV-cure) and a minor increase in absorption at 6 eV.

The FTIR analysis (fig. 4.23) of the cured matrix samples revealed a significant Si-CH_3 bond reduction, but no increase of Si-H. Consequently, the mechanism of the UV-cure of the matrix itself is different than that of the mixture with the porogen. In the as-deposited matrix material, we observe also some traces of CH_x, and their removal during the cure. The matrix material exhibits the dominant absorption of network-bonded Si-O-Si (the peak at 1050 cm^{-1}). An increase of the hydrophilicity of the UV-exposed matrix can be seen as the increase of the FTIR absorption related to the OH groups at 3300 to 3700 cm^{-1}.

We assume the possibility of creation of amorphous carbon clusters in the UV-treated matrix material from the carbon originally bonded to the skeleton. This process would be similar to the porogen residue creation in the hybrid material, where the carbon residues might be originating both from the porogen and from the matrix material. This hypothesis can also explain the different evolution of the spectra of porogen and hybrid films
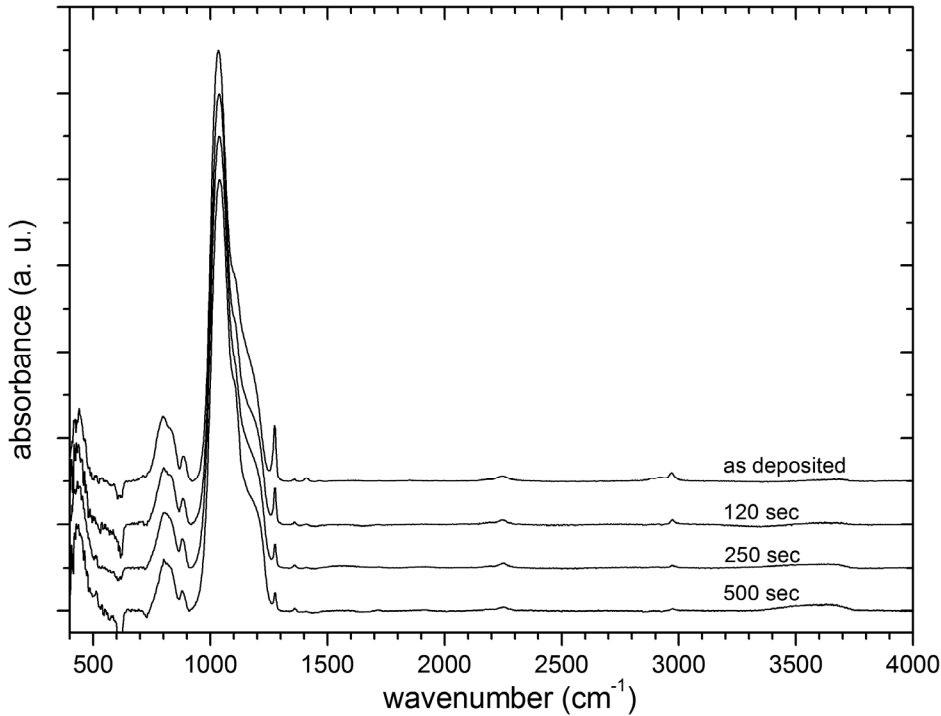
Figure 4.23. FTIR absorbances of the SiCOH matrix films treated by the monochromatic UV lamp.

around 4.5 eV. However, no measurable C=C signature was observed in the FTIR spectra of the UV-treated matrix material.

The ellipsometric porosimetry detected no porosity in the matrix films.

FTIR Mixing

Figure 4.24 shows FTIR spectra of the matrix, porogen and the uncured and cured (300 sec) low-*k* films. The spectra of the low-*k* hybrid film have been discussed in detail above. In the spectra of the SiCOH matrix itself we observe a strong peak at 1035 cm^{-1} related to the Si-O-Si network structure, shifted by the presence of silicon sub-oxide, the Si-CH$_3$ vibration at 1275 cm^{-1}, Si-H bonds at 890 and 2240 cm^{-1} and C-H vibrations in the hydrocarbon (CH$_x$) band at 2900 cm^{-1}. The spectrum of as deposited porogen contains structures related to hydrocarbons at 1460 and 2900 cm^{-1}, carbonyl (C=O) stretching at 1705 cm^{-1} and aromatic or amorphous C=C sp^2 bonds at 1600 cm^{-1}.

Although the plasma conditions have been slightly different during the deposition of porogen, matrix and the low-*k* film, the FTIR spectra of the hybrid film can be modeled as a simple combination of the spectra of the constituents (the features of the porogen: C=C, C=O, CH$_x$ are present in the as-deposited low-*k* sample), apart from 3 important differences: 1) The matrix film shows a dominant Si-O-Si network peak, while the hybrid contains also the cage-arranged bonds. 2) The matrix films contain a relatively high amount of the Si-H bonds compared to the as-deposited hybrid. 3) The hybrid film contains more Si-CH$_3$ bonds than inherited directly from the matrix. We assume that the porogen precursor can donate the CH$_3$ groups and allowing incorporation into the matrix
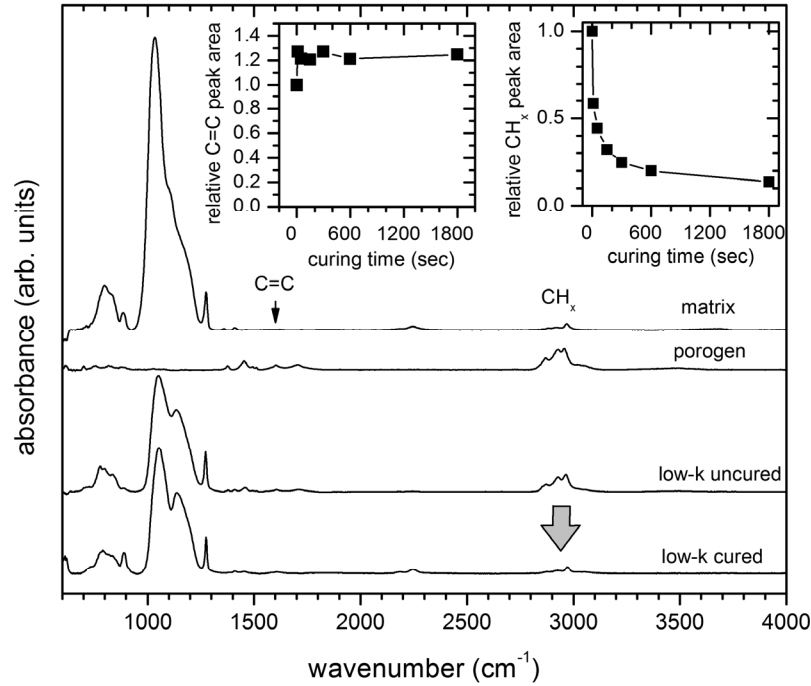
Figure 4.24. Infrared absorbance of studied films: matrix material, porogen film, as deposited low-*k* and cured low-*k*. The inset graphs show: left) the evolution of the peak area at 1600 cm^{-1} attributed to C=C and right) the peak area around 2900 cm^{-1} attributed to the removal of CH$_x$ from the low-*k* material.

structure via the initial Si-H sites. The resulting structure is distorted due to the presence of larger methyl groups.

Point-by-point calculation

We have performed a point-by-point calculation of the dielectric functions of selected samples to check the consistency of the G-L model. Figure 4.25 shows the results for uncured matrix, uncured porogen and overcured porogen films. In the case of the porogen, an additional structure is observed at 3.3 eV and the band at 4.5 eV exhibits two peaks: at 4.18 and 4.56 eV (similarly to the case of hybrid films). The broad absorption of matrix films around 6 eV becomes pronounced as a small peak at 4.66 eV, followed by a plateau with an additional shoulder at 7.06 eV.

4.3.4. Mixing model

The measured spectra of the low-*k* dielectrics can be simulated in the visible and UV range as a response of effective media, using the measured optical properties of the matrix material and the porogen UV-cured for various times. The Bruggeman effective media (BEMA) dielectric function ε is given by the following equation,

$$v_a \frac{\varepsilon_a - \varepsilon}{\varepsilon_a + 2\varepsilon} + v_m \frac{\varepsilon_m - \varepsilon}{\varepsilon_m + 2\varepsilon} + v_p \frac{\varepsilon_p - \varepsilon}{\varepsilon_p + 2\varepsilon} = 0, \tag{4.2}$$

where v_a, v_m, v_p are the volume fractions of air, matrix material and porogen, respectively, and ε_a, ε_m, ε_p their dielectric functions.
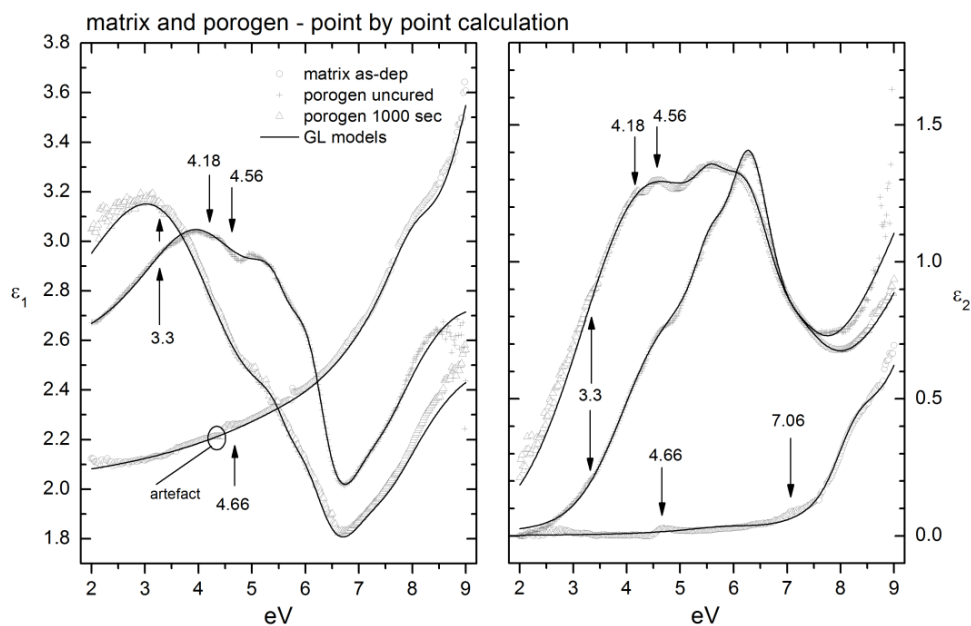
Figure 4.25. Point-by-point extraction of the dielectric functions of uncured and overcured porogen films and as-deposited matrix film. The arrows point to additional features not contained in the G-L model.

Using the value of the relative volume of voids, measured by ellipsometric porosimetry (open porosity), we have calculated the optical properties of the solid part (mixture of porogen and matrix) of the films. Then we have approximated the resulting spectra by the Bruggeman model, with the measured matrix (as deposited) and porogen (UV-cured for comparable time) optical properties. Matching the Bruggeman model with the data, the ratio of the solid constituents can be found (see fig. 4.26). The simultaneous match of both real and imaginary part of the dielectric function proves that no closed porosity is present.

The shape of the dielectric function modeled by the Bruggeman approximation does not match exactly the measured properties of the UV-cured low-*k* samples. In particular, the 4.5 eV band is more pronounced in

Table 4.7. The measured porosity, shrinkage and calculated matrix and porogen residue percentages for cured low-*k* films. The first sample is uncured. The next three samples were cured by the monochromatic light source for various times. The additional sample was cured with the broadband UV light source.

| Sample	Porosity (%)	Matrix (%)	Porogen residue (%)	Shrinkage (%)
Uncured	15	38	47	0
50 sec	33	40	27	6
300 sec	31	45	24	14
1800 sec	26	48	26	23
broadband	36	48	16	14
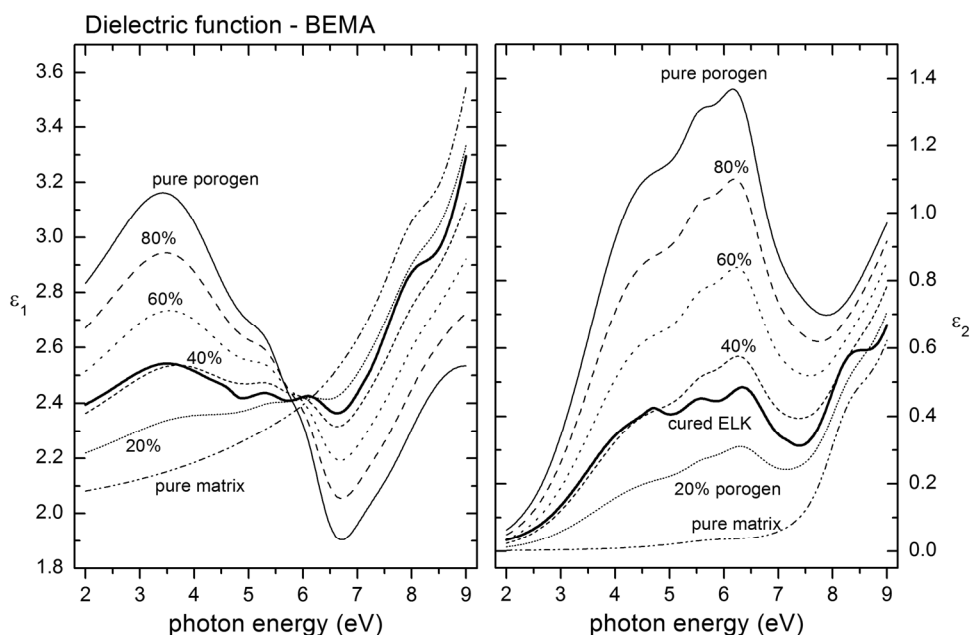
Figure 4.26. BEMA mixing of matrix and porogen. Thick solid line represents the solid part of cured Alpha1 film.

the measured spectra. The difference might be explained by an additional clustering of the carbon released from methyl groups originally bonded to the matrix. The hybrid material may also contain a porogen of a different chemical structure than in the porogen layer alone, due to different plasma chemistries. This difference may also enhance the decomposition of the porogen to the residues during the UV-cure of the hybrid film, compared to the porogen alone.

In Table 4.7 we present the estimated percentages of the constituents of selected films. The studied films are compared with one sample cured by broadband UV source. The evolution of the porosity is driven by a fast removal of the porogen during the early stages of the cure, and following pore collapse for the longer curing times. Maximum porosity is observed at 50 seconds of the cure, while the minimum of RI (1.37) and k-value (2.29) is reached between 250 and 300 seconds. This is a consequence of the fact that the values of RI and k of the porogen are much higher than the ones of the matrix. The growing percentage of the matrix with increasing curing time is related to the shrinkage of the film. If the percentages in the table were normalized to initial thickness, the normalized percentage of the matrix material would represent 38% (± 1%) of the initial volume for all samples cured by the monochromatic lamp (see fig. 4.27).

The shrinkage therefore occurs through the porogen and void volume reduction. The possible intrinsic shrinkage of the matrix material itself through the removal of CH_3 groups would be detectable, and a small decrease of the volume (normalized percentage) has been actually observed (~ 1%), but this value is below the sensitivity of the method (the estimated uncertainty is ± 3%).
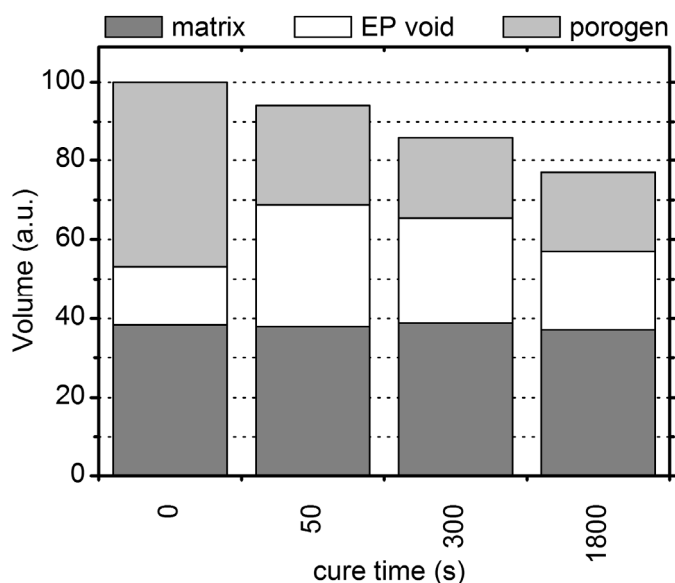
Figure 4.27. Volume composition of selected UV-cured low-*k* samples.

A possible deficiency of the proposed model should be pointed out. We were not successful in measuring the porosity of the porogen itself and assumed a dense material. However, some toluene can be absorbed by the material during the EP measurement. The porogen alone swells when exposed to the toluene vapors, and a similar behavior can occur inside the porous hybrid film. Consequently, the porosity might be overestimated, leading to a small overestimation of the dielectric function of the dense part of the mixture. That could result in a slight underestimation of the matrix content of the low-*k*. For example; if 25% porosity of the porogen itself was assumed, the matrix content of ~45% would result from the model in the case of the uncured sample.

The mixing approach has been validated by the porogen removal from the UV-cured low-*k* film using a He/H$_2$ high temperature plasma strip process (see subsection 4.4.4). In those experiments, a layer with porosity reaching 50% was created, without any shrinkage or Si-CH$_3$ depletion. The optical properties of the clean layer were identical with the (porous) matrix material.

Another verification can be attempted using the reverse calculation: if we assume the percentage of matrix material in uncured film to be 38%, and no changes of the matrix volume during the cure, the total porosity of the cured films can be extracted from the optical properties and known shrinkage. These calculations also result in values comparable with the experimental ones (measured by ellipsometric porosimetry) with a maximum difference of only 3%, i.e. within the experimental error.

The additional sample cured by the broadband (λ>200 nm) lamp shows a lower porogen residue percentage (with a comparable shrinkage). The changes of the deposition and curing conditions can lead to a different behavior of the hybrid film not only in the framework of the mixing model, but also might cause changes to the chemical and nano-pore network structure. Optimal conditions should be selected to support the porogen removal instead of the degradation in the pores' interior. The existence of
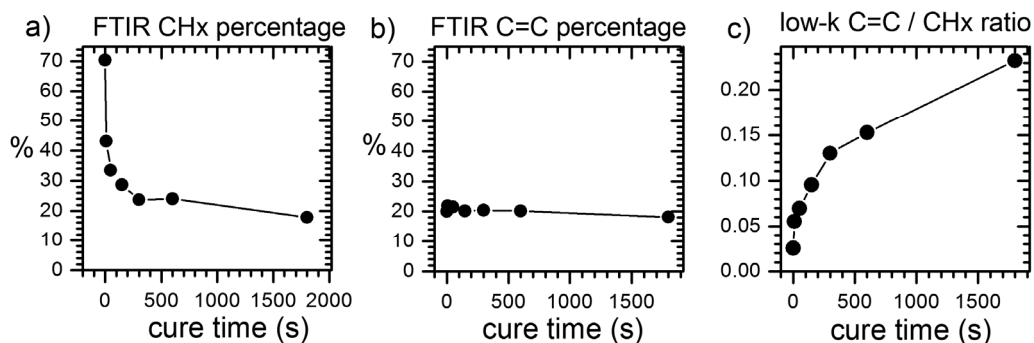
Figure 4.28. A rough estimation of the porogen content in low-*k* hybrid films from the FTIR absorption: a) calculated using CH$_x$ band b) calculated using C=C band c) the evolution of C=C and CH$_x$ ratio for low-*k* hybrid material.

porogen residues might have a negative influence on the material's mechanical[121] and dielectric[122] properties and the impact of the residues on the low-*k* integration should be examined.

4.3.5. Discussion: a comparison of FTIR and PUV SE

We have observed a reduction of the CH$_x$ traces in the FTIR spectra of UV cured (both monochromatic and broadband) low-*k* hybrid films. Apart from that, the presence of C=C structures is detected in the uncured and cured films. The broadband lamp causes a reduction of the C=C peak at 1600 cm^{-1}, while the monochromatic lamp does not affect the peak. It was shown by Urbanowicz[121] that a reduction of the C=C peak is possible using otherwise non-damaging plasma strip process (subsection 4.4.4).

In the PUV SE spectra of the low-*k* films, we observe the dominant peak at 6.4 eV in the uncured samples, which is almost identical to the as-deposited porogen. Moreover, the peak is substantially reduced during the UV-cure; it was attributed by Eslava[82] to the porogen part of the low-*k* hybrid.

The band around 4.5 eV appeared in the cured samples, being more pronounced in the samples cured by the monochromatic lamp. A similar behavior has been observed in the case of UV-cured porogen, while the effect is not so strong compared to the hybrid material.

None of the above mentioned phenomena was observed in the as-deposited and UV-treated SiCOH matrix, apart from a slight growth of the band around 6 eV, which remains unexplained.

We conclude that the porogen removal is not as efficient as expected (particularly in the case of the monochromatic lamp with the high energy,

---

[121] A. M. Urbanowicz, K. Vanstreels, D. Shamiryan, S. De Gendt and M. R. Baklanov, *Effect of Porogen Residue on Chemical, Optical, and Mechanical Properties of CVD SiCOH Low-k Materials*, Electrochem. Solid-State Lett. **12,** H292-H295 (2009).

[122] G. Aksenov, D. De Roest, P. Verdonck, F. N. Dultsev, P. Marsik, D. Samiryan, H. Arai, N. Takamure, M. R. Baklanov, *Optimization of low-k UV curing: effect of wavelength on critical properties of the dielectric*, Material Research Society Spring Meeting 2009, San Francisco, April 13-17 (2009).

7.2 eV, photons). Instead of the removal, a part of the decomposed porogen remains in the pores in form of amorphous carbon *porogen residue*. The residue was generally overlooked,[123] because the FTIR C=C peak is barely visible and VIS/UV ellipsometry data were not available.

We have attempted a rough estimate of the porogen and residue percentage in the hybrid FTIR spectra. We have used the normalized absorbance (i.e., the quantity comparable to the absorption coefficient) of the low-*k* films and of the porogen to calculate the ratio directly. Figure 4.28 shows the results of the calculation on the series of samples cured by the monochromatic lamp. Using different spectral ranges, we have obtained differing results.

Graph a) shows the ratio of the CH_x band area around 2900 cm^{-1}. The percentage seems to be overestimated, but this can be influenced by the response from the Si bonded CH_3 groups in the case of hybrid material.

Graph b) shows the ratio of 1600 cm^{-1} C=C band areas. The porogen percentage in the uncured sample is unexpectedly low. No rapid removal ocurs in the early stages of cure (compare to porogen, fig. 4.21, where a fast removal in the first 40 seconds has been observed).

Graph c) shows the evolution of C=C and CH_x area ratio for the low-*k* hybrid films. This figure can be compared to the analogous one of the porogen. Again, the presence of C=C is lower than expected, caused partly by the presence of bonded CH_3 groups in the CH_x band.

We assume that the deposition for the low-*k* hybrid supports the –CH_3 bonding (as already discussed in previous subsections) instead of the C=C formation in the as-deposited material. However, upon the UV-cure, the Si-C and C-H bonds are quickly broken, while the C=C part remains relatively untouched or is even generated by clustering of the carbon ions.

To explain the dominating band at 4.5 eV for long curing times we should notice that the UV band is caused by electronic transition in the sp^2 bonded carbons, while the FTIR vibration is due to the carbon double bond, not necessarily present in the amorphous phase.

Even if sensitive measurements of C=C absorption were available, the role of UV ellipsometry in the porogen residue detection would be of primary importance.

4.3.6. Summary

We have investigated the optical properties of a UV-cured PECVD low-*k* dielectric and its constituents in the visible and ultraviolet range: the SiCOH matrix and the organic porogen. We found that the optical properties of the low-*k* films between 2 and 9 eV are mostly determined by the presence of the porogen and its removal during the UV-cure, because the response of the SiCOH matrix is similar to SiO_2. The behavior

---

[123] Even it was already noticed as we discussed in the introduction of this chapter.
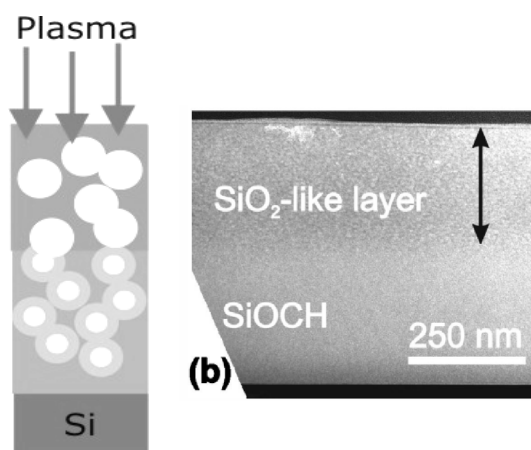
Figure 4.29. Schematic view of plasma damage process. b) TEM picture of heavily O$_2$ damaged low-*k* layer.

of the refractive index in the visible range is influenced by the presence of absorption bands in the near ultraviolet.

The fact that the absorption bands in the ultraviolet range, attributed to the porogen, do not disappear even for long curing times, leads to the conclusion of the existence of porogen residues in the low-*k* material. The incomplete removal has also been observed for deposited porogen layers, treated with the UV-cure process. We assume the residues to be mainly sp^2 bonded (amorphous or aromatic) carbon, because of the presence of the absorption of C=C vibrations in infrared and the п-п* electronic transitions between sp^2 carbon orbitals in ultraviolet. Using the three media mixing model for the VIS/UV spectra, we have estimated the volume fraction of the residues to be 25% for our cured samples cured with monochromatic lamp with a typical uncertainty of $\pm 3\%$. The amount of the residues can be controlled through the varying porogen chemistry and composition, deposition and curing conditions, but the underlying mechanism is not completely understood yet.

4.4. Plasma damage of Alpha1 and Alpha2

During the microprocessor fabrication, the low-*k* materials undergo many operations involving plasma exposures. 1) Trenches and vias are etched using anisotropic dry-etch process with fluorocarbon plasmas. 2) The photoresist is stripped using oxygen and chlorium based plasmas. 3) After deposition of copper interconnects the surface is cleaned by ammonia based plasma.

The low-*k* dielectrics are vulnerable to plasma damage – the plasmas can cause the carbon depletion and the following hydrophilisation of the material. Moreover, the volume of the dielectric can be easily damaged due to the presence of pores. The plasma damage is the most important issue in low-*k* integration these days. Figure 4.29 shows a schematic picture of the plasma damage process. The reactive ions from the plasma penetrate the pore network and remove the organic part of the low-*k* hybrid: the porogen residues, but also the Si bonded CH$_3$ groups.
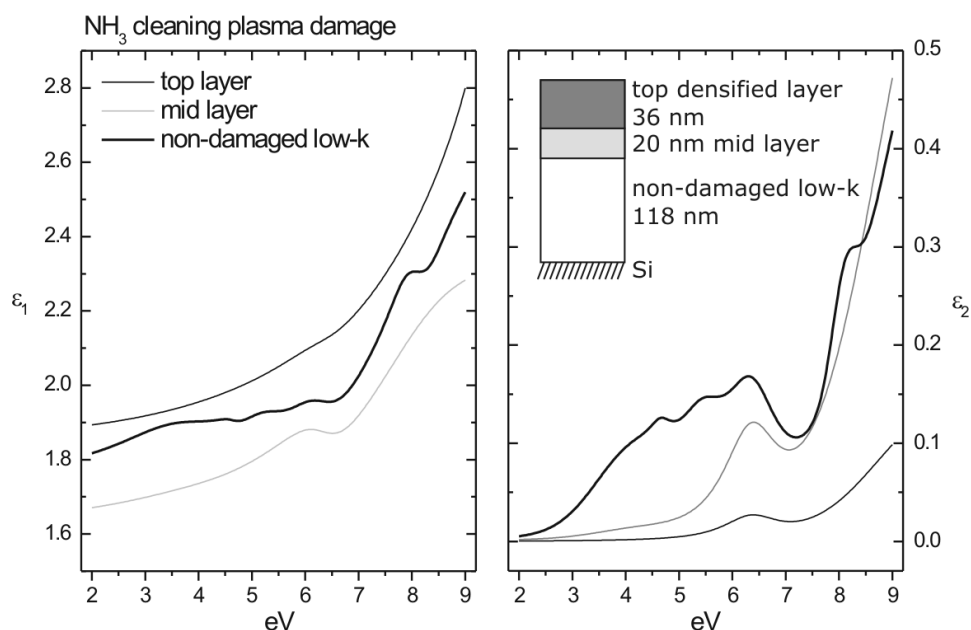
Figure 4.30. Dielectric functions of NH₃ plasma damaged low-*k* dielectric. The three-layer model reveals reduction of absorption band between 3 and 7 eV (attributed to organic compound of the material) in the top layers and a densification of the topmost layer.

The surface layer becomes highly hydrophilic and can be detected by various techniques. Figure 4.29b) is adopted from literature.[124]

To control the level of damage in production conditions, nondestructive and fast optical methods must be used. For a correct implementation of optical models for high precision in-situ scatterometry and ellipsometry, optical properties of the low-*k* materials and their changes during plasma treatments have to be known and understood.

For Alpha1 and Alpha2 low-*k* films, one etching plasma and two different strip-plasma chemistries were used. We have prepared a set of samples based on the low-*k* dielectric Alpha with varying deposition and curing conditions, and damaged the samples by a 10 sec flash of NH₃ plasma in ICP (inductively coupled plasma) reactor. Limited number of samples was damaged by O_2 and O_2/Cl_2 based strip-plasmas in the ICP chamber. To study the effect of $CF_4/CH_2F_2/Ar$ ICP etching recipes on the optical properties, the $CF_4:CH_2F_2$ ratio was modified to obtain different etching rates and to control the by-production of polymer residues.[125]

The set of samples was completed with referential non-damaged samples of the dielectrics.

To evaluate the optical characteristics of the samples, we have performed spectroscopic ellipsometry measurements in the range from 2 to 9 eV, using various angles of incidence between 55 and 85 degrees using the

---

[124] D. Shamiryan, M. R. Baklanov, S. Vanhaelemeersch, and K. Maex, *Comparative study of SiCOH low-k films with varied porosity interacting with etching and cleaning plasma*, J. Vac. Sci. Technol. B **20,** 1923-1928 (2002).
[125] A. Zaka, unpublished report, IMEC (2007).
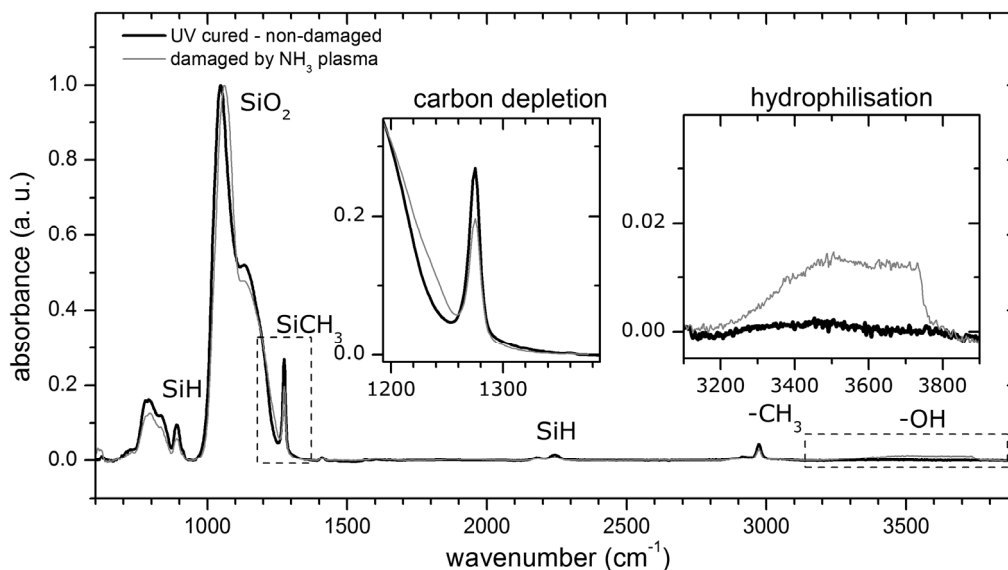
Figure 4.31. FTIR spectra of non-damaged and NH₃ plasma damaged low-*k*.

nitrogen-purged Sopra GES5 PUV-SE in the rotating analyzer configuration.

The measured ellipsometric angles Ψ, Δ were fitted by layered optical models using the following algorithm: 1) Non-damaged layers were measured and the data were fitted by a proper harmonic oscillator optical model. 2) The total thickness of the plasma-treated film was estimated, using the optical model of the undamaged material. 3) The model layer was sliced to two (or three) sub-layers, keeping the total thickness as a starting point and then all the thicknesses and the properties of the top layer (or, top two layers) were optimized in iterative steps, while the properties of the bottom layer were kept fixed.

Atomic concentration (Si, C, O, H) profiles were obtained from TOF-SIMS (time-of-flight secondary ion mass spectroscopy) measurements.[126]

4.4.1. Effect of NH₃ strip-plasma on Alpha1 and Alpha2

A set of samples of low-*k* dielectric Alpha has been prepared, varying the deposition and curing conditions and reaching various porosities and compositions (see next chapter for detailed information). The samples were exposed for 10 seconds to NH₃ plasma (used for CuOₓ reduction during the Cu/low-*k* integration) in ICP reactor.

Spectroscopic ellipsometry and FTIR

All samples were measured by spectroscopic ellipsometry and their properties were evaluated using a three layer model, because a model using two layers (top damaged and bottom non-damaged) was not representing the data well. The author is aware of the approximate character of such a model. Although the set of samples resulted in a heterogeneous set of results, a relation between the porosity and depth of damage (thickness of the two top layers) can be stated.

---

[126] Courtesy of A. Franquet, IMEC (2007).
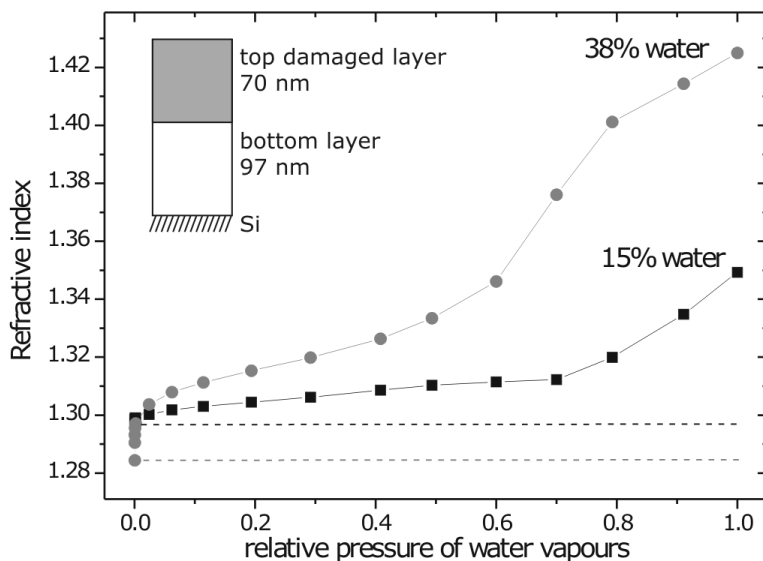
Figure 4.32. The water based ellipsometric porosimetry (WEP) detects a higher hydrophilicity in the top layer.

The Alpha1 samples prepared with the higher porogen load for the target porosity of 35% (±3%) exhibit the depth of damage of (73 ± 5) nm and the Alpha2 samples with the target porosity of 27% (±2%) exhibit the depth of damage of (58 ± 6) nm.

A typical example of the optical properties of the material is plotted in fig. 4.30. After stripping, the absorption band between 3 and 7 eV is substantially reduced, resulting in porous SiO_2-like top hydrophilic layer. The topmost layer exhibits increased refractive index, attributed to densification. The FTIR absorbance spectra (fig. 4.31) show a clear reduction of the $Si-CH_3$ bonds, and an increase of the -OH groups in the damaged material.

Double layer water EP

Water-based ellipsometric porosimetry experiment has been performed to track the changes of the layers upon the change of the ambient humidity. In this case, the most damaged sample from the set was chosen for the experiment, and a two-layer model was used for the evaluation.

Figure 4.32 shows the refractive index changes (at 633 nm) during the increase of water vapor pressure in the vacuum chamber. RI of the top layer is initially lower (in vacuum) than that of the non-damaged bottom layer, because the porogen residues are removed from the pores of the damaged layer. With increasing pressure, RI of the top layer increases rapidly. This means that the hydrophilic surface of the pores absorbs the water. The growth of RI in the bottom layer is slow. At the equilibrium pressure, around 15% of the bottom layer is filled by water, which can be attributed to the condensation on the porogen residues and autocatalytic effect of water. The final percentage of water in the top layer is 38%, reaching the value of open porosity.
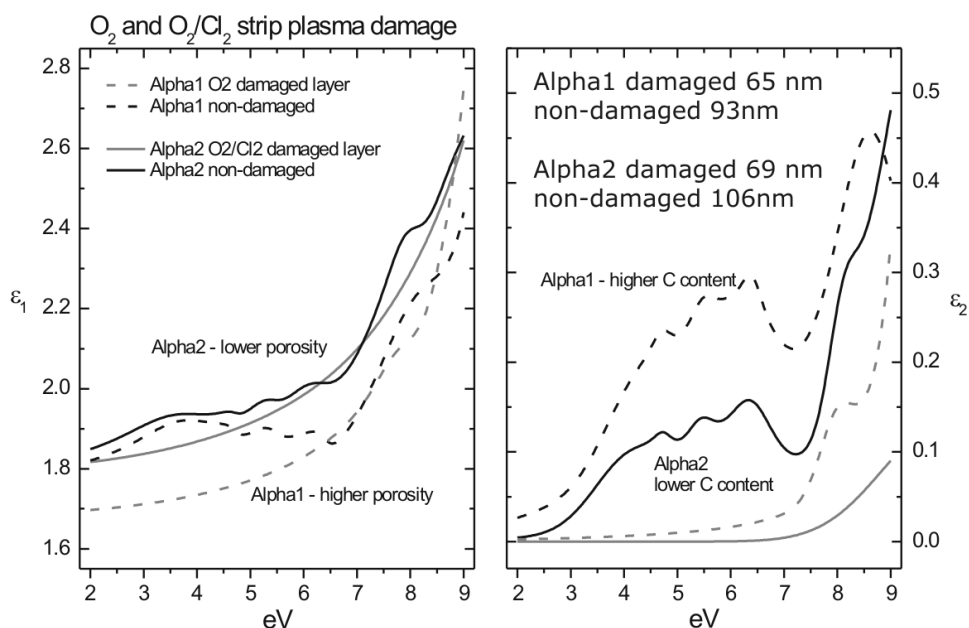
Figure 4.33. Dielectric functions of two samples of low-k with higher (Alpha1) and lower (Alpha2) porosity, damaged by O_2 and O_2/Cl_2 strip-plasma.

4.4.2. Effect of O_2/Cl_2 strip-plasma on Alpha1 and Alpha2

The effect of 10 sec exposition of O_2 and O_2/Cl_2 strip-plasmas in CCP reactor on our samples is similar to that of NH_3 plasma. A top, carbon depleted layer has been detected by the spectroscopic ellipsometry, but no further densification (fig. 4.33). The difference between the damaged and non-damaged layer can be observed by TOF-SIMS (fig. 4.34) as a decrease in the C and H concentrations, and a small increase of the Si and O concentrations. Ellipsometric porosimetry measurements detected increased pore size and porosity, as the organic material is removed from the pore interior.
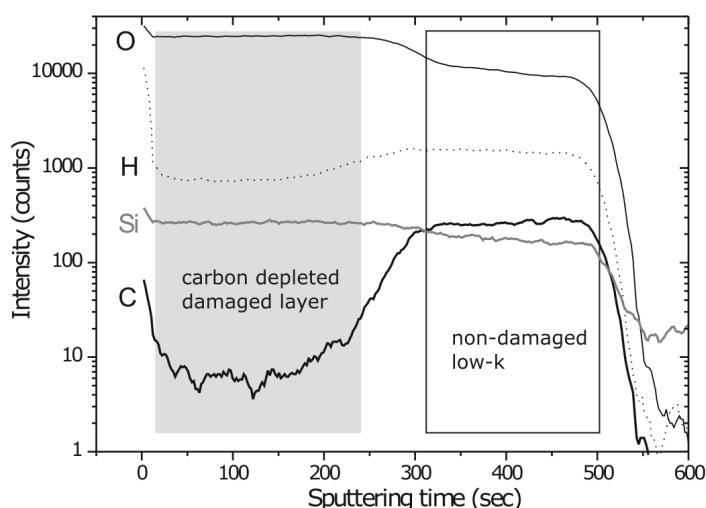

Figure 4.34. Removal of organics from the top layer observed in the TOF-SIMS profiles of atomic concentrations of Si, C, O and H.

CF$_4$/CH$_2$F$_2$ etch plasma byproduct
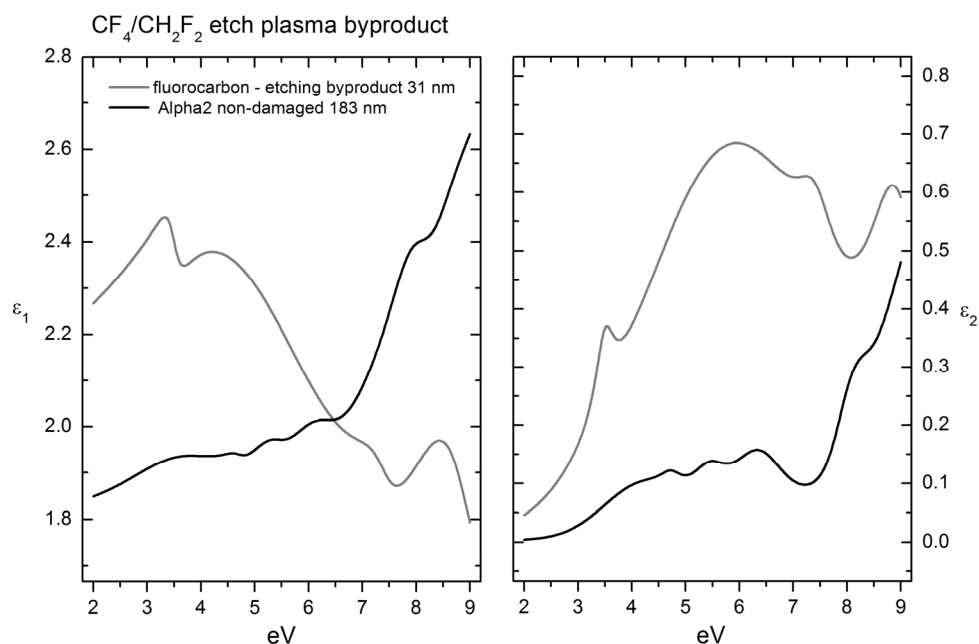
Figure 4.35. Dielectric functions of fluorocarbon by-product from (4:4:2) CF$_4$/CH$_2$F$_2$/Ar etch plasma. The polymer forms a 31nm thick layer on top of the non-damaged film.

4.4.3. Effect of CF$_4$/CH$_2$F$_2$/Ar etch plasma on Alpha2

CF$_4$/CH$_2$F$_2$/Ar based CCP chemistries are used for patterning the low-*k* materials by anisotropic etching. The process is known for leaving fluorocarbon byproducts on the sidewalls and bottoms of the trenches/vias in non-favorable cases. On blanket wafers, it was observed[125] that the etching rate can vary, when the CF$_4$ and CH$_2$F$_2$ ratio is changed and also that the process can result in a pure deposition of the fluorocarbon for the ratio of 4:4. We have studied a sample of the Alpha2 dielectric prepared by a 16 sec treatment by such plasma, and observed a 31nm thick layer on the non-damaged material by spectroscopic ellipsometry (fig. 4.35).
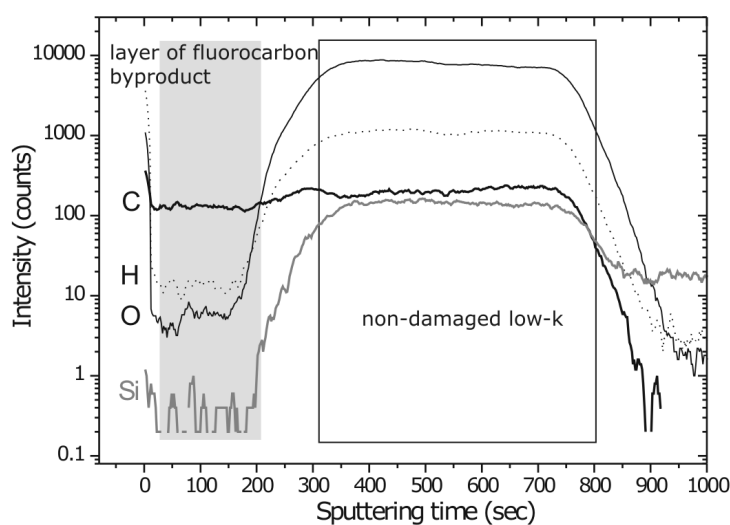

Figure 4.36. TOF-SIMS depth profiles showing a carbon-rich layer on the sample surface.
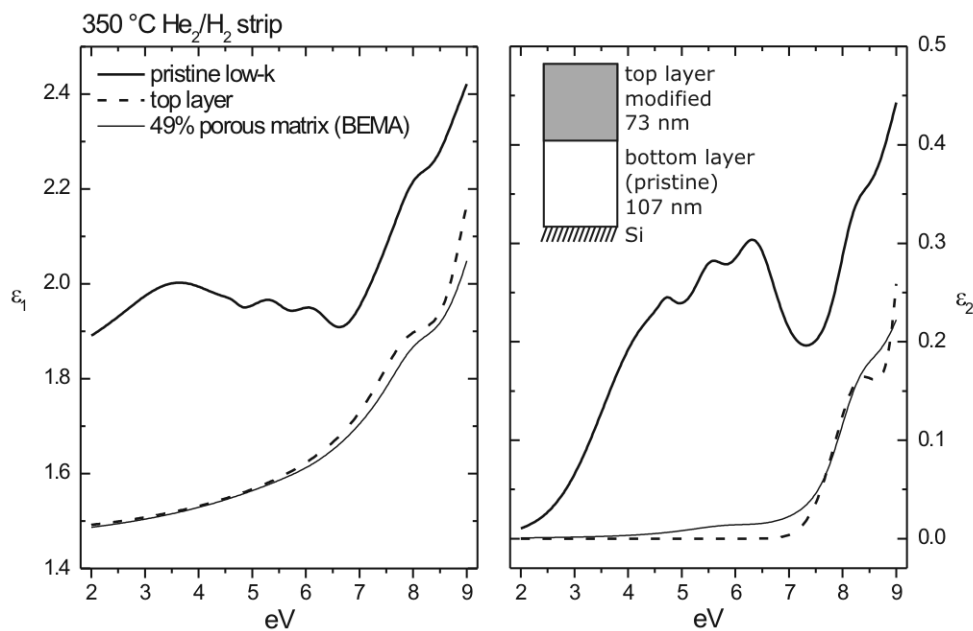
Figure 4.37. Dielectric functions of the pristine and He$_2$/H$_2$ plasma treated low-*k* films. Calculated dielectric function of 49% porous matrix is plotted for comparison.

This layer has also been detected in the TOF-SIMS profile (fig. 4.36); however, the thickness cannot be directly estimated from the profile due to unknown sputtering rates. A fluorocarbon layer of this thickness seals the pores, as can be proven by means of ellipsometric porosimetry.

For the standard etching chemistry with the ratio of 7:1:2 (CF$_4$/CH$_2$F$_2$/Ar), the removal of material is observed without causing significant changes to the optical properties of the low-*k* material. However, EP experiments suggest pore sealing; therefore a thin layer of fluorocarbon byproduct is expected on the top of the etched blanket low-*k*. This layer is not clearly visible in the TOF-SIMS profile and a direct trial of ellipsometric modeling was not successful; however, if the optical properties of the top layer are fixed as obtained from the thicker layer, the model can be improved, resulting in thickness of the fluorocarbon layer of 4 nm. It has to be mentioned that the quality of this layer might be different from the deposited fluorocarbon, containing the etching byproducts and diffusing into the near-surface pores.

4.4.4. Effect of He$_2$/H$_2$ high temperature strip on Alpha1

The high temperature (350 °C) He$_2$/H$_2$ plasma-assisted strip process was tested on the low-*k* dielectric films. It has been shown,[127,121] that this process is efficient in the photoresist removal, while no damage (Si-CH$_3$ depletion) is caused to the porous low-*k* films in tests with blanket wafers.

---

[127] A. M. Urbanowicz, D. Shamiryan, P. Marsik, Y. Travaly, P. Verdonck, K. Vanstreels, A. Ferchichi, D. De Roest, H. Sprey, K. Matsushita, S. Kaneko, N. Tsuji, S. Luo, O. Escorcia, I. Berry, C. Waldfried, S. De Gendt and M. R. Baklanov, *Improved Low-k Dielectric Properties Using He/H2 Plasma for Resist Removal*, Advanced Metallization Conference 2008, San Diego, October 8-10 (2008).
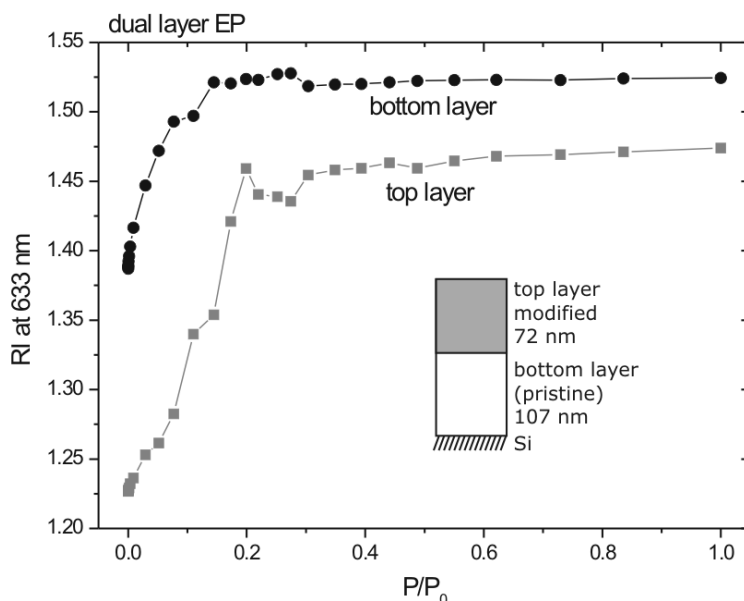
Figure 4.38. EP: Refractive index changes during the toluene absorption in He$_2$/H$_2$ plasma treated low-*k* material.

Moreover, it was found that the process removes also the porogen residues from the top layer of the low-*k* film, while the thickness of the film remains unchanged.

Apart from the technological benefits of such process, these experiments support the interpretation of the facts discussed in the previous section.

- The carbon content is lowered in the top layer, while that of Si-CH$_3$ in not affected.
- Ellipsometry detects a clean top layer and unchanged thickness (see below).
- WEP hydrophilicity decreased in the case of the He$_2$/H$_2$ plasma treated samples (we assume that the hydrophilicity of the non-damaged low-*k* material is caused by presence of the residues – as explained in the next chapter).
- *k*-value slightly decreased for the He$_2$/H$_2$ plasma treated samples.
- EP can detect an increased porosity.

Spectroscopic ellipsometry

We have performed VIS/UV ellipsometry measurements on the series of Alpha1 and Alpha2 samples. All samples were optimally UV-cured. Subsequently, the samples were treated by He$_2$/H$_2$ plasma at varying temperature. The results of this study will be published elsewhere.[128]

We fitted the ellipsometric measurements with a double layer model, fixing the properties of the bottom[129] layer as pristine, and searching for

---

[128] A. M. Urbanowicz, P. Marsik et al., in preparation.
[129] Without fixing the bottom layer, the model becomes unstable; nevertheless, it shows the tendency to increase absorption in the bottom layer. It is possible that some of the thermally activated residue may condense in the bottom layer.
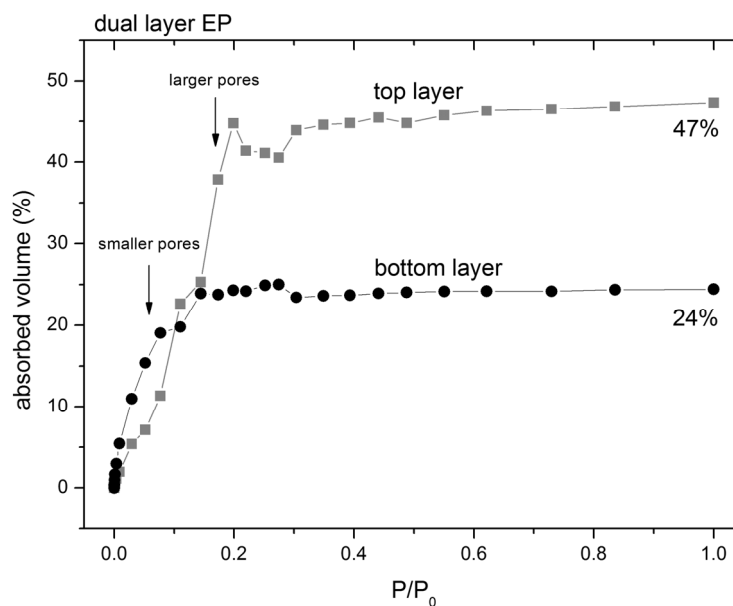
Figure 4.39. EP: Calculated volume of the toluene absorption in He_2/H_2 plasma treated low-*k* material.

both thicknesses and properties of the top layer. Figure 4.37 shows an example of the obtained optical functions. We found that the optical properties of the top layer suggest a removal of the porogen residues, while the remaining material can be seen as the 49% porous matrix. This can be compared with Table 4.7; the estimated percentage of available open porosity (partially filled with residues) reaches 55%.

The initial thickness of the sample was 180 nm and the thicknesses of the layers after the plasma step were found to be 73 nm (top layer) and 107 nm (bottom layer).

Dual layer EP

We performed an ellipsometric porosimetry experiment with the toluene absorption, and evaluated the results using a double layer model with a fixed thickness and absorption (merely phenomenological) of the bottom layer, and fitted the Cauchy model to both layers together with the thickness of the top layer.

Figure 4.38 shows the evolution of the refractive indices (at 633 nm) of the bottom and top layer in the model. The thickness of the top layer was found to be constant (72$\pm$1 nm).

Figure 4.39 presents the volume percentages calculated from the RI values. The porosity of the top layer was estimated to be 47%, which is comparable with a direct estimation from the VIS/UV spectra. The porosity in the bottom layer is 24% which is lower than expected 33% of the non-treated material. The behavior of the absorption isotherms allows a qualitative statement about pore sizes: we conclude that the pores are larger in the top layer, because their volume is filled more slowly than that of the bottom layer.
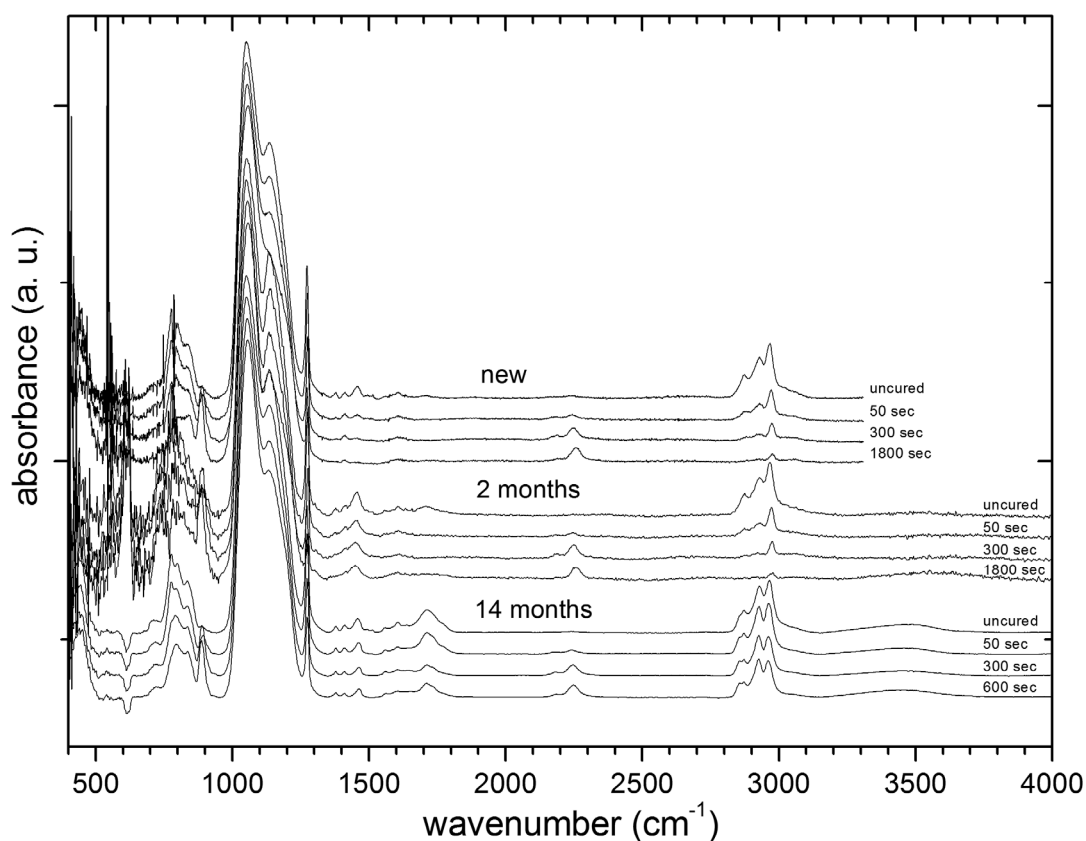
Figure 4.40. FTIR: Ageing of low-*k* films.

4.4.5. Ageing and contamination

Ageing

The studied sample series were re-measured by FTIR after 2 months and 14 months of storing in the atmosphere. Figure 4.40 shows the results of the experiments. We observe a contamination by an unknown organic species and also the presence of –OH ($\sim$3500 cm^{-1}), probably in the absorbed moisture.

Contamination

Suspicions about a contamination of the samples in the high vacuum chamber from oil-pump were raised[130] from the routinely observed fact that refractive index, measured repeatedly by the ellipsometer mounted on the EP vacuum chamber increased during time, while the chamber was pumped down to high vacuum.

We have tested the suspicion on one of the UV-cured low-*k* samples. We measured the FTIR and PUV SE spectra of the sample initially (the sample was already weathered, approximately 3 month old) and left for 40 days in the cleanroom atmosphere. Then, we have re-measured the spectra to assess possible changes. Finally, we left the sample for 12 hours in the pumped-down EP chamber and then measured again.

---

[130] S. Eslava, personal communication and unpublished report.
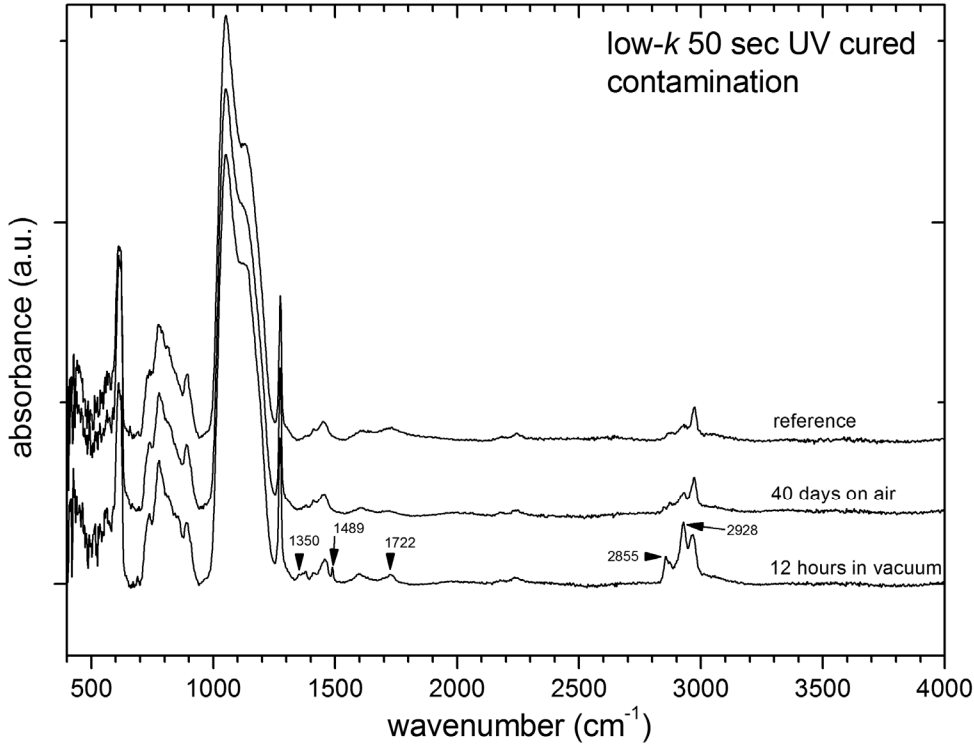
Figure 4.41. FTIR: Contamination of low-*k* film.

The FTIR spectra are shown in fig. 4.41. While only minor changes are observed during atmosphere weathering, several new absorption bands appeared in the spectra after the overnight storage in the high vacuum chamber.

Figure 4.42 shows the PUV SE spectra from this experiment. We observe an increase of the real part of dielectric function, and an increased absorption in the ultraviolet range.
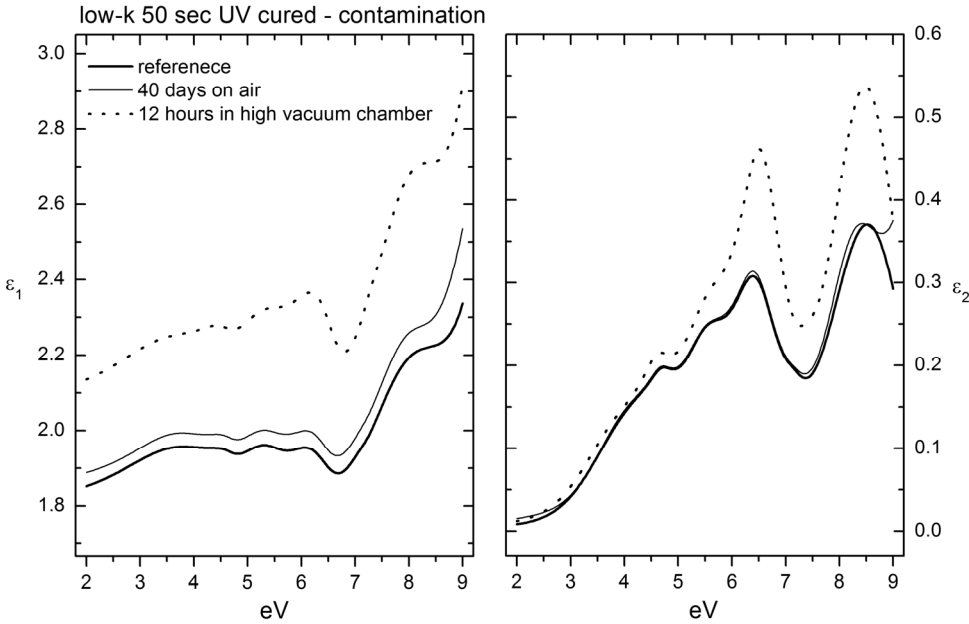
Figure 4.42. PUV SE: Contamination of low-*k* film.

4.4.6. Summary

The changes of the optical properties after stripping, etching and cleaning plasmas and contamination of the low-*k* films were investigated.

We confirmed the assumption that the stripping and cleaning plasmas create a carbon depleted layer on top of the film, as observed previously by TEM and TOF-SIMS. Using spectroscopic ellipsometry, it is possible to detect the double layer structure with the bottom layer similar to the non-damaged sample, and the top layer showing a decrease of the absorptions in UV and lower RI. In some cases, a densification of the very top layer is assumed from the behavior of a triple layer optical model.

Typical thickness of the plasma affected layer was found to be 50 to 70 nm.

We have demonstrated a possible use of double layer models in EP estimation of hydrophilicity and porosity of the damaged top layer.

A promising non-damaging strip recipe was investigated, showing the porogen residue removal from the plasma affected top layer. This result supports the mixing approach discussed in the previous subsection.

Brief experiments with ageing and storing showed the sensitivity of the porous low-*k* material to contamination by unknown species from the ambient.

4.5.   Properties of Beta material

The Beta material is the second studied in this work. It has been developed by different company than the previously discussed Alpha material. The films have been deposited by PECVD, and cured by the broadband UV light source (with $\lambda > 200$ nm). The deposition and curing details are proprietary of the manufacturer and cannot be disclosed. We will focus on experimental observations. Basic properties of the material are summarized in Table 4.8. The Beta2 material is higher porosity version of the material Beta, but has not been studied extensively in this work.

Table 4.8. Basic characteristics of Beta low-*k* dielectrics: open porosity measured by toluene EP, refractive index at 633 nm and *k*-value.

material	porosity	RI	k
Beta	21	1.35	~2.5
Beta2	36	1.33	~2.3
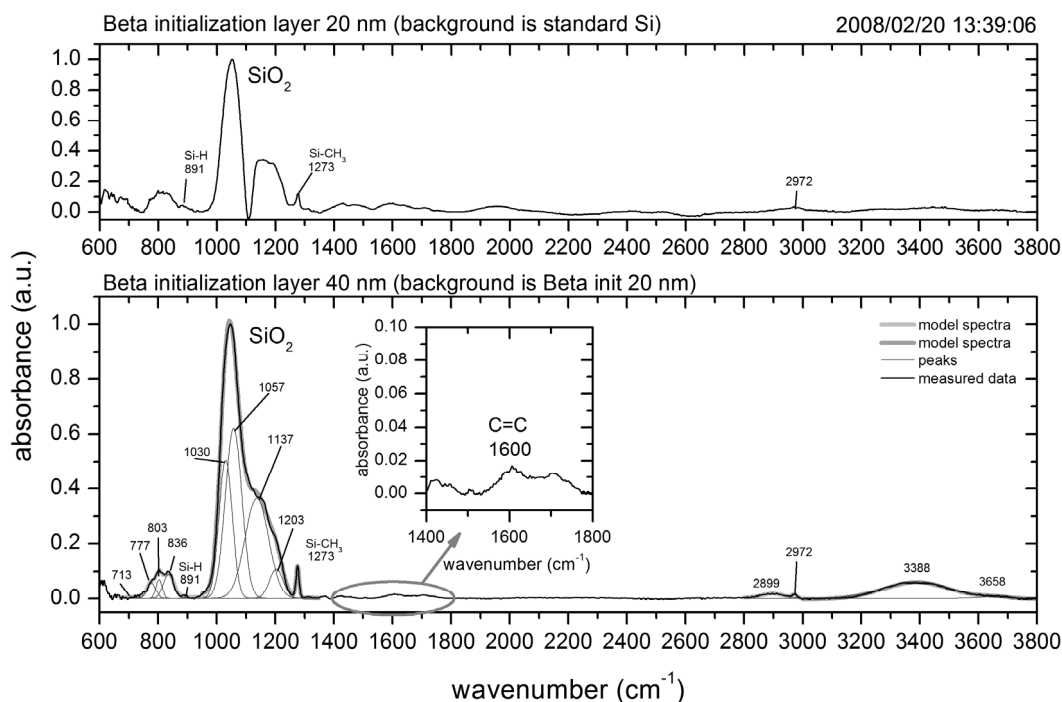
Figure 4.43. FTIR spectra of transition layer samples. Top: Absorbance of the "Initlayer 20nm" sample with a generic Si wafer taken as the background. Bottom: Absorbance of "Initlayer 40 nm" sample with the "Initlayer 20 nm" taken as the background.
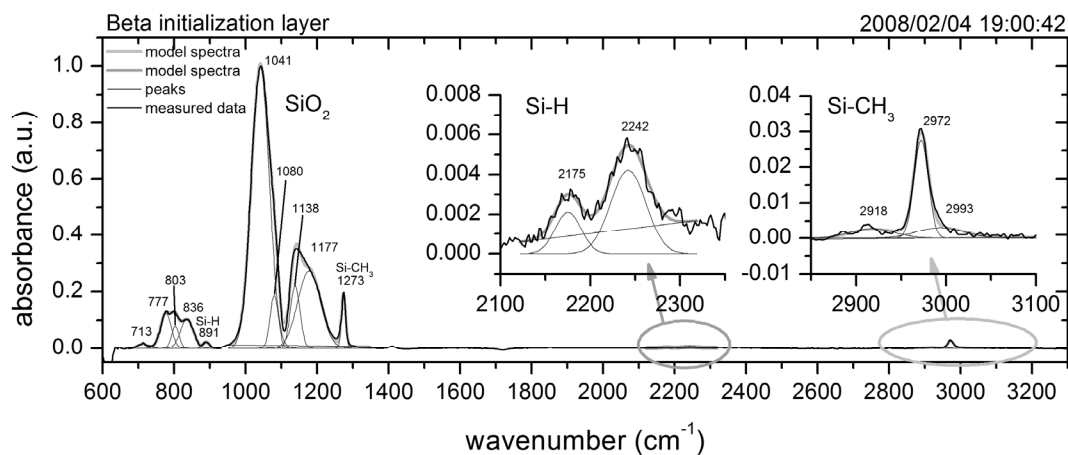
Figure 4.44. FTIR measurements on transition layer sample "Initlayer 65 nm".

4.5.1. Transition layer

The standard deposition process included a deposition of transition (or initialization) layer between the silicon substrate and the Beta film itself. We have studied several samples with the transition layer itself and observed variation in the optical spectra. Table 4.9 overviews the studied samples. For future reference, the coworkers who provided the samples are listed.

Table 4.9. List of transition layer samples.

label	thickness (nm)	via
Transition layer	20.2	Eymery, Eslava
Initlayer 20nm	19.4	Urbanowicz, Heijlen
Initlayer 40nm	47	Urbanowicz, Heijlen
Initlayer 65nm	71	Urbanowicz, Van Besien

FTIR

Figure 4.43 shows the absorbance spectra of "Initlayer 20 nm" and "Initlayer 40 nm". The former is distorted by the substrate baseline removal, but the second spectrum was measured using the first sample as the background leading to a reasonable result.

We observe the dominant Si-O-Si network structure with some bonded CH_3 groups, but also a significant presence of the C=C bonds. Figure 4.44 shows FTIR spectra of the sample "Initlayer 65 nm". The result is quite different from the above. Apart from the different Si-O-Si structure, more Si-CH_3 bonds are detected, no significant C=C contribution and some amount of Si-H. The "Transition layer" was not studied by FTIR.
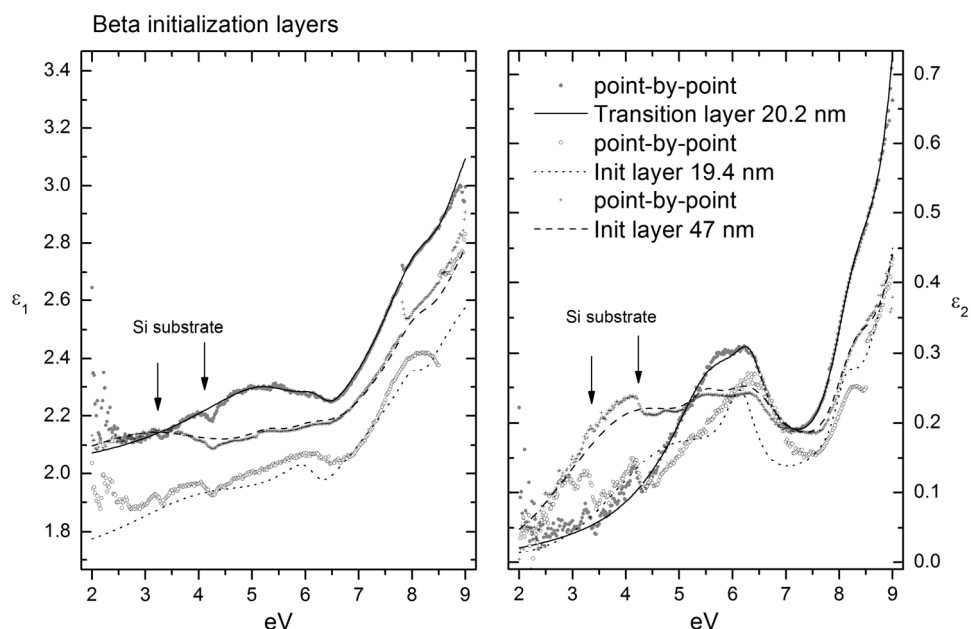

Figure 4.45. Dielectric functions of the transition layers measured by spectroscopic ellipsometry. The lines represent parameterized model and the points result of point-by-point calculation. The sharp structures around 3.4 eV and 4.2 eV originate from the substrate silicon.

Beta (no initialization layer) broadband UV-cure
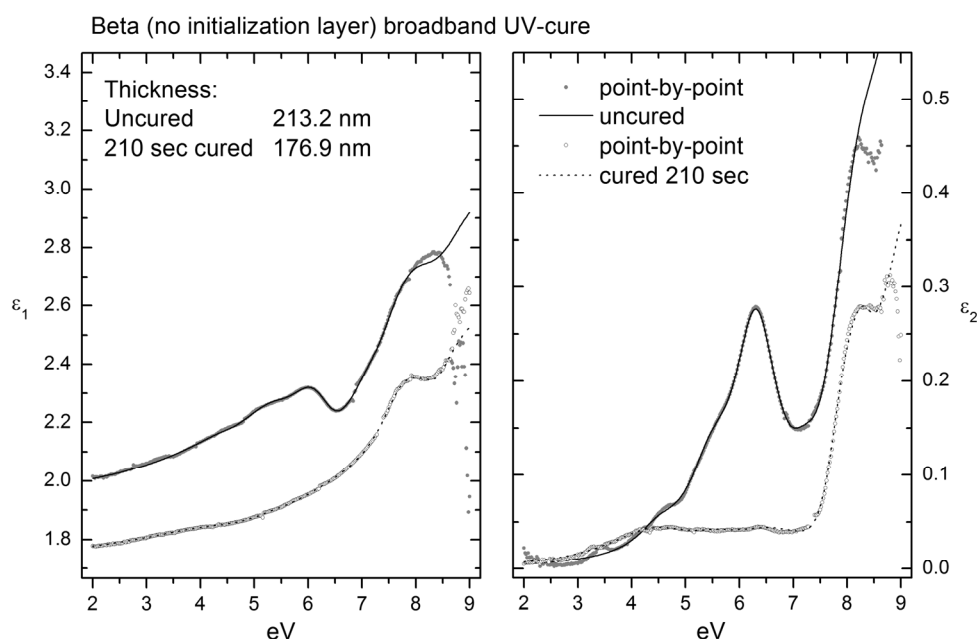
Figure 4.46. Dielectric functions of the uncured and cured low-*k* Beta.

Spectroscopic ellipsometry

Figure 4.45 shows the results of VIS/UV ellipsometric measurements analyzed using parameterized models and point-by-point calculation. The agreement between the approaches is not excellent, particularly, we observe some structures above 3 eV and 4 eV that might be attributed to the critical points of Si substrate visible in the point-by-point fits due to imperfections of the model (i.e., the assumption of a single homogeneous layer).

Nevertheless, we again observe differences between the samples. In the case of "Initlayer 40 nm" we detect a significant absorption band around 4 eV which might be related to the presence of C=C bonds in the form of amorphous carbon. The sample "Initlayer 65 nm" was not measured by VIS/UV ellipsometry.

4.5.2. Optical properties of Beta low-*k*

In the published work[131] the samples deposited with the transition layers were studied, but the optical model used for the analysis of ellipsometric data consisted of a single layer. To avoid complications, I present here the model dielectric functions of samples prepared without the initialization layer.[132]

---

[131] S. Eslava, G. Eymery, P. Marsik, F. Iacopi, C. E. A. Kirschhock, K. Maex, J. A. Martens, and M. R. Baklanov, *Optical property changes in low-k films upon ultraviolet-assisted curing*, J. Electrochem. Soc. **155,** G115-G120 (2008).
[132] Unpublished part of the work cited above.
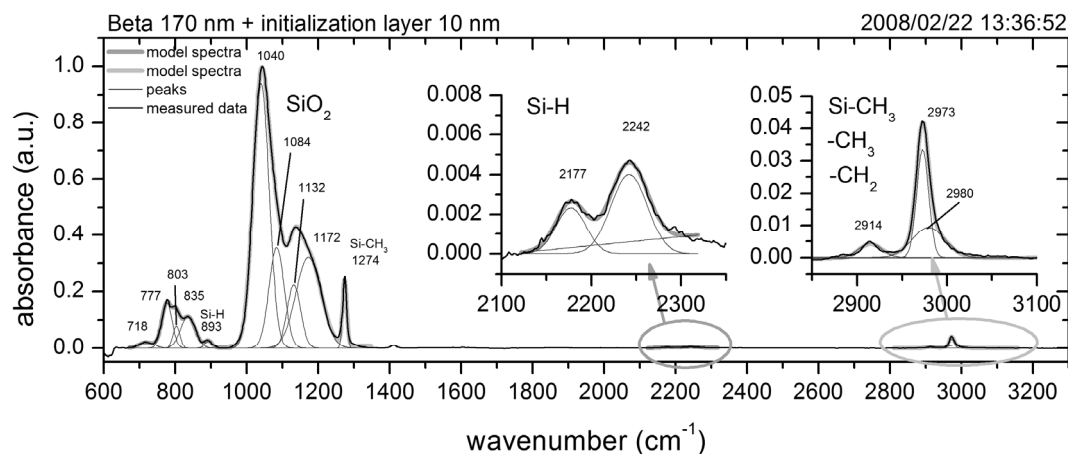
Figure 4.47. FTIR spectra of cured low-*k* Beta.

Spectroscopic ellipsometry

Figure 4.46 shows the spectra of uncured and broadband UV-cured low-*k* dielectric Beta. We observe the dominant 6.4 eV porogen peak and its almost complete removal by the cure.

FTIR

In fig. 4.47 we present the FTIR absorbance spectra of UV-cured low-*k* Beta. The spectra indicate quite a strong presence of Si-CH$_3$ and almost no traces of the porogen. The C=C content is detectable, but was not systematically studied in this case.

EP

We performed EP measurements on the cured Beta sample and detected 21% of open porosity with the typical pore diameter of 1.6 nm (see fig. 4.48).
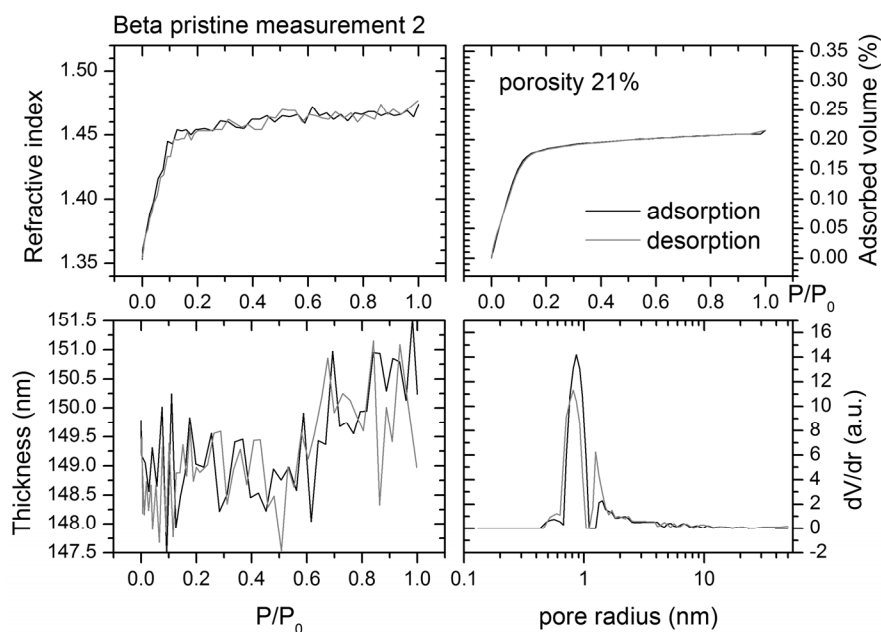
Figure 4.48. EP of cured low-*k* Beta.

4.5.3. Effect of strip-plasmas on optical properties of Beta

We focused our study to the damage that low-k material Beta suffers during the photoresist strip. The exposition to plasma causes mostly the CH_3 depletion and subsequent hydrophilisation of the material.

The samples Beta were deposited on 300 mm Si wafers including the initialization layer. All samples were UV-cured by the broadband lamps (standard for Beta). Two different stripping recipes were applied to the samples with varying time of treatment to observe the evolution of the changes. The first recipe was based on O_2, and performed in CCP (capacitively coupled plasma) reactor during 20 and 30 seconds. The second recipe was based on H_2N_2 chemistry and we treated the samples for 10, 20 and 30 seconds. The set of samples was completed with referential non-damaged samples of the dielectrics and also initialization layers, based on more dense and non-porous low-k material (see subsection 4.5.1).

To evaluate the optical characteristics of the samples, we performed spectroscopic ellipsometry measurement in the range from 2 to 9 eV, using various angles of incidence between 55 and 85 degrees on nitrogen-purged Sopra GES5 PUV-SE in the rotating analyzer configuration.

The measured ellipsometric angles Ψ, Δ were fitted by layered optical models using the following algorithm: 1) The optical properties of initialization layers were obtained independently from the single layer samples and were fixed in all subsequent fitting steps. 2) Non-damaged layers were measured and the data were fitted by a proper harmonic oscillator optical model. The thicknesses of the initialization layer (11 nm) and the low-k film (171 nm) were determined.

Then, for the damaged samples: 3) The thickness and properties of the treated film in total were estimated (see the column "dual layer" in Table 4.10 and Table 4.11) 4) The model layer was sliced into two sub-layers, keeping the total thickness as a starting point and then the thicknesses of the non-damaged and damaged top layer and the properties of the top layer were optimized in iterative steps, while the properties of the bottom layer were kept fixed at the values of the pristine material.
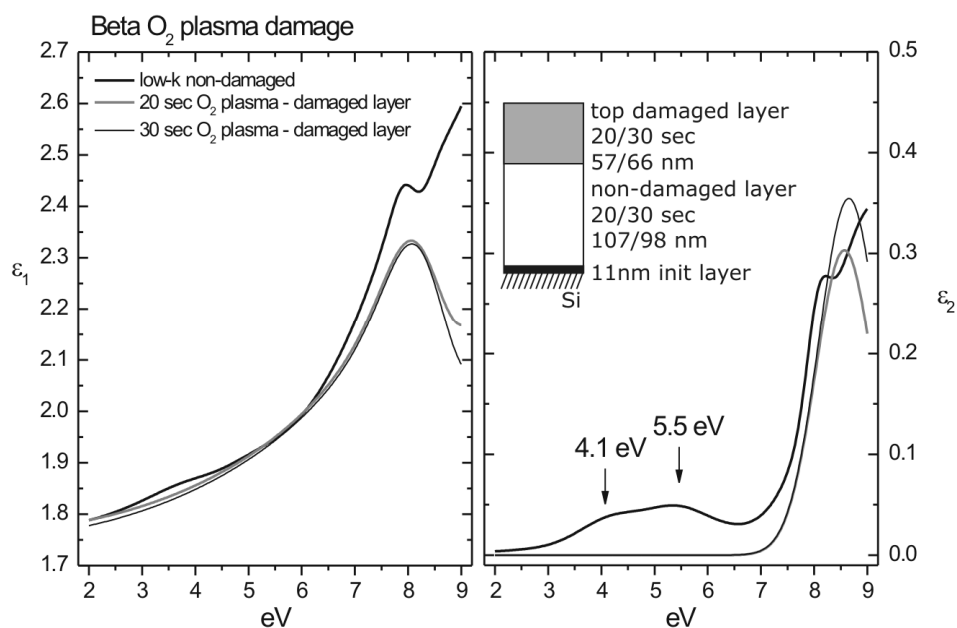
Figure 4.49. Dielectric functions of the non-damaged low-k Beta and of the top layer treated by O_2 plasma in CCP reactor for 20 and 30 seconds. The reduction of absorption bands between 3 and 7 eV is observed, but no significant evolution in the real part of ε.

Effect of O_2 strip-plasma

We treated the Beta low-k dielectric by the O_2 plasma in CCP reactor for 20 and 30 seconds. The toluene EP reveals pore sealing and the water EP shows 5% of absorbed water in saturation pressure for both samples (while the non-damaged sample absorbs less than 1%). The determination of the top damaged layer from ellipsometric measurements was not possible for this set of samples because of the low contrast between the refractive index of damaged and non-damaged sub-layers, but a reduction of UV absorption in the top layer related to porogen residue removal can be detected (fig. 4.49). Table 4.10 summarizes the results of fitting the measured ellipsometric data to the dual or triple layer models. The additional layer has not improved the overall fit.

Table 4.10. Thicknesses of the layers in the model of pristine and O_2 plasma damaged Beta films.

| thickness (nm)	fit: pristine	dual layer 20 sec O2	dual layer 30 sec O2	triple layer 20 sec O2	triple layer 30 sec O2
initlayer	11	11	11	11	11
nondamaged	171			107	98
damaged		167	166	57	66
σ	8.5	10.5	12	10.8	13.1
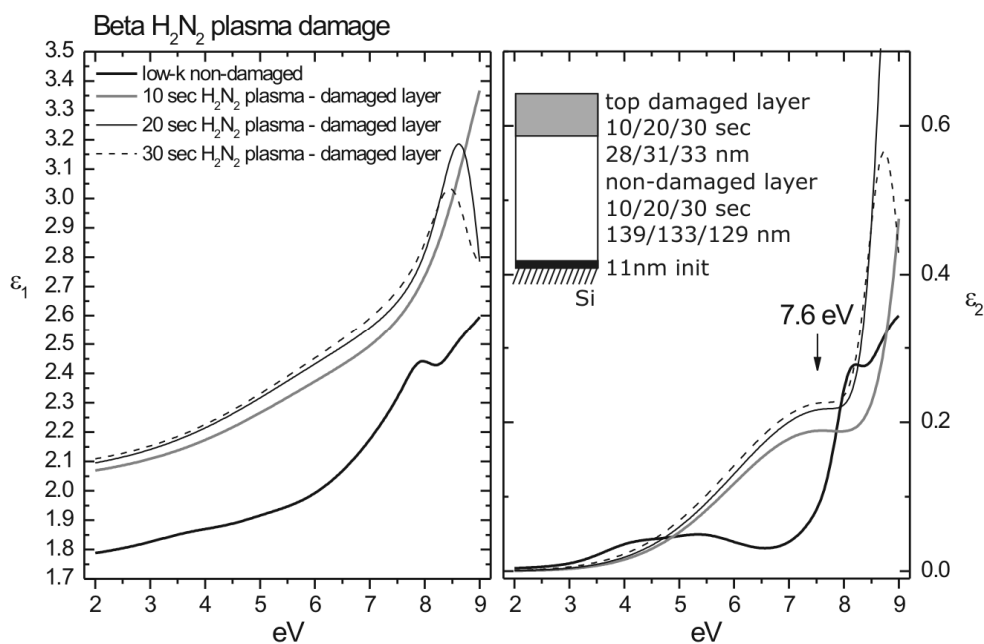
Figure 4.50. Dielectric functions of the non-damaged low-*k* Beta and of the top layer treated by H$_2$N$_2$ CCP for 10, 20 and 30 seconds. Increasing RI is detected with increasing treatment time as well as the formation of 7.6 eV band.

Effect of H$_2$N$_2$ strip-plasma

Alternative strip-plasma for Beta based on the H$_2$N$_2$ CCP chemistry was applied for 10, 20 and 30 seconds to the samples. The EP implicates sealing of pores for toluene and low hydrophilisation, resulting in 3% of the absorbed water in the saturation pressure. The spectroscopic ellipsometry can detect clearly the densified top layer with increasing RI with longer treatment time, and formation of the absorption band around 7.6 eV (fig. 4.50). The origin of this absorption is not understood and will require a further study. The absorption band at 4.1 eV is no longer observed in the plasma treated samples. Table 4.11 summarizes the results of fitting the measured ellipsometric data to the dual or triple layer models. The improvement of the fit with the additional layer justifies the use of the triple layer model.

Table 4.11. Thicknesses of the layers in the model of pristine and H$_2$N$_2$ plasma damaged Beta films.

thickness (nm)	fit: pristine	dual layer			triple layer		
		10 sec H2N2	20 sec H2N2	30 sec H2N2	10 sec H2N2	20 sec H2N2	30 sec H2N2
initlayer	11	11	11	11	11	11	11
nonamaged	171				139	133	129
damaged		156	147	145	28	31	33
σ	8.5	14	15	16	8	7.8	8.2
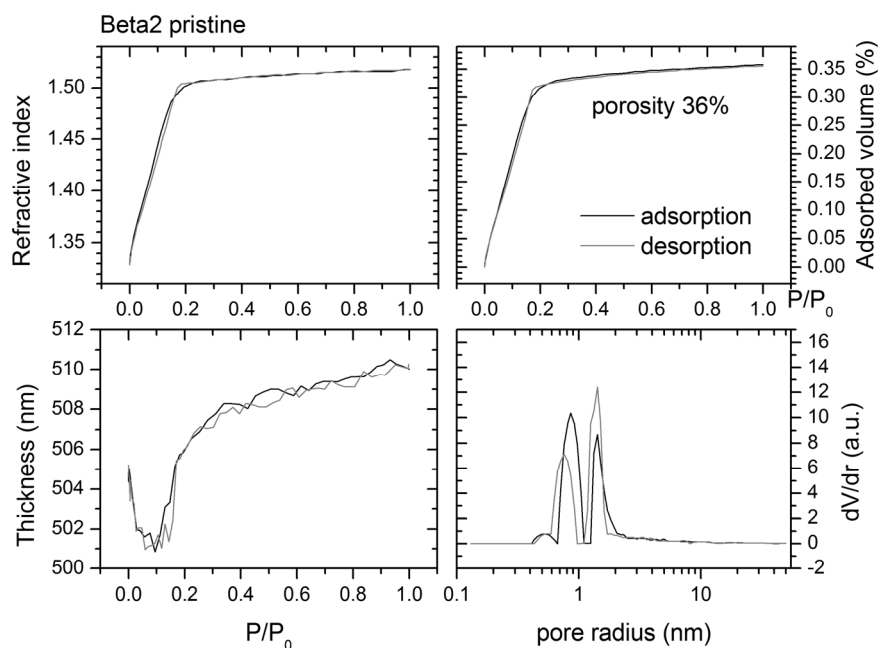
Figure 4.51. EP of Beta2.

4.5.4. Porosimetry of Beta2

Beta2 is the successor of Beta. The deposition conditions (particularly the precursor flow ratio) have been modified to obtain higher porosities (36%). Ellipsometric porosimetry measurements were performed on Beta2 sample and are summarized in fig. 4.51. The refractive index of the material measured in vacuum is 1.33.

4.5.5. Beta porogen curing

A series of porogen samples was prepared using the CVD technology and chemistry of Beta material. The material was deposited as 150 nm thick films on Si substrate. The primary goal of the experiment was to study the UV decomposition of the organic material for the air-gap application.[133]
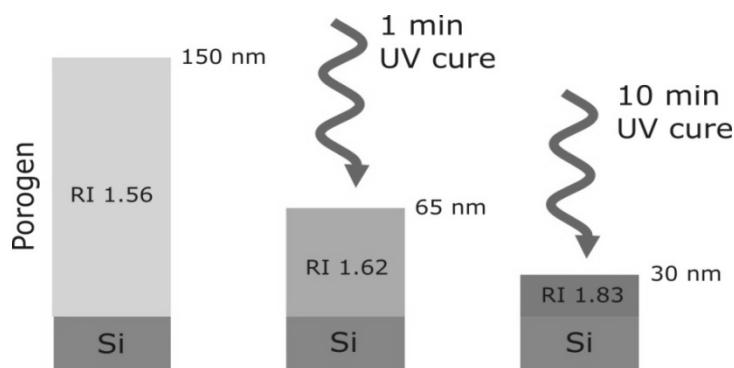
Figure 4.52. The UV-cure of the porogen films causes thickness and mass removal and changes the optical properties of the residual material.

---

[133] M. Pantouvaki, A. Humbert, E. Van Besien, E. Camerotto, Y. Travaly, O. Richard, M. Willegems, H. Volders, K. Kellens, R. Daamen, R.J.O.M. Hoofman and G. Bayer, *Air-gap formation by UV-assisted decomposition of CVD material*, Microelectronic Engineering **85,** 2071-2074 (2008).
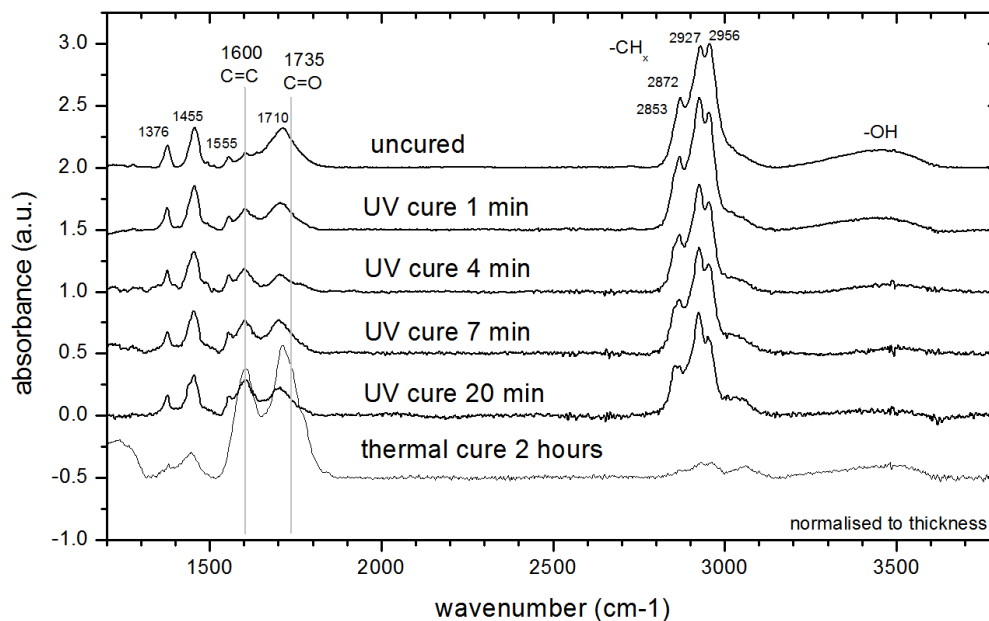
Figure 4.53. FTIR spectra of films of Beta porogen UV-cured for various times and annealed for 2 hours in nitrogen atmosphere.

The samples were exposed to broadband UV light for variable time, from 1 to 20 minutes. One sample was annealed for 2 hours in N_2 atmosphere at 425 °C. It was observed that the UV exposure causes the removal of the material (see fig. 4.52), and changes the optical properties. Nevertheless, even for long curing times, some material remained. The thickness and mass limit of the removal was estimated to be ~80%.

FTIR

We have performed a series of FTIR measurements and the results (normalized absorbances) are plotted in fig. 4.53. The composition of the material changes from the CH_x to C=C structure (see fig 4.54). In directly measured absorbances, one can see the removal of C=C in the early stages of the cure; then, from 2 minutes on, the C=C signature remains almost constant. Surprisingly, the thermal cure completely changes the structure of the material. The thickness of the remaining thermally cured layer was 47 nm.
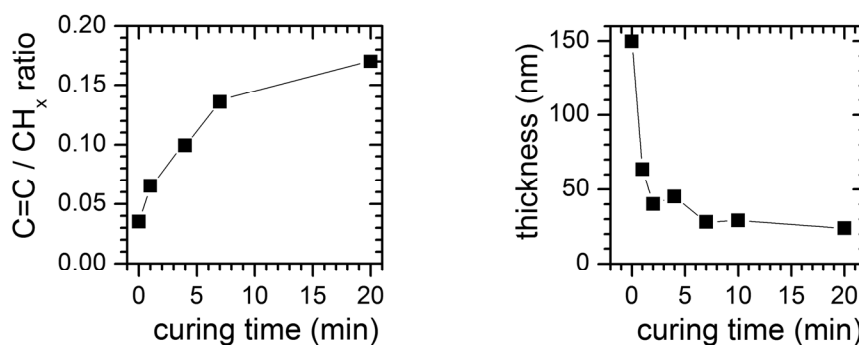
Figure 4.54. Left: Evolution of the ratio of the C=C vibration at 1600 cm^{-1} and the CH_x band around 2900 cm^{-1}. Right: film thickness during the UV cure.
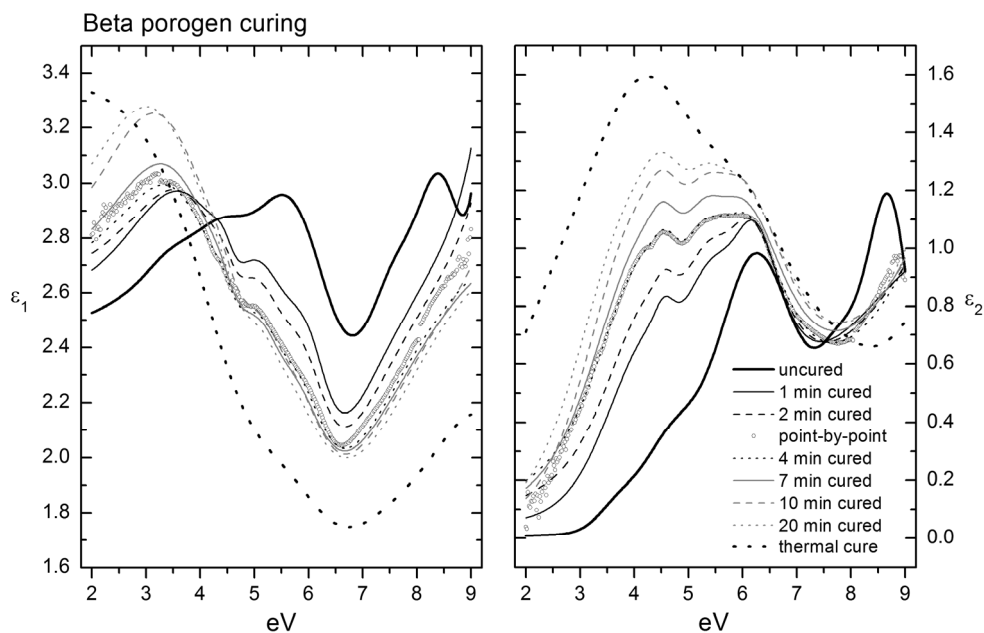
Figure 4.55. Dielectric functions of films of the Beta porogen UV-cured for various times and annealed for 2 hours in nitrogen atmosphere. The 4 minutes treated sample was also fitted point-by-point to check the consistency of the model.

Spectroscopic ellipsometry

We have measured the samples using PUV SE; the results of model fitting to the raw data are shown in fig. 4.55. The evolution of the thickness is plotted in fig. 4.54. The increasing UV treatment time generates a sharp band at 4.5 eV. The thermal cure resulted in dominant absorption structure at 4 eV.

4.5.6. Summary

A brief study of the optical properties of the material Beta, including transition layers and changes caused by UV-curing and plasma treatments has been performed.

We have observed behavior similar to the material Alpha, discussed in more detail in previous sections.

The cured material Beta shows a noticeably lower absorption in the UV range related to the porogen and its residues. We conclude that the used broadband UV-curing lamp enables an efficient removal of the porogen.

4.6.   Conclusions

We have studied a range of samples of the SiCOH low-*k* dielectrics using spectroscopic ellipsometry in the range from 1.4 to 9 eV, and evaluated the optical properties and their changes during various treatments.

The study was supported by porosimetry measurements and FTIR.

We have used the measured properties of the constituents (porogen and matrix), and the measured porosity, to interpret the observed behavior of the VIS/UV dielectric function of the low-k materials as the mixture of porogen, matrix and voids. The model allows us to estimate the actual porogen and matrix percentage.

The validity of the mixing model has been supported by experiments with a non-damaging plasma strip process. The operation caused the porogen residue removal from the pore interior without a collapse, leaving the material with a high porosity (~50%) as deduced from the mixing model.

An important practical result is that the behavior of single value of RI cannot be directly related to the film density (porosity); it is strongly influenced by presence of porogen and its residues.

The comparison of the materials cured by different UV-sources reveals a strong advantage of the broadband curing in terms of the porogen removal efficiency (this topic will be discussed in the next chapter).

It can be expected that the presence of large amounts of the porogen residues deteriorates the mechanical properties.

It was shown that the plasma damage can be detected by optical methods. This suggests an application of the fast and non-destructive optical metrology methods in the manufacturing environment.

4.6.1. Outlook

The mechanism of the porogen residue formation and its structure should be studied further. We have assumed that the structure is similar to amorphous carbon; nevertheless, the FTIR spectra show additional features (for example a peak attributed to the C=O vibrations).

While the presence of CH_3 groups bonded to SiO_2 skeleton results in changes of the dielectric constant (k-value), the impact on the VIS/UV spectra is still not known. It is possibly related to the observed 8.5 eV band of the matrix.

The behavior of the matrix itself during the UV-cure should be examined by other methods, to explain the origin and behavior of the 6 eV band.

Our experiments were influenced adversely by the presence of the porogen residues. The described He_2/H_2 non-damaging strip process can be used to prepare thin films (affected thickness around 70 nm) of relatively clean porous SiCOH material which could be subsequently studied.

The ellipsometric measurements might be expanded into infrared range.

Chapter 5 : UV-cure of low-*k* films

A study of the effect of varying deposition and curing conditions on the basic properties, and the plasma damage resistance of the low-k dielectrics; performed in IMEC in 2007 and 2008 in cooperation with A. Urbanowicz, P. Verdonck, D. De Roest, H. Sprey and M.R. Baklanov.

Based on the knowledge contained in the previous chapter, a large series of samples of the dielectric Alpha has been prepared to assess the influence of various deposition and curing conditions on the material properties. As-deposited and plasma exposed films were investigated by various techniques: infrared spectroscopy, spectroscopic ellipsometry in the range from 2 to 9 eV and ellipsometric porosimetry with toluene and water as an absorbent. The wide variety of samples enabled a quantitative analysis of the relations between the observed properties. This chapter[134] presents a detailed description of the results.

---

[134] P. Marsik, A. Urbanowicz, P. Verdonck, D. De Roest, H. Sprey and M.R. Baklanov, *Effect of Ultraviolet Curing Wavelength on Low-k Dielectric Material Properties and Plasma Damage Resistance*, in preparation

In section 1 we review the state of the art in the low-*k* and UV-curing technology and introduce the study. Section 2 describes the experimental conditions, studied samples and the measurement techniques. In section 3 we present results obtained on non-damaged and damaged samples. Various quantitative parameters of the analysis techniques are correlated and the observed phenomena discussed.

5.1.   State of the art

The industrial low-*k* dielectric material codenamed Alpha has been deposited by the plasma enhanced chemical vapor deposition (PE CVD) as a mixture of SiCOH matrix precursor and sacrificial phase - organic porogen. To remove the porogen and create the porosity in the deposited material, ultraviolet assisted thermal cure has been applied (UV-cure). The samples are heated up to over 400 °C and exposed to ultraviolet radiation for a few minutes in the nitrogen atmosphere. The UV radiation decomposes the porogen. The decomposed porogen fragments evaporate and leave behind an interconnected network of open pores.

Studied materials have the open porosities in the range of 25% to 40% with the mean pore sizes of approximately 2 nm in the diameter, and the target *k*-values of 2.3 or 2.5.[135,136,137] Apart from the porogen removal, the UV light promotes changes in the chemical and structural properties of the SiCOH matrix.

The two most commonly used low-*k* curing approaches are (i) thermal cure (annealing) without UV[138,139,140,141] and (ii) UV assisted thermal cure

[135] N. Kemeling, K. Matsushita, N. Tsuji, K. Kagami, M. Kato, S. Kaneko, H. Sprey, D. de Roest, and N. Kobayashi, *A robust k similar to 2.3 SiCOH low-k film formed by porogen removal with UV-cure*, Microelectron. Eng. **84,** 2575-2581 (2007).

[136] P. Verdonck, D. De Roest, S. Kaneko, R. Caluwaerts, N. Tsuji, K. Matsushita, N. Kemeling, Y. Travaly, H. Sprey, M. Schaekers, and G. Beyer, *Characterization and optimization of porogen-based PECVD deposited extreme low-k materials as a function of UV-cure time*, Surf. Coat. Technol. **201,** 9264-9268 (2007).

[137] P. Marsik, P. Verdonck, D. Schneider, D. De Roest, S. Kaneko and M. R. Baklanov, *Spectroscopic ellipsometry and ellipsometric porosimetry studies of CVD low-k dielectric films*, Phys. Status Solidi C **5,** 1253-1256, (2008).

[138] S. M. Gates, D. A. Neumayer, M. H. Sherwood, A. Grill, X. Wang, and M. Sankarapandian, *Preparation and structure of porous dielectrics by plasma enhanced chemical vapor deposition*, J. Appl. Phys. **101** (2007).

[139] A. Grill and V. Patel, *Ultralow dielectric constant pSiCOH films prepared with tetramethylcyclotetrasiloxane as skeleton precursor*, J. Appl. Phys. **104,** 9 (2008).

[140] L. Favennec, V. Jousseaume, G. Gerbaud, A. Zenasni, and G. Passemard, *Ultralow k using a plasma enhanced chemical vapor deposition porogen approach: Matrix structure and porogen loading influences*, J. Appl. Phys. **102** (2007).

[141] A. Zenasni, F. Ciaramella, V. Jousseaume, C. Le Cornec, and G. Passemard, *Investigation of porogen behavior during the curing process of ultralow-k spin-on materials - Chemical transformation-kinetics*, J. Electrochem. Soc. **154,** G6-G12 (2007).
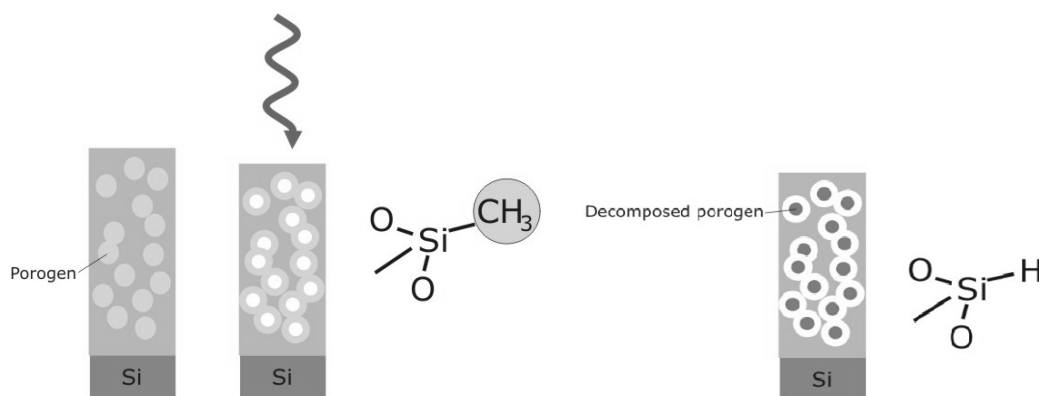
Figure 5.1. Schematic illustration of the UV-cure process. Efficient cure (left) removes the porogen and leaves the Si-CH₃ untouched. Undesired effects of the UV-cure (right) are the porogen residue formation, and the Si-CH₃ scission and replacement by the Si-H bonds.

with monochromatic or broadband light sources.[142,143,144,145,146] Recent work of Grill et al.[139] focuses on the behavior of annealed low-*k* films under variable deposition temperature, RF power and porogen choice. Our work is focused on the comparison between the UV-cures using the monochromatic light with the photon energy of 7.2 eV (λ=172 nm, lamp A) and broadband UV light with photon energies lower than 6.2 eV (λ>200 nm, lamp B). We correlate the lamp effects with other process variables (deposition conditions), and study their impact on the physical-chemical properties (porosity, composition) of the UV-cured films.

The Si-CH₃ bonds are broken by the UV photons,[142,147] the energy threshold for the Si-CH₃ scission has been estimated at approximately 6.5 eV from quantum-chemical calculations[148] and the fundamental difference

[142] S. I. Nakao, J. Ushio, T. Ohno, T. Hamada, Y. Kamigaki, M. Kato, K. Yoneda, S. Kondo and N. Kobayashi, *UV/EB cure mechanism for porous PECVD/SOD low-k SiCOH materials*, *Proceedings of the Interconnect Technology Conference* (IEEE, New York), 66-68 (2006).

[143] S. Eslava, F. Iacopi, A. M. Urbanowicz, C. E. A. Kirschhock, K. Maex, J. A. Martens, and M. R. Baklanov, *Ultraviolet-assisted curing of organosilicate glass low-k dielectric by excimer lamps*, J. Electrochem. Soc. **155,** G231-G236 (2008).

[144] A. Zenasni, V. Jousseaume, P. Holliger, L. Favennec, O. Gourhant, P. Maury, and G. Gerbaud, *The role of ultraviolet radiation during ultralow k films curing: Strengthening mechanisms and sacrificial porogen removal*, J. Appl. Phys. **102** (2007).

[145] A. M. Urbanowicz, B. Meshman, D. Schneider, M.R. Baklanov, *Stiffening and hydrophilisation of SOG low-k material studied by ellipsometric porosimetry, UV ellipsometry and laser-induced surface acoustic waves*, Phys. Status Solidi A **205,** 829 (2008).

[146] T. S. Kim, N. Tsuji, K. Matsushita, N. Kobayashi, D. Chumakov, H. Geisler, E. Zschech, and R. H. Dauskardt, *Tuning depth profiles of organosilicate films with ultraviolet curing*, J. Appl. Phys. **104,** 6 (2008).

[147] J. Ushio, T. Ohno, T. Hamada, S. I. Nakao, K. Yoneda, M. Kato, and N. Kobayashi, *Ultraviolet-curing mechanism of porous-SiOC*, Jpn. J. Appl. Phys. Part 2-Letters & Express Letters **46,** L405-L407 (2007).

[148] L. Prager, P. Marsik, J. W. Gerlach, M. R. Baklanov, S. Naumov, L. Pistol, D. Schneider, L. Wennrich, P. Verdonck, M. R. Buchmeiser, *Effect of pressure on efficiency of UV curing of CVD-derived low-k material at different wavelengths*, Microelectron. Eng. **85,** 2094-2097 (2008).

between the UV-curing wavelengths in the effect on bonding structure of low-*k* films was already observed.[143,145,146,149] With enough photon energy, the Si-CH$_3$ bond is replaced by the more stable Si-H bond or Si-O-Si crosslink, leading to shrinkage, densification, improved mechanical properties[144,147,150] and a rearrangement of the silica backbone towards the more rigid "network" structure.[136,151]

Another important difference between the curing conditions (see fig. 5.1), in particular UV sources, is the porogen removal efficiency. Only a little attention is paid to the porogen residue (incompletely removed porogen), and its impact on the physical-chemical properties of the low-*k* dielectric.[139,140,141,152] The issue of possible existence of the porogen residues was partially discussed in the recent work,[138,144] but remains overlooked due to a limited sensitivity of the conventional FTIR spectroscopy to the C=C absorbance band.

In the previous chapter we have presented a sensitive method of the porogen residues detection, applying spectroscopic ellipsometry in the UV range. We have concluded that the changes of refractive index in the visible range, commonly denoted as RI and measured at 633 nm, cannot be directly related to density, and must be interpreted in terms of changes of the optical absorption in UV. The absorption spectra in the range from 3 to 7 eV (wavelengths from 400 down to 180 nm) are attributed to the presence of the organic porogen[137,153] and its residues, identified as an amorphous carbon-like material.

We have performed identical analyses on the studied samples, combining the ellipsometric porosimetry, spectroscopic ellipsometry to get information about the composition of matrix, porogen residues and air mixture. This approach provides a complementary information to the chemical composition from FTIR analyses.

The low-*k* dielectrics are exposed to various etching, stripping and cleaning plasmas in the Cu/low-*k* integration scheme. The chemical and mechanical stability is therefore a key merit of the material optimization. It was shown that oxidizing and reducing plasma chemistries for the

---

[149] M. Matsuura, K. Goto, N. Miura, S. Hashii and K. Asai, *Film Characterization of Ultra Low-k Dielectrics Modified by UV Curing with Different Wavelength Bands* Material Research Society Symposium Proceedings **914,** 0914-F01-06 (2006).

[150] F. Iacopi, Y. Travaly, B. Eyckens, C. Waldfried, T. Abell, E. P. Guyer, D. M. Gage, R. H. Dauskardt, T. Sajavaara, K. Houthoofd, P. Grobet, P. Jacobs, and K. Maex, *Short-ranged structural rearrangement and enhancement of mechanical properties of organosilicate glasses induced by ultraviolet radiation*, J. Appl. Phys. **99,** 053511 (2006).

[151] C. H. Huang, H. L. Huang, C. I. Hung, N. F. Wang, Y. H. Wang, and M. P. Houng, *Bond structure in porous SiOCH low-k film fabricated by ultraviolet irradiation*, Jpn. J. Appl. Phys. **47,** 1532-1535 (2008).

[152] A. Zenasni, B. Remiat, C. Waldfried, Ch. Le Cornec, V. Jousseaume, G. Passemard, *Thermal furnace cure and Ultraviolet assisted curing impact on SiCOH spin-on low dielectric constant material*, Thin Solid Films,**516,** 1097-1103 (2008).

[153] S. Eslava, G. Eymery, P. Marsik, F. Iacopi, C. E. A. Kirschhock, K. Maex, J. A. Martens, and M. R. Baklanov, *Optical property changes in low-k films upon ultraviolet-assisted curing*, J. Electrochem. Soc. **155,** G115-G120 (2008).

photoresist mask removal affect the porous dielectric,[154,155] causing the CH$_3$ depletion in the surface layer, leading to hydrophilic SiO$_2$ like material.[156] The presence of water deteriorates the dielectric properties and is therefore highly undesired. The plasma damage can be quantified by the surface or volume hydrophilicity, FTIR –OH signature[157] and by the thickness of the modified layer; the letter can be detected by TEM or TOF-SIMS[156] or ellipsometry either directly,[158] or after the removal of the damaged surface layer with a HF dip.[155]

The effect of the NH$_3$ cleaning plasma[159] on the blanket low-*k* layers is studied here, and the plasma damage is correlated with the properties of the UV-cured samples.

5.2. Experiment

We have deposited the low-*k* material as 200 nm thick films on un-doped 300 mm silicon (100) wafers in the ASM Eagle 12® system using variable flow rates of the porogen and matrix precursors, and variable substrate temperature and RF power.

5.2.1. Deposition conditions

Two precursor ratios were chosen in order to achieve (i) the material with a higher target porosity around 33%, and the target *k*-value of 2.3, denoted as "Alpha1" and (ii) the material with a lower porosity around 25%, and the target *k*-value of 2.5, denoted as "Alpha2" as shown in Table 5.1. The deposition conditions were chosen as (i) higher substrate temperature (300°C) and higher RF power (1850 – 1900 W), further denoted by the abbreviation "Hi" and (ii) lower temperature (250°C) and lower RF power (1400 W), denoted by the abbreviation "Lo".

---

[154] N. Posseme, T. Chevolleau, T. David, M. Darnon, O. Louveau, and O. Joubert, *Mechanisms of porous dielectric film modification induced by reducing and oxidizing ash plasmas*, J. Vac. Sci. Technol.B **25,** 1928-1940 (2007).

[155] X. F. Hua, M. S. Kuo, G. S. Oehrlein, P. Lazzeri, E. Iacob, M. Anderle, C. K. Inoki, T. S. Kuan, P. Jiang, and W. L. Wu, *Damage of ultralow k materials during photoresist mask stripping process*, J. Vac. Sci. Technol. B **24,** 1238-1247 (2006).

[156] D. Shamiryan, M. R. Baklanov, S. Vanhaelemeersch, and K. Maex, *Comparative study of SiOCH low-k films with varied porosity interacting with etching and cleaning plasma*, J. Vac. Sci. Technol. B **20,** 1923-1928 (2002).

[157] A. M. Urbanowicz, D. Shamiryan, M. R. Baklanov, and S. De Gendt, *Oxygen chemiluminescence in He plasma as a method for plasma damage evaluation,* Microelectron. Eng. **85,** 2164-2168 (2008).

[158] P. Marsik, A. M. Urbanowicz, K. Vinokur, Y. Cohen and M. R. Baklanov, *Changes of UV Optical Properties of Plasma Damaged Low-k Dielectrics for Sidewall Damage Scatterometry*, Material Research Society Symposium Proceedings **1079,** 1079-N07-04 (2008).

[159] A. M. Urbanowicz, M. R. Baklanov, J. Heijlen, Y. Travaly and A. Cockburn, *Damage reduction and sealing of low-k films by combined He and NH3 plasma treatment*, Electrochem. Solid-State Lett. **10,** G76-G79 (2007).

Table 5.1. The samples and notation. The Alpha1 or Alpha2 denotes the material, A or B refers to lamp, Hi or Lo refers to higher or lower deposition temperature and RF power, and the last number 1 or 2 denotes increasing curing time.

Material – target *k*		Alpha1-2.3	Alpha2-2.5	Alpha1-2.3	Alpha2-2.5
Light source		Monochromatic-A		Broadband-B	
Deposition conditions, curing time	Hi	Alpha1AHi1	Alpha2AHi1	Alpha1BHi1	Alpha2BHi1
		Alpha1AHi2	Alpha2AHi2	Alpha1BHi2	Alpha2BHi2
	Lo	Alpha1ALo1	Alpha2ALo1	Alpha1BLo1	Alpha2BLo1
		Alpha1ALo2	Alpha2ALo2	Alpha1BLo2	Alpha2BLo2

5.2.2. UV sources used for curing

The deposited samples were treated by the UV-cure at the temperature above 400°C in a nitrogen purged ambient. Two curing lamps were used for the experiment: (i) monochromatic lamp "A" emitting photons with the energy of 7.2 eV (λ=172 nm) and (ii) broadband lamp "B" with photon energies below 6.2 eV (λ>200 nm). For both lamps, two curing times were chosen. Shorter time "1" is a half of the longer time "2", which is set to the curing time for standard process. We have worked with 16 (2^4) samples with variable properties as shown in table I. Only already UV-cured samples were analyzed in this work, however, the thicknesses were measured before and after the UV-cure, allowing the calculation of shrinkages of the films.

5.2.3. Plasma damage resistance test

Two identical sets of 16 UV-cured samples were prepared. One set was subjected to cleaning plasma to evaluate the impact of the material properties on the plasma damage. We have applied 10 sec of NH_3 plasma, used for post-CMP Cu cleaning at 350 °C in the PECVD chamber, at the pressure of 4.2 Torr.

5.2.4. Analytical methods

The 32 samples (16 non-damaged and 16 NH_3 plasma damaged) were analyzed by using Fourier-transform infrared spectroscopy (FTIR), spectroscopic ellipsometry in the UV range (PUVSE), and ellipsometric porosimetry (EP).

FTIR

The infrared absorption in the range of 400-4000 cm^{-1} was measured using a FTIR spectrophotometer Biorad QS2200 ME, with the 4 cm^{-1} spectral resolution. The optical response has been evaluated as absorbance; then the absorbance of the substrate silicon wafer has been subtracted, and the resulting spectrum treated by the baseline subtraction and renormalization. For improved accuracy and minimization of background artifacts, each substrate spectra was measured on a piece from the same wafer as the respective film sample.

All of the 32 FTIR spectra were fitted by multiple (23-27) Gaussian peaks in the regions covering important features. The areas of the peaks were calculated from the fitted parameters and normalized to the area of the

dominant SiO_2 band. In the following, all the conclusions related to FTIR are drawn from these quantitative data.

Spectroscopic ellipsometry

The optical response of the materials in the visible and ultraviolet range was measured using a variable-angle of incidence spectroscopic ellipsometer Sopra GES5 PUV in the range from 2 to 9 eV (wavelengths from 620 to 138 nm). For all of the samples, we have measured at three angles of incidence of 60, 70 and 80 degrees.

In the case of non-damaged samples, the measured spectra of the ellipsometric angles Ψ and Δ were fitted by a single layer G-L optical model (substrate – layer – ambient) using the Marquardt-Levenberg algorithm.

As shown recently,[146,153] the depth inhomogeneity of the UV-cure is determined by the nature of light propagation.[160] However, in the case of our ellipsometric measurements, the single layer models were sufficient to match the measured data. We presume that the construction of the industrial curing chamber, used in our research, might be responsible for the improved homogeneity of the curing effect: several powerful lamps are located near the wafer surface, therefore not only the normal-incident rays are present in the film subjected to the cure. The total curing field is given by a continuum of rays incoming to the sample from all directions. Moreover, the dynamics of the curing process, particularly the shrinkage, probably blurs the interference pattern recorded in the film across its thickness.

On the other hand, the ellipsometric measurements of the plasma damaged samples required more complex ellipsometric models (see previous chapter, subsection 4.4.1). We have tested: 1) a double layer model (substrate – non-damaged layer – damaged layer - ambient) or 2) a triple layer model (substrate – non-damaged layer – carbon depleted layer – densified damaged layer – ambient), where the properties of the non-damaged bottom layer were taken from the fit of the non-damaged sample and the damaged layer (layers) were fitted with a limited number of parameters, based again on the model of non-damaged material. The relevancy of such models will be discussed further in next section.

Ellipsometric porosimetry

The porosity measurements were performed using a prototype ellipsometric porosimeter EP10, equipped with a fixed angle of incidence (70 deg) ellipsometer Sentech 801, operating in the wavelength range between 350 and 850 nm, mounted on a high vacuum chamber with a controllable pressure of solvent vapors. The principle of ellipsometric porosimetry (EP) is based on the pressure dependent adsorption of a fluid (in our case toluene or water) into the pores. The absorbed fluid modifies the optical properties of the porous sample in the means of effective media and the changes are measured by ellipsometry. In the case of

---

[160] G. Lippmann, in: *Nobel Lectures, Physics 1901-1921*, Elsevier Publishing Company, Amsterdam (1967).

toluene, the volume ratio of the open pores is then obtained as well as the pore-size distribution. By using water as the absorbent, information about the internal hydrophilicity of the porous sample interior is collected.

Mixing model

In the previous chapter, we proposed an interpretation of the optical response of the low-*k* materials in the visible and ultraviolet range in terms of the Bruggeman mixture of matrix SiCOH material, porogen and voids.

The analysis of the optical spectra combined with the porosity measured using the EP allows a sensitive detection of the volume composition of the samples. We have performed this analysis on the 16 non-damaged samples, and correlated the resulting values with other relevant properties. We show that most of the behavior of low-*k* dielectrics (RI, hydrophilicity and plasma damage) is based on the 3 phase composition of the films.

Statistical correlation

For a simplification of the enormous amount of information contained in the above mentioned analysis of 32 samples, we present further graphs showing the most important relations between individual quantities. Some other relations between properties of the 16 resp. 32 samples will be quantified using statistical correlation coefficients:

$$r_{xy} = \frac{n\sum x_i y_i - \sum x_i \sum y_i}{\sqrt{n\sum x_i^2 - \left(\sum x_i\right)^2}\sqrt{n\sum y_i^2 - \left(\sum y_i\right)^2}} \ , \qquad (5.1)$$

where x_i and y_i are particular quantities of each sample, and n is the number of samples in the set, with the summations from 1 to n . The value of the correlation coefficient varies between $r=1$ (showing a strong positive correlation) and $r=-1$ (for a negative correlation – anticorrelation). Low absolute values of r indicate a weak coupling of the involved quantities.

5.3.   Results and discussion

The results and discussion are divided in two main parts. In the first part an effect of deposition and UV curing conditions on physical-chemical properties of the low-*k* films is discussed. In the second part the effect of NH$_3$ plasma (used for the CuO$_x$ reduction in the Cu/low-*k* integration) on differently prepared low-*k* films is investigated.

5.3.1. Effect of deposition and curing conditions on physical-chemical properties of the low-*k* material

In this subsection we discuss the FTIR, porosimetry and spectroscopic ellipsometry studies of as deposited and UV cured low-*k* films. We show that the UV-cure with lamp A is leading to stronger effects than lamp B in
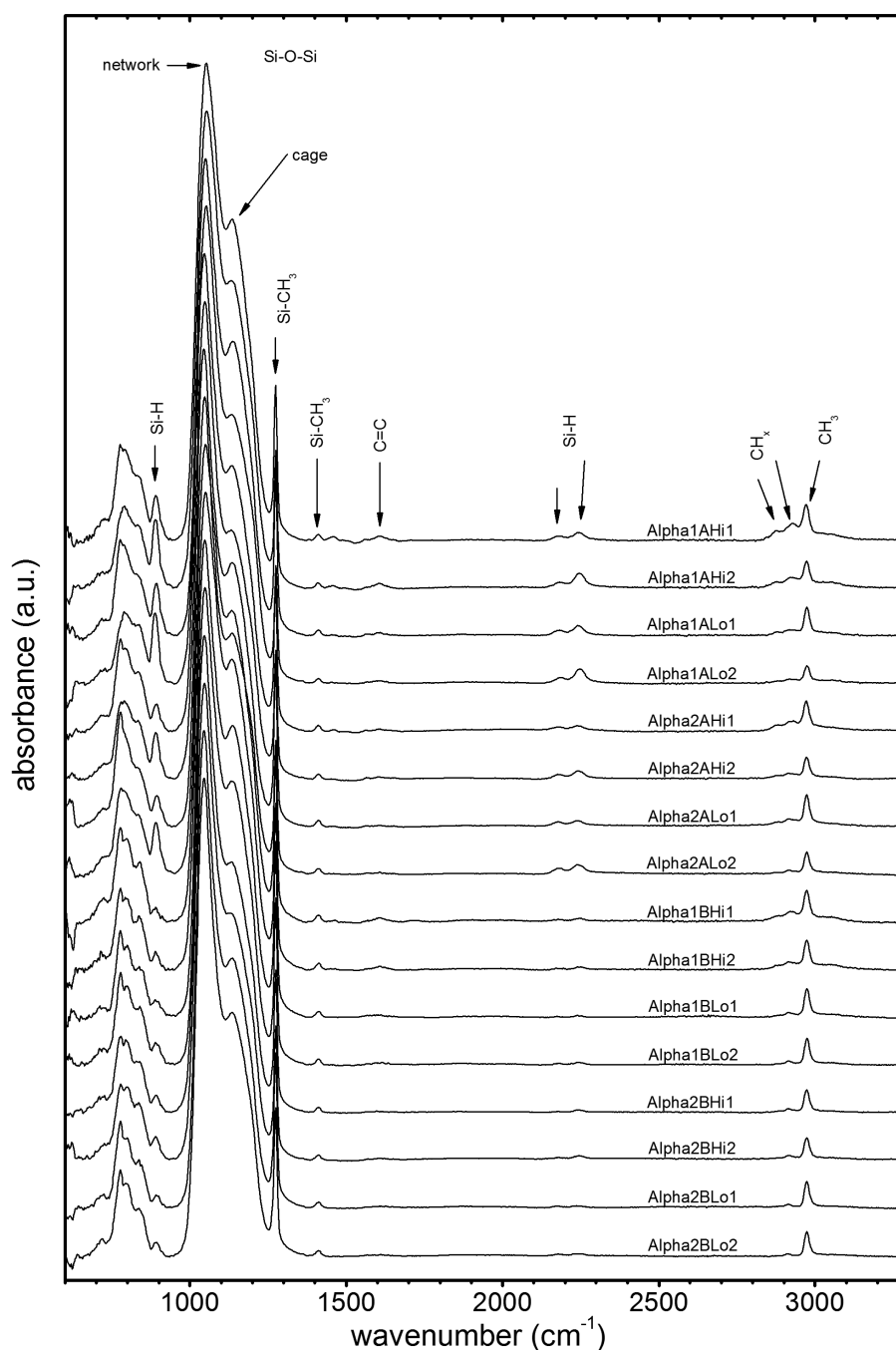
Figure 5.2. Infrared absorbance of UV-cured films.

most of the mentioned processes (shrinkage, "networking", -CH$_3$ scission) except for the porogen (CH$_x$) removal. As expected, the increasing UV-curing time always introduces greater changes to the composition. Analysis of the volume composition shows a significant variance of the porogen residue content depending on both deposition and curing conditions.

FTIR

Figure 5.2 presents the FTIR absorbance spectra of the deposited and UV-cured samples. The chosen condition led to similar samples. We focused our attention on the following features in the spectra. The porogen CH$_x$
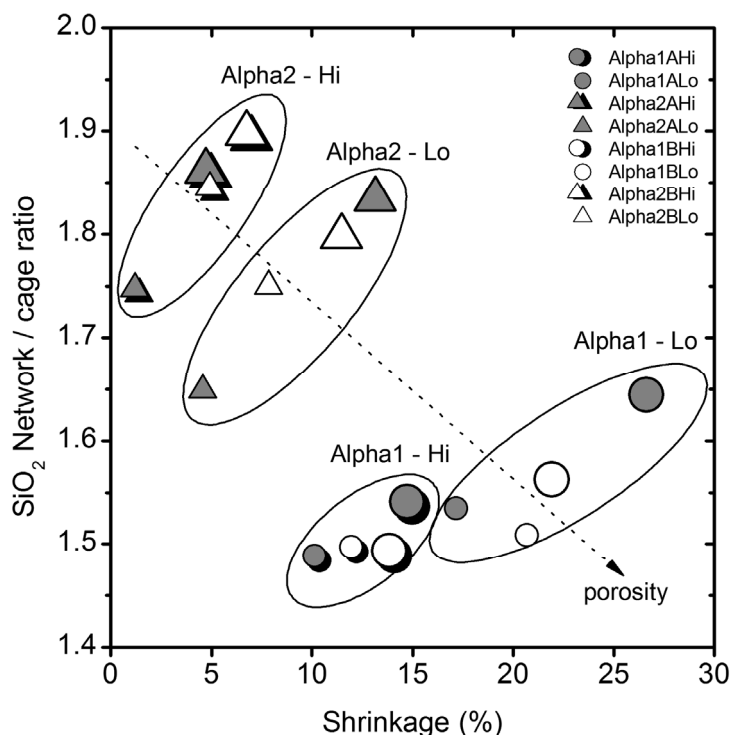
Figure 5.3. Ratio of FTIR peak areas related to SiO$_2$ network and cage versus the shrinkage of the UV-cured films. Increasing symbol size denotes increasing curing time. The dashed arrow follows the direction to higher porosities.

absorption band composed of multiple peaks is observed around 2900 cm^{-1}; the highest peak at 2973 cm^{-1}, attributed to CH$_3$, shows a response also from methyl groups bonded in the SiCOH matrix. The Si-CH$_3$ signature is pronounced at 1275 cm^{-1} and 1412 cm^{-1}. The SiO$_2$ band is observed as a dominant double peak structure localized at 1135 cm^{-1} (cage) and 1063 cm^{-1} (network). The Si-H bond vibration is detected around 2220 cm^{-1} and at 890 cm^{-1}. We observe also the presence of C=C bonds in all the samples as a low-amplitude band at 1600 cm^{-1}. The C=C band remains present during the UV-cure and is attributed to the decomposed porogen residues.

FTIR – porogen removal

One can see from the FTIR analysis that the UV curing time and the UV source used has the most pronounced effect on the bonding structure of low-*k* material. At the given curing times, lamp B UV-cure results in a lower porogen CH$_x$ signature in most of the cases. We have fitted the CH$_x$ absorbance around 2900 cm^{-1} using four Gaussian peaks (at 2878, 2918, 2973 cm^{-1}, and broad band at 2984 cm^{-1}). The fitted parameters were used to calculate the integrated area, excluding the 2973 cm^{-1} peak attributed to CH$_3$. To compare the UV-lamps, we have calculated 8 ratios of the peak areas between samples in otherwise matching pairs. The average ratio was 1.4 in favor of lamp B (1.4x lower CH$_x$ content).
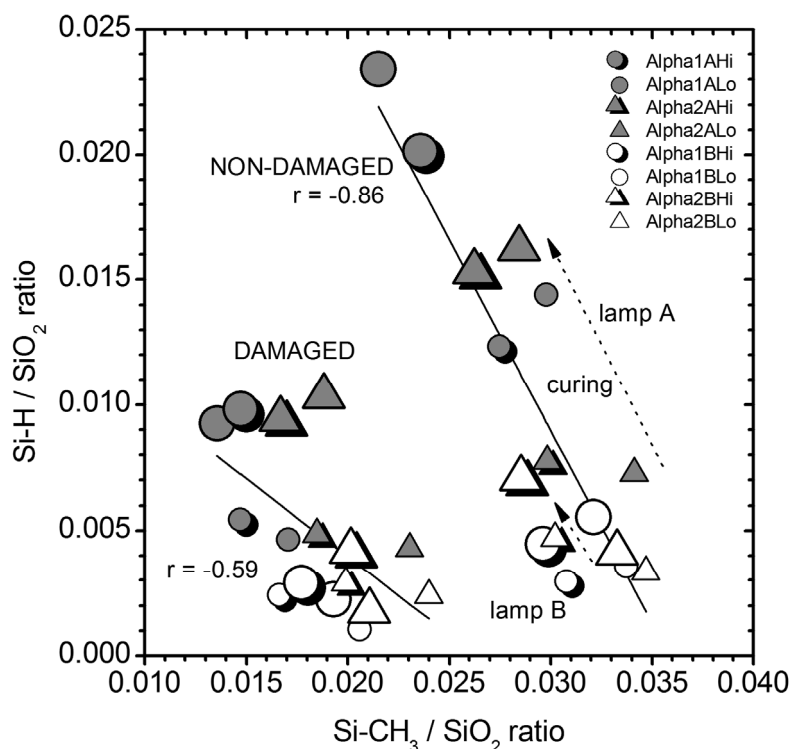
Figure 5.4. Area of FTIR peaks of Si-H versus Si-CH$_3$ bond vibrations, normalized to the peak area of SiO$_2$ for UV-cured non-damaged samples and NH$_3$ plasma damaged samples. Increasing symbol size denotes increasing curing time. The solid lines represent the linear regressions of the each respective 16 points.

FTIR – Si-O-Si structure

There is also a variability in the sample set related to the SiO$_2$ backbone structure. Figure 5.3 shows the ratio of the fitted Gaussian peaks assigned to the network (around 1063 cm^{-1}) and cage structure (around 1135 cm^{-1}) of the SiO$_2$ skeleton ("networking") compared to the shrinkage of the film during the UV-cure. We observe the correlation between the "networking" and the shrinkage with increasing curing time, but this correlation occurs separately in the groups of the same material, deposited at given conditions. In all four groups, the monochromatic lamp A induces more changes than the lamp B. Among the groups, this correlation is suppressed in spite of porosity; from material to material, the porosity is the leading factor influencing the shrinkage and the "networking": 1) The samples with higher porosities show also a higher shrinkage (with the correlation r=0.80) and 2) higher porosity is followed by a lower network to cage ratio (anticorrelation, r=-0.87). The former suggests that the pore collapse has a stronger impact on the material shrinkage than the replacement of Si–CH$_3$ by Si–H, as commented below. The latter might be the result of a distortion of the matrix by the porogen removal, or simply a secondary effect of an insufficient shrinkage and densification.
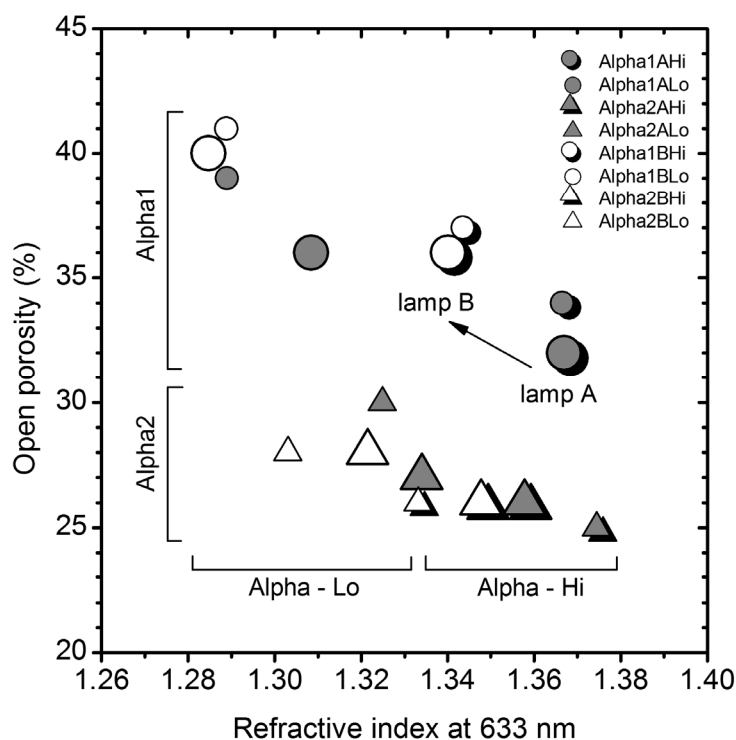
Figure 5.5. Porosity measured by toluene EP and the refractive index measured at 633 nm in vacuum. Increasing symbol size denotes increasing curing time.

FTIR – CH$_3$ depletion

We observe a strong anticorrelation (r=-0.86) of Si-CH$_3$ absorption band positioned at 1275 cm^{-1} and the Si-H absorption band at 890 cm^{-1} (fig. 5.4). In all cases the increased curing time leads to a higher -CH$_3$ depletion and Si-H generation and the effect is much stronger for the monochromatic 172 nm lamp A. The mechanism of the Si-CH$_3$ scission and replacement by Si-H has been described in the literature.[142,147] Comparing the Si-CH$_3$ removal and Si-H replacement data with the shrinkages of the samples, we cannot attribute this mechanism to be crucial for the shrinkage in our set of samples.[144] The higher shrinkage is related to a lower SiCH$_3$ signature only through a weak anticorrelation (r=-0.27). As mentioned before, the porosity is a much stronger factor within this set of various samples. In the NH$_3$ plasma damaged set of 16 samples, the Si-CH$_3$ and Si-H anticorrelation is reduced to r=-0.59, and the dependence of the two parameters is modified. The change of the derivative of the linear fit (see fig. 5.4) shows a stronger reduction of Si-H bonds during the plasma exposure and therefore suggests a higher sensitivity of the Si-H rich materials to the plasma damage.

VIS/UV spectroscopic ellipsometry and porosity

Differences related to choice of the lamp are observed in the optical measurements in visible range. Figure 5.5 shows the refractive index at the wavelength of 633 nm compared with the measured open porosity. The open porosity has been determined by the ellipsometric porosimetry with toluene. The Alpha1 material deposited and cured under various conditions exhibits porosities between 32% and 41% and the Alpha2 material exhibit porosities between 25% and 30%. The separation of the
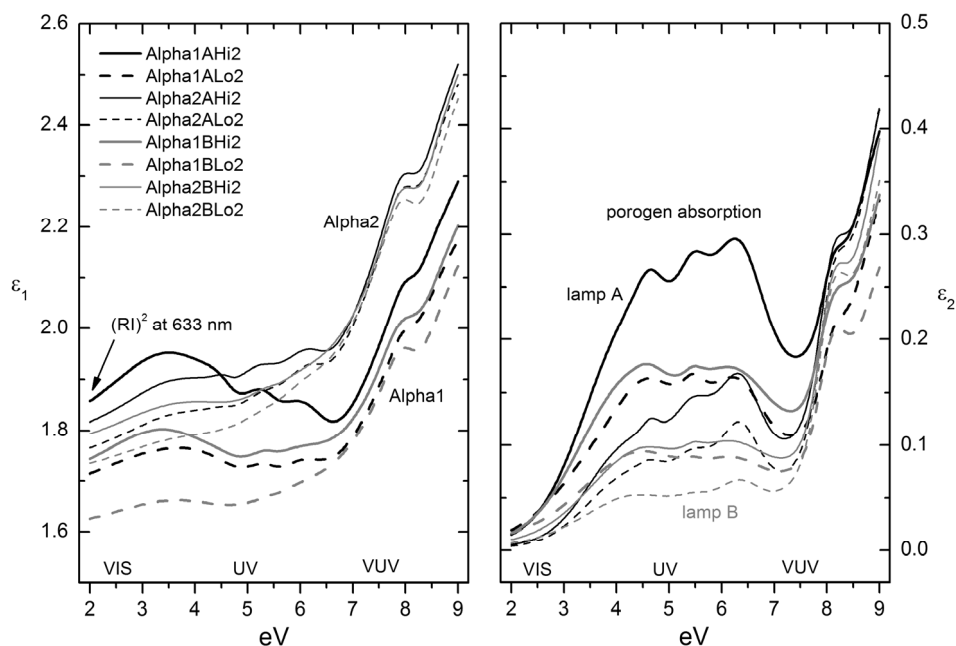
Figure 5.6. Dielectric functions of selected UV-cured samples; only results on samples with the longer curing time are shown.

materials must be expected as the flow ratio of the matrix and of the porogen precursor during the deposition differs. Nevertheless, there is also a significant effect of the deposition conditions and of the curing lamp. The samples deposited using lower temperature and RF power are more porous and have a lower refractive index than the ones deposited using the higher temperature and RF power. The same is valid for the broadband lamp B compared to the monochromatic lamp A. The effect of the UV curing time is not significant in this plot, because both refractive index and porosity reach extreme values between the two applied curing times.

It is important to notice here that the reciprocal relation of the porosity and refractive index is not completely due to the dependence of the refractive index on the density and therefore porosity; the ranges of refractive indices of the two materials overlap, while they differ in the porosities.

In fig. 5.6, we plot the dielectric functions obtained by fitting the ellipsometric data in the range from 2 to 9 eV. We have selected only the samples with longer curing time, as the evolution of the spectra during the UV-cure was already explained in the previous chapter. The optical properties of our low-k films are given by the nature of SiO_x backbone, resulting in the overall Cauchy-like dispersion, and the presence of an absorption edge above 8 eV. The porogen and its residues are observable as the triple-peak structure in absorption between 3 and 7 eV, and the corresponding structure in the real part of ε, leading to changes in the visible range. Particularly the RI value at 633 nm (1.96 eV) is shifted due to the presence of the porogen residues.

The material Alpha1 is more porous than Alpha2; consequently, the real part of ε is lower, which is valid only above 6 eV due to the effect of the

Table 5.2. The structural parameters of the samples: measured EP porosity, estimated matrix and residue percentage, measured shrinkage, modal pore radius and PSD width.

Sample	EP void (%)	Matrix (%)	Porogen reisidue (%)	Shrinkage (%)	Pore radius (nm)	PSD width (nm)
Alpha1AHi1	34	43	23	10	0.9	0.5
Alpha1AHi2	32	44	24	15	0.9	0.5
Alpha1ALo1	39	50	11	17	1.6	1.8
Alpha1ALo2	36	52	12	27	1.4	1.5
Alpha2AHi1	25	63	12	1	0.8	0.4
Alpha2AHi2	26	62	12	5	0.9	0.4
Alpha2ALo1	30	64	6	5	1.1	0.8
Alpha2ALo2	27	66	7	13	1.1	0.7
Alpha1BHi1	37	46	17	12	1.1	0.8
Alpha1BHi2	36	49	15	14	1.1	0.8
Alpha1BLo1	41	51	8	21	1.9	1.6
Alpha1BLo2	40	53	7	22	1.9	1.6
Alpha2BHi1	26	67	7	5	0.9	0.6
Alpha2BHi2	26	67	7	7	0.9	0.6
Alpha2BLo1	28	68	4	8	1.2	1.0
Alpha2BLo2	28	69	3	11	1.2	1.0

residues. Accordingly, Alpha1 contains also more residues as the initial porogen content is higher. From the signature of the porogen in the UV absorption, we conclude that the lamp B is more efficient in the porogen removal then lamp A, and the deposition conditions also play an important role: using the lower deposition temperature and lower RF power setting (250°C at 1400 W, 300°C at 1900 W) leads to a lower porogen residue content.

Volume composition

In previous chapter, we have proposed a method for the estimation of the volume composition of the matrix, air and porogen mixture using the measured porosity and known optical spectra of porogen material and dense SiCOH matrix. Applying this method, we have obtained the volume compositions of the 16 UV-cured samples, summarized in Table 5.2.

Figure 5.7 shows the volume composition of the samples calculated from the percentages by applying the measured shrinkage. Therefore, the actual volumes are presented (in arbitrary units), setting the initial (as-deposited) volume to 100 (a.u.). We observe basic difference between the matrix volumes of the material Alpha1 (deposited with less matrix precursor and more porogen) and Alpha2 (more matrix precursor, less porogen), while the volume of the matrix remains almost constant during the cure and the shrinkage occurs mostly through the reduction of porogen and void volume.

However, in most of the cases, the matrix volume is reduced with increasing curing time, and the effect is stronger for the monochromatic lamp A, which supports directly the proposed mechanism of shrinkage due
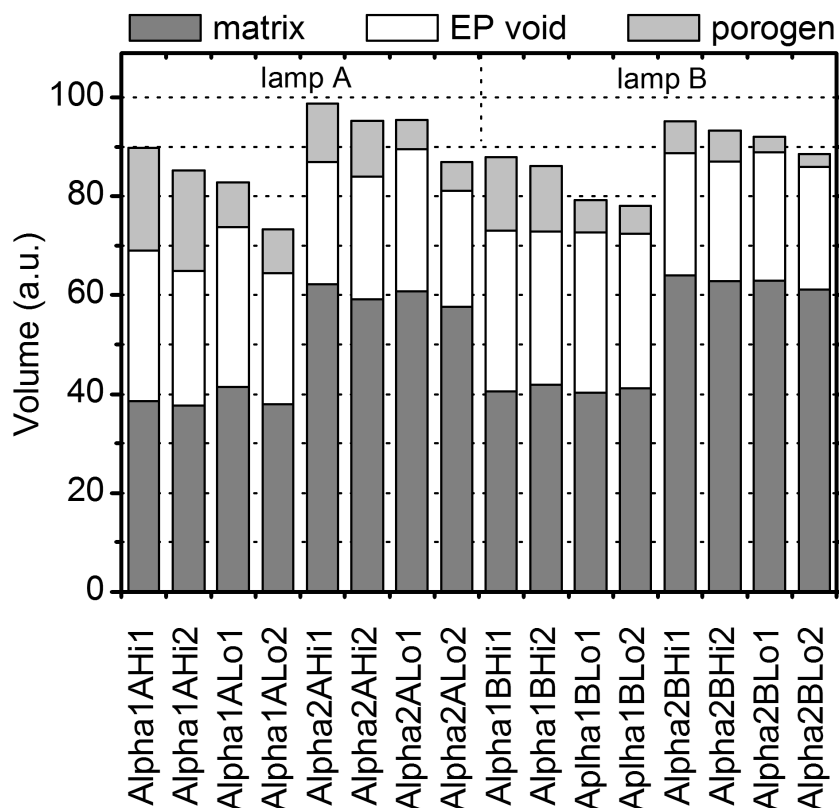
Figure 5.7. Estimated compositions of the samples recalculated to arbitrary volume units using the measured shrinkage.

to the $SiCH_3$ removal. The mean volumes (in arbitrary units) of the matrix for the four groups of samples with given material and curing lamp are: Alpha1A (38.9±1.7), Alpha1B (41.0±0.8), Alpha2A (60.0±2.0), Alpha2B (62.8±1.2). These data show quantitatively that the lamp A leads to 1) a stronger reduction of volume of the matrix (a lower actual volume) and 2) greater changes from sample to sample (a wider dispersion of values).

It should be noted that the porogen removal (creation of pores) is competing with the shrinkage of the samples (collapsing the pore volume). We have observed the reduction of porosity by 0-2% for the longer curing time compared to shorter curing time for every given combination of material, deposition and curing lamp. Thus, for given moderate curing times, the shrinkage is the stronger effect and leads to the collapse of the pores.

However, for the full set of samples, the higher shrinkages are observed on samples with higher porosities, as mentioned before.

Ellipsometric porosimetry with toluene as an absorbent

The porosity and pore size distribution (PSD) was measured by EP for all 16 non-damaged samples. We represent the measured distribution of radii by the modal value and arbitrary chosen width of the distribution. In Table 5.2 we have summarized the porosity (EP void), the modus of PSD (pore radius) and the PSD width. Figure 5.8 shows the pore size and porosity of the UV-cured samples. In most of the cases the detected pore
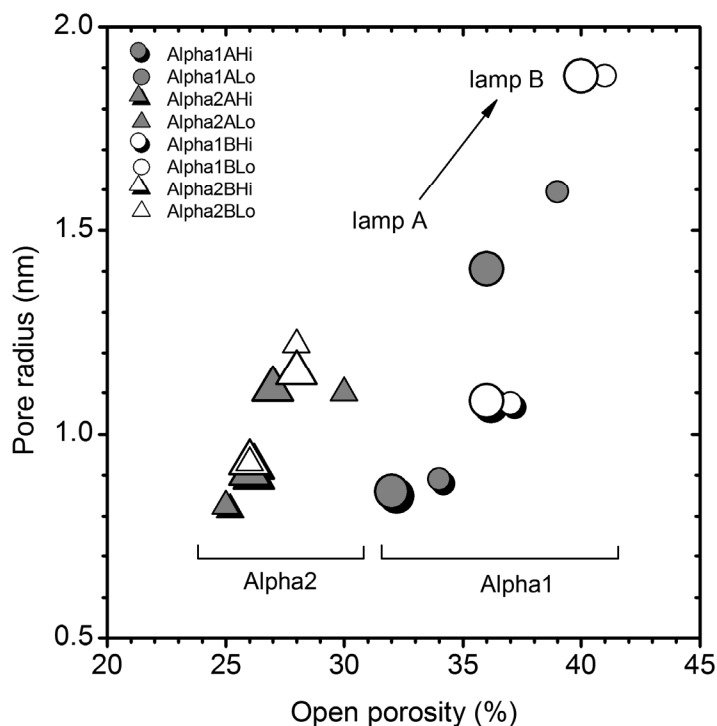
Figure 5.8. The pore radius and the total open porosity of the samples measured by ellipsometric porosimetry with toluene.

size and the PSD width is greater for samples cured by the broadband lamp B than those cured by the monochromatic lamp A. Significant variation to the PSD is observed comparing the samples deposited at differing conditions. The samples deposited using the lower temperature and RF power contain larger pores, with widely distributed sizes. The presence of a variety of different pore sizes might result in a better interconnectivity, improve the porogen removal efficiency and eventually explain the different amount of porogen residues for the samples deposited under different conditions, when the other variables (i.e. material, curing lamp and time) are fixed.

The two materials exhibit quite similar pore size distributions, the pore sizes in the lower porosity material (Alpha2) are smaller and the PSD is narrower compared to the material high porosity material (Alpha1). The UV curing time does not introduce any significant changes to the PSD in most of the cases.

5.3.2. Plasma damage resistance versus deposition conditions

In order to evaluate the plasma damage resistance and to identify the material properties responsible for the resistance, we have exposed the samples to NH_3 plasma for 10 seconds. The damage caused by the plasma has been evaluated and related to the properties presented in the previous subsection.

The strip plasmas affect the porous low-*k* films by a carbon (-CH$_3$) depletion (fig. 5.4) from the surface layer (usually tens of nanometers thick), followed by the hydrophilisation (measurable as the increase of
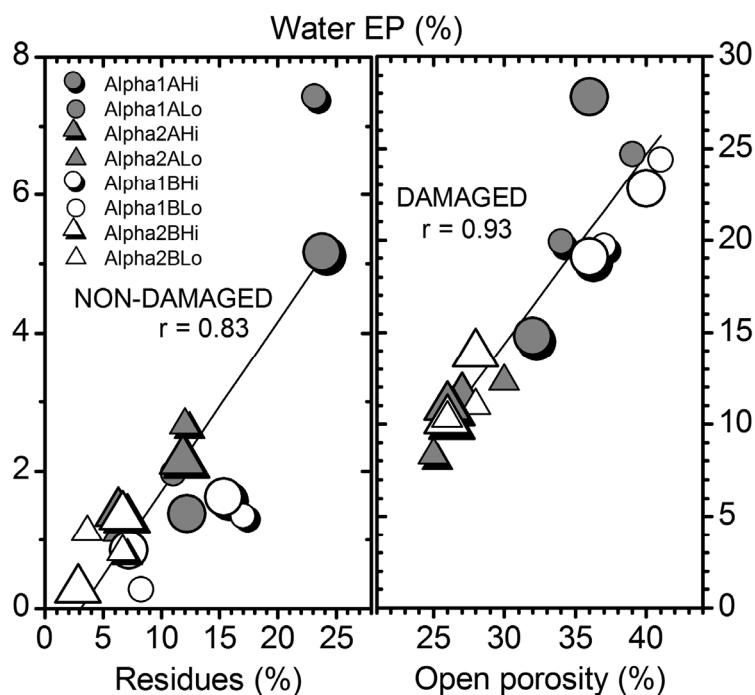
Figure 5.9. The amount of absorbed water at the saturation pressure measured by water based EP for the UV-cured non-damaged samples as a function of porogen residues percentage (left) and for the NH$_3$ plasma damaged samples as a function of porosity (right). Increasing symbol size denotes increasing curing time. The solid lines represent the linear regressions of each respective 16 points.

WEP or the presence of –OH in infrared absorbance) and shrinkage (collapse of damaged layer). The porogen residues are removed from the surface layer.

Ellipsometric porosimetry with water as an absorbent

The internal hydrophilicity of the non-damaged and damaged samples has been measured by water based EP (fig. 5.9). No correlation between the WEP values of the non-damaged and damaged samples can be found (r=0.02). The water absorption in the non-damaged set is determined by the deposition and curing conditions: The samples deposited at the low temperature and RF power and cured by the broadband lamp B show least water absorption and vice versa. The porosity of the material has no impact on the non-damaged hydrophilicity (r=-0.002), but a high correlation with the porogen residues (r=0.83) suggest that they may work as the condensation seeds for the water absorption (correlation with the Si-CH$_3$ depletion or Si-H is very low as well).

In the NH$_3$ plasma damaged samples, the amount of absorbed water is driven by porosity (r=0.93) in two ways: the higher porosity allows an easier penetration of the plasma-generated radicals and simply the higher porosity provides more space for the absorbed water, as the percentages are close to the total open porosities. The higher porosity is a result of the more efficient porogen removal and therefore the porogen residues actually prevent or slow down the plasma damage process.
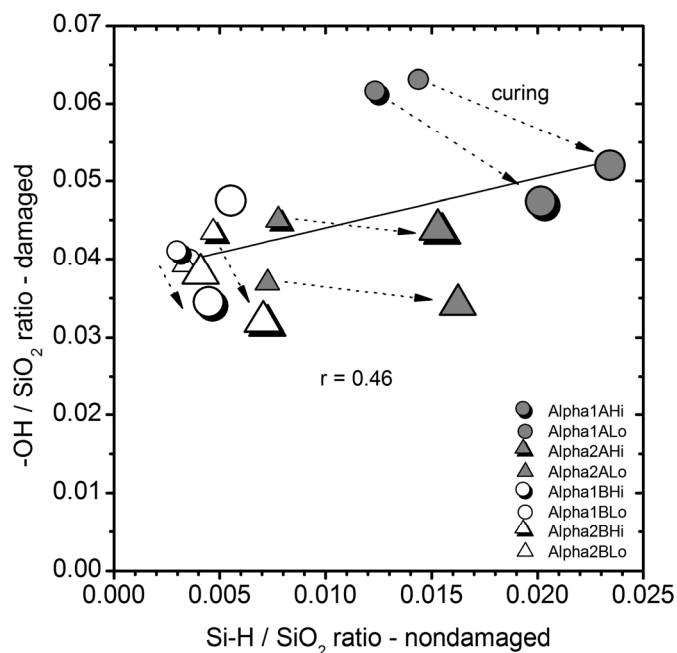
Figure 5.10. The FTIR peak areas of the absorbance of -OH groups (between 3100 cm^{-1} and 3800 cm^{-1}) in the NH$_3$ plasma damaged samples related to Si-H bond peak (at 891 cm^{-1}) area in UV-cured non-damaged samples, normalized to the peak area of SiO2. The solid line represents the linear regression of the 16 points. Increasing symbol size denotes increasing curing time.

FTIR

The FTIR absorption band between 3100 and 3800 cm^{-1} observed in the plasma damaged samples indicates the presence of -OH groups, either bonded or in the water molecule. Figure 5.10 shows the relation of the absorption band of the –OH groups and H$_2$O in the plasma damaged samples with the Si-H peak area in the as-deposited and UV-cured samples, normalized to the SiO$_2$ peak. As mentioned above (see fig. 5.4), it is expected that Si-H presence in the UV-cured samples might reduce the plasma damage resistance. However, only a moderate correlation between the quantities is found (r=0.46) and the damaged samples cured by the monochromatic lamp A contain more -OH groups. Although for all samples the increasing UV-curing time results in more Si-H groups, for 7 of the 8 pairs of samples, the increased curing times leads to a reduction of the -OH signature in the damaged samples.

The measures of damage: the percentage of absorbed water in saturation pressure (WEP) and the FTIR –OH signature (atmospheric pressure, N$_2$ purged) are not highly correlated (r=0.53) in our set of samples, due to the variability in porosity and pore-network structure. Therefore we have compared the volume-based parameters and FTIR results separately.

VIS/UV spectroscopic ellipsometry

The plasma exposure leads to the porogen residues removal. The top layer is more transparent and can be distinguished by the variable angle spectroscopic ellipsometry; however, the interface between the non-damaged and damaged layer is not sharp and the modeling of the data suggested that the damaged layer can be separated into two: 1) highly

damaged top layer, which is already densified (higher RI) and 2) less damaged mid-layer, where the residues are partly removed and the density is lower (lower RI). The fitting of the data by these complicated models has not been completely stable and more sensitive measurements should be performed to obtain reliable results. We have detected differences in the thickness of the damaged layer (bi-layer) related to material: The samples of material Alpha1 with the higher target porosity exhibit the depth of damage of (74 ± 4) nm, and the samples of Alpha2 with the lower target porosity exhibit the depth of damage of (55 ± 6) nm.

5.4.   Conclusions

The impact of the deposition and curing conditions of low-*k* materials on their basic properties, chemical composition and particularly the plasma damage resistance has been evaluated. We found that the choice of curing lamp has a strong impact on the physical-chemical properties of the low-*k* material. The monochromatic UV light source with λ=172 nm (lamp A) leads to the stronger -CH$_3$ depletion, Si-H creation, cage to network transition and shrinkage than broadband UV source with λ lower than 200 nm (lamp B). Further, it was found that the curing process with lamp B is more efficient in the porogen removal than the curing process with lamp A. The low-*k* materials cured by lamp B show a lower CH$_x$ signature as measured by FTIR, and lower porogen related absorption in UV and therefore also lower RI as measured by UV spectroscopic ellipsometry. Curing process using lamp B results in an increased porosity and larger pores of exposed low-k films.

The plasma damage, as measured by WEP (bulk hydrophilisation), is mainly related to the porosity. The FTIR signature of the –OH content is only weakly related to the Si-H groups formation (–CH$_3$ depletion), however the behavior of the data suggest that more complex mechanism is in play in the –OH formation.

It has been observed that, although the SiCOH matrix volume percentages vary between 43% and 53% for material Alpha1 and between 62% and 69% for material Alpha2, the actual volumes remain comparable among the samples of the same material and therefore the shrinkage of the film must be attributed primarily to the porogen removal followed by the pore collapse. The detected volume percentages of the porogen residues are ranging between 3% and 23% for all of the samples.

As mentioned above, the choice of lamp has a strong effect on the amount of porogen residues. An important difference in the porogen residues volume is observed also between samples deposited under different conditions. The samples deposited at lower temperature and lower RF power show higher porosities and larger pores, and also a lower residues content. We presume that a favorable pore size distribution and pore interconnectivity created during deposition enhances the porogen removal.

The detected variability in the amount of porogen residues promises the possibility of a controlled modification of the deposition and curing process towards a material with improved mechanical and dielectric properties, especially in the case of highly porous material, where the impact of the residues is crucial.

5.4.1. Outlook

What is the origin of the observed shrinkage? It has been shown that the shrinkage of low-*k* hybrid is caused by the collapse of the material after the porogen removal. Nevertheless, the reduction of the volume of the matrix itself is observed. It is probably caused either by removal of the bulkier $-CH_3$ ending groups and their replacement by either Si-H bonds or Si-O-Si crosslinks. The impact of the curing conditions on the proposed reactions should be examined.

What is the origin of the improvements of the mechanical properties? The UV-cure improves the mechanical properties, but this can be just the effect of shrinkage and densification. The benefit of the UV-curing lamp choice should be studied.

As proposed in the outlook of the previous chapter, the He_2/H_2 high-temperature plasma strip process can be used for sample preparation, particularly to prepare samples clean of any residues. Then the effects of the UV-cure on porous matrix itself can be observed.

It is possible to imagine the combinations of multiple steps of porogen removal and curing techniques. For example, a pre-curing by lamp B, followed by a high temperature strip to remove the residues (the depth of penetration could be sufficient in the case of patterned low-*k* films) and finalized by a short lamp A exposure to stiffen the matrix.

Our studies focused mostly on the primary constituents, their structure and their behavior under deposition and curing conditions. The observed facts should be related to the properties important from the technological point of view: the mechanical stability and dielectric constant.

Appendix 1:
Detailed calculations

Expanded calculations from chapters 1 (Fresnel coefficients) and 2 (sum of squares).

1. Fresnel coefficients

In this section we perform the textbook derivation of the Fresnel coefficients.

Comparison with literature

First, let us show equivalence of the formulation of the coefficients used in the chapter 1 and the classic form.[161] Figure i. is adopted from the literature and defines the notation of the components. Note that the $R_\parallel$ component is inverted with respect to r_p defined in the chapter 1.

[161] M. Born, E. Wolf, *Principles of Optics (7th edition)*, Cambridge University Press, page 40 (1999).
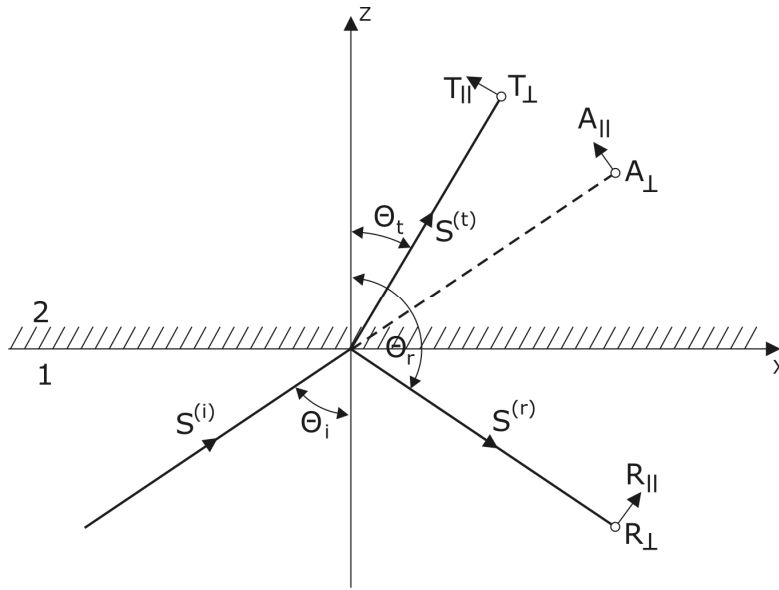
Figure i. Refraction and reflection of a plane wave. Plane of incidence.

The formulas read:

$$R_\perp = \frac{n_1 \cos\Theta_i - n_2 \cos\Theta_t}{n_1 \cos\Theta_i + n_2 \cos\Theta_t} A_\perp , \qquad (6.1)$$

$$T_\perp = \frac{2n_1 \cos\Theta_i}{n_1 \cos\Theta_i + n_2 \cos\Theta_t} A_\perp , \qquad (6.2)$$

$$R_\parallel = \frac{n_2 \cos\Theta_i - n_1 \cos\Theta_t}{n_2 \cos\Theta_i + n_1 \cos\Theta_t} A_\parallel , \qquad (6.3)$$

$$T_\parallel = \frac{2n_1 \cos\Theta_i}{n_2 \cos\Theta_i + n_1 \cos\Theta_t} A_\parallel . \qquad (6.4)$$

Now, the z-components of the incident and transmitted wave-vectors are given by

$$k_{z1} = k_0 n_1 \cos\Theta_i , \qquad k_{z2} = k_0 n_2 \cos\Theta_t . \qquad (6.5)$$

According to definitions (1.13) we obtain after inserting (6.5) into (6.1) and (6.2):

$$r_s \equiv \frac{R_\perp}{A_\perp} = \frac{k_{z1} - k_{z2}}{k_{z1} + k_{z2}} , \qquad (6.6)$$

$$t_s \equiv \frac{T_\perp}{A_\perp} = \frac{2k_{z1}}{k_{z1} + k_{z2}} . \qquad (6.7)$$

In the case of (6.3) and (6.4) we need to expand both numerator and denominator by $n_1 n_2$ obtaining

$$-r_p \equiv \frac{R_\parallel}{A_\parallel} = \frac{n_2^2 n_1 \cos\Theta_i - n_1^2 n_2 \cos\Theta_t}{n_2^2 n_1 \cos\Theta_i + n_1^2 n_2 \cos\Theta_t} = \frac{\varepsilon_2 k_{z1} - \varepsilon_1 k_{z2}}{\varepsilon_2 k_{z1} + \varepsilon_1 k_{z2}} , \tag{6.8}$$

$$t_p \equiv \frac{T_\parallel}{A_\parallel} = \frac{2 n_1 n_2 n_1 \cos\Theta_i}{n_2^2 n_1 \cos\Theta_i + n_1^2 n_2 \cos\Theta_t} = \frac{2\sqrt{\varepsilon_1 \varepsilon_2}\, k_{z1}}{\varepsilon_2 k_{z1} + \varepsilon_1 k_{z2}} , \tag{6.9}$$

where we inserted the (6.5) again and the dielectric functions

$$\varepsilon_1 = n_1^2 , \quad \varepsilon_2 = n_2^2 . \tag{6.10}$$

The formulas (6.6) to (6.9) are identical with the ones presented in chapter 1 except the sign of (6.8).

Before we express the Fresnel coefficients, we first develop some basic relations that will be used in the further discussion.

Orthogonality of *k*, *E*, *H*

If we insert a plane wave

$$\bar{E} = \bar{E}_0 e^{i(\bar{k}\bar{x} - \omega t)} , \quad \bar{H} = \bar{H}_0 e^{i(\bar{k}\bar{x} - \omega t)} \tag{6.11}$$

into Maxwell's equations and restrict ourselves to the nonmagnetic materials without charges or currents, we obtain following relations

$$\operatorname{div}\bar{D} = \varepsilon\varepsilon_0 \nabla \cdot \bar{E} = \varepsilon\varepsilon_0 \bar{k} \cdot \bar{E} = 0 ,$$

$$\bar{k} \cdot \bar{E} = 0 , \tag{6.12}$$

$$\operatorname{rot}\bar{H} = \nabla \times \bar{H} = i\bar{k} \times \bar{H} = \frac{\partial\bar{D}}{\partial t} = \varepsilon\varepsilon_0 \frac{\partial\bar{E}}{\partial t} = -i\omega\varepsilon\varepsilon_0 \bar{E} ,$$

$$\frac{\bar{k} \times \bar{H}}{\varepsilon\varepsilon_0\omega} = -\bar{E} , \tag{6.13}$$

$$\operatorname{rot}\bar{E} = \nabla \times \bar{E} = i\bar{k} \times \bar{E} = -\frac{\partial\bar{B}}{\partial t} = -\mu_0 \frac{\partial\bar{H}}{\partial t} = i\omega\mu_0 \bar{H} ,$$

$$\frac{\bar{k} \times \bar{E}}{\omega\mu_0} = \bar{H} , \tag{6.14}$$

$$\operatorname{div}\bar{B} = \mu_0 \nabla \cdot \bar{H} = \bar{k} \cdot \bar{H} = 0 ,$$

$$\bar{k} \cdot \bar{H} = 0 . \tag{6.15}$$

Particularly in the case of wave propagating in the x-z plane

$$\bar{k} = (k_x, 0, k_z) , \tag{6.16}$$

the components of the fields will be

$$E_x = \frac{k_z H_y}{\omega \varepsilon \varepsilon_0} , \quad E_y = \frac{k_x H_z - k_z H_x}{\omega \varepsilon \varepsilon_0} , \quad E_z = -\frac{k_x H_y}{\omega \varepsilon \varepsilon_0} , \qquad (6.17)$$

$$H_x = -\frac{k_z E_y}{\omega \mu_0} , \quad H_y = \frac{k_z E_x - k_x E_z}{\omega \mu_0} , \quad H_z = \frac{k_x E_y}{\omega \mu_0} . \qquad (6.18)$$

Continuity of fields on the planar interface

Each of four Maxwell's equations can be used for determination of continuity of the perpendicular and in-plane components of *E*, *D*, *H* and *B*.

If no charges are present on the interface, we can construct an infinitesimal cubic volume across the interface, with two faces parallel to the surface – one below and one above. As the divergences of both inductions *D* and *B* are equal to zero, the net flow of the fields through the faces of the cube is zero as well (Gauss' theorem). If the height of the cube is decreased towards zero, the contribution of the side faces (in-plane components) vanish and therefore the perpendicular components must obey

$$D_{\perp 1} = D_{\perp 2} , \quad B_{\perp 1} = B_{\perp 2} , \qquad (6.19)$$

i. e. the normal components of the inductions *D* and *B* are conserved on the interface.

Accordingly, if no currents are present on the interface, we construct infinitesimal rectangle loop with two sides perpendicular and two parallel with the interface. Then we integrate the remaining two Maxwell's equations over the enclosed area:

$$\int \mathrm{rot}\, \bar{H}\, ds = \oint \bar{H} \cdot d\bar{l} = \int \frac{\partial \bar{D}}{\partial t} ds , \qquad (6.20)$$

$$\int \mathrm{rot}\, \bar{E}\, ds = -\oint \bar{E} \cdot d\bar{l} = -\int \frac{\partial \bar{B}}{\partial t} ds , \qquad (6.21)$$

where we applied the Stokes' theorem. Here again, when the height of the rectangle is decreased to zero the areas on the right-hand side vanish and therefore

$$H_{\parallel 1} = H_{\parallel 2} , \quad E_{\parallel 1} = E_{\parallel 2} , \qquad (6.22)$$

the in-plane components of electric and magnetic intensities are conserved.

t_p problem

While three of the Fresnel coefficients can be expressed as ratio of particular Cartesian components of the electric field, the coefficient t_p is defined otherwise. Here we express the t_p coefficient with the Cartesian components of the electric and magnetic fields and the Cartesian components of the wave-vectors.

Let us consider p-polarized wave incident on interface between media 1 and 2. In following we introduce index $i=1,2$ for media 1 and 2. Assuming (6.16) and using (6.12) we have

$$\bar{E}_{ip}\bar{k}_i = 0, \quad \text{i.e.} \quad E_{ipx}k_{ix} = -E_{ipz}k_{iz},$$

Now we square the equation and introduce the magnitude of k_i and $\bar{E}_{ip}\bar{E}_{ip}$

$$E_{ipx}^2 k_{ix}^2 = (\bar{E}_{ip}\bar{E}_{ip} - E_{ipx}^2)k_{iz}^2,$$

$$E_{ipx}^2 k_{ix}^2 = \bar{E}_{ip}\bar{E}_{ip}k_{iz}^2 - E_{ipx}^2(k_i^2 - k_{ix}^2),$$

$$\bar{E}_{ip}\bar{E}_{ip}k_{iz}^2 = E_{ipx}^2 k_i^2 \quad \text{and} \quad k_i^2 = k_0^2 \varepsilon_i,$$

$$\bar{E}_{ip}\bar{E}_{ip}k_{iz}^2 = E_{ipx}^2 k_0^2 \varepsilon_i. \tag{6.23}$$

The Fresnel coefficient for transmission of p-polarized wave is defined as

$$t_p = \frac{E_{2p}}{E_{1p}}, \tag{6.24}$$

where the amplitudes E_{ip} are complex and are related to the intensities $\bar{E}_{ip}$ through

$$\bar{E}_{ip} = E_{ip}\bar{e}_{ip}, \tag{6.25}$$

Where the $\bar{e}_{ip}$ is real unit vector defining the p-polarization in each media. Then the scalar product $\bar{E}_{ip}\bar{E}_{ip}$ can be written as

$$\bar{E}_{ip}\bar{E}_{ip} = E_{ip}E_{ip}\left|e_{ip}\right|^2 = E_{ip}E_{ip}, \tag{6.26}$$

Now we insert square-root of (6.23) into (6.24), with help of the previous relation to obtain

$$t_p = \frac{\sqrt{\varepsilon_2}k_{1z}E_{2x}}{\sqrt{\varepsilon_1}k_{2z}E_{1x}}. \tag{6.27}$$

Finally, we obtained expression of t_p using the Cartesian components of electric intensities.

Alternatively, if we express the product $E_{ip}E_{ip}$ in both media, and insert (6.17) we get

$$E_{ip}E_{ip} = E_{ipx}^2 + E_{ipz}^2 = \frac{k_{iz}^2 H_{iy}^2}{(\omega \varepsilon_i \varepsilon_0)^2} + \frac{k_{ix}^2 H_{iy}^2}{(\omega \varepsilon_i \varepsilon_0)^2} = \frac{\bar{k}_i \bar{k}_i H_{iy}^2}{(\omega \varepsilon_i \varepsilon_0)^2} = \frac{k_0^2 \varepsilon_i H_{iy}^2}{(\omega \varepsilon_i \varepsilon_0)^2} = \frac{k_0^2}{(\omega \varepsilon_0)^2}\frac{H_{iy}^2}{\varepsilon_i},$$

Then the equation (6.24) can be rewritten as

$$t_p = \frac{\sqrt{\varepsilon_1}H_{2y}}{\sqrt{\varepsilon_2}H_{1y}} \; . \qquad (6.28)$$

Here we have the coefficient t_p defined using Cartesian components of magnetic intensities.

Fresnel coefficients

Coefficient r_s

This coefficient is defined as ratio of amplitudes of s-polarized waves: reflected and incident

$$r_s = \frac{E_{Rs}}{E_{Is}} = \frac{E_{Ry}}{E_{Iy}} \; . \qquad (6.29)$$

We will use the continuity of the in-plane components of electric and magnetic intensities

$$E_{Iy} + E_{Ry} = E_{Ty} \, , \quad H_{Ix} + H_{Rx} = H_{Tx} \; . \qquad (6.30)$$

We express the second condition using (6.18)

$$\frac{k_{Iz}E_{Iy}}{\omega\mu_0} + \frac{k_{Rz}E_{Ry}}{\omega\mu_0} = \frac{k_{Tz}E_{Ty}}{\omega\mu_0} \, , \qquad (6.31)$$

then using $k_{Rz} = -k_{Iz}$ we obtain

$$k_{Iz}E_{Iy} - k_{Iz}E_{Ry} = k_{Tz}E_{Ty} \, , \qquad (6.32)$$

and then using first condition of (6.30) we have

$$k_{Iz}E_{Iy} - k_{Iz}E_{Ry} = k_{Tz}E_{Iy} + k_{Tz}E_{Ry} \, ,$$

$$r_s = \frac{k_{Iz} - k_{Tz}}{k_{Iz} + k_{Tz}} \equiv \frac{k_{1z} - k_{2z}}{k_{1z} + k_{2z}} \; . \qquad (6.33)$$

The last expression is identical with (6.6).

Coefficient t_s

The t_s coefficient is defined as ratio of amplitudes of s-polarized waves: transmitted and incident

$$t_s = \frac{E_{Ts}}{E_{Is}} = \frac{E_{Ty}}{E_{Iy}} \; . \qquad (6.34)$$

We will use again the conditions (6.30) and expression (6.32), where we insert the first condition of (6.30) in form $E_{Ry} = E_{Ty} - E_{Iy}$

$$k_{Iz}E_{Iy} - k_{Iz}(E_{Ty} - E_{Iy}) = k_{Tz}E_{Ty},$$

$$t_s = \frac{2k_{Iz}}{k_{Iz} + k_{Tz}} \equiv \frac{2k_{1z}}{k_{1z} + k_{2z}}. \tag{6.35}$$

The last expression is identical with (6.7).

Coefficient r_p

In case of p-polarized light, the electric field is polarized in the plane of incidence (x-z) and magnetic field in the direction of y-axis, therefore the conserved components of the field intensities will be

$$E_{Ix} + E_{Rx} = E_{Tx}, \quad H_{Iy} + H_{Ry} = H_{Ty}. \tag{6.36}$$

The r_p coefficient is defined as ratio of amplitudes of p-polarized waves: reflected and incident

$$r_p = \frac{E_{Rp}}{E_{Ip}} = \frac{E_{Rx}}{E_{Ix}} = -\frac{H_{Ry}}{H_{Iy}}, \tag{6.37}$$

where the minus sign originates from the convention used in this work. For example, in the case of normal incidence, according to our definition, $E_{Rp} = E_{Rx}$ and $E_{Ip} = E_{Ix}$, therefore the direction defined as positive for magnetic intensities must change because the k, E, H system must be right-handed (6.14).

We choose the ratio of the y-components the amplitudes of the intensity of magnetic field, since they are equal to the amplitudes themselves. We express the first condition of (6.36) using (6.17)

$$\frac{k_{Iz}H_{Iy}}{\omega\varepsilon_1\varepsilon_0} + \frac{k_{Rz}H_{Ry}}{\omega\varepsilon_1\varepsilon_0} = \frac{k_{Tz}H_{Ty}}{\omega\varepsilon_2\varepsilon_0}, \tag{6.38}$$

then using $k_{Rz}=-k_{Iz}$ we obtain

$$\varepsilon_2 k_{Iz}(H_{Iy} - H_{Ry}) = \varepsilon_1 k_{Tz}H_{Ty}, \tag{6.39}$$

and then using second condition of (6.36) we have

$$\varepsilon_2 k_{Iz}(H_{Iy} - H_{Ry}) = \varepsilon_1 k_{Tz}(H_{Iy} + H_{Ry}),$$

$$-H_{Ry}(\varepsilon_2 k_{Iz} + \varepsilon_1 k_{Tz}) = H_{Iy}(\varepsilon_1 k_{Tz} - \varepsilon_2 k_{Iz}),$$

$$r_p = \frac{\varepsilon_1 k_{Tz} - \varepsilon_2 k_{Iz}}{\varepsilon_2 k_{Iz} + \varepsilon_1 k_{Tz}} \equiv \frac{\varepsilon_1 k_{2z} - \varepsilon_2 k_{1z}}{\varepsilon_1 k_{2z} + \varepsilon_2 k_{1z}}. \tag{6.40}$$

The last expression is identical with (6.8).

Coefficient t_p

As expressed in previous subsection, the t_p is given by y-components of magnetic intensities (6.28)

$$t_p = \frac{\sqrt{\varepsilon_1} H_{2y}}{\sqrt{\varepsilon_2} H_{1y}} .$$

We again use the equation (6.38) and insert second relation of (6.36)

$$\varepsilon_2 k_{Iz}(H_{Iy} - (H_{Ty} - H_{Iy})) = \varepsilon_1 k_{Tz} H_{Ty} ,$$

$$H_{Iy} 2\varepsilon_2 k_{Iz} = H_{Ty}(\varepsilon_1 k_{Tz} + \varepsilon_2 k_{Iz}) ,$$

$$t_p = \frac{\sqrt{\varepsilon_1}\, 2\varepsilon_2 k_{Iz}}{\sqrt{\varepsilon_2}(\varepsilon_1 k_{Tz} + \varepsilon_2 k_{Iz})} \equiv \frac{\sqrt{\varepsilon_1 \varepsilon_2}\, 2 k_{1z}}{\varepsilon_1 k_{2z} + \varepsilon_2 k_{1z}} . \qquad (6.41)$$

And this formula is identical with (6.9).

Now we have formulated four Fresnel coefficients according to the definition by ratio of complex scalar field amplitudes (see (6.25)), particularly for the coefficient t_p.

We may define also this one coefficient by ratio of Cartesian components of electric field and later show, that for practical use in the calculations, our definition is beneficial.

Coefficient t_{px}

We define the t_{px} coefficient as

$$t_{px} = \frac{E_{Tx}}{E_{Ix}} , \qquad (6.42)$$

that is, by using (6.17) equal to

$$t_{px} = \frac{E_{Tx}}{E_{Ix}} = \frac{\varepsilon_1 k_{Tz} H_{Ty}}{\varepsilon_2 k_{Iz} H_{Iy}} \equiv \frac{2\varepsilon_1 k_{2z}}{\varepsilon_1 k_{2z} + \varepsilon_2 k_{1z}} . \qquad (6.43)$$

The expression of the fifth coefficient is now analogical to the first three: r_s, t_s and r_p.

Relations between the coefficients

Consequence of continuity

Several important relations between the Fresnel coefficients might be expressed. For s-polarization we can divide the equation for continuity of in-plane component of electric field (6.30) by incident amplitude

$$E_{Iy} + E_{Ry} = E_{Ty} \quad \big| : E_{Iy} ,$$

$$1 + \frac{E_{Ry}}{E_{Iy}} = \frac{E_{Ty}}{E_{Iy}} \, ,$$

$$1 + r_s = t_s \, . \tag{6.44}$$

Analogically for p-polarized wave and amplitudes of magnetic intensity

$$H_{Iy} + H_{Ry} = H_{Ty} \quad \left| : H_{Iy} \, , \right.$$

$$1 + \frac{H_{Ry}}{H_{Iy}} = \frac{H_{Ty}}{H_{Iy}} \, ,$$

$$1 - r_p = \sqrt{\frac{\varepsilon_2}{\varepsilon_1}} t_p \, . \tag{6.45}$$

Or by using the in-plane components of electric field we obtain

$$E_{Ix} + E_{Rx} = E_{Tx} \quad \left| : E_{Ix} \, , \right.$$

$$1 + \frac{E_{Rx}}{E_{Ix}} = \frac{E_{Tx}}{E_{Ix}} \, ,$$

$$1 + r_p = t_{px} \, . \tag{6.46}$$

Here again, the use of the additional coefficient result in analogical equation for s- and p-polarization.

Normal incidence

In the case of normal incidence the z-components of the wave-vectors become $k_{1z} = k_0\sqrt{\varepsilon_1}$, $k_{2z} = k_0\sqrt{\varepsilon_2}$ and the Fresnel coefficients will be

$$r_s = \frac{\sqrt{\varepsilon_1} - \sqrt{\varepsilon_2}}{\sqrt{\varepsilon_1} + \sqrt{\varepsilon_2}} \, , \quad t_s = \frac{2\sqrt{\varepsilon_1}}{\sqrt{\varepsilon_1} + \sqrt{\varepsilon_2}} \, ,$$

$$r_p = \frac{\varepsilon_1\sqrt{\varepsilon_2} - \varepsilon_2\sqrt{\varepsilon_1}}{\varepsilon_1\sqrt{\varepsilon_2} + \varepsilon_2\sqrt{\varepsilon_1}} = \frac{\sqrt{\varepsilon_1} - \sqrt{\varepsilon_2}}{\sqrt{\varepsilon_1} + \sqrt{\varepsilon_2}} = r_s \, ,$$

$$t_p = \frac{2\varepsilon_1\sqrt{\varepsilon_2}}{\varepsilon_1\sqrt{\varepsilon_2} + \varepsilon_2\sqrt{\varepsilon_1}} = \frac{2\sqrt{\varepsilon_1}}{\sqrt{\varepsilon_1} + \sqrt{\varepsilon_2}} = t_s \, ,$$

$$t_{px} = \frac{2\varepsilon_1\sqrt{\varepsilon_2}}{\varepsilon_1\sqrt{\varepsilon_2} + \varepsilon_2\sqrt{\varepsilon_1}} = t_p = t_s \, .$$

As should have been expected, the r_s and r_p are identical as well as t_s, t_p and t_{px}.

Reverse propagation

If we are interested in the Fresnel coefficients valid for reverse propagation, i. e. if the media 1 and 2 are interchanged, we obviously obtain for reflection coefficients:

$$r_{(2,1)s} = -r_{(1,2)s}, \quad r_{(2,1)p} = -r_{(1,2)p}, \tag{6.47}$$

where the subscript (2,1) or (1,2) denotes reflection from the media 2 on media 1 and reflection on media 2 from media 1 respectively.

And for transmission coefficients, we have:

$$t_{(1,2)s}t_{(2,1)s} = \frac{2k_{1z}}{k_{1z}+k_{2z}}\frac{2k_{2z}}{k_{1z}+k_{2z}} = \frac{4k_{1z}k_{2z}}{(k_{2z}+k_{1z})^2},$$

$$r_{(1,2)s}^2 = \frac{k_{1z}-k_{2z}}{k_{1z}+k_{2z}}\frac{k_{2z}-k_{2z}}{k_{1z}+k_{2z}} = \frac{k_{1z}^2-2k_{1z}k_{2z}+k_{2z}^2}{(k_{1z}+k_{2z})^2}, \text{ then}$$

$$t_{(1,2)s}t_{(2,1)s} + r_{(1,2)s}^2 = 1.$$

$$t_{(1,2)p}t_{(2,1)p} = \frac{\sqrt{\varepsilon_1\varepsilon_2}\,2k_{1z}}{\varepsilon_1 k_{2z}+\varepsilon_2 k_{1z}}\frac{\sqrt{\varepsilon_1\varepsilon_2}\,2k_{2z}}{\varepsilon_1 k_{2z}+\varepsilon_2 k_{1z}} = \frac{4\varepsilon_1\varepsilon_2 k_{1z}k_{2z}}{(\varepsilon_1 k_{2z}+\varepsilon_2 k_{1z})^2},$$

$$t_{(1,2)px}t_{(2,1)px} = \frac{2\varepsilon_1 k_{2z}}{\varepsilon_1 k_{2z}+\varepsilon_2 k_{1z}}\frac{2\varepsilon_2 k_{1z}}{\varepsilon_1 k_{2z}+\varepsilon_2 k_{1z}} = \frac{4\varepsilon_1\varepsilon_2 k_{2z}k_{1z}}{(\varepsilon_1 k_{2z}+\varepsilon_2 k_{1z})^2},$$

$$r_{(1,2)p}^2 = \frac{(\varepsilon_1 k_{2z})^2-2\varepsilon_1\varepsilon_2 k_{1z}k_{2z}+(\varepsilon_2 k_{1z})^2}{(\varepsilon_1 k_{2z}+\varepsilon_2 k_{1z})^2}, \text{ then}$$

$$t_{(1,2)p}t_{(2,1)p} + r_{(1,2)p}^2 = 1, \quad t_{(1,2)px}t_{(2,1)px} + r_{(1,2)p}^2 = 1. \tag{6.48}$$

Therefore, the relation is valid for s-polarization and for both choices of p-polarization transmission coefficient.

Propagation through multilayer

We have seen that the transmission coefficients t_p and t_{px} are bound as

$$t_{(1,2)px} = \frac{\sqrt{\varepsilon_1}k_{2z}}{\sqrt{\varepsilon_2}k_{1z}}t_{(1,2)p}, \tag{6.49}$$

Therefore transmission through multiple layers (1..*N*) will be described as

$$t_{(1,2)px}t_{(2,3)px}t_{(3,4)px}\ldots t_{(4,N)px} =$$

$$= \frac{\sqrt{\varepsilon_1}k_{2z}}{\sqrt{\varepsilon_2}k_{1z}}\frac{\sqrt{\varepsilon_2}k_{3z}}{\sqrt{\varepsilon_3}k_{2z}}\frac{\sqrt{\varepsilon_3}k_{4z}}{\sqrt{\varepsilon_4}k_{3z}}\ldots\frac{\sqrt{\varepsilon_4}k_{Nz}}{\sqrt{\varepsilon_N}k_{4z}}t_{(1,2)p}t_{(2,3)p}t_{(3,4)p}\ldots t_{(4,N)p} =$$

$$= \frac{\sqrt{\varepsilon_1}k_{Nz}}{\sqrt{\varepsilon_N}k_{1z}} t_{(1,2)p}t_{(2,3)p}t_{(3,4)p}\ldots t_{(4,N)p}. \tag{6.50}$$

And since the propagation matrix approach includes only multiplication by factor $(1/t)$ for every interface, the total matrix of the stack will be multiplied by the above expressed pre-factor when using t_{px} instead of t_p.

Because we usually measure in reflection mode, the pre-factor will not play any role in the ellipsometric calculation. In the case of transmission measurements, we can expect the same ambient media on the front and back side of the sample and therefore the pre-factor becomes unity.

Summary

In the first section of the appendix we developed the Fresnel coefficients from the Maxwell's equations using the framework of z-components of wave-vectors.

We have introduced an additional coefficient for transmission of x-component of intensity of electric field of p-polarized light. We have shown that using this coefficient, the related formulas become symmetrical to analogical formulas for s-polarization.

2. mAB2PD - sum of squares

Here we will show how the weighted sum of squared differences between the average and the individual points x_i transforms to sum of squares of mutual differences between the points. The sum of squares as written in the chapter 2 reads:

$$S = \sum_i w_i \left(x_i - \tilde{x} \right)^2,$$

inserting the weighted average, we get

$$S = \sum_i w_i \left(x_i - \frac{\sum_j w_j x_j}{\sum_j w_j} \right)^2 = \frac{1}{(\sum_j w_j)^2} \sum_i w_i \left[\sum_j w_j(x_i - x_j) \right]^2 =$$

Expand square to multiplication of sums, with new summation index k:

$$= \frac{1}{(\sum_j w_j)^2} \sum_i w_i \left[\sum_j w_j(x_i - x_j) \right]\left[\sum_k w_k(x_i - x_k) \right] =$$

Simplify.

$$= \frac{1}{(\sum_j w_j)^2} \sum_i \sum_j \sum_k w_i w_j w_k (x_i - x_j)(x_i - x_k) =$$

Now we separate to two sums, for $i=j$ term vanishes.

$$= \frac{1}{(\sum_j w_j)^2} \sum_k w_k \left[\sum_{i<j} \sum w_i w_j (x_i - x_j)(x_i - x_k) + \sum_{i>j} \sum w_i w_j (x_i - x_j)(x_i - x_k) \right] =$$

Then move minus sign to second bracket in the second term.

$$= \frac{1}{(\sum_j w_j)^2} \sum_k w_k \left[\sum_{i<j} \sum w_i w_j (x_i - x_j)(x_i - x_k) + \sum_{i>j} \sum w_i w_j (x_j - x_i)(-x_i + x_k) \right] =$$

Rename i to j and vice versa in second term.

$$= \frac{1}{(\sum_j w_j)^2} \sum_k w_k \left[\sum_{i<j} \sum w_i w_j (x_i - x_j)(x_i - x_k) + \sum_{j>i} \sum w_j w_i (x_i - x_j)(-x_j + x_k) \right] =$$

Put together, the x_k vanishes, and the result is:

$$= \frac{1}{(\sum_j w_j)^2} \sum_k w_k \left[\sum_{i<j} \sum w_i w_j (x_i - x_j)(x_i - x_j) \right] = \frac{1}{2\sum_j w_j} \sum_i \sum_j w_i w_j (x_i - x_j)^2 \ .$$

We obtained the sum of squares in terms of mutual differences between the points.

Bibliography

In alphabetical order (by first author), then chronologically.

D. K. Aitken, J. H. Hough, *Spectral Modulation, or Ripple, in Retardation Plates for Linear and Circular Polarization*, Publ. Astron. Soc. Pac. **113,** 1300-1305 (2001).

G. Aksenov, D. De Roest, P. Verdonck, F. N. Dultsev, P. Marsik, D. Samiryan, H. Arai, N. Takamure, M. R. Baklanov, *Optimization of low-k UV curing: effect of wavelength on critical properties of the dielectric*, Material Research Society Spring Meeting 2009, San Francisco, April 13-17 (2009).

I. An, J. A. Zapien, C. Chen, A. S. Ferlauto, A. S. Lawrence, R. W. Collins, *Calibration and data reduction for a UV-extended rotating-compensator multichannel ellipsometer*, Thin Solid Films **455-456,** 132-137 (2004).

M. Asar, D. E. Aspnes, *Optical anisotropy relevant to rotating-compensator polarimeters: application of the monoplate retarder*, Thin Solid Films **455-456,** 50-53 (2004).

M. Asar, D. E. Aspnes, *The nearly aligned rotating-monoplate compensator*, Phys. Stat. Sol. A **205,** 739-742 (2008).

D. E. Aspnes, *Optical properties of thin films*, Thin Solid Films **89,** 249-262 (1982).

M. R. Baklanov, K. P. Mogilnikov, V. G. Polovinkin and F. N. Dultsev, *Determination of pore size distribution in thin films by ellipsometric porosimetry*, Vac. Sci. Technol. B **18,** 1385-1391 (2000).

M. R. Baklanov and K. P. Mogilnikov, *Non-destructive characterization of porous low-k dielectric films*, Microelectron. Eng **64,** 335-349 (2005).

M. R. Baklanov, K. Maex and M. Green (Eds.), *Dielectric Films for Advanced Microelectronics*, Wiley (2008).

C. Bernhard, J. Humlicek, B. Keimer, *Far-infrared ellipsometry using synchrotron light source – the dielectric response of cuprate high Tc superconductors*, Thin Solid Films **455-456,** 143-149 (2004).

M. Born, E. Wolf, *Principles of Optics (7th edition)*, Cambridge University Press (1999).

B. Boulbry, B. Bousquet, B. Le Jeune, Y. Guern, J. Lotrian, *Polarization errors associated with zero-order achromatic quarter-wave plates in the whole visible spectral range*, Optics Express **9,** 225-235 (2001).

C. Chen, I. An, G. M. Ferreira, N. J. Podraza, J. A. Zapien, and R. W. Collins, *Multichannel Mueller matrix ellipsometer based on the dual rotating compensator principle,* Thin Solid Films **455-456,** 14-23 (2004).

R. W. Collins, *Automatic rotating element ellipsometers: Calibration, operation and real-time applications*, Rev. Sci. Instrum. **61,** 2029-2062 (1990).

R. W. Collins, I. An, C. Chen, in: H. Tompkins, E. Irene (Eds.), *Handbook of Ellipsometry (chapter 5.6)*, William Andrew Publishing, New York (2005).

M. J. Dodge, *Refractive properties of magnesium fluoride*, Appl. Opt. **23,** 1980-1985 (1984).

K. Ebert, D. E. Aspnes, *Biplate artifacts in rotating-compensator ellipsometers* Thin Solid Films **455,** 779-783 (2004).

S. Eslava, G. Eymery, P. Marsik, F. Iacopi, C. E. A. Kirschhock, K. Maex, J. A. Martens, and M. R. Baklanov, *Optical property changes in low-k films upon ultraviolet-assisted curing*, J. Electrochem. Soc. **155,** G115-G120 (2008).

S. Eslava, F. Iacopi, A. M. Urbanowicz, C. E. A. Kirschhock, K. Maex, J. A. Martens, and M. R. Baklanov, *Ultraviolet-assisted curing of organosilicate glass low-k dielectric by excimer lamps*, J. Electrochem. Soc. **155,** G231-G236 (2008).

S. Eslava, personal communication and unpublished report

N. Esser, M. Rakel, C. Cobet, W. G. Schmidt, W. Braun and M. Cardona, *VUV-ellipsometry on GaN: Probing conduction band properties by core level excitations*, Phys. Stat. Sol. B **242,** 2601-2609 (2005).

L. Favennec, V. Jousseaume, G. Gerbaud, A. Zenasni, and G. Passemard, *Ultralow k using a plasma enhanced chemical vapor deposition porogen approach: Matrix structure and porogen loading influences*, J. Appl. Phys. **102** (2007).

S. M. Gates, D. A. Neumayer, M. H. Sherwood, A. Grill, X. Wang, and M. Sankarapandian, *Preparation and structure of porous dielectrics by plasma enhanced chemical vapor deposition*, J. Appl. Phys. **101** (2007).

G. Ghoaadwd G. Ghosh, *Dispersion-equation coefficients for the refractive index and birefringence of calcite and quartz crystals*, Opt. Commun. **163,** 95-102 (1999).

M. Gioti, S. Logothetidis, *Dielectric function, electronic properties and optical constants of amorphous carbon and carbon nitride films*, Diamond Relat. Mater. **12,** 957-962 (2003).

A. V. Goncharenko, *Generalizations of the Bruggeman equation and a concept of shape-distributed particle composites*, Phys. Rev. E **68,** 041108 (2003).

A. Grill and V. Patel, *Low dielectric constant films prepared by plasma-enhanced chemical vapor deposition from tetramethylsilane*, J. Appl. Phys. **85,** 3314-3318 (1999).

A. Grill and V. Patel, *Ultralow-k dielectrics prepared by plasma-enhanced chemical vapor deposition*, Appl. Phys. Lett. **79,** 803-805 (2001).

A. Grill, V. Patel, K.P. Rodbell, E. Huang, M.R. Baklanov, K.P. Mogilnikov, M. Toney, H.C. Kim, *Porosity in plasma enhanced chemical vapor deposited SiCOH dielectrics: A comparative study*, J. Appl. Phys. **94,** 3427 (2003).

A. Grill and D.A. Neumayer, *Structure of low dielectric constant to extreme low dielectric constant SiCOH films: Fourier transform infrared spectroscopy characterization*, J. Appl. Phys. **94,** 6697 (2003).

A. Grill and V. Patel, *Ultralow dielectric constant pSiCOH films prepared with tetramethylcyclotetrasiloxane as skeleton precursor*, J. Appl. Phys. **104,** 9 (2008).

X. F. Hua, M. S. Kuo, G. S. Oehrlein, P. Lazzeri, E. Iacob, M. Anderle, C. K. Inoki, T. S. Kuan, P. Jiang, and W. L. Wu, *Damage of ultralow k materials during photoresist mask stripping process*, J. Vac. Sci. Technol. B **24,** 1238-1247 (2006).

C. H. Huang, H. L. Huang, C. I. Hung, N. F. Wang, Y. H. Wang, and M. P. Houng, *Bond structure in porous SiOCH low-k film fabricated by ultraviolet irradiation*, Jpn. J. Appl. Phys. **47,** 1532-1535 (2008).

J. Humlicek, *Optimized computation of the Voigt and complex probability functions*, J. Quant. Spectrosc. Radiat. Transfer **27,** 437-444 (1982).

J. Humlicek, *Evaluation of derivatives of reflectance and transmittance by stratified structures and solution of the inverse problem of ellipsometry*, Optica Acta, **30,** 97-105 (1983).

J. Humlicek, *Sensitivity extrema in multiple-angle ellipsometry*, J. Opt. Soc. Am. A **2,** 713-720 (1985).

J. Humlicek, *Sensitivity of Optical Measurements on Planar Stratified Structures and Reduction on Experimental Data*, FOLIA Fac. Sci. Nat. Uni. Brunensis Masarykianae, Physica **49** (1992).

J. Humlicek, in: H. Tompkins, E. Irene (Eds.), *Handbook of Ellipsometry*, William Andrew Publishing, New York (2005).

F. Iacopi, Y. Travaly, B. Eyckens, C. Waldfried, T. Abell, E. P. Guyer, D. M. Gage, R. H. Dauskardt, T. Sajavaara, K. Houthoofd, P. Grobet, P. Jacobs, and K. Maex, *Short-ranged structural rearrangement and enhancement of mechanical properties of organosilicate glasses induced by ultraviolet radiation*, J. Appl. Phys. **99,** 053511 (2006).

E. A. Irene, *Brief History of Ellipsometry*, presented in Ostuni, Italy (2008).

S. Jain, V. Zubkov, T. Nowak, A. Demos, and J. C. Rocha, *Porous low-k dielectrics using ultraviolet curing*, Solid State Technology **48,** 43 (2005).

B. Johs, *Regression calibration method for rotating element ellipsometers*, Thin Solid Films **234,** 395-398 (1993).

S. Kassavetis, P. Patsalas, S. Logothetidis, J. Robertson, S. Kennou, *Dispersion relations and optical properties of amorphous carbons,* Diamond Relat. Mater. **16,** 1813-1822 (2007).
N. Kemeling, K. Matsushita, N. Tsuji, K. Kagami, M. Kato, S. Kaneko, H. Sprey, D. de Roest, and N. Kobayashi, *A robust k similar to 2.3 SiCOH low-k film formed by porogen removal with UV-cure*, Microelectron. Eng. **84,** 2575-2581 (2007).

J. Y. Kim, M.S. Hwang, Y. H. Kim, H. J. Kim, Y. Lee, *Origin of low dielectric constant of carbon-incorporated silicon oxide film deposited by plasma enhanced chemical vapor deposition*, J. Appl. Phys. **90,** 2469 (2001).

T. S. Kim, N. Tsuji, K. Matsushita, N. Kobayashi, D. Chumakov, H. Geisler, E. Zschech, and R. H. Dauskardt, *Tuning depth profiles of organosilicate films with ultraviolet curing*, J. Appl. Phys. **104,** 6 (2008).

J. Lee, P. I. Rovira, I. An, R. W. Collins, *Alignment and calibration of the MgF2 biplate compensator for application in rotating compensator multichannel ellipsometry*, J. Opt. Soc. Am. **18,** 1980-1985 (2001).

G. Lippmann, in: *Nobel Lectures, Physics 1901-1921*, Elsevier Publishing Company, Amsterdam (1967).

K. Maex, M.R. Baklanov, D. Shamiryan, F. Iacopi, S.H. Brongersma, Z.S. Yanovitskaya, *Low dielectric constant materials for microelectronics*, J. Appl. Phys. **93,** 8793-8841 (2003).

P. Marsik and J. Humlicek: *Multi-plate misalignment artifacts in rotating-compensator ellipsometry: Analysis and data treatment*, Physica Status Solidi (c) **5** 1064 (2008).

P. Marsik, P. Verdonck, D. Schneider, D. De Roest, S. Kaneko and M. R. Baklanov, *Spectroscopic ellipsometry and ellipsometric porosimetry studies of CVD low-k dielectric films*, Phys. Status Solidi C **5,** 1253-1256, (2008).

P. Marsik, A. M. Urbanowicz, K. Vinokur, Y. Cohen and M. R. Baklanov, *Changes of UV Optical Properties of Plasma Damaged Low-k Dielectrics for Sidewall Damage Scatterometry*, Material Research Society Symposium Proceedings **1079,** 1079-N07-04 (2008).

P. Marsik, P. Verdonck, D. De Roest and M. R. Baklanov, *Porogen residues detection in optical properties of low-k dielectrics cured by ultraviolet radiation*, Thin Solid Films, doi:10.1016/j.tsf.2009.12.110 (2010).

P. Marsik, A. Urbanowicz, P. Verdonck, D. De Roest, H. Sprey and M.R. Baklanov, *Effect of Ultraviolet Curing Wavelength on Low-k Dielectric Material Properties and Plasma Damage Resistance*, in preparation

M. Matsuura, K. Goto, N. Miura, S. Hashii and K. Asai, *Film Characterization of Ultra Low-k Dielectrics Modified by UV Curing with Different Wavelength Bands* Material Research Society Symposium Proceedings **914,** 0914-F01-06 (2006).

K. P. Mogilnikov, V. G. Polovinkin, F. N. Dultsev and M. R. Baklanov, *Calculation of pore size distribution in the ellipsometric porosimetry*, Material Research Society Symposium Proceedings **565,** 81-86 (2000).

K. P. Mogilnikov and M. R. Baklanov, *Determination of Young's Modulus of Porous Low-k Films by Ellipsometric Porosimetry,* Electrochem. Solid-State Lett. **5,** F29-F31 (2002).

S. I. Nakao, J. Ushio, T. Ohno, T. Hamada, Y. Kamigaki, M. Kato, K. Yoneda, S. Kondo and N. Kobayashi, *UV/EB cure mechanism for porous PECVD/SOD low-k SiCOH materials*, *Proceedings of the Interconnect Technology Conference* (IEEE, New York), 66-68 (2006).

C. Nguyen, D. D. Do, *The Dubinin-Radushkevich equation and the underlying microscopic adsorption description*, Carbon **39,** 1327-1336 (2001).

G. Pacchioni, L. Skuja, and D. L. Griscom (Eds.), *Defects in SiO2 and related dielectrics: Science and Technology*, Kluwer, Dordrecht (2000).

D. Paehler, D. Schneider, M. Herben, *Nondestructive characterization of sub-surface damage in rotational ground silicon wafers by laser acoustics,* Microelectron. Eng **84,** 340-354 (2007).

M. Pantouvaki, A. Humbert, E. Van Besien, E. Camerotto, Y. Travaly, O. Richard, M. Willegems, H. Volders, K. Kellens, R. Daamen, R.J.O.M. Hoofman and G. Bayer, *Air-gap formation by UV-assisted decomposition of CVD material*, Microelectronic Engineering **85,** 2071-2074 (2008).

L. Prager, P. Marsik, J. W. Gerlach, M. R. Baklanov, S. Naumov, L. Pistol, D. Schneider, L. Wennrich, P. Verdonck, M. R. Buchmeiser, *Effect of pressure on efficiency of UV curing of CVD-derived low-k material at different wavelengths*, Microelectron. Eng. **85,** 2094-2097 (2008).

N. Posseme, T. Chevolleau, T. David, M. Darnon, O. Louveau, and O. Joubert, *Mechanisms of porous dielectric film modification induced by reducing and oxidizing ash plasmas*, J. Vac. Sci. Technol.B **25,** 1928-1940 (2007).

K. Postava, T. Yamaguchi, *Optical functions of low-k materials for interlayer dielectrics*, J. Appl. Phys. **89,** 2189 (2001).

P. I. Ravikovitch and A. V. Neimark, *Density functional theory of adsorption in spherical cavities and pore size characterization of templated nanoporous silicas with cubic and three-dimensional hexagonal structures*, Langmuir **18,** 1550-1560 (2002).

P. I. Ravikovitch and A. V. Neimark, *Density Functional Theory Model of Adsorption Deformation,* Langmuir, **22,** 10864-10868 (2006).

D. Schneider, S. Fruhauf, S. E. Schulz, T. Gessner, *The current limits of the laser-acoustic test method to characterize low-k films*, Microelectron. Eng **82,** 393-398 (2005).

D. Shamiryan, M. R. Baklanov, S. Vanhaelemeersch, and K. Maex, *Comparative study of SiOCH low-k films with varied porosity interacting with etching and cleaning plasma*, J. Vac. Sci. Technol. B **20,** 1923-1928 (2002).

A. M. Urbanowicz, M. R. Baklanov, J. Heijlen, Y. Travaly and A. Cockburn, *Damage reduction and sealing of low-k films by combined He and NH3 plasma treatment*, Electrochem. Solid-State Lett. **10,** G76-G79 (2007).

A. M. Urbanowicz, D. Shamiryan, M. R. Baklanov, and S. De Gendt, *Oxygen chemiluminescence in He plasma as a method for plasma damage evaluation,* Microelectron. Eng. **85,** 2164-2168 (2008).

A. M. Urbanowicz, B. Meshman, D. Schneider, M.R. Baklanov, *Stiffening and hydrophilisation of SOG low-k material studied by ellipsometric porosimetry, UV ellipsometry and laser-induced surface acoustic waves*, Phys. Status Solidi A **205,** 829 (2008).

A. M. Urbanowicz, D. Shamiryan, P. Marsik, Y. Travaly, P. Verdonck, K. Vanstreels, A. Ferchichi, D. De Roest, H. Sprey, K. Matsushita, S. Kaneko, N. Tsuji, S. Luo, O. Escorcia, I. Berry, C. Waldfried, S. De Gendt and M. R.

Baklanov, *Improved Low-k Dielectric Properties Using He/H2 Plasma for Resist Removal*, Advanced Metallization Conference 2008, San Diego, October 8-10 (2008).

A. M. Urbanowicz, K. Vanstreels, D. Shamiryan, S. De Gendt and M. R. Baklanov, *Effect of Porogen Residue on Chemical, Optical, and Mechanical Properties of CVD SiCOH Low-k Materials*, Electrochem. Solid-State Lett. **12,** H292-H295 (2009).

A. M. Urbanowicz, P. Marsik et al., in preparation.

J. Ushio, T. Ohno, T. Hamada, S. I. Nakao, K. Yoneda, M. Kato, and N. Kobayashi, *Ultraviolet-curing mechanism of porous-SiOC*, Jpn. J. Appl. Phys. Part 2-Letters & Express Letters **46,** L405-L407 (2007).

P. Verdonck, D. De Roest, S. Kaneko, R. Caluwaerts, N. Tsuji, K. Matsushita, N. Kemeling, Y. Travaly, H. Sprey, M. Schaekers, and G. Beyer, *Characterization and optimization of porogen-based PECVD deposited extreme low-k materials as a function of UV-cure time*, Surf. Coat. Technol. **201,** 9264-9268 (2007).

www.wikipedia.org

A. Zaka, unpublished report, IMEC (2007).

A. Zenasni, F. Ciaramella, V. Jousseaume, C. Le Cornec, and G. Passemard, *Investigation of porogen behavior during the curing process of ultralow-k spin-on materials - Chemical transformation-kinetics*, J. Electrochem. Soc. **154,** G6-G12 (2007).

A. Zenasni, V. Jousseaume, P. Holliger, L. Favennec, O. Gourhant, P. Maury, and G. Gerbaud, *The role of ultraviolet radiation during ultralow k films curing: Strengthening mechanisms and sacrificial porogen removal*, J. Appl. Phys. **102** (2007).

A. Zenasni, B. Remiat, C. Waldfried, Ch. Le Cornec, V. Jousseaume, G. Passemard, *Thermal furnace cure and Ultraviolet assisted curing impact on SiCOH spin-on low dielectric constant material*, Thin Solid Films,**516,** 1097-1103 (2008).

Acknowledgements